This is to certify that the

dissertation entitled

NONLINEAR DYNAMICS OF SHAFTS ROTATING AT
NONCONSTANT SPIN RATES

presented by

Chih-Kao Ma

has been accepted towards fulfillment
of the requirements for

Ph.D. degree in Mechanical Engineering

Dr A. G. Haddow
Major professor

Date 18 Feb. 1991

NONLINEAR DYNAMICS OF SHAFTS ROTATING AT NONCONSTANT SPIN RATES

By

Chih-Kao Ma

A DISSERTATION

Submitted to
Michigan State University
in partial fulfillment of the requirements
for the degree of

DOCTOR OF PHILOSOPHY

Department of Mechanical Engineering

1991

ABSTRACT

NONLINEAR DYNAMICS OF SHAFTS ROTATING AT NONCONSTANT SPIN RATES

By

Chih-Kao Ma

This study investigates both theoretically and experimentally the effects of nonconstant spin rates upon the nonlinear dynamics of a shaft rotating about its longitudinal axis. It is assumed that the spin rate can be written as the sum of a steady-state part and a small periodic fluctuation. In particular, the spin rate is taken to be of the form $\Omega = \Omega_s + \varepsilon\Omega_A \sin(\omega\tau)$. The fluctuating component gives rise to time dependent coefficients in the system's governing equations and thus a variety of resonant responses result which depend on the relationship between Ω_s, $\varepsilon\Omega_A$, ω and the system's natural frequencies ω_1 and ω_2.

Both pre-buckled and post-buckled behavior of two main classifications, a cantilevered beam and a simply supported shaft, are considered in this study. The theoretical investigation involves obtaining approximate solutions to the governing nonlinear differential equations by application of the method of multiple scales. A variety of resonant conditions, including parametric resonance, main resonance, subharmonic resonance and combination resonance, are investigated in detail. The influence which an additional constraint of $\omega_2 \approx 3\,\omega_1$ has on the pre-buckled behavior of the simply supported shaft is of predominant interest. Numerous numerical examples of these steady-state solutions are presented which highlight a variety of phenomena such as non-existence of steady-state motions, coexistence of steady-state motions and amplitude modulate motions, and re-stabilization of trivial solutions. For the cantilevered beam case, Melnikov's method is used to show that chaotic motions may exist.

Results from an experimental study on a spinning cantilevered beam is used to confirm the presence of a variety of phenomena which were theoretically predicted to exist. Finally, numerical simulations are employed to check a number of the approximate solutions obtained by the method of multiple scales. They are also used to investigate non-steady-state responses.

DEDICATION

To my parents,

and

To my wife.

ACKNOWLEDGMENTS

I would like to express my sincere gratitude to my advisor Dr. Alan G. Haddow for his advice, support, and guidance through this dissertation. I should like to state that it has been a pleasure to work with him. I am very grateful to claim him as a friend and a mentor.

I would like to thank my committee members, Dr. Steven W. Shaw, Dr. Chang-Yi Wang, and Dr. Joseph E. Whitesell, for their comments concerning this dissertation. Also I would like to thank Michael Tamar, Leonard Eisele, and Bob Rose, who worked on the complicated designs and equipment necessary for the experiments in this work.

I would like thank all of my friends at Michigan State, especially my officemate, Ole Buesing for his friendship and effort in setting up the experimental equipment.

I would like to express my sincere appreciation to my wife, Yumei for her constant support, encouragement and patience when I was in graduate school. Additionally I would like to thank my parents, younger sister and younger brothers for their encouragement and support.

Finally, I would like to thank my country, Taiwan, R. O. C., for giving me the financial support while I studied in the United States. This work was partially supported by NSF under grants MSS 8805985 and 8810390. This support is gratefully acknowledged.

TABLE OF CONTENTS

LIST OF TABLES

LIST OF FIGURES

LIST OF SYMBOLS

A	cross-sectional area of the shaft.
E	Young's modulus of elasticity.
I_{xx} , I_{yy}	moment of inertia of the cross section.
l	length of shaft.
$S(z,t)$	the undeformed arc length of the neutral axis(z-axis).
$s(z,t)$	the deformed arc length of the neutral axis.
X_i	the undeformed position of a particle on the shaft.
x_i	the deformed position of a particle on the shaft.
$\vec{i}, \vec{j}, \vec{k}$	the unit vectors in the x, y, and z directions, respectively.
T	the total kinetic energy of the shaft.
ΔT	the kinetic energy per unit length of the shaft.
V	the total potential energy of the shaft.
ΔV	the potential energy per unit length of the shaft.
u, v, w	the displacement components of a particle on the neutral axis in the x, y, and z directions, respectively.
$\bar{u}, \bar{v}, \bar{w}$	the displacement components of a arbitrary particle in the cross-section in the x, y, and z directions, respectively.
$Q(\tau)$, $U(\tau)$	the nondimensional modal displacement in the x direction.
$V(\tau)$	the nondimensional modal displacement in the y direction.
x, y, z	the rotating coordinate frame.
$\Omega\ (\tau)$	the spin rate of the shaft.
Ω_s	mean component of the rotational speed

Ω_A	the amplitude of the sinusoidally oscillating part of the rotational speed
Ω_0	the flexural vibration frequency of small oscillations of the first mode of the non-rotating shaft.
ω	the frequency of the sinusoidally oscillating part of the rotational speed.
ω_0	the spinning natural frequency of the pre-buckled cantilevered beam.
ω_0	the natural frequency of the post-buckled cantilevered beam as it vibrates about the buckled position.
ω_1, ω_2	the natural frequencies of the shaft.
δ	the difference between I_{xx} and I_{yy}, $I_{xx} = (1 + \delta) I_{yy}$.
ρ	the density of the shaft.
ε	the square of slenderness ratio, which is very small.
σ	the detuning parameter.
σ_1	the external detuning parameter.
σ_2	the internal detuning parameter.
μ_i, μ_e	the internal and external damping constants, respectively.
φ	the angle of rotation of an element of the shaft about the y axis.
ϕ	the angle of rotation of an element of the shaft about the x axis.
$(\,)'$	$\frac{\partial()}{\partial z}$.
$\dot{(\,)}$	$\frac{\partial()}{\partial \tau}$.

CHAPTER 1

INTRODUCTION

1.1 Motivation

In the design of turbomachinery one will always encounter rotating components. The shaft is a common example among these components and often they spin at high speeds. It is well known that high rotational speeds can induce vibrations via forces from mass unbalances and from instabilities caused by destabilizing forces such as internal damping, dry friction, hydrodynamic bearings, aerodynamic forces, magnetic, and electrodynamic forces. These vibrations will greatly limit the performance of the design and can even lead to failure. Therefore, the study of the dynamic behavior of shafts and the associated instabilities is an important consideration in turbomachine design.

A great deal of research has been undertaken in the general area of rotating shafts. Attention has focused on such topics as support stiffness, shaft alignment and mass unbalance, non-symmetric stiffness, internal and external damping, and bearing stability. The literature on these topics is immense (e.g., see the books : Dimentberg [1961], Bolotin [1963], Tondl [1965], Vance [1987] and the references contained therein). Past studies have investigated the dynamics of the system during run-up and run-down conditions, i.e., when the speed of rotation changes, monotonically, from zero to its final rotation speed (or vice-versa) (see, Lewis [1932], Iwatsubo et al. [1972], Nonami and Miyashita [1978, 1979], Victor and Ellyin [1981] and Ishida et al. [1987]). Other studies have been concerned with the dynamics when the rotational speed is held constant. However, in practice, the rotational speed of a shaft can only be kept approximately constant due to external perturbations upon the system. Often, the fluctuating component of the rotational speed is sufficiently small (as compared to the mean value of the rotational speed) and the rotating shafts will run at, or close to, a constant speed. However, even small fluctuations can have large effects which may give rise to various types of resonances, such as two-mode internal resonance phenomena, sub, super, and combination resonances, and parametric instabilities.

The aim of this thesis is to report on the influence of an unsteady spin rate, $\Omega(t)$, on the nonlinear dynamic behavior of a flexible shaft rotating about its longitudinal axis. A range of cross sections will be considered, varying from rectangular, in which the shaft is assumed to be infinitely stiff in one direction, to circular. In particular, the spin rate is taken to be of the form $\Omega(t) = \Omega_s + \varepsilon\, \Omega_A \sin(\omega t)$, i.e., a constant spin rate, Ω_s, which has a small sinusoidal fluctuation superimposed upon it. The fluctuating component gives rise to time dependent coefficients in the system's governing equations (i.e., parametric excitation) and thus a variety of resonant responses result which depend on the relationship between Ω_s, $\varepsilon\Omega_A$, ω and the system's natural frequencies. In this study, attention is focused on the parametric resonances and the effect of the internal resonance (i.e., $\omega_2 \approx 3\,\omega_1$, where ω_1 and ω_2 are the linear natural frequencies of the system).

1.2 Literature Review

It is well beyond the scope of this introduction to review the current literature regarding rotating shafts in general and so only studies which are considered to have been most relevant to this thesis shall be cited. For more general information, the reader is refereed to the texts cited in Section 1.1.

1.2.1 Rotating Beams

The dynamics of rotating elastic beams have been the subject of many investigations over the past years. Most describe the case in which the beam lies in the plane of rotation (e.g., turbine blades and propellers). These are classed as radially rotating beams. Fewer studies have been concerned with the dynamics of beams rotating about their longitudinal axis. Amongst these are works by Shaw [1988] who showed, by using a version of Melnikov's method, that chaotic motions exist for a slender beam rotating about its longitudinal axis, acted on by pulsating torques. Wang [1982] investigated the bifurcation branches of a fixed-free beam rotating at a constant rate. Odeh and Tadjbakhsh [1965] and Atanackovic [1984, 1986] also considered axially rotating fixed-free beams whereas a work by Bauer [1980] studied the linear dynamic behavior of a beam rotating with constant spin about its longitudinal axis for a wide variety of end conditions. He also presented the response to harmonically forced oscillations of the beam. Laurenson [1976] used finite element techniques to determine the modal characteristic of rotating beams. Krousgrill and Bajaj [1987] studied a single degree-of-freedom dynamic system rotating at a prescribed rate about a vertical axis. The form of the prescribed rotation rate is given by a constant spin rate which has a small sinusoidal fluctuation superimposed upon it. They found chaotic motions resulting from period-doubling bifurcations.

In the early part of the last decade, spacecraft missions and satellites began to require the use of long flexible appendages to accommodate spin stabilization and for other reasons e.g., antennas and booms. These flexible appendages can be accurately modeled as beams and/or shafts. Generally, the dimensions of these rotating appendages are very large. The flexibility of these rotating appendages, therefore, could no longer be ignored. The determination of the nonlinear dynamic behavior became and remains a subject of prime importance. The effect of booms oriented along the axis of rotation has been treated by Meirovitch and Nelson [1966]. Robe and Kane [1967] investigated the effects of elastic deformation on the stability of a rotating satellite composed of two elastically connected rigid bodies. They found the performance of the system can be highly sensitive to dimension and spin rate changes. Kulla [1972] studied flexible satellite booms under fixed-free boundary conditions in connection with the dynamic behavior of such a satellite.

1.2.2 Rotating Shafts

As long ago as Rankine [1869], problems were being studied regarding shaft vibrations. Jeffcott [1919] proposed a linear model in order to analyze the response of high speed rotating machines to rotor unbalance. Stodola [1924] made theoretical and experimental studies of many fundamental phenomena (e.g., gyroscopic effect, secondary resonance and stability, etc.) of rotating shafts. The critical speeds of shafts with distributed mass were examined by Grammel [1929]. Kimball [1924] and Newkirk and Taylor [1925] were the first to show the possibility of shaft instability in the post-critical range due to nonconservative loads. Kimball found that the cause of instability was internal hysteresis, whereas Newkirk and Taylor identified oil films in journal bearings as another source of instability. Shaw [1989] used methods from dynamical systems and bifurcation theories to investigate the instabilities and resonances of rotors caused by internal hysteresis, fluid film bearing forces, and mass unbalance.

A book by Tondl [1965] presents an extensive collection of experimental results and detailed theoretical analyses associated with the subject of rotor dynamics. Nonlinear and internal resonance conditions are both treated. Yamamoto and his colleagues have been very active over the years, dealing experimentally and theoretically with problems of rotating shafts arising from nonlinear, parametric, combination, and internal resonances.

Lengthy reports have been presented, for example, Yamamoto [1960,1961], Yamamoto and Hayashi [1963] and Ishida et al. [1986,1989,1990].

Parametric instabilities can be induced in rotating systems due to pulsating speeds and torques. Eshleman [1967] developed the equation of motion and the corresponding boundary conditions of this problem, but he did not succeeded in solving the equations. Unger and Brull [1981] presented an analytical and numerical investigation to determine the stability regions of the shaft due to a pulsating torque applied at its ends. They investigated cases of principal and combination parametric resonances and found that the most common and dangerous parametric instabilities arise as a result of combination resonances. Ariaratnam and Namachchivaya [1986] used the method of averaging to examine the bifurcation behavior of parametrically perturbed rotating systems with nonlinear characteristics. A paper by Kammer and Schlack [1987] reported on the effects of nonconstant spin rate on the linear dynamics of rotating shafts. They found that parametric resonances exist for shafts whose cross sections have unequal principal area moments of inertia. However, when the two moments of inertia are equal, the shaft cannot be parametrically excited.

A book by Bolotin [1963] presents an extensive summary of the instabilities of a rotating shaft due to the effects of nonconservative loads. Ehrich [1964] investigated the instability in rotating systems induced by internal damping in the rotor and gave a stability boundary defined in terms of the ratio of external damping of the system to the internal damping in the shaft. Gunter [1967] and Gunter and Trumpler [1969] evaluated the stability of high speed rotors with internal friction on damped, anisotropic supports and attempted to theoretically explain many of the experimental observations of Newkirk [1924] concerning stability due to internal rotor friction. Genin and Maybee [1970] have used energy methods and presented results in the form of boundedness and growth theorems for the problem of whirl motions of a linear viscoelastic continuous shaft. Crandall [1980] gives detailed physical explanations of the destabilizing effects of damping in rotating parts.

The instability phenomena of asymmetric rotating shafts (caused either by the shaft having a non-circular cross section or by slots on key ways) are significantly different from those shafts which have symmetrical cross sections. The first extensive investigation of the vibration of asymmetric shafts was made by Smith [1933], who discussed the cases in which the shaft, or the bearings, or both were asymmetric. Taylor [1940] and Foote et al. [1943] investigated the effect of an asymmetric cross section on the whirling characteristics of high speed rotors. Brosens and Crandall [1961] investigated the motion of the elastically supported rotors having unequal diametral moments of inertia. Crandall and Brosens [1961] studied the stability of a rotating system whose rotor and shaft both are asymmetric. Hull [1961] experimentally investigated the whirling for three shafts with different cross sections in combination with uniform or asymmetric stiffness bearing supports. Ariaratnam [1965] studied the effect of both external and internal damping on the transverse vibration of unsymmetrical rotating shafts. Inagaki et al. [1980] presented an analytical method for the evaluation of the synchronous response of a general asymmetric rotor-bearing system. Genta [1988] derived the equations of motion for a general (an asymmetric rotor running on an asymmetric supporting structure), multi-degree of freedom rotor, based on the finite element method. He then used a series solution to solve these equations. Day [1987] used numerical simulations and the method of multiple scales to investigate the nonlinear Jeffcott model which considered nonlinearities arising from deadband, side forces and rubbing. Mazzilli [1989] used the method of multiple scales to study the effect of a geometric imperfection on the large amplitude vibrations of a horizontal, rotating shaft.

1.3 Scope and Organization of the Thesis

The main task of this study is to investigate by means of analyses, numerical simulations, and experimentation, the dynamic response of a flexible shaft rotating at nonconstant speeds. Particular attention will be focused on the nonlinear behavior of the shaft.

There are two main classifications in this study:

(1) In which the shaft is assumed very stiff in one direction, i.e., we have a beam with a rectangular cross section.

(2) In which the shaft is (a) exactly circular or (b) close to circular.

The general approach adopted to study both of these classifications is to first derive the equations of motion. This is accomplished using Hamilton's principle, and the resulting pair of coupled nonlinear, partial differential equations are reduced to two ordinary differential equations by assuming that the first mode dynamics dominate the shaft's response. The method of multiple scales (Nayfeh and Mook [1979] and Nayfeh [1981]) is then employed to find approximate solutions to these equations. The accuracy of these approximate solutions are then checked by direct numerical integration of the equations of motion.

An important part of the overall study is the inclusion of a physical model. It is used to obtain a realistic range of values for the parameters used in the mathematical model. Moreover, the results obtained from the experimental part of the work will, it is hoped, add credence to the simplifying assumptions used in the theoretical component of the study. Experimental results may also uncover responses that the theory did not predict. Hence the experimental work can be used to refine the theoretical approach. It is also believed that working with the experimental set up will give better insight into the physics of the problem.

In particular, the arrangement of the thesis is as follows:

In Chapter 2, a mathematical model which characterizes the rotating shaft is derived. Three partial differential equations are obtained using Hamilton's principal which are then reduced to two nonlinear ordinary differential equations in terms of the first modal amplitudes. These equations are the basis for all subsequent analyses.

The nonlinear dynamics of a cantilevered beam rotating at a nonconstant spin rate about its longitudinal axis are investigated in Chapters 3 and 4. In Chapter 3 we restrict our investigation to a mean spin rate Ω_s less than Ω_0 (where Ω_0 is the flexural vibration frequency of small oscillations of the first mode of the non-rotating shaft). The equation of motion is homogeneous with time dependent coefficients and cubic nonlinearities. The principal parametric resonance is studied (i.e., $\omega \approx 2\,\omega_0$ where ω_0 is the natural frequency of the beam as it rotates). If the mean rotating speed Ω_s is greater than Ω_0, the beam will buckle to a non-zero equilibrium position. This is the case discussed in Chapter 4. Using a coordinate transformation, the equations of motion governing the shaft's motions about the buckled position are obtained and are found to be nonhomogeneous, containing quadratic and cubic nonlinearities and time dependent coefficients. Attention is focused on two resonances, $\omega \approx 2\,\omega_0$ and $\omega \approx \omega_0$, and approximate solutions are obtained for oscillations around the buckled position. Numerical simulation are employed to track the beam's behavior as the motion changes from oscillating about one buckled position, to a motion that encompasses both buckled positions. Bifurcated and chaotic motions are observed in this instance and so use is made of Melnikov's method to determine the parameter conditions for the possible existence of chaos.

In Chapters 5 and 6 we deal with the dynamics of a shaft with circular and close to circular cross section. The problem now involves two, coupled, nonlinear ordinary differential equations, and hence there exists the possibility of an internal resonances between the two rotating natural frequencies ω_1 and ω_2. Chapter 5 examines the pre-critical behavior of the rotating shaft. In particular, four cases of external resonance are studied: $\omega \approx 2\omega_1$, $\omega \approx 2\omega_2$, $\omega \approx \omega_1 + \omega_2$ and $\omega \approx \omega_2 - \omega_1$, both in the presence of, and the absence of, internal resonance. Chapter 6 is concerned with the post-critical behavior of the shaft. When the shaft is buckled, low order internal resonances did not exist. However, there is the added complication of the possibility of chaotic motions. This is studied using numerical simulations.

Chapter 7 describes the experimental setup and presents the results obtained from experiments completed on a cantilevered beam. These are compared, qualitatively, with the theoretical results of Chapters 3 and 4. Finally, conclusions and recommendations for future work are presented in Chapter 8.

CHAPTER 2

MATHEMATICAL MODELLING OF THE SYSTEM

2.1 General

This chapter is concerned with the mathematical modelling of the system which is illustrated in Figure 2.1. The general configuration investigated in this study consists of a long slender shaft of length l, rotating about its longitudinal axis at a nonconstant rate, $\Omega(t)$, executing motions which can be described by deflections (u,v,w) measured relative to a rotating coordinate frame (x,y,z) which is also rotating at $\Omega(t)$. In the analysis the following assumptions are made: (a) the effects of applied forces, torques and gravity are negligible, (b) the thickness of the shaft is so small compared to the length, that the effects of shearing deformation and rotatory inertia of the shaft can be neglected, (c) the bearings are rigid and axially symmetric, (d) the frequency of excitation is far below the first axial and torsional resonances, and (e) that plane sections remain plane and so we may neglect inertial torsional and axial effects. Hence, the shaft can be mathematically modeled using Bernoulli-Euler beam theory. Having found the kinetic and potential energy of the shaft, the equations of motion are derived using Hamilton's principle and the resulting coupled nonlinear, partial differential equations are reduced to ordinary differential equations by assuming that the first mode dynamics dominate the shaft's response. The equations of motion contain nonlinearities up to order three. Two classifications of boundary condition will be investigated in this study: (a) cantilever and (b) simply supported.

Employing the above beam theory assumptions, the displacement of an arbitrary point in the cross section is given by

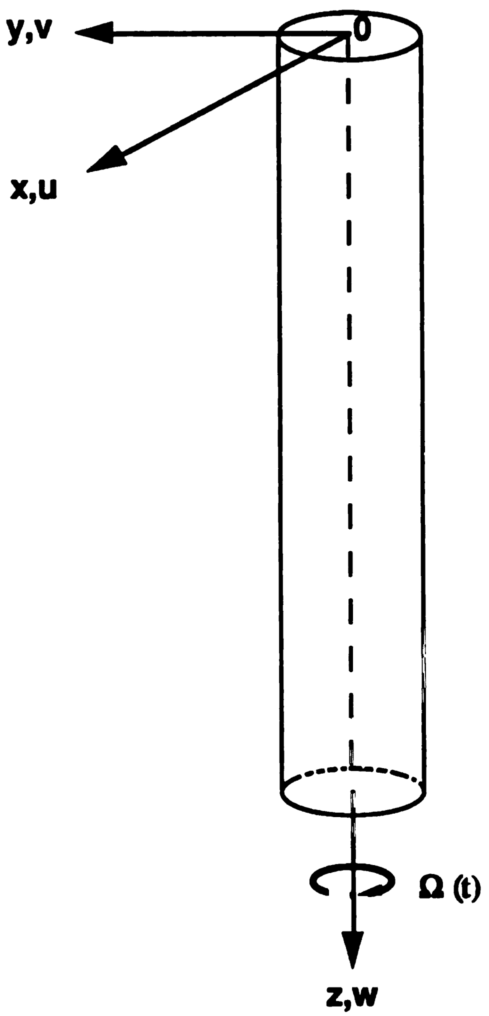

Figure 2.1 The coordinate system.

$$\bar{u}\,(x, y, z, t) = u(z,t) \tag{2.1}$$

$$\bar{v}\,(x, y, z, t) = v(z,t) \tag{2.2}$$

$$\begin{aligned}\bar{w}(x, y, z, t) &= w(z,t) - x\varphi(z,t) - y\phi(z,t) + \varepsilon_0 z \\ &= \eta_1(z,t) + \eta_2(z,t) - x\varphi(z,t) - y\phi(z,t) + \varepsilon_0 z \end{aligned} \tag{2.3}$$

where the z-axis is the neutral axis of the shaft and the x, y-axes are axes of symmetry for the cross-section (the principal centroidal axes of the shaft's cross-section); u, v and w are the displacement components of a point on the neutral axis in the x,y and z directions, respectively; φ and ϕ are the angles of rotation of an element of the shaft about the y and x axes, respectively. Note that the axial displacement $\overline{w}(x, y, z,t)$ is composed of five components: (a) displacement, $\eta_1(z,t)$, which is defined as being associated with uniform elastic extension of the neutral axis; (b) displacement, $\eta_2(z,t)$, which is defined as being associated with the "foreshortening effect", i.e., the axial displacement of the shaft due to large transverse displacements; (c and d) displacements, $x\varphi$ and $y\phi$, associated with fiber strain of "plane sections" bending; (e) initial strain $\varepsilon_0 z$.

We assume $\varepsilon_0 = 0$ in this study. The displacement of an arbitrary particle in the cross section of the shaft can then be written as

$$\begin{aligned} \vec{r} &= \overline{u}(x, y, z,t)\, \vec{i} + \overline{v}(x, y, z,t)\, \vec{j} + \overline{w}(x, y, z,t)\, \vec{k} \\ &= u(z,t)\, \vec{i} + v(z,t)\, \vec{j} + [w(z,t) - x\varphi(z,t) - y\phi(z,t)]\, \vec{k} \end{aligned} \tag{2.4}$$

where ($\vec{i}, \vec{j}, \vec{k}$) are the usual unit vectors.

The velocity of this particle is given by

$$\begin{aligned} \vec{V}_e &= \dot{\vec{r}} + \vec{\Omega} \times \vec{r} \\ &= (\dot{u} - v\Omega)\vec{i} + (\dot{v} + u\Omega)\vec{j} + (\dot{w} - x\dot{\varphi} - y\dot{\phi})\vec{k} \end{aligned} \tag{2.5}$$

where $\vec{\Omega} = \Omega\, \vec{k}$.

The kinetic energy per unit length of the shaft ΔT can be written as

$$\begin{aligned}\Delta T &= \frac{1}{2}\int_A \vec{V}_e \bullet \vec{V}_e \, \rho dA \\ &= \frac{1}{2}\int_A \rho\left[(\dot{u}-v\,\Omega)^2+(\dot{v}+u\,\Omega)^2+\dot{w}^2+x^2\,\dot{\varphi}^2+y^2\,\dot{\phi}^2-2(x\,\dot{\varphi}+y\,\dot{\phi})\dot{w}+2\,x\,y\,\dot{\varphi}\,\dot{\phi}\right] dA\end{aligned} \tag{2.6}$$

In the modelling, we are not including the effects of rotary inertia and hence the total kinetic energy of the shaft T is found to be

$$\begin{aligned}T &= \frac{1}{2}\int_0^l \Delta T \, dz \\ &= \frac{1}{2}\rho A \int_0^l \left[(\dot{u}-v\,\Omega)^2+(\dot{v}+u\,\Omega)^2+\dot{w}^2\right] dz\end{aligned} \tag{2.7}$$

In the next two sections we will find the potential energy of the shaft and then use Hamilton's principle to derive the equations of motion for two different systems, a cantilevered beam and a simply supported shaft.

2.2 The Case of a Rotating Cantilever Beam

For this case the shaft is assumed to be infinitely stiff in one direction (i.e., a beam). We also use the following assumptions: (a) If the beam is kept relatively short (e.g., less than 20 beam width), the transverse vibration is purely planar (i.e., v = 0); (b) The axial deformation of the neutral axis is negligible; (c) the beam has a moderately large curvature.

Define extensional strain of the neutral axis as

$$\varepsilon_{zz} = \frac{1}{2}\,\frac{ds^2 - dS^2}{dS^2} \tag{2.8}$$

where S is the undeformed arc length of the neutral axis and s is the deformed arc length of the neutral axis. Using this definition, it can be shown (Ho, Scott and Eisley [1975]) that the only non-zero strain component ε_{zz} in terms of displacement components is

$$\begin{aligned}\varepsilon_{zz} &= \overline{w}' + \tfrac{1}{2}\left[\overline{u}'^2 + \overline{w}'^2\right] \\ &= w' - x\varphi' + \tfrac{1}{2}\left[\overline{u}'^2 + \overline{w}'^2\right]\end{aligned} \tag{2.9}$$

It is assumed that the longitudinal motions are small, i.e., $\overline{w}'^2 \approx 0$. Hence we can obtain

$$\varepsilon_{zz} = w' - x\varphi' + \tfrac{1}{2}\, u'^2 \tag{2.10}$$

From assumption (c), it can be shown that (see Appendix A).

$$\frac{\partial\varphi}{\partial z} \approx u''\left[1 + \frac{1}{2}\, u'^2\right]. \tag{2.11}$$

The potential energy per unit length of the shaft ΔV can then be written as

$$\begin{aligned}\Delta V &= \int_A \frac{E\varepsilon_{zz}{}^2}{2}\, dA \\ &= \frac{E}{2}\left[A w'^2 + A w' u'^2 + I_{yy}\, u''^2\, (1 + \frac{1}{2} u'^2)^2 + \frac{A}{4} u'^4\right]\end{aligned} \tag{2.12}$$

Note that the potential energy is composed of two components: (a) the elastic potential energy due to bending; (b) the elastic potential energy due to stretching of the shaft.

The total potential energy of the shaft V can be found as

$$\begin{aligned}V &= \int_0^l \Delta V\, dz \\ &= \frac{E}{2}\int_0^l \left[A w'^2 + A w' u'^2 + I_{yy} u''^2 \left(1+\frac{1}{2}u'^2\right)^2 + \frac{A}{4}u'^4\right] dz\end{aligned} \tag{2.13}$$

Hence the Lagrangian function is given by L(t) = T(t)-V(t). According to Hamilton's principle, we must determine the functions u(z,t) and w(z,t) which render stationary $\int_{t_1}^{t_2} L(t)\,dt$. A straightforward application of the methods of calculus of variations yields the equations of motion:

$$\rho A \ddot{w} - EA\frac{\partial}{\partial z}\left[w' + \frac{1}{2}u'^2\right] = 0 \tag{2.14}$$

$$\begin{aligned}&\rho A \ddot{u} + EI_{yy}\left(u'''' + u''''u'^2 + 4\,u'u''u''' + u''^3\right) - \rho A \Omega^2 u \\ &\quad - EA\frac{\partial}{\partial z}\left[w' + \frac{1}{2}u'^2\right]u' - EA\left[w' + \frac{1}{2}u'^2\right]u'' = 0\end{aligned} \tag{2.15}$$

Equation (2.14) can be simplified by the following manipulations. Integrate it to obtain

$$EA\left[w' + \frac{1}{2}u'^2\right] = \int_0^z \rho A \ddot{w}(\xi,t)\,d\xi + C(t) \tag{2.16}$$

where C (t) is an arbitrary time dependent function. The normal force on any shaft cross-section is

$$\begin{aligned}N(z,t) &= \int_A \sigma\, dA \\ &= \int_A E\, \varepsilon_{zz}(z,t)\, dA \\ &= E\int_A\left[w' - x\varphi' + \tfrac{1}{2}u'^2\right] dA \\ &= E\,A\left[w' + \tfrac{1}{2}u'^2\right]\end{aligned} \tag{2.17}$$

Now, since N(l,t) = 0, we may combine this with equations (2.16) and (2.17) to conclude that

$$N(z,t) = -\int_z^l \rho A \ddot{w}(\xi,t)\, d\xi \qquad (2.18)$$

Substituting equations (2.17) and (2.18) into the equation (2.15), we obtain

$$\begin{aligned}&\rho A\ddot{u} + EI_{yy}\left(u'''' + u''''u'^2 + 4\,u'u''u''' + u''^3 \right) - \rho A\Omega^2 u + \mu_e \dot{u} - \\ &\qquad \rho A \ddot{w}\, u' + u'' \int_z^l \rho A \ddot{w}(\xi,t)\, d\xi = 0 \end{aligned} \qquad (2.19)$$

where μ_e is a viscous damping term added to the equation to allow for some energy dissipation.

The function w(z,t) can be eliminated from equation (2.19) by using the following expression (see Appendix B)

$$w(z,t) \equiv -\frac{1}{2}\int_0^z u'^2(\xi,t)\, d\xi \qquad (2.20)$$

The governing integro-differential equation which determines u(z,t) is found by substituting equation (2.20) into equation (2.19) . The equation is:

$$\begin{aligned}&\rho A\ddot{u} + EI_{yy}\left(u'''' + u''''u'^2 + 4u'u''u''' + u''^3 \right) - \rho A\Omega^2 u + \mu_e \dot{u} \\ &\quad + \frac{1}{2}\rho A\, u' \frac{\partial^2}{\partial t^2}\int_0^z \left[u'^2(\xi,t)\right] d\xi - \frac{1}{2}\rho A\, u'' \int_z^l \frac{\partial^2}{\partial t^2} \left\{ \int_0^\xi \left[u'^2(\eta,t)\right]\, d\eta \right\} d\xi = 0\end{aligned}$$

(2.21)

In order to transform equation (2.21) to dimensionless form, we use the following non-dimensional variables:

$$\bar{z} = \frac{z}{l}, \quad \bar{u} = \frac{u}{l}, \quad \tau = \sqrt{\frac{E I_{yy}}{\rho A_0 l^4}}\, t = \Gamma t$$

$$\bar{\Omega} = \frac{\Omega}{\Gamma}, \quad \bar{\mu}_e = \frac{\mu_e}{\rho A_0 \Gamma} .$$

Equation (2.21) then rescales to (dropping the overbars for convenience)

$$\ddot{u} + (u'''' + u''''u'^2 + 4u'u''u''' + u''^3) - \Omega^2 u + \mu_e \dot{u}$$
$$+ \frac{1}{2} u' \frac{\partial^2}{\partial \tau^2} \int_0^z u'^2(\xi,\tau)\, d\xi - \frac{1}{2} u'' \int_z^1 \frac{\partial^2}{\partial \tau^2} \left\{ \int_0^\xi u'^2(\eta,\tau)\, d\eta \right\} d\xi = 0 \tag{2.22}$$

where

$$(\dot{\ }) = \frac{\partial(\,)}{\partial \tau}$$

$$(\,)' = \frac{\partial(\,)}{\partial z} .$$

Equation (2.22) can be reduced to a nonlinear ordinary differential equation by using Galerkin's method. We take a first mode approximation to the solution using the eigenfunction , $\Phi(z)$, of the linearized fixed-free beam as the coordinate function.

Let

$$u(z,\tau) = Q(\tau)\, \Phi(z) \tag{2.23}$$

where

$Q(\tau)$ is the nondimensional modal displacement

$\Phi(z) = \cosh \beta_1 z - \cos \beta_1 z - 0.7341 (\sinh \beta_1 z - \sin \beta_1 z)$

$\beta_1 = 1.8751.$

Substituting equation (2.23) into equation (2.22) and applying Galerkin's method then yields:

$$\ddot{Q} + d\,(Q^2 \ddot{Q} + Q \dot{Q}^2) + \mu_e \dot{Q} + b\,Q^3 + (\Omega_0{}^2 - \Omega^2)\,Q = 0 \tag{2.24}$$

where

$$d = \int_0^1 \left[\int_0^z \Phi'^2 d\xi \right] \Phi'\Phi\, dz - \int_0^1 \left\{ \int_z^1 \left[\int_0^\xi \Phi'^2 d\eta \right] d\xi \right\} \Phi''\Phi\, dz \tag{2.25}$$

$$b = \int_0^1 \Phi'''' \Phi'^2 \Phi\, dz + \int_0^1 \Phi' \Phi'' \Phi''' \Phi\, dz + \int_0^1 \Phi''^3 \Phi\, dz \tag{2.26}$$

$$\Omega_0{}^2 = \beta_1{}^4 .$$

Numerical values for the constant d and b are obtained by numerical integration of equations (2.25) and (2.26), and they are

$b = 4.60$

$d = 40.44.$

2.3 The Case of a Rotating, Simply Supported Shaft

For this case we assume: (a) the longitudinal inertia force is negligible, and (b) the curvature is small (i.e., linear curvature). As will be shown, the source of the nonlinearity is from mid-plane stretching which arises on account of the distance between the supports being fixed.

The potential energy per unit length of the shaft ΔV can be written as

$$\Delta V = \int_A \frac{E\varepsilon_{zz}{}^2}{2}\, dA$$
$$= \frac{E}{2}\left[A w'^2 + A w'(u'^2 + v'^2) + I_{yy} u''^2 + I_{xx} v''^2 + \frac{A}{4}(u'^2 + v'^2)^2\right] \tag{2.27}$$

The total potential energy of the shaft V can be found as

$$V = \int_0^l \Delta V\, dz$$
$$= \frac{E}{2}\int_0^l \left[A w'^2 + A w'(u'^2 + v'^2) + I_{yy} u''^2 + I_{xx} v''^2 + \frac{A}{4}(u'^2 + v'^2)^2\right] dz \tag{2.28}$$

The equations of motion are then obtained by applying Hamilton's principle which result in the following

$$\rho A \ddot{w} - EA\frac{\partial}{\partial z}\left[w' + \frac{1}{2}(u'^2 + v'^2)\right] = 0 \tag{2.29}$$

$$\rho A\ddot{u} + EI_{yy}\, u'''' - 2\rho A\Omega\, \dot{v} - \rho A\Omega^2 u - \rho A v\, \dot{\Omega} + \mu_e(\dot{u} - v\Omega)$$
$$- EA\frac{\partial}{\partial z}\left[w' + \frac{1}{2}(u'^2 + v'^2)\right] u' + \mu_i \dot{u} - EA\left[w' + \frac{1}{2}(u'^2 + v'^2)\right] u'' = 0 \tag{2.30}$$

$$\rho A\ddot{v}+EI_{xx}v'''' +2\rho A\Omega\dot{u}-\rho A\Omega^2 v+\rho Au\dot{\Omega}+\mu_e(\dot{v}+u\Omega)$$
$$-EA\frac{\partial}{\partial z}\left[w'+\frac{1}{2}(u'^2+v'^2)\right]v'+\mu_i\dot{v}-EA\left[w'+\frac{1}{2}(u'^2+v'^2)\right]v''=0 \tag{2.31}$$

We have also simply added external and internal damping terms in the equations of motion such that the external damping force is proportional to the absolute velocity, while the internal damping force is proportional to the shaft's velocity relative to the rotating coordinate system. The z component of these equations is simplified by assuming the longitudinal inertial force $\rho A\ddot{w}=0$ and by assuming that the shaft carries no initial axial load; it is given by

$$\frac{\partial}{\partial z}\left[w'+\frac{1}{2}(u'^2+v'^2)\right]=0 \tag{2.32}$$

Integrating equation (2.32) with respect to z and using the boundary conditions w(0) = w(l) = 0, yields

$$w'+\frac{1}{2}(u'^2+v'^2)=\frac{1}{2l}\int_0^l (u'^2+v'^2)\,dz \tag{2.33}$$

The dependent function w(z,t) can be eliminated by substituting equations (2.32) and (2.33) into equations (2.30) and (2.31) to yield

$$\rho A\ddot{u}+EI_{yy}u'''' -2\rho A\Omega\dot{v}-\rho A\Omega^2 u-\rho Av\dot{\Omega}+\mu_e(\dot{u}-v\Omega)$$
$$+\mu_i\dot{u}-\frac{EA}{2l}u''\int_0^l(u'^2+v'^2)\,dz=0 \tag{2.34}$$

$$\rho A\ddot{v}+EI_{xx}v'''' +2\rho A\Omega\dot{u}-\rho A\Omega^2 v+\rho Au\dot{\Omega}+\mu_e(\dot{v}+u\Omega)$$
$$+\mu_i\dot{v}-\frac{EA}{2l}v''\int_0^l(u'^2+v'^2)\,dz=0 \tag{2.35}$$

In order to transform equations (2.34) and (2.35) to dimensionless form, we use the following non-dimensional variables :

$$\bar{z} = \frac{z}{l}\,, \quad \bar{u} = \frac{1}{\sqrt{2}}\frac{l}{r_{yy}^{\,2}}\,u\,, \quad \bar{v} = \frac{1}{\sqrt{2}}\frac{l}{r_{yy}^{\,2}}\,v$$

$$\tau = \sqrt{\frac{EI_{yy}}{\rho A l^4}}\;t = \Gamma\;t\,, \quad \bar{\Omega} = \frac{\Omega}{\Gamma}$$

$$\bar{\mu}_e = \frac{1}{2}\left(\frac{l}{r_{yy}}\right)^2 \frac{1}{\rho A\,\Gamma}\mu_e\,, \quad \bar{\mu}_i = \left(\frac{l}{r_{yy}}\right)^2 \frac{1}{\rho A\,\Gamma}\mu_i$$

and relationships:

$$I_{xx} = (1+\delta)\,I_{yy}$$

$$I_{yy} = A\,r_{yy}^{\,2}.$$

Equations (2.34) and (2.35) can then be rescaled to (dropping all the overbars for convenience)

$$\ddot{u} + u'''' - 2\Omega\dot{v} - \Omega^2 u - v\dot{\Omega} - \left(\frac{r_{yy}}{l}\right)^2 u'' \int_0^1 (u'^2 + v'^2)\,dz$$
$$+ 2\left(\frac{r_{yy}}{l}\right)^2 \mu_e(\dot{u} - v\Omega) + \left(\frac{r_{yy}}{l}\right)^2 \mu_i\,\dot{u} = 0 \tag{2.36}$$

$$\ddot{v} + (1+\delta)v'''' + 2\Omega\dot{v} - \Omega^2 v + u\dot{\Omega} - \left(\frac{r_{yy}}{l}\right)^2 v'' \int_0^1 (u'^2 + v'^2)\,dz$$
$$+ 2\left(\frac{r_{yy}}{l}\right)^2 \mu_e(\dot{v} + u\Omega) + \left(\frac{r_{yy}}{l}\right)^2 \mu_i\,\dot{v} = 0 \tag{2.37}$$

Equations (2.36) and (2.37) can be reduced to nonlinear ordinary differential equations by using Galerkin's method. To this end, a first mode approximation to the solution is assumed using $\Phi(z)$, the eigenfunction of the linearized simply supported shaft.

Let

$$u = U(\tau)\,\Phi(z) \tag{2.38}$$

$$v = V(\tau)\,\Phi(z) \tag{2.39}$$

where

$U(\tau), V(\tau)$ are unknown functions of time τ

$\Phi(z) = \sqrt{2}\,\sin \pi z.$

Substituting equations (2.38) and (2.39) into equations (2.36) and (2.37) and applying Galerkin's method then yields

$$\begin{aligned}&\ddot{U} + (\Omega_0{}^2 - \Omega^2)\,U - 2\,\Omega\,\dot{V} - V\,\dot{\Omega} + 2\,\varepsilon\,\mu_e\,(\dot{U} - V\Omega)\\ &\quad + \varepsilon\,\mu_i\dot{U} + \varepsilon\,\Omega_0{}^2 U(\,U^2 + V^2) = 0\end{aligned} \tag{2.40}$$

$$\begin{aligned}&\ddot{V} + ((1+\delta)\,\Omega_0{}^2 - \Omega^2)\,V + 2\,\Omega\,\dot{U} + U\,\dot{\Omega} + 2\,\varepsilon\,\mu_e\,(\dot{V} + U\,\Omega\,)\\ &\quad + \varepsilon\,\mu_i\dot{V} + \varepsilon\,\Omega_0{}^2 V(\,U^2 + V^2) = 0\end{aligned} \tag{2.41}$$

where $\varepsilon = \left(\frac{r_{yy}}{l}\right)^2$.

It is important to note the definition and interpretation of a few of the terms in equations (2.40) and (2.41):

Ω_0	the flexural vibration frequency of small oscillations of the first mode of the non-rotating shaft.
ε	the square of slenderness ratio, which is very small.
δ	the difference between I_{xx} and I_{yy}, $I_{xx} = (1+\delta)\,I_{yy}$.
$U(\tau)$	nondimensional modal displacement in the x direction.
$V(\tau)$	nondimensional modal displacement in the y direction.

2.4 Summary of the Chapter

Equations of motion have been presented for a shaft rotating about its longitudinal axis at a nonconstant rotational speed. The equations of motion were derived using Hamilton's principle and the resulting coupled nonlinear, partial differential equations were reduced to ordinary differential equations by assuming that the first mode dynamics dominate the shaft's response. Two different systems were investigated in this chapter: (a) a cantilevered beam and (b) a simply supported shaft. The equations of motion contain nonlinearities up to order three.

CHAPTER 3

ANALYSIS OF A ROTATING CANTILEVER BEAM WITH $\Omega_s < \Omega_0$

3.1 Introduction

In this chapter we investigate the nonlinear, planar motion of a uniform, initially straight, elastic beam rotating about its longitudinal axis at a nonconstant spin rate. The spin rate is expressed as the sum of a steady-state term (i.e., Ω_s) and a relatively small sinusoidal perturbation. The beam is considered to be fixed at one end and free at the other. For a beam with these end conditions, nonlinearities can arise due to moderately large curvatures and the longitudinal inertial forces (Atluri [1973]). We will restrict our investigation to mean spin rates, Ω_s, less than these required to buckle the beam, i.e., $\Omega_s < \Omega_0$ where Ω_0 is the flexural vibration frequency of small oscillations of mode one of the non-rotating beam. In Chapter 4 we will analyze the case of $\Omega_s > \Omega_0$ (i.e., post-buckled), in which the beam stops oscillating about the static equilibrium position and buckles to one side or the other.

The pair of coupled nonlinear, partial differential equations which were derived in Chapter 2 are reduced to one ordinary differential equation by assuming that the motion can be described by a single, in plane mode. Experimental work on a physical system indicate that such an assumption is valid. Approximate solutions to the governing equation of motion are sought using the method of multiple scales and the results are compared to these obtained by direct numerical integration.

3.2 Equations of Motion

From Chapter 2 (see Section 2.2) we know the equation of motion will have the following form:

$$\ddot{Q} + d\,(Q^2\ddot{Q} + Q\dot{Q}^2) + \mu_e\dot{Q} + bQ^3 + (\Omega_0{}^2 - \Omega^2)\,Q = 0 \tag{3.1}$$

where $Q(\tau)$ is the nondimensional modal displacement of the beam.

Note that equation (3.1) describes the first mode response of the rotating beam in the x-z plane subject to assumptions outlined in Chapter 2. It is valid for any form of rotational speed, Ω. In the remaining sections of this chapter, attention will be focused on the solution of equation (3.1) for rotational speeds below the buckling speed, i.e., $\Omega < \Omega_0$. Moreover, the form of Ω will be taken as

$$\Omega = \Omega_s + \varepsilon\Omega_A \sin\omega\tau \tag{3.2}$$

where

ε is an arbitrary small but finite parameter

Ω_s is mean component of the rotational speed

Ω_A is amplitude of the sinusoidally oscillating part of the rotational speed

ω is frequency of the sinusoidally oscillating part of the rotational speed.

3.3 Approximate Solution of the Governing Equation of Motion

The method of multiple scales will be employed to obtain an approximate solution to equation (3.1). To this end, we first reorder the equation by introducing

$$Q = \varepsilon^{\frac{1}{2}} q \tag{3.3}$$

Substituting equation (3.3) into equation (3.1), we obtain

$$\ddot{q} + \varepsilon\, d\,(q\,\dot{q}^2 + q^2\,\ddot{q}) + 2\,\varepsilon\,\mu\,\dot{q} + \varepsilon\, b\, q^3 + (\Omega_0{}^2 - \Omega^2)\, q = 0 \tag{3.4}$$

where $\mu_e = 2\,\varepsilon\,\mu$.

We now seek a first-order uniform solution of the form

$$q(\tau;\varepsilon) = q_0(T_0, T_1) + \varepsilon\, q_1(T_0, T_1) \tag{3.5}$$

where $T_n = \varepsilon^n \tau$.

In terms of T_n, the time derivatives become

$$\frac{d}{d\tau} = D_0 + \varepsilon\, D_1 + \varepsilon^2 D_2 + \cdots\cdots\cdots \tag{3.6}$$

$$\frac{d^2}{d\tau^2} = D_0{}^2 + 2\,\varepsilon\, D_0\, D_1 + \varepsilon^2\,(2\, D_0\, D_2 + D_1{}^2) + \cdots\cdots\cdots \tag{3.7}$$

where $D_n = \dfrac{\partial}{\partial T_n}$.

Substituting equations (3.2), (3.6), (3.7) and (3.8) into equation (3.4) and equating coefficients of like powers of ε, yields

$$D_0^2 q_0 + (\Omega_0^2 - \Omega_s^2)\, q_0 = 0 \tag{3.8}$$

$$\begin{aligned} D_0^2 q_1 + (\Omega_0^2 - \Omega_s^2)\, q_1 = -2\, D_0 D_1 q_0 - d\, [q_0 (D_0 q_0)^2 + q_0^2 D_0^2 q_0] \\ -2\, \mu\, D_0 q_0 - b\, q_0^3 + 2\, \Omega_s \Omega_A \sin \omega\tau\, q_0 \end{aligned} \tag{3.9}$$

The solution of equation (3.8) can be written as

$$q_0 = A \exp(i\omega_0 T_0) + \overline{A} \exp(-i\omega_0 T_0) \tag{3.10}$$

where $\omega_0 = \sqrt{\Omega_0^2 - \Omega_s^2}$ and $\overline{A}$ is the complex conjugate of A.

Then, equation (3.9) becomes

$$\begin{aligned} D_0^2 q_1 + \omega_0^2 q_1 = 2\, d\, \omega_0^2 A^2 [A \exp(3i\omega_0 T_0) + \overline{A} \exp(i\omega_0 T_0)] \\ -2i\, \mu\, \omega_0\, A \exp(i\omega_0 T_0) - b\, A^2 [A \exp(3i\omega_0 T_0) + 3\overline{A} \exp(i\omega_0 T_0)] \\ -2i\omega_0 A' \exp(i\omega_0 T_0) - i A \Omega_s \Omega_A \{ \exp[i(\omega_0 + \omega) T_0 - \exp[i(\omega_0 + \omega) T_0] \} + cc \end{aligned} \tag{3.11}$$

where cc stands for the complex conjugate of the preceding terms and the prime stands for the derivative with respect to T_1. If $\omega \approx 2\omega_0$ we can see that additional secular producing terms will arise in equation (3.11), i.e., a principal parametric response will occur. To quantitatively describe the nearness of ω to the resonances, we introduce a detuning parameter σ defined according to

$$\omega = 2\omega_0 + \varepsilon\sigma \tag{3.12}$$

Substituting equation (3.12) into equation (3.11) and setting the secular producing terms to zero, yields

$$-2\, i\, \omega_0 (A' + \mu A) + (2\, d\, \omega_0^2 - 3\, b)\, A^2 \overline{A} - i\, \overline{A}\, \Omega_A\, \Omega_s \exp(i\, \sigma\, T_1) = 0 \quad (3.13)$$

To solve equation (3.13), it is convenient to write A in the polar form

$$A = \frac{a}{2} e^{i\beta} \quad (3.14)$$

where a and β are real.

Substituting equation (3.14) into equation (3.13) and separating real and imaginary parts yields

$$\omega_0\, a' = -\, \mu\, \omega_0\, a - \frac{a}{2} \Omega_s\, \Omega_A \cos\gamma \quad (3.15)$$

$$a\, \omega_0\, \gamma' = \sigma\, \omega_0\, a - \frac{3\, b\, a^3}{4} + \frac{d\, \omega_0^2\, a^3}{2} + a\, \Omega_s\, \Omega_A \sin\gamma \quad (3.16)$$

where $\gamma = \sigma\, T_1 - 2\, \beta$. (3.17)

Of particular interest are the steady-state motions resulting from $a' = \gamma' = 0$. Hence we have a trivial steady-state solution, a = 0 or

$$\sin\gamma = \frac{1}{\Omega_s\, \Omega_A} \left[-\sigma\, \omega_0 + \frac{a^2}{4} (3\, b - 2\, d\, \omega_0^2) \right] \quad (3.18)$$

$$\cos\gamma = \frac{1}{\Omega_s\, \Omega_A} [-\, 2\, \mu\, \omega_0] \quad (3.19)$$

Squaring and adding equations (3.18) and (3.19), we obtain

$$a^2 = \frac{4\left\{\sigma\,\omega_0 \pm \left[(\Omega_s\Omega_A)^2 - 4\,\mu^2\,\omega_0^{\,2}\right]^{\frac{1}{2}}\right\}}{(3\,b - 2\,d\,\omega_0^{\,2})} \tag{3.20}$$

or, rearranging this equation, we have

$$\sigma = \frac{\frac{a^2}{4}(3\,b - 2\,d\,\omega_0^{\,2}) \pm \left[(\Omega_s\Omega_A)^2 - 4\,\mu^2\,\omega_0^{\,2}\right]^{\frac{1}{2}}}{\omega_0} \tag{3.21}$$

Using equations (3.3), (3.5),(3.10), (3.14) and (3.17) it is found that

$$Q = \varepsilon^{\frac{1}{2}}\, a \cos\left[\frac{\omega\tau - \gamma}{2}\right] + O(\varepsilon^{\frac{3}{2}}) \tag{3.22}$$

Numerical examples of these steady-state responses will be given in Section 3.4.

Their stability can be ascertained by adding a small perturbation to the steady-state value and checking if this perturbation grows or decays. For the trivial solution this results in a unstable solution for $-\sigma_1 < \sigma < \sigma_1$ where

$$\sigma_1 = \left[\left(\frac{\Omega_s\Omega_A}{\omega_0}\right)^2 - 4\,\mu^2\right]^{\frac{1}{2}} \tag{3.23}$$

The analysis to check the stability of the non-trivial steady-state value, a and γ, results in the following inequality for a stable solution

$$\frac{a^2}{2\omega_0}\,\Omega_s\Omega_A \sin\gamma\left[\omega_0 d - \frac{3\,b}{2\omega_0}\right] < 0 \tag{3.24}$$

The figures in Section 3.4 show the results of this stability analysis. A solid line denotes a stable solution, a dashed line indicates an unstable solution. It can be proved that the upper branch is always stable, whereas the lower branch is always unstable.

3.4 Numerical Results

In this section we present representative solutions of the equations derived in Section 3.3. Values for various parameters are based on a physical system which was used in laboratory tests. The parameter values used, unless otherwise stated, are:

$\Omega_s = 2.8$, $\varepsilon\Omega_A = 0.1$, $\varepsilon = 0.01$, $\Omega_0 = 3.516$, $b = 40.44$, $d = 4.60$, (and hence $\omega_0 = 2.1266$), and $2\varepsilon\mu = 0.00422$.

Figure 3.1 shows a typical frequency response curve for a non-zero mean spin rate ($\Omega_s = 2.8$). This shows the variation of the steady-state amplitude as a function of the oscillating component of the spin. Clearly, the overall non-linearity of the system is of the hardening type. To the order of approximation used in the present analysis, the stable and unstable non-trivial solutions continue to a exist as σ is increased. A higher order analysis would rectify this deficiency which of course could not occur in practice. The results obtained from directly numerically integrating equation (3.1) are also shown on this figure and are discussed later.

A series of results presented in Figure 3.2 show the effect of the mean spin rate, Ω_s, on the steady-state amplitude, a. Three plots are presented for different values of σ. In each, when Ω_s approaches $\Omega_0 = 3.516$ the results become invalid since the analysis used in Section 3.3 is restricted to $\Omega_s < \Omega_0$. It is interesting to note that for some values of,σ (Figures 3.2b and c), the steady-state amplitude decreases as Ω_s is increased. There also exist regions in which the jump phenomenon can be observed.

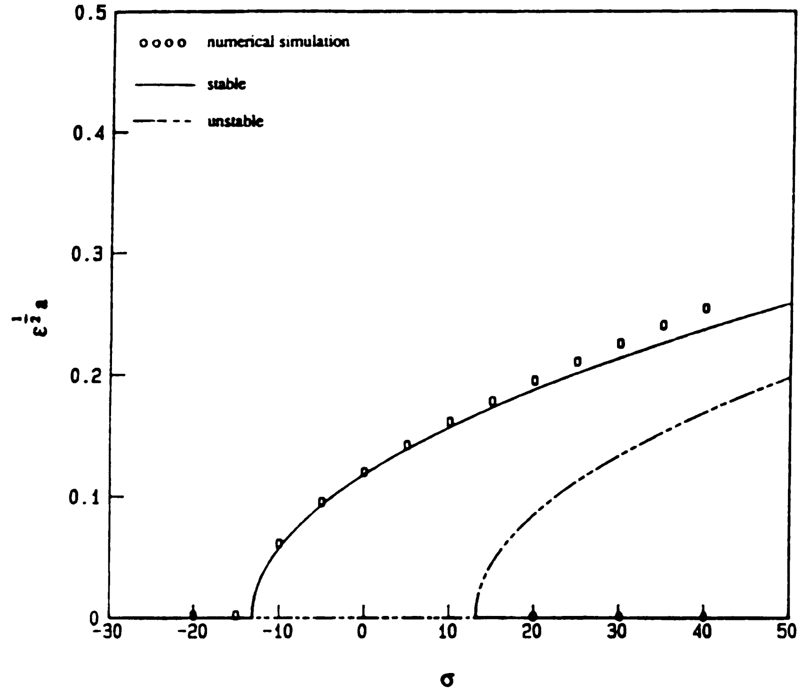

Figure 3.1 Variation of the Steady-State Amplitude, a, with σ.

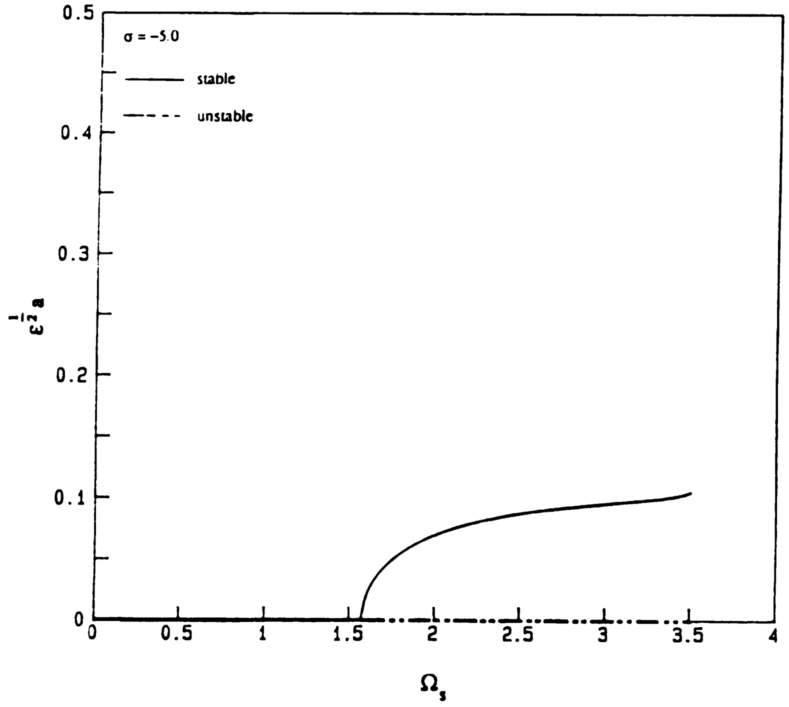

Figure 3.2a Variation of the Steady-State Amplitude, a, with Ω_s for σ = -5.0.

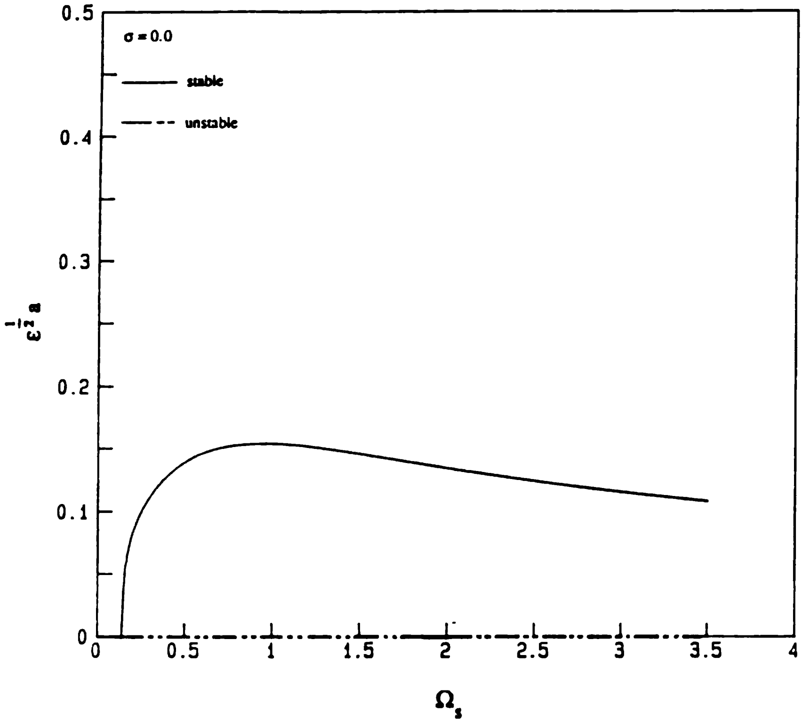

Figure 3.2b Variation of the Steady-State Amplitude, a, with Ω_s for $\sigma = 0.0$.

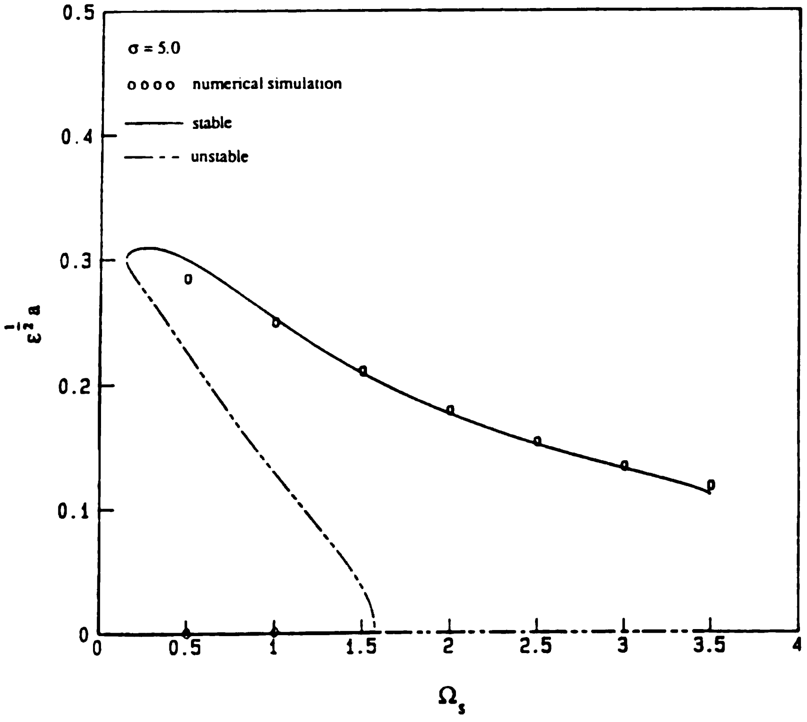

Figure 3.2c Variation of the Steady-State Amplitude, a, with Ω_s for $\sigma = 5.0$.

Figure 3.3 presents results showing the variation of the steady-state amplitude as a function of $\varepsilon\Omega_A$, the amplitude of the oscillating component of the spin. Figure 3.3a is plotted for a detuning value of -20 and shows that there is always only one stable steady-state, whereas Figure 3.3b shows that for a detuning value of 20, multiple steady-states are possible.

The results obtained using the method of multiple scales can be checked by directly numerically integrating equation (3.1). This was undertaken for a number of different cases and the results have been plotted as "numerical simulation" on Figures 3.1 and 3.2c. The comparison is good in all the cases tested. In situations where two stable, steady-states exist, the solution adopted depends on the choice of the initial conditions. A few examples of these simulations corresponding to Figure 3.1 are presented as time traces in Figure 3.4. It should be noted that only the envelope of the solution, $Q(\tau)$, is plotted in these figures.

3.5 Summary of the Chapter

We have investigated the pre-buckled behavior of a fixed-free beam rotating about its longitudinal axis at a nonconstant spin rate. The spin rate was expressed as the sum of a steady-state part and a relatively small sinusoidally varying component. The approximate analytical solutions were obtained using the method of multiple scales and it was clearly demonstrated that a principal parametric resonance can occur at mean spin rates well below the first critical speed of the beam. For this type of resonance, the nonlinearities were of a hardening type. The perturbation solutions accurately predict the amplitude of the steady-state motions and their stability as compared to the numerical simulation results.

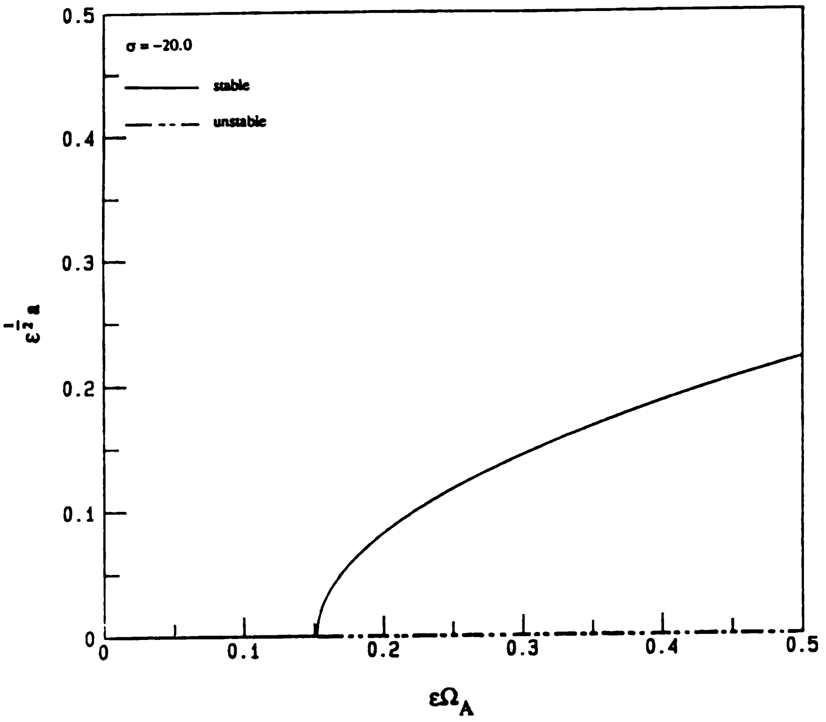

Figure 3.3a Variation of the Steady-State Amplitude, a, with $\epsilon\Omega_A$ for $\sigma = -20.0$.

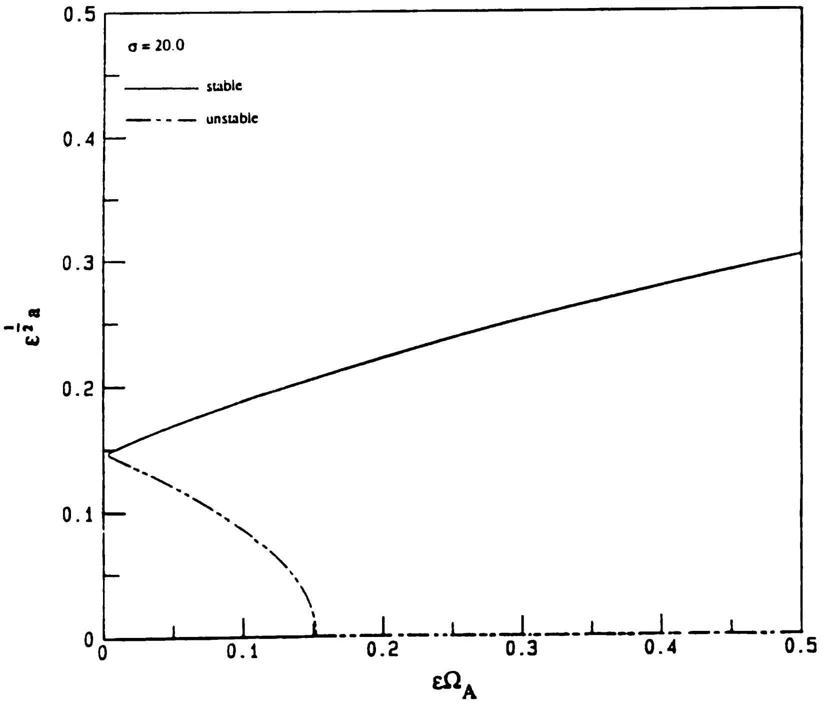

Figure 3.3b Variation of the Steady-State Amplitude, a, with $\epsilon\Omega_A$ for $\sigma = 20.0$.

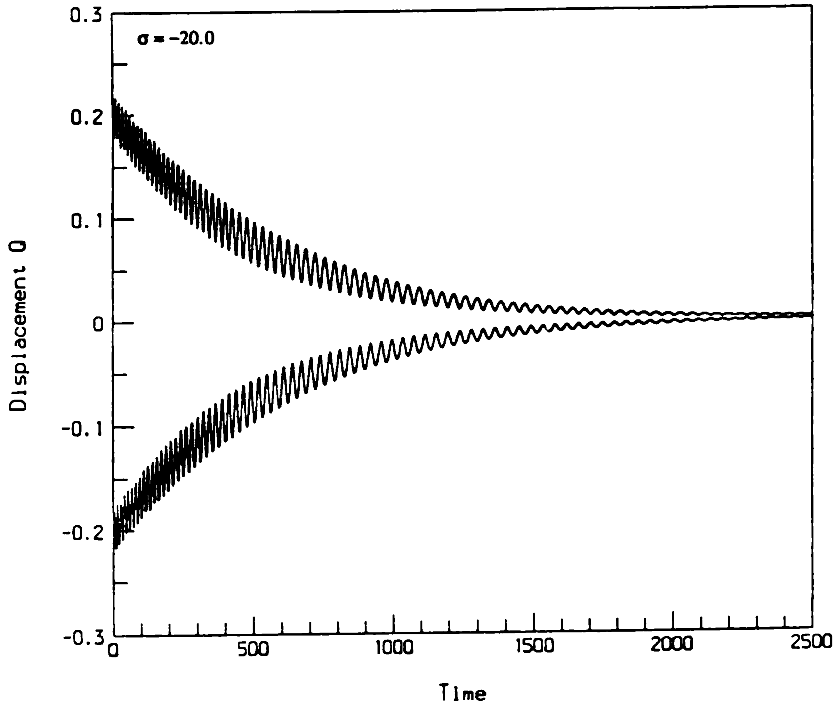

Figure 3.4a Time History of the Envelope of Q (τ) for $\sigma = -20.0$; $Q(0) = 0.2$, $\dot{Q}(0) = 0.0$.

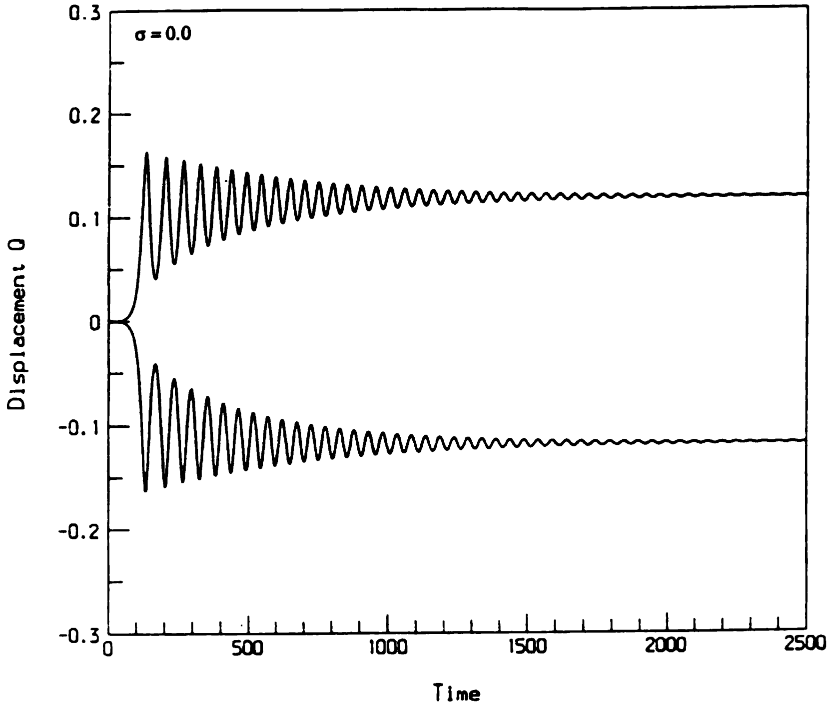

Figure 3.4b Time History of the Envelope of Q (τ) for σ = 0.0; Q(0) = 0.01, $\dot{Q}(0) = 0.0$.

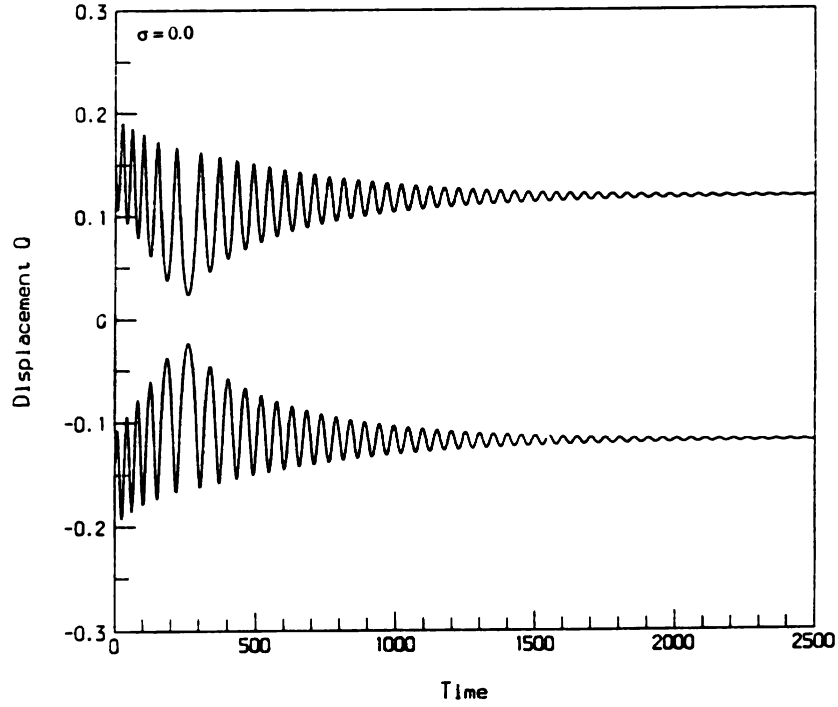

Figure 3.4c Time History of the Envelope of Q (τ) for σ = 0.0; Q(0) = 0.15, $\dot{Q}(0) = 0.0$.

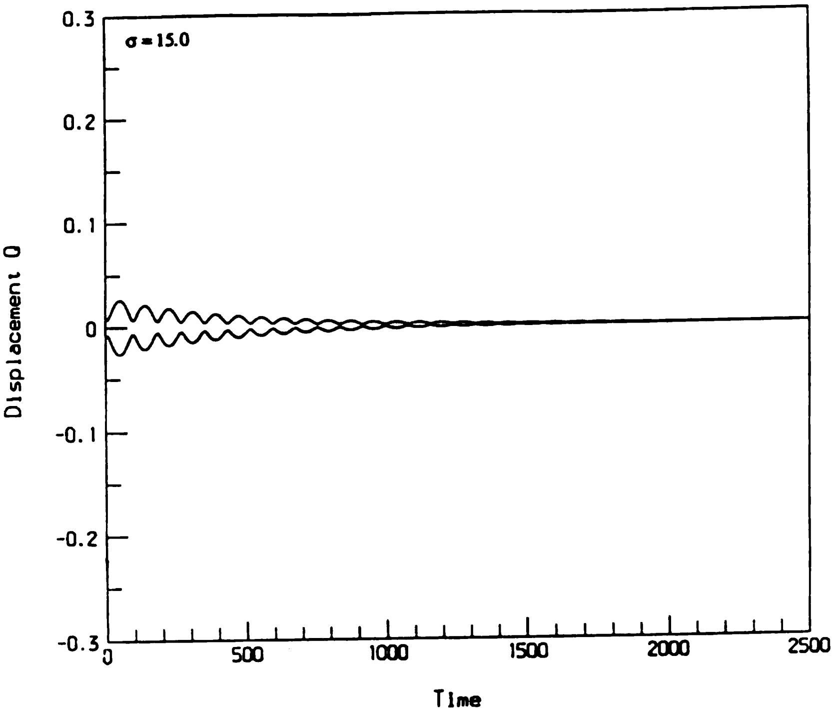

Figure 3.4d Time History of the Envelope of Q (τ) for σ = 15.0; Q(0) = 0.01, $\dot{Q}(0)$ = 0.0.

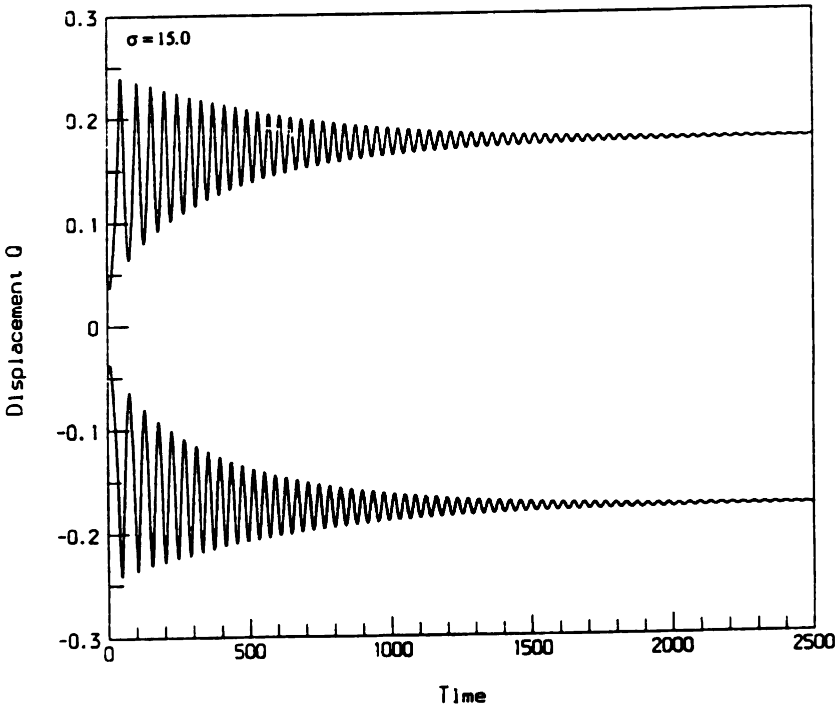

Figure 3.4e Time History of the Envelope of Q (τ) for σ = 15.0; Q(0) = 0.05, $\dot{Q}(0)$ = 0.0.

CHAPTER 4

ANALYSIS OF A ROTATING CANTILEVER BEAM WITH $\Omega_s > \Omega_0$

4.1 Introduction

The nonlinear, planar motion of a uniform, initially straight, elastic beam rotating about its longitudinal axis at a nonconstant spin rate is investigated in this chapter. In Chapter 3 we restricted our investigation to spin rates Ω_s less than Ω_0. However, in the present chapter we will focus our investigation on $\Omega_s > \Omega_0$, i.e., under this condition, the straight equilibrium position of the beam is unstable and the beam buckles to one side or the other due to centrifugal effects.

When the mean rotational speed Ω_s is greater than Ω_0, the linear stiffness term in equation (2.24) will become negative with the consequence that small oscillations around $Q = 0$ become unstable. To investigate the oscillations around the buckled position, we transfer the coordinate of the equation of motion such that the new coordinate describes the motion about the buckled position. The form of Ω will be taken as $\Omega = \Omega_s + \varepsilon^2 \Omega_A \sin \omega\tau$. As in the previous chapter, we focus our attention on the principal parametric resonance $\omega \approx 2\,\omega_0$ where ω_0 is the natural frequency of the beam as it vibrates about the buckled position. However, as will be shown in the subsequent sections, the coordinate transformation gives rise to a nonhomogeneous term and so we will also investigate the case of a main resonance, $\omega \approx \omega_0$. The accuracy of the approximate solutions will be checked by direct numerical integration of the original equation of the motion. We also investigate the possibility of chaotic motion which can arise since the system is essentially a double-well potential problem. We use Melnikov's method to find the regions in the parameter space where chaotic motion may exist. The results are then checked by numerical simulations.

4.2 Equation of Motion

As in Chapter 3, we begin with the one mode equation of motion as it was obtained in Chapter 2.

$$\ddot{Q} + d(Q^2\ddot{Q} + Q\dot{Q}^2) + 2\varepsilon\mu\dot{Q} + bQ^3 + (\Omega_0{}^2 - \Omega^2)Q = 0 \tag{4.1}$$

where $\Omega = \Omega_s + \varepsilon^2\Omega_A \sin\omega\tau$.

Before using the method of multiple scales to obtain an approximate solution about the buckled position, we first transfer the coordinate of the equation of motion to the buckled position. The buckled position, s, is obtained by setting $\Omega = \Omega_s$ and all time derivatives in equation (4.1) equal to zero. Hence we have

$$s = \left[\frac{\Omega_s{}^2 - \Omega_0{}^2}{b}\right]^{\frac{1}{2}}. \tag{4.2}$$

Let the new coordinate be q, such that

$$Q = s + q \tag{4.3}$$

Substituting equations (4.2) and (4.3) into equation (4.1), we obtain

$$\ddot{q}+\alpha_1(2q\ddot{q}+\dot{q}^2)+\alpha_2(q^2\ddot{q}+q\dot{q}^2)+2\varepsilon\mu\dot{q}+\omega_0{}^2q+\gamma_1q^2+\gamma_2q^3$$
$$=\varepsilon^2(g_1+g_2q)\sin\omega\tau+\varepsilon^4(g_3+g_4q)(\sin\omega\tau)^2 \qquad (4.4)$$

where ω_0, γ_i, α_i and g_i are defined in Appendix C.

It is important to note that the equation (4.4) governs the beam's motion about the buckled position. Comparing equation (4.1) with equation (4.4) we can observe that the coordinate transformation has resulted in the addition of quadratic nonlinearities and a direct forcing term.

4.3 Method of Solution

The method of multiple scales will be employed to obtain an approximate solution to equation (4.4). We express the solution in the form

$$q(\tau;\varepsilon)=\varepsilon\, q_1(T_0,T_1,T_2)+\varepsilon^2q_2(T_0,T_1,T_2)+\varepsilon^3q_3(T_0,T_1,T_2)+\cdots\cdots \qquad (4.5)$$

Substituting equations (4.5), (3.6) and (3.7) into equation (4.4) and equating coefficients of like powers of ε yields

$$D_0{}^2q_1+\omega_0{}^2q_1=0 \qquad (4.6)$$

$$D_0{}^2q_2+\omega_0{}^2q_2=-2D_0D_1q_1-2\alpha_1q_1D_0{}^2q_1-\alpha_1(D_0q_1)^2$$
$$-2\mu D_0q_1-\gamma_1q_1{}^2+g_1\sin\omega T_0 \qquad (4.7)$$

$$\begin{aligned} D_0^2 q_3 + \omega_0^2 q_3 = &-2\, D_0\, D_1\, q_0 - 2\, \alpha_1\, q_1\, D_0^2\, q_2 - \alpha_2\, q_1\, (\, D_0 q_1\,)^2 \\ &-(\, D_1^2 + 2\, D_0 D_2\,)\, q_1 - 4\, \alpha_1 q_1 D_0 D_1 q_1 - \alpha_2\, q_1^2 D_0^2\, q_1 \\ &-2\, \alpha_1\, q_2\, D_0^2 q_1 - 2\, \gamma_1\, q_1 q_2 - 2\, \gamma_2\, q_1^3 \\ &-2\, \mu\, D_1\, q_1 + g_2\, q_1 \sin \omega T_0 \end{aligned} \tag{4.8}$$

The solution of equation (4.6) can be expressed in the complex form

$$q_1 = A(\, T_1, T_2\,)\, e^{i\, \omega_0 T_0} + \overline{A}(\, T_1, T_2\,)\, e^{-i\, \omega_0 T_0} \tag{4.9}$$

where $\overline{A}$ is the complex conjugate of A.

Then equation (4.7) becomes

$$\begin{aligned} D_0^2 q_2 + \omega_0^2 q_2 = &-2\, i\, \omega_0\, (\, D_1 A + \mu A\,)\, e^{i\, \omega_0 T_0} \\ &+ (\, 3\, \alpha_1 \omega_0^2 - \gamma_1\,)\, A^2 e^{i\, 2\, \omega_0 T_0} - (\, \alpha_1 \omega_0^2 + \gamma_1\,)\, A\overline{A} + \frac{g_1}{2\, i} e^{i\, \omega\, T_0} + cc \end{aligned} \tag{4.10}$$

where cc stands for the complex conjugate of the preceding terms.

Depending on the inter-relationships between ω and ω_0, various conditions for elimination of secular terms may be extracted from equations (4.8) and (4.10). In the next sections we will consider two cases: (a) $\omega \approx 2\, \omega_0$ and (b) $\omega \approx \omega_0$.

4.4 The Case of $\omega \approx 2\omega_0$

4.4.1 Steady-State Solutions

Eliminating secular producing terms from equation (4.10) yields

$$D_1 A = -\mu A. \tag{4.11}$$

Consequently, the solution of equation (4.7) becomes

$$q_2 = \left(\frac{\alpha_1 \omega_0^2 - \gamma_1}{\omega_0^2}\right) A \bar{A} - \left(\frac{3\alpha_1 \omega_0^2 - \gamma_1}{3\omega_0^2}\right) A^2 e^{i 2 \omega_0 T_0} - \frac{i g_1}{2(\omega_0^2 - \omega^2)} e^{i \omega T_0} + cc \tag{4.12}$$

To investigate the resonance $\omega \approx 2\omega_0$, we introduce the detuning parameter σ defined according to

$$\omega = 2\omega_0 + \varepsilon^2 \sigma \tag{4.13}$$

Substituting equations (4.9), (4.12) and (4.13) into (4.8) and eliminating the terms that lead to secular terms yields

$$-2 i \omega_0 D_2 A - D_1^2 A - 2\mu D_1 A + i\left(-6\alpha_1 F_3 \omega_0^2 - \frac{g_2}{2} + 2\gamma_1 F_3\right) \bar{A} e^{\varepsilon^2 \sigma T_0} + [2\alpha_2 \omega_0^2 - 3\gamma_2 - 6\alpha_1 F_2 \omega_0^2 + 2\gamma_1 (F_2 - F_1) + 2\alpha_1 \omega_0^2 F_1] A^2 \bar{A} = 0 \tag{4.14}$$

where

$$F_1 = \frac{2(\alpha_1 \omega_0^2 - \gamma_1)}{\omega_0^2}$$

$$F_2 = \frac{3\alpha_1 \omega_0^2 - \gamma_1}{3\omega_0^2}$$

$$F_3 = \frac{-g_1}{6\omega_0^2}.$$

At this stage we have to employ the technique of reconstitution to continue with the analysis. This involves recalling that

$$\dot{A} = \frac{dA}{d\tau} = D_0 A + \varepsilon D_1 A + \varepsilon^2 D_2 A \tag{4.15}$$

where $D_n = \dfrac{\partial}{\partial T_n}$,

and noting that $D_0A = 0$ and an expression for D_1A has already been found (see equation (4.11)). From equations (4.15) and (4.11), we thus have

$$D_2 A = \frac{\dot{A} + \varepsilon \mu A}{\varepsilon^2} \tag{4.16}$$

Substituting equations (4.11) and (4.16) into equation (4.14) yields

$$\begin{aligned} &-2i\omega_0(\dot{A} + \varepsilon\mu A) + \varepsilon^2\{i\,(-6\,\alpha_1 F_3\,\omega_0^2 - \frac{g_2}{2} + 2\,\gamma_1 F_3)\,\overline{A}\,e^{\varepsilon^2 \sigma T_0} + \mu^2 A \\ &+ (2\,\alpha_2\,\omega_0^2 - 3\,\gamma_2 - 6\,\alpha_1\,F_2\,\omega_0^2 + 2\,\gamma_1(F_2 - F_1) + 2\,\alpha_1\omega_0^2 F)A^2A\} = 0 \end{aligned} \tag{4.17}$$

To solve equation (4.17), it is convenient to express A in the polar form given in equation (3.14). Substituting equation (3.14) into equation (4.17) and separating real and imaginary parts yields

$$\dot{a} = -\varepsilon\, \mu\, a - \varepsilon^2 \left[3\, \alpha_1 F_3\, \omega_0\, a + \frac{g_2\, a}{4\, \omega_0} - \frac{\gamma_1 F_3\, a}{\omega_0} \right] \cos\gamma \tag{4.18}$$

$$\begin{aligned} a\dot{\gamma} = {} & \varepsilon^2 \left[\frac{\mu^2\, a}{\omega_0} + \sigma\, a + 2\, (\, 3\, \alpha_1 F_3\, \omega_0\, a + \frac{g_2\, a}{4\, \omega_0} - \frac{\gamma_1 F_3\, a}{\omega_0}\,) \sin\gamma \right] \\ & - \varepsilon^2 \left[\left(-\frac{3}{2}\, \alpha_1 F_2\, \omega_0 + \frac{1}{2}\, \alpha_1 F_1\, \omega_0 + \frac{1}{2}\, \alpha_2\, \omega_0 - \frac{3\, \gamma_2}{4\, \omega_0} + \frac{\gamma_1 (\, F_2 - F_1\,)}{2\, \omega_0} \right) a^3 \right] \end{aligned} \tag{4.19}$$

where $\gamma = \varepsilon^2\, \sigma\, \tau - 2\, \beta.$ (4.20)

Periodic motions of the rotating beam correspond to the constant solutions of equations (4.18) and (4.19), which in turn corresponds to $\dot{a} = \dot{\gamma} = 0$. Hence we have a trivial steady-state solution, a = 0, or

$$\cos\gamma = -\frac{\mu}{\varepsilon\, G} \tag{4.21}$$

$$\sin\gamma = \frac{1}{2\, G} \left[-\, \sigma - \frac{\mu^2}{\omega_0} + H\, a^2 \right] \tag{4.22}$$

where

$$G = 3\, \alpha_1 F_3\, \omega_0 + \frac{g_2}{4\, \omega_0} - \frac{\gamma_1 F_3}{\omega_0}$$

$$H = \frac{3}{2}\alpha_1 F_2 \omega_0 - \frac{1}{2}\alpha_1 F_1 \omega_0 - \frac{1}{2}\alpha_2 \omega_0 + \frac{3\gamma_2}{4\omega_0} + \frac{\gamma_1(F_1 - F_2)}{2\omega_0} \cdot$$

Squaring and adding equations (4.21) and (4.22), we obtain

$$a^2 = \frac{1}{H}\left[\sigma + \frac{\mu^2}{\omega_0} \pm 2\sqrt{G^2 - \frac{\mu^2}{\varepsilon^2}}\right] \tag{4.23}$$

Substituting equations (4.9), (4.12) and (4.20) into equation (4.5), the steady-state solution has the form

$$\begin{aligned} q &= \varepsilon\, a \cos\left(\frac{\omega\tau - \gamma}{2}\right) \\ &\quad + \varepsilon^2 \left\{ a^2 \left[\frac{\alpha_1 \omega_0^{\,2} - \gamma_1}{2\,\omega_0^{\,2}} - \frac{3\,\alpha_1 \omega_0^{\,2} - \gamma_1}{6\,\omega_0^{\,2}} \cos(\omega\tau - \gamma) \right] + \frac{g_1}{\omega_0^{\,2} - \omega^2} \sin\omega\tau \right\} + O(\varepsilon^3) \end{aligned} \tag{4.24}$$

Note that the last term in the above approximate steady-state solution comes from the direct forcing terms $\varepsilon^2 g_1 \sin\omega\tau$ and does not depend on "a" .

4.4.2 Stability of the Steady-State Solutions

To investigate the stability of the trivial steady-state solutions, we will first convert equation (4.17) from polar form into an autonomous Cartesian form. To this end we introduce the complex coefficient, B, such that

$$A = B\,\exp\left(\frac{i\,\varepsilon^2 \sigma\,\tau}{2}\right) \tag{4.25}$$

where $B = B_r + i\, B_i$.

Substituting equation (4.25) into equation (4.17) and separating real and imaginary parts, we obtain

$$\dot{B}_r = -\varepsilon\, \mu\, B_r + \varepsilon^2 \left(\frac{\mu^2}{2\omega_0} B_i + \frac{\sigma}{2} - \frac{G}{\omega_0} B_r - \frac{H}{\omega_0} B_i\, B_r^{\,2} \right) \tag{4.26}$$

$$\dot{B}_i = -\varepsilon\, \mu\, B_i + \varepsilon^2 \left(-\frac{\mu^2}{2\omega_0} B_r - \frac{\sigma}{2} + \frac{G}{\omega_0} B_i + \frac{H}{\omega_0} B_r\, B_i^{\,2} \right) \tag{4.27}$$

To determine the stability of the steady-state solutions, we can add an infinitesimal perturbation to the steady-state solution and check to see if this perturbation grows or decays.

In vector form, this may be expressed as

$$\boldsymbol{\varphi} = \overline{\boldsymbol{\varphi}} + \mathbf{y} \tag{4.28}$$

where $\boldsymbol{\varphi} = (B_r , B_i)^T$, $\overline{\boldsymbol{\varphi}}$ is the steady-state solution, and $\|\mathbf{y}\| << 1$.

Substituting equation (4.28) into equations (4.26) and (4.27) and linearizing the resulting equations, one obtains

$$\dot{\mathbf{y}} = \mathbf{M}\, \mathbf{y} \tag{4.29}$$

where

$$M=\begin{bmatrix} -\varepsilon\mu-\dfrac{\varepsilon^2 G}{\omega_0} & \dfrac{\varepsilon^2\mu^2}{2\omega_0} \\ -\dfrac{\varepsilon^2\mu^2}{2\omega_0} & -\varepsilon\mu+\dfrac{\varepsilon^2 G}{\omega_0} \end{bmatrix}. \qquad (4.30)$$

The stability of the trivial steady-state solution is governed by the stability of y in equation (4.29) and thus by the eigenvalues of **M**. The steady-state solution is stable, if and only if the real parts of all eigenvalues are less than zero. For the trivial solution this result in an unstable solution for $\sigma_1 < \sigma < \sigma_2$, where

$$\sigma_1 = -\frac{\mu^2}{\omega_0} - 2\sqrt{G^2 - \frac{\mu^2}{\varepsilon^2}} \qquad (4.31)$$

$$\sigma_2 = -\frac{\mu^2}{\omega_0} + 2\sqrt{G^2 - \frac{\mu^2}{\varepsilon^2}}. \qquad (4.32)$$

To investigate the stability of the non-trivial steady-state solutions we can follow the same procedure. However, it is not necessary to first convert equation (4.17) into Cartesian forms: the stability analysis may be completed directly on equations (4.18) and (4.19).

In this case we find the Jacobian matrix **M** to be

$$M=\begin{bmatrix} -\varepsilon\mu-\varepsilon^2 G\cos\bar{\gamma} & \varepsilon^2 G\bar{a}\sin\bar{\gamma} \\ -2\varepsilon^2 H\bar{a} & 2\varepsilon^2 G\cos\bar{\gamma} \end{bmatrix} \qquad (4.33)$$

where the overbar denotes a steady-state value.

The results of this stability analysis are shown in subsequent figures of this chapter.

4.4.3 Numerical Results of Approximate Solutions

In this section we present representative solutions of the equations derived in Section 4.4.1. Values for the various parameters are based on a physical system that has been used in laboratory tests. Results from the experimental investigation will be reported in Chapter 7. The parameter values used, unless otherwise stated, are:

$\Omega_s = 3.7$, $\varepsilon^2\Omega_A = 0.05$, $2\,\varepsilon\,\mu = 0.00422$, $\Omega_0 = 3.516$ and $\varepsilon = 0.1$.

Figure 4.1 shows a typical frequency response curve for a non-zero mean spin rate of $\Omega_s = 3.7$. Note that in this and subsequent figures, we plot εa which is the magnitude of the first order term in the approximation of q (see equation (4.24)). Clearly, we can observe that the overall nonlinearity of the system is of a softening type, whereas in pre-buckling case (i.e., $\Omega_s < \Omega_0$) the overall nonlinearity was of a hardening type. As before, a stable solution is denoted by a solid line whereas a unstable solution is denoted by a chained line. It can be shown that the upper branch is always stable, whereas the lower branch is always unstable.

Figures 4.2a-b present results showing the variation of the steady-state amplitude as a function of $\varepsilon^2\Omega_A$. Figure 4.2a shows a case for which there is only one stable steady-state solution, i.e., $\sigma = 0.0$, whereas Figure 4.2b shows a case where multiple steady-state solutions are possible, i.e., $\sigma = -28.0$. Figure 4.3 shows the effect of the mean spin rate, Ω_s, on the steady-state solutions, for three different values of σ. For clarity, only the stable steady-state solutions are shown. Because of the post-buckled condition, starting points of all the curves in Figure 4.3 are slightly above the point $\Omega_0 = 3.516$ (since the equation are not valid for $\Omega_s < \Omega_0$). It is interesting to note that for $\sigma = 0.0$ and 10, the steady-state amplitude decreases as Ω_s increases. The overall effect on the response may

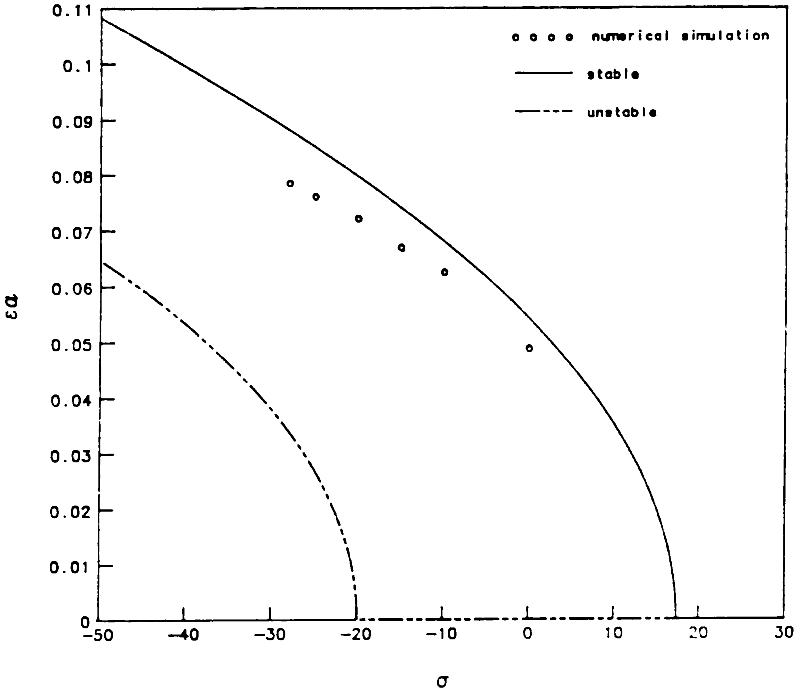

Figure 4.1 Variation of the Steady-State Amplitude, a, with σ.

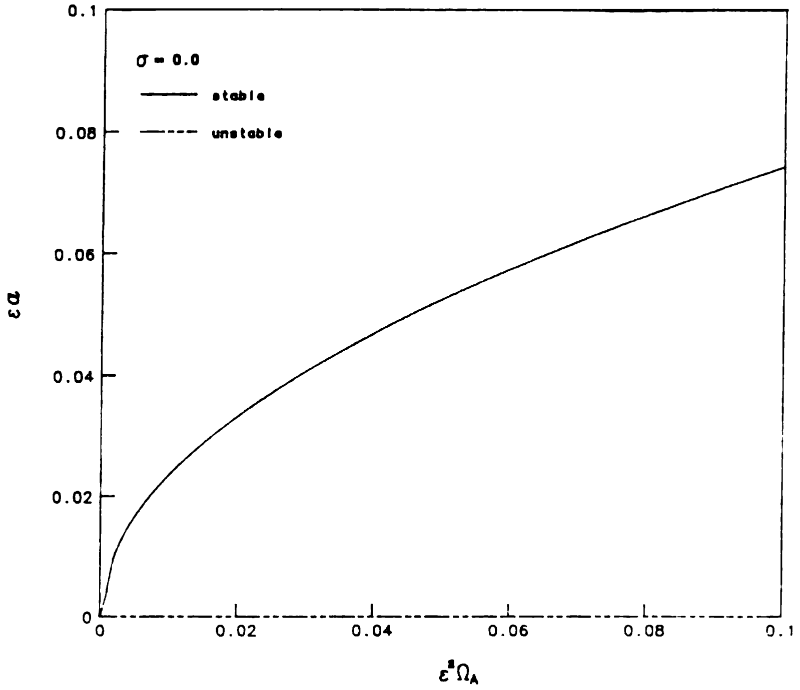

Figure 4.2a Variation of the Steady-State Amplitude, a, with $\varepsilon^2\Omega_A$ for $\sigma = 0.0$.

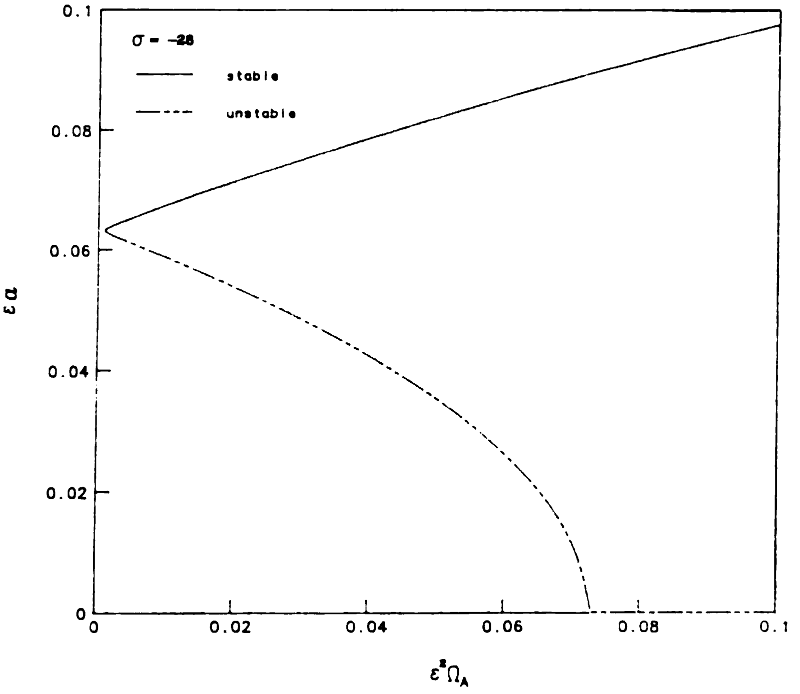

Figure 4.2b Variation of the Steady-State Amplitude, a, with $\varepsilon^2\Omega_A$ for $\sigma = -28$.

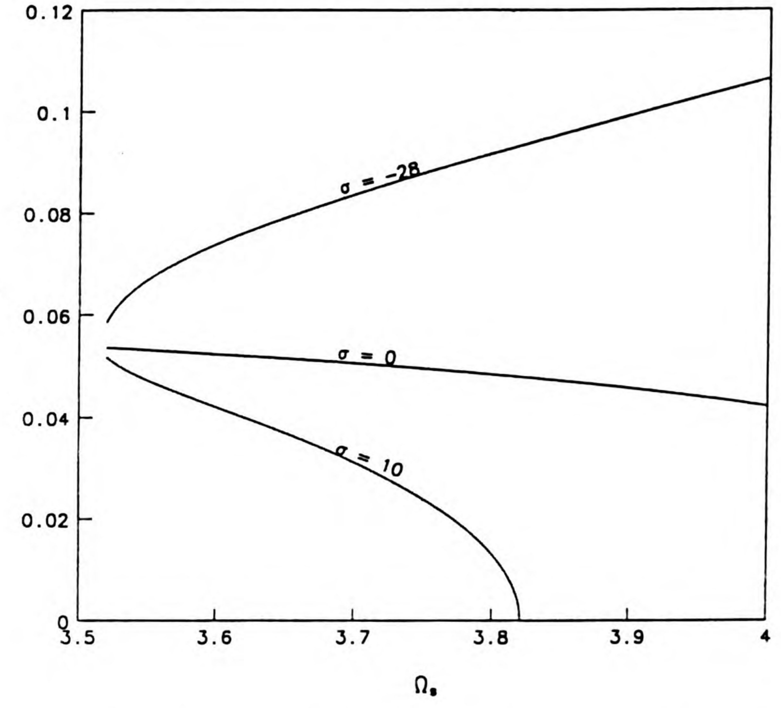

Figure 4.3 Variation of the Steady-State Amplitude, a, with Ω_s for σ = -28, 0, 10.

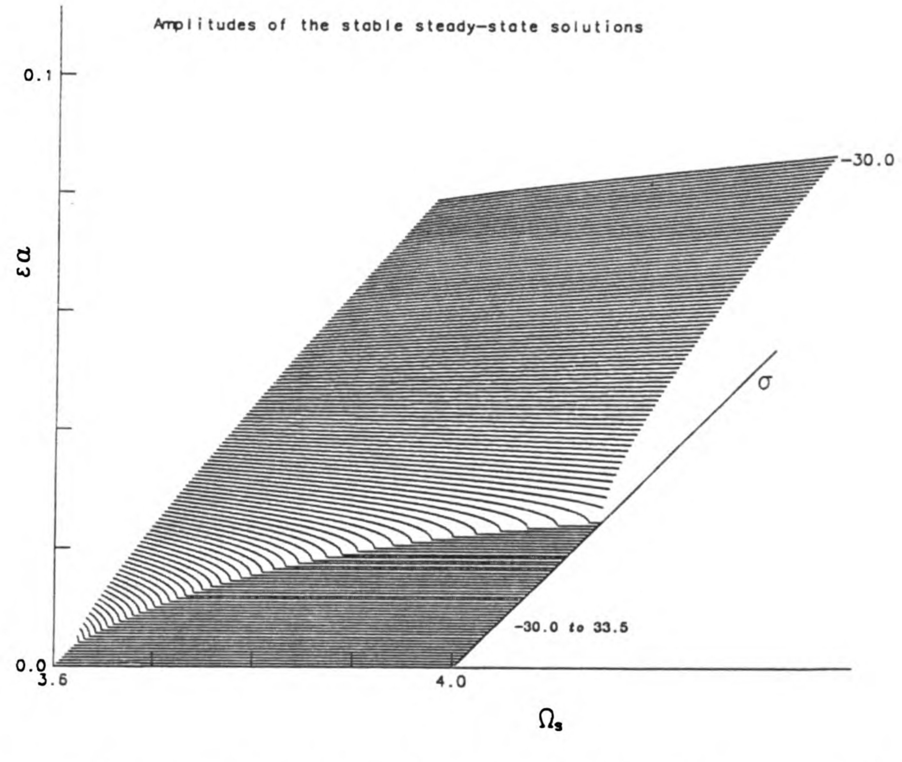

Figure 4.4a εa, σ, Ω_s - Plot for Stable Steady-State Solutions, (3-D representations).

be better visualized by considering the response surface in the (a, σ, Ω_s) space. A three-dimensional representations of this for both stable and unstable solutions are shown in Figure 4.4a and 4.4b, respectively, for fixed values of μ and $\varepsilon^2\Omega_A$.

In Figure 4.4, to move along a constant σ line, we need to continually adjust ω (since ω_0 is a function of Ω_s and $\omega = 2\omega_0 + \varepsilon^2\sigma$). However, in practice we would be more likely to hold ω fixed and not try to constrain σ. Hence, Figure 4.5 has been plotted to show contours of constant ω values. Again, for clarity, only stable solutions have been shown.

Figure 4.6 represents a bifurcation diagram which dictates which type of steady-state solution exists in the $\omega - \varepsilon^2\Omega_A$ parameter space. This space is divided into three regions by the curves: $\sigma = -\mu^2/2\omega_0{}^2 \pm \sqrt{G^2 - \mu^2/\varepsilon^2}$ and $\mu = \varepsilon$ G. Note that the boundaries of these regions are dependent on the coefficients of the quadratic nonlinear terms and independent of the coefficients of the cubic nonlinear terms. In region I, only the stable trivial solution exists. In region II, two solutions exist: the unstable trivial solution and a stable non-trivial one. In region III, there are three solutions: the stable trivial one and two non-trivial solutions, one stable, the other unstable. Figure 4.7 shows the effect of Ω_s on these regions. We observe that the region II decreases as Ω_s increases.

In order to check the results obtained by using the method of multiple scales, equation (4.1) is numerically integrated. The results have been plotted as "numerical simulation" on Figure 4.1 and represent one half of the peak to peak value of Q, obtained by the numerical integration. The comparison is qualitatively good in all the cases tested. Figures 4.8a-b present time traces of the steady-state solution Q of the numerical integration results for σ = -28. Figure 4.8a results from one set of initial conditions from which the solution is attracted to the trivial solution (i.e., a = 0). Note that even when a = 0, we

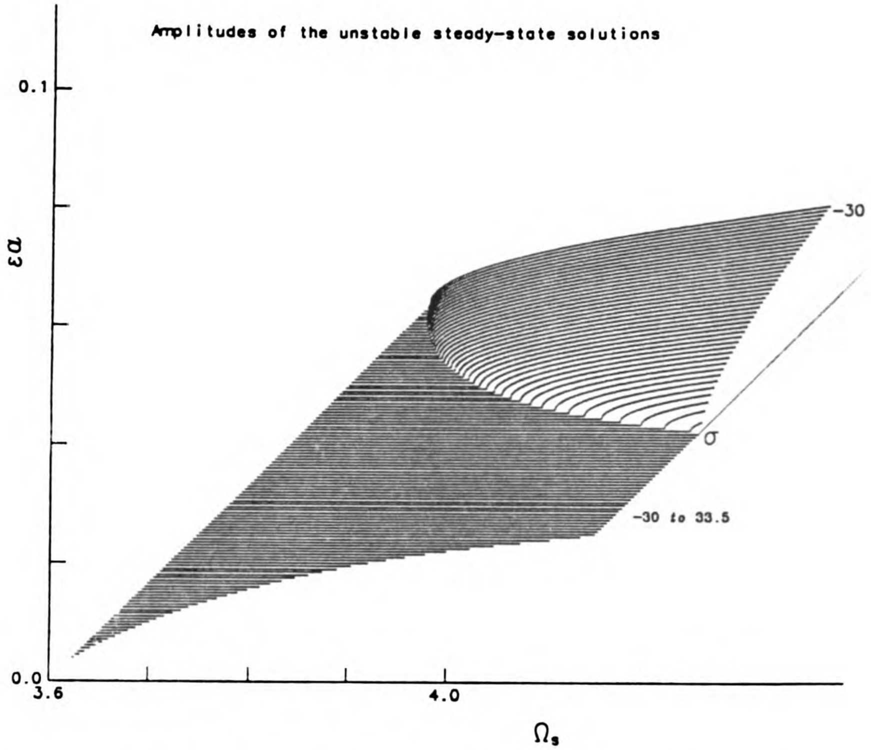

Figure 4.4b εa, σ, Ω_s - Plot for Unstable Steady-State Solutions, (3-D representations).

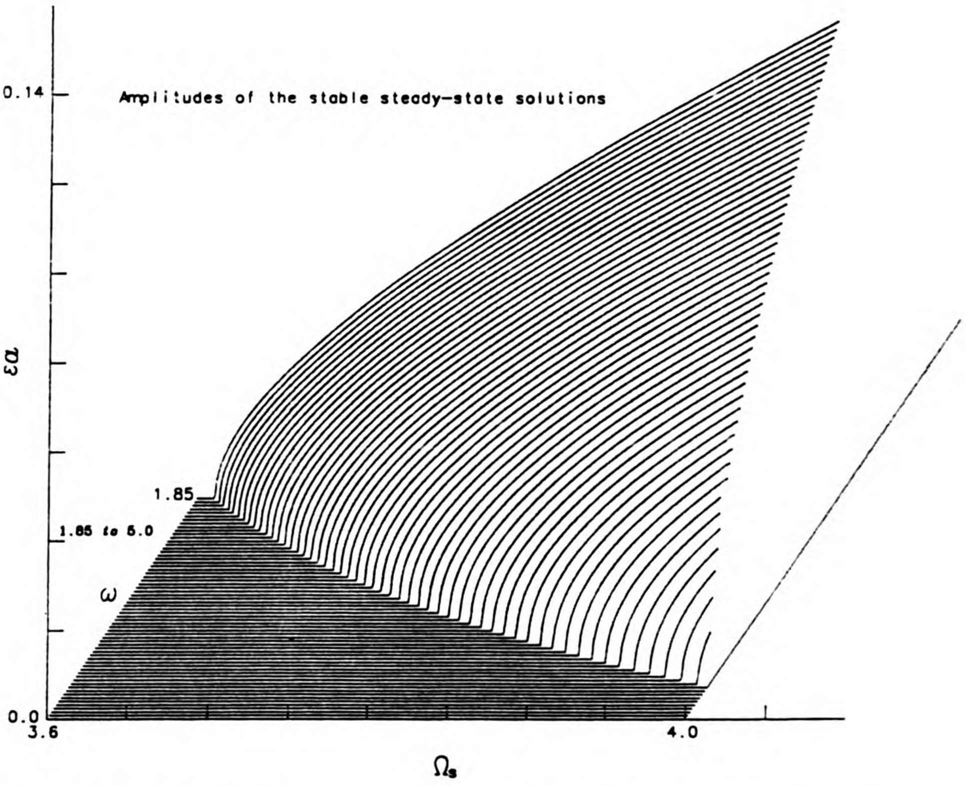

Figure 4.5 εa, ω, Ω_s - Plot for Stable Steady-State Solutions, (3-D representations).

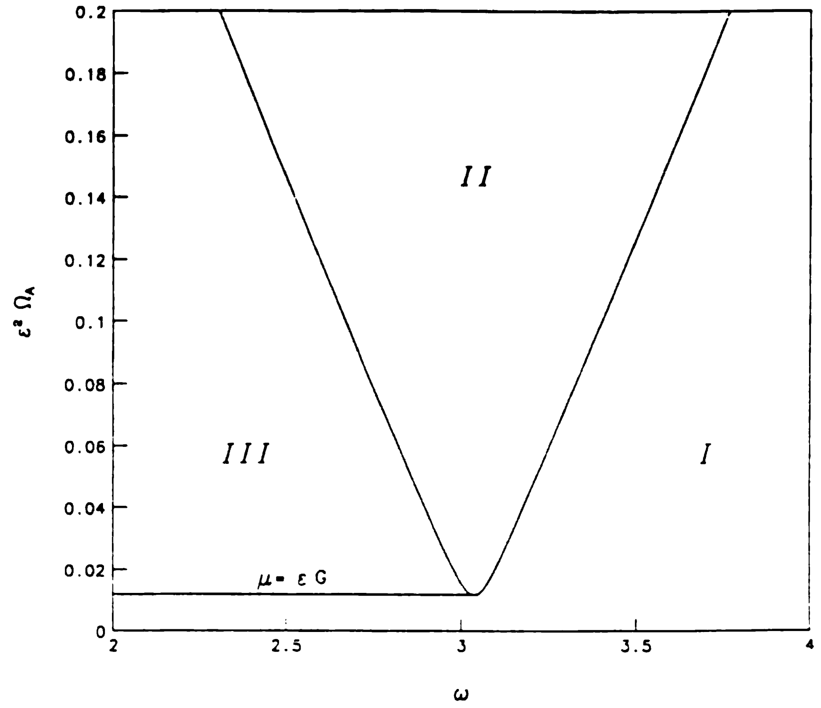

Figure 4.6 Bifurcation Diagram in the ω–$\varepsilon^2\Omega_A$ Parameter Space for $\Omega_s = 3.70$.

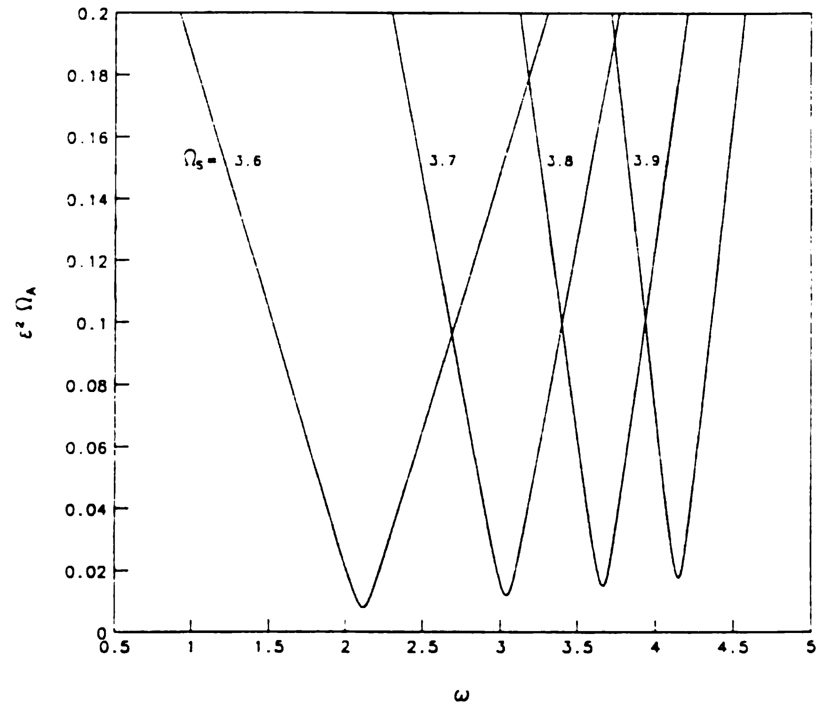

Figure 4.7 Effect of Ω_s on the Bifurcation Diagram in the ω–$\varepsilon^2\Omega_A$ Parameter Space.

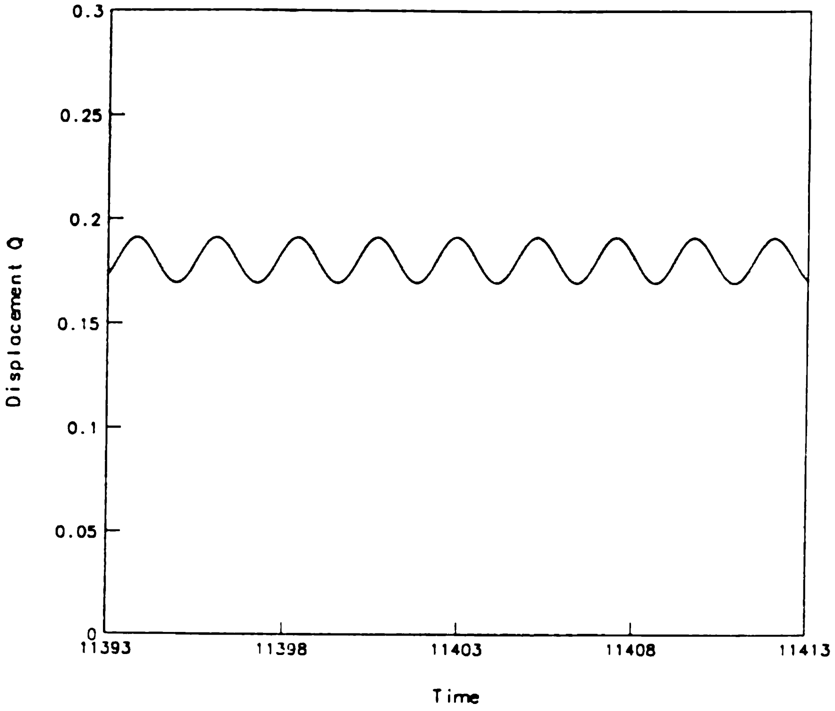

Figure 4.8a Time Trace of the Steady-State Solution Q for $\sigma = -28$; $Q(0) = 0.2, \dot{Q}(0) = 0.0$.

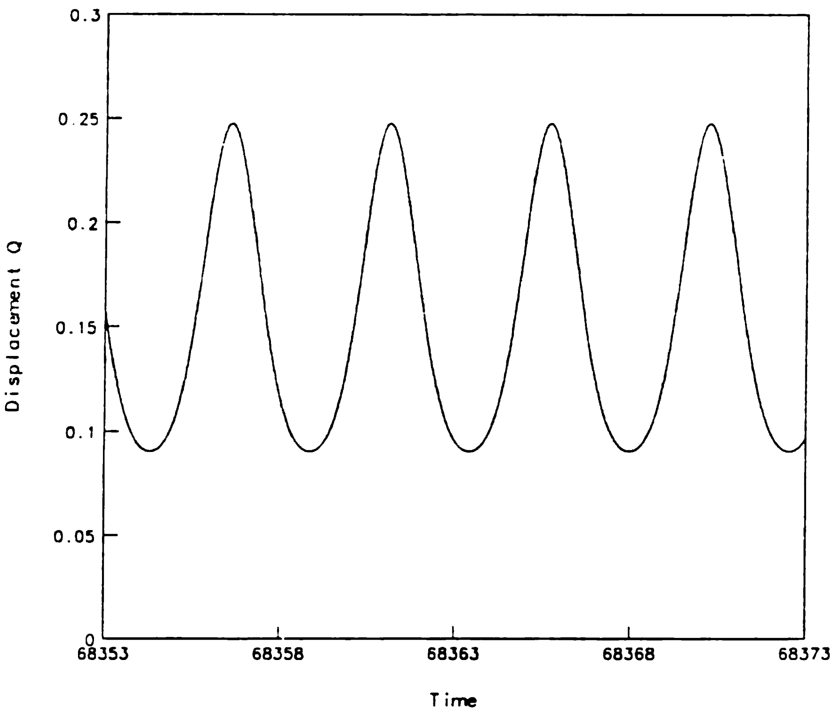

Figure 4.8b Time Trace of the Steady-State Solution Q for $\sigma = -28$; $Q(0) = 0.1, \dot{Q}(0) = 0.0$.

would expect to see a small component of Q which arises from the direct forcing term $\varepsilon^2 g_1 \sin \omega\tau$ (see equation (4.4)). The frequency of the response depicted in Figure 4.8a is that of the excitation term, ω. Figure 4.8b shows the results for the same parameter values as in Figure 4.8a, but using a different set of initial conditions. The solution is now attracted toward the non-trivial solution set, corresponding to $a \neq 0$. The main frequency of this solution is $\frac{\omega}{2}$ (i.e., subharmonic motion), which is consistent with the method of multiple scales prediction of equation (4.24). The corresponding phase portraits of these two time traces are shown in Figure 4.9.

It is interesting to note that for yet another set of initial conditions, a third type of steady-state solution can be found. In contrast to the preceding two, which were associated with oscillation about the buckled position, we may also observe a large orbit which encompasses both buckled positions (i.e., $Q=\pm s$). The period of this oscillation is twice that of the forcing period (i.e., period 2 motion). The time trace of the steady-state solution Q of this case is shown in Figure 4.10. If we decrease the σ value further (e.g., down to -30), numerical simulations can only find this type of motion, i.e., non-trivial oscillations centered around a buckled position are no longer possible (but, of course, the small, directly forced response can be found). Numerical simulations results for different σ values are shown in Figure 4.11. From Figure 4.11 we observe that the snap-through motion of the beam is of hardening type.

We also present the numerical simulations of equation (4.1) in terms of non-rotating (i.e., laboratory) coordinates. Figure 4.12a shows a trajectory of the beam as it vibrates about one of the buckled positions. The trace represents approximately 67 revolutions of the beam. Figure 4.12b shows a trajectory associated with a motion that encompasses both buckled positions.

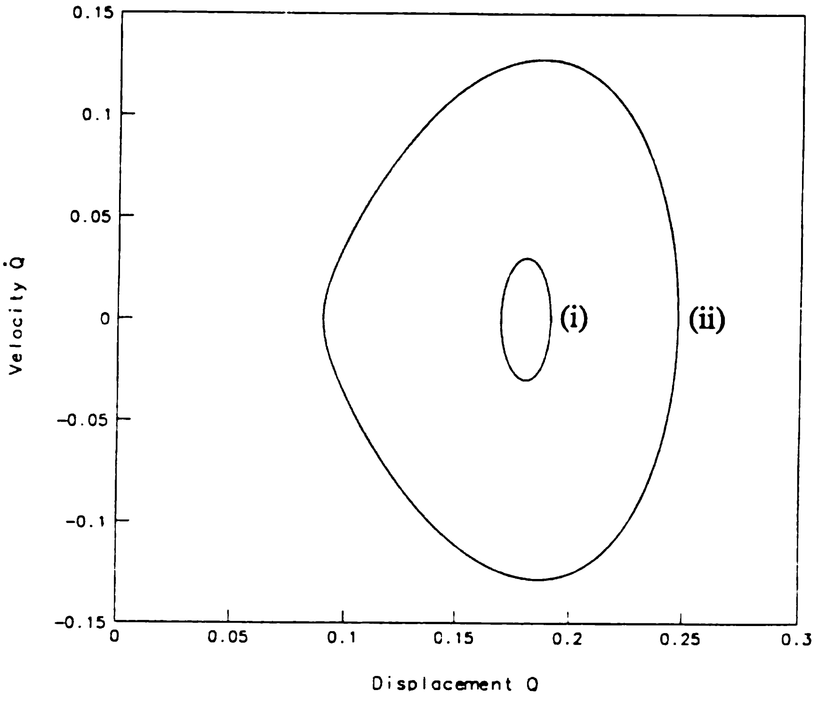

Figure 4.9 **Phase Portraits of the Steady-State Solution Q for $\sigma = -28$;**
(i) $Q(0) = 0.2$, $\dot{Q}(0) = 0.0$, (ii) $Q(0) = 0.1$, $\dot{Q}(0) = 0.0$.

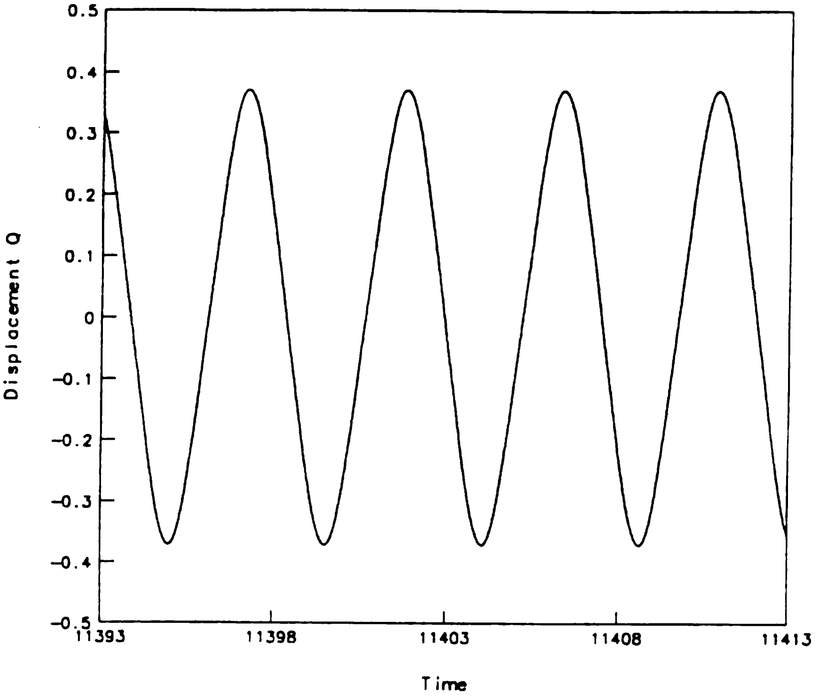

Figure 4.10 Time Trace of the Steady-State Solution Q for σ = -28; $Q(0) = 0.05, \dot{Q}(0) = 0.0$.

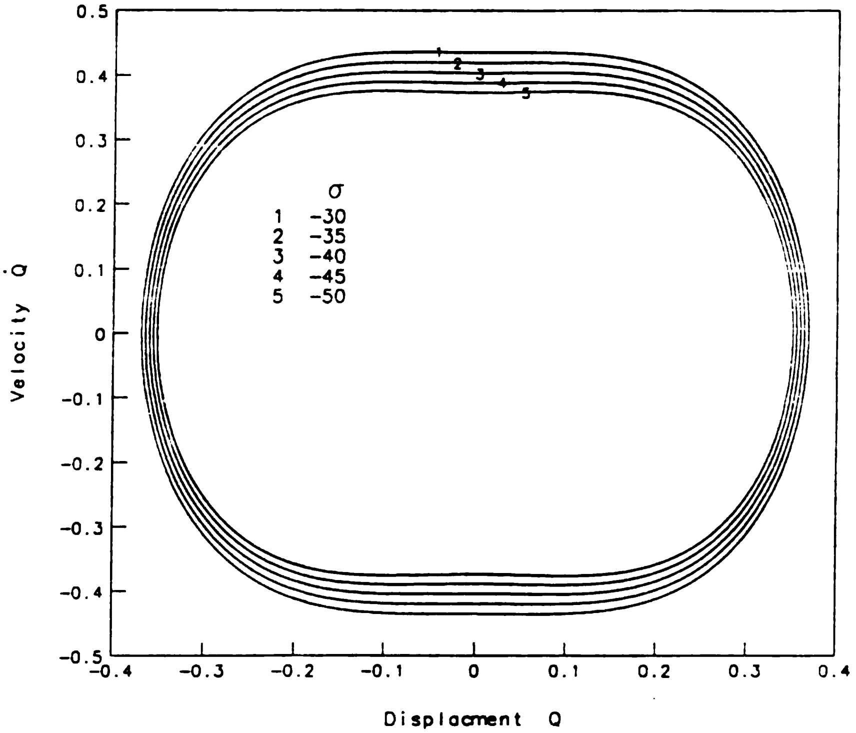

Figure 4.11 Phase Portraits of the Steady-State Solution Q for σ = -30, -35, -40, -45, -50.

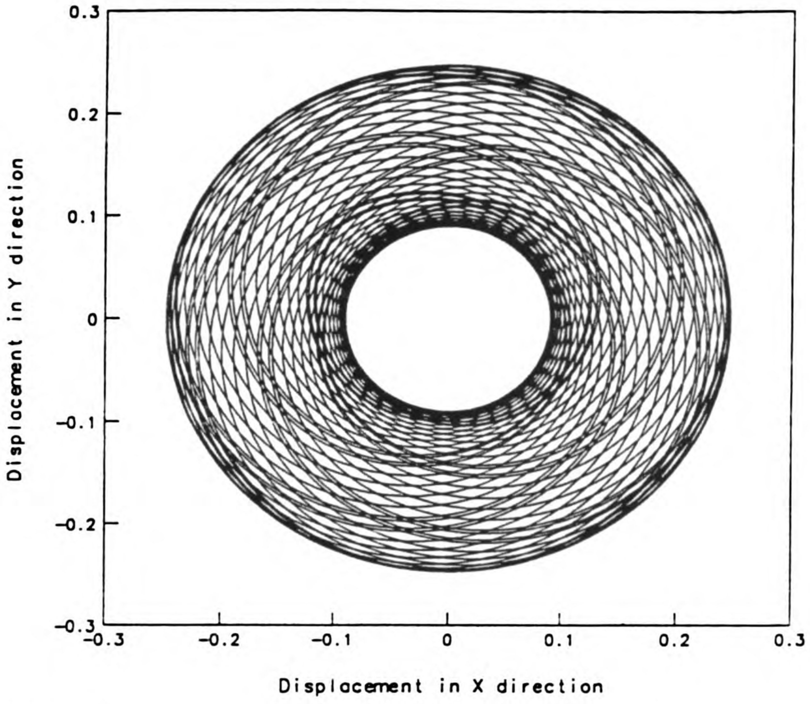

Figure 4.12a Trajectory of the Steady-State Solution Q in Non-rotating Coordinates for $\sigma = -28$; $Q(0) = 0.1$, $\dot{Q}(0) = 0.0$.

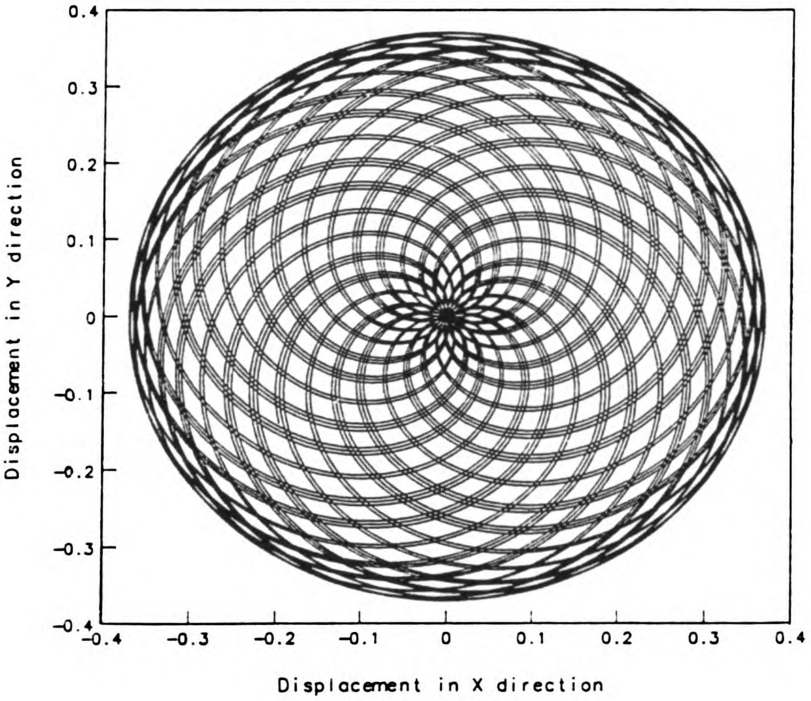

Figure 4.12b Trajectory of the Steady-State Solution Q in Non-rotating Coordinates for $\sigma = -28$; $Q(0) = 0.05$, $\dot{Q}(0) = 0.0$.

4.5 The Case of $\omega \approx \omega_0$

In this section the frequency ω is taken to be close to ω_0 and the proximity of ω to ω_0 is quantified by the external detuning parameter, σ, which will be defined by

$$\omega = \omega_0 + \varepsilon^2 \sigma \tag{4.34}$$

The secular terms and small-divisor terms are now eliminated from equation (4.10) if

$$D_1 A = -\mu A - \frac{g_1}{4\omega_0} e^{i(\omega-\omega_0)T_0} \tag{4.35}$$

Then, the solution of equation (4.7) becomes

$$q_2 = \left(\frac{\alpha_1 \omega_0^2 - \gamma_1}{\omega_0^2}\right) A \bar{A} - \left(\frac{3\alpha_1 \omega_0^2 - \gamma_1}{3\omega_0^2}\right) A^2 e^{i 2\omega_0 T_0} + cc \tag{4.36}$$

Substituting equations (4.9), (4.36) and (4.34) into equation (4.8) and eliminating secular producing terms yields

$$\begin{aligned} -2 i \omega_0 D_2 A - D_1^2 A - 2\mu D_1 A + [\, 2\alpha_2 \omega_0^2 - 3\gamma_2 - 6\alpha_1 F_2 \omega_0^2 \\ + 2\gamma_1 (F_2 - F_1) + 2\alpha_1 \omega_0^2 F_1] A^2 \bar{A} = 0 \end{aligned} \tag{4.37}$$

As in Section 4.4.1, to proceed we use the technique of reconstitution. Substituting equations (4.35) and (4.16) into equation (4.37) yields

$$-2 i \omega_0 (\dot{A} + \varepsilon \mu A + \varepsilon F_4 e^{\varepsilon^2 \sigma T_0}) + \varepsilon^2 [-\mu^2 A - \mu F_4 e^{\varepsilon^2 \sigma T_0} + F_5 A^2 \bar{A}] = 0 \qquad (4.38)$$

where

$$F_4 = \frac{g_1}{4 \omega_0}$$

$$F_5 = (-2 \alpha_2 \omega_0{}^2 + 3 \gamma_2 + 6 \alpha_1 F_2 \omega_0{}^2 - 2 \gamma_1 (F_2 - F_1) - 2 \alpha_1 \omega_0{}^2 F_1 \, .$$

Substituting equation (3.14), the polar form of A, into equation (4.38) and separating the results into real and imaginary parts, yields

$$\dot{a} = -\varepsilon \mu a - 2 \varepsilon F_4 \cos\gamma + \frac{\varepsilon^2 \mu F_4}{\omega_0} \sin\gamma \qquad (4.39)$$

$$a \dot{\gamma} = \varepsilon^2 \sigma a + 2 \varepsilon F_4 \sin\gamma + \frac{\varepsilon^2 \mu^2 a}{2 \omega_0} + \frac{\varepsilon^2 \mu F_4}{\omega_0} \cos\gamma - \frac{\varepsilon^2 F_5 a^3}{8 \omega_0} \qquad (4.40)$$

where $\gamma = \varepsilon^2 \sigma \tau - \beta$. (4.41)

Again, it is possible to simplify these equations should only the steady-state responses be sought. For such a case, equations (4.39) and (4.40) reduced

$$-2 \varepsilon F_4 \cos\gamma + \frac{\varepsilon^2 \mu F_4}{\omega_0} \sin\gamma = \varepsilon \mu a \qquad (4.42)$$

$$2 \varepsilon F_4 \sin\gamma + \frac{\varepsilon^2 \mu F_4}{\omega_0} \cos\gamma = -\varepsilon^2 \sigma a + \frac{\varepsilon^2 F_5 a^3}{8 \omega_0} - \frac{\varepsilon^2 \mu^2 a}{2 \omega_0} \qquad (4.43)$$

Squaring and adding (4.42) and (4.43) gives

$$c_3\, a^6 + c_2\, a^4 + c_1\, a^2 + c_0 = 0 \tag{4.44}$$

where

$$c_3 = F_5^2$$

$$c_2 = -8\, F_5\, (\, \mu^2 + \omega_0\, \sigma\,)$$

$$c_1 = -16\, (\, 4\, \omega_0\, \sigma\, \mu^2 + 4\, \omega_0^2\, \sigma^2 + \mu^4 + \frac{4\, \mu^2\, \omega_0^2}{\varepsilon^2})$$

$$c_0 = -64\, (\, \frac{4\, F_4^2\, \omega_0^2}{\varepsilon^2} + \mu^2\, F_4^2\,).$$

Given a set of values for the parameters, the steady-state amplitude "a" may be found directly from equation (4.44). Since this equation is a 6th order polynomial in "a" with only even powers present, it may have up to three non-negative real roots. Also, because $c_0 \neq 0$, no trivial solutions exist. Reconstructing the approximate solution to q, we find

$$\begin{aligned} q &= \varepsilon\, a \cos[\omega \tau - \gamma] \\ &\quad + \varepsilon^2 \left[a^2 \left(\frac{\alpha_1\, \omega_0^2 - \gamma_1}{2\, \omega_0^2} - \frac{3\, \alpha_1 \omega_0^2 - \gamma_1}{6\, \omega_0^2} \cos[2(\omega \tau - \gamma)] \right) \right] + O(\varepsilon^3) \end{aligned} \tag{4.45}$$

The stability of this case may be investigated by adopting the same procedure as was used in Section 4.4.2. In this instance, the Jacobian matrix **M** obtained from equations (4.39) and (4.40) is

$$\mathbf{M}=\begin{bmatrix} -\varepsilon\mu & -\varepsilon^2\,\bar{a}\,(\sigma+\dfrac{\mu^2}{2\,\omega_0}-\dfrac{F_5\,\bar{a}^2}{8\,\omega_0}) \\ \dfrac{\varepsilon^2}{\bar{a}}(\sigma+\dfrac{\mu^2}{2\,\omega_0}-\dfrac{3\,F_5\,\bar{a}^2}{8\,\omega_0}) & -\varepsilon\mu \end{bmatrix}$$

where the overbar denotes the steady-state value.

The results of this investigation indicate that the steady-state motions are unstable when

$$\varepsilon^2\left[\ (\sigma+\frac{\mu^2}{2\,\omega_0})^2-(\sigma+\frac{\mu^2}{2\,\omega_0})(\frac{F_5\bar{a}^2}{2\,\omega_0})+\frac{3\,F_2{}^2\,\bar{a}^4}{64\,\omega_0{}^2}\ \right]+\mu^2<0 \qquad (4.46)$$

and are otherwise stable.

A typical frequency response curve is shown in Figure 4.13. The parameter values used are:

$\Omega_s = 3.7$, $\varepsilon^2\Omega_A = 0.02$, $2\,\varepsilon\,\mu = 0.1$, $\Omega_0 = 3.516$ and $\varepsilon = 0.1$.

The nonlinear inertia terms bend the frequency response curve to the left (i.e., softening type). Comparing the approximate solutions with the numerical simulations shows qualitative agreement. Figure 4.13 shows, over certain regions, the response curves become multi-valued. This gives rise to the well documented jump phenomenon. This means the steady-state amplitudes can undergo spontaneous jumps due to an infinitesimal change in σ. Figures 4.14a-b show time traces of the steady-state solution of Q obtained from numerical integration of equation (4.1) for $\sigma = -35$. Two different sets of initial conditions are used. The corresponding phase portraits of these two time traces are shown in Figure 4.15. These figures clearly demonstrate that the frequency response curve is multi-valued. Once more, it is interesting to note that for yet another set of initial

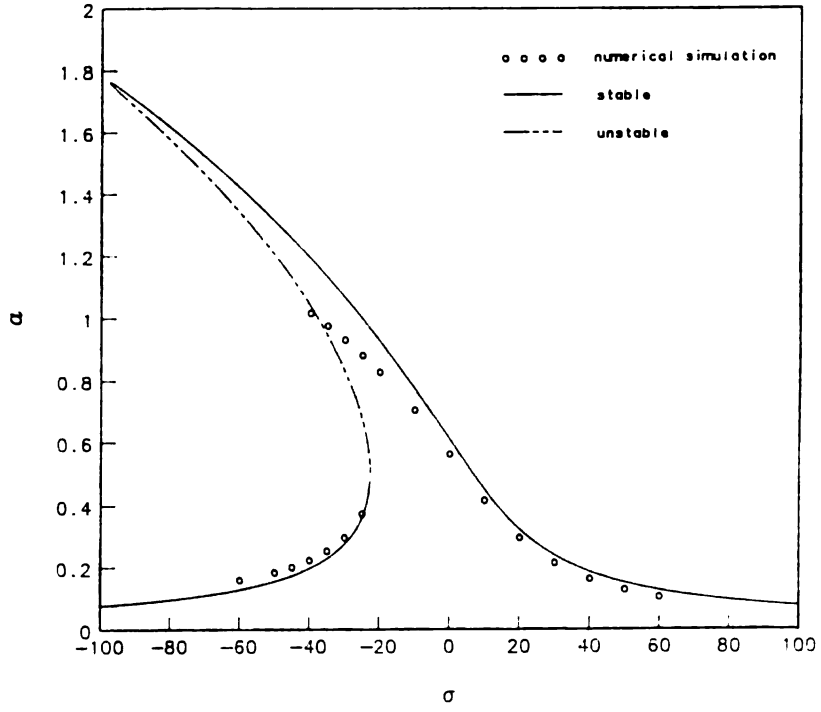

Figure 4.13 Variation of the Steady-State Amplitude, a, with σ.

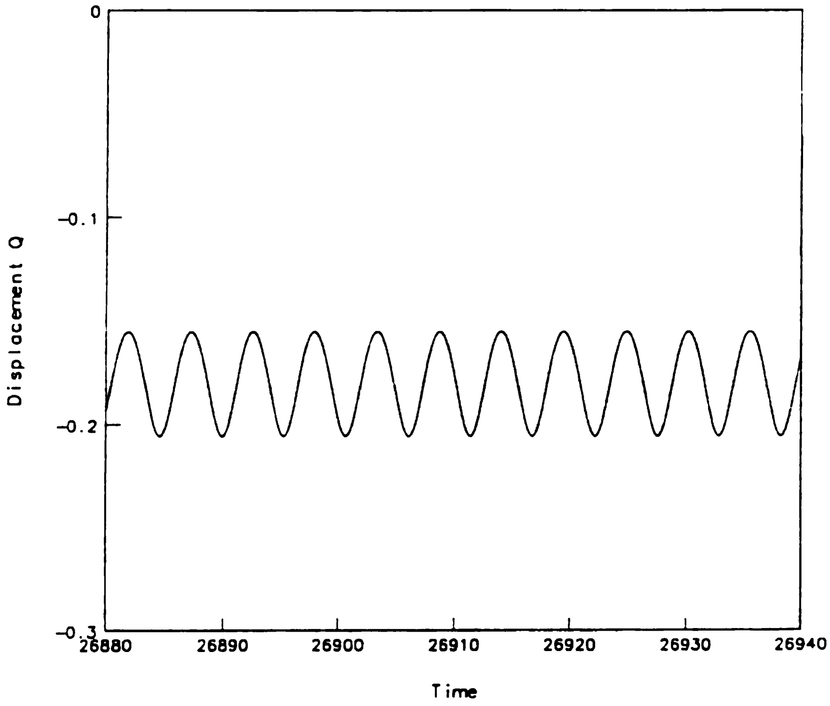

Figure 4.14a Time Trace of the Steady-State Solution Q for σ = -35;
$Q(0) = 0.05$, $\dot{Q}(0) = 0.0$.

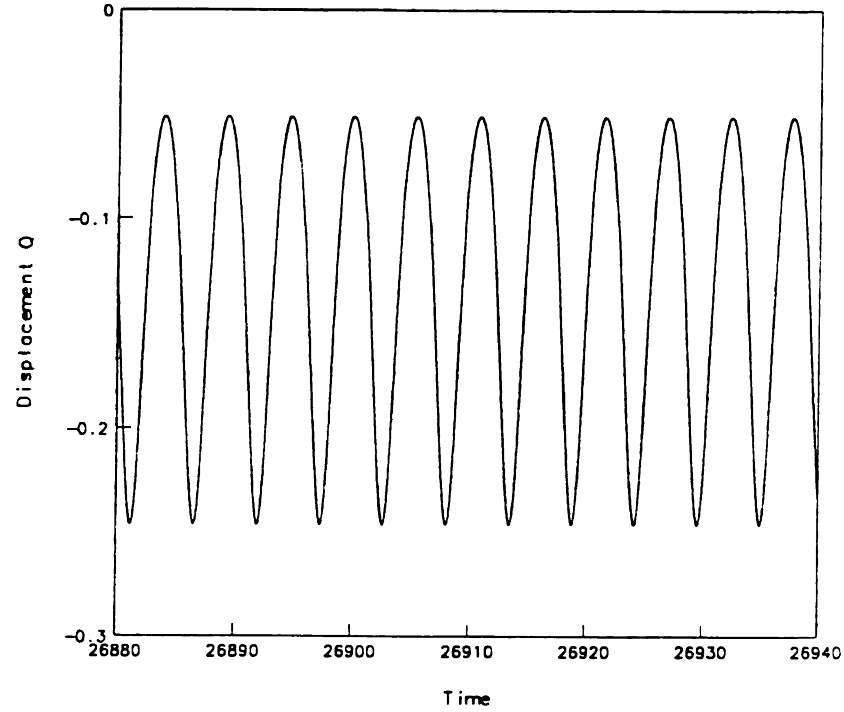

Figure 4.14b Time Trace of the Steady-State Solution Q for σ = -35; $Q(0) = 0.1, \dot{Q}(0) = 0.0$.

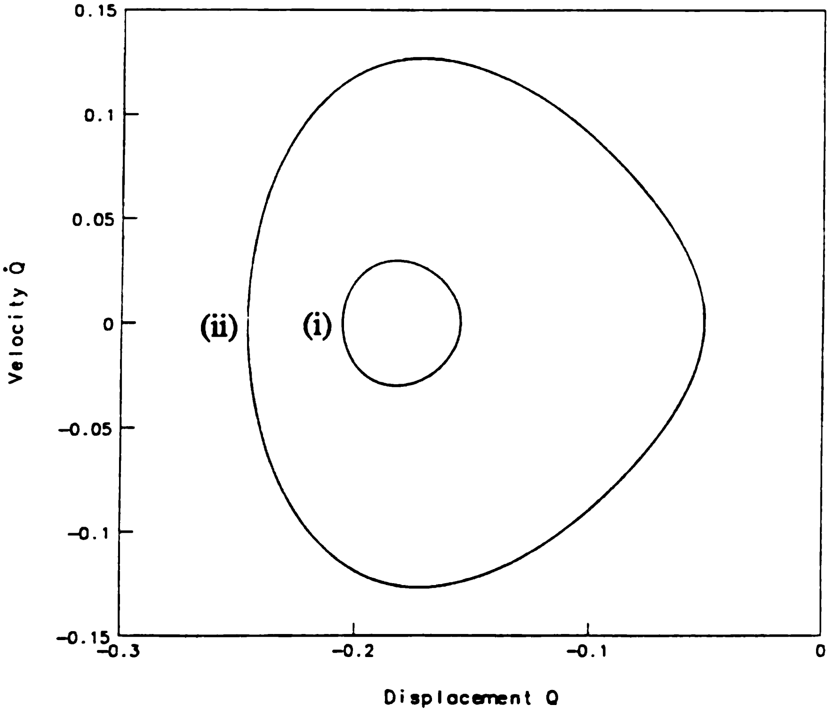

Figure 4.15 Phase Portraits of the Steady-State Solution Q for σ = -35; (i) $Q(0) = 0.05, \dot{Q}(0) = 0.0$, (ii) $Q(0) = 0.1, \dot{Q}(0) = 0.0$.

conditions, a subharmonic motion which encompasses both buckled positions can be found. The corresponding time trace and phase portrait of such a case are shown in Figure 4.16a and 4.16b, respectively.

4.6 Simulation and Observations of Chaotic Motions

In this section we will use an analytical method and numerical simulations to explore the chaotic motions of a rotating buckled beam. A chaotic motion is a non-periodic but bounded motion with a broadband spectrum and a high degree of sensitive to initial condition. As a system parameter is varied, a periodic motion may undergo a series of bifurcations. This series of bifurcations, if it continues, will lead to a chaotic motion. In the simulations, we will concentrate on two regions: (a) primary resonance $\omega \approx \omega_0$ and (b) subharmonic resonance $\omega \approx 2\,\omega_0$. The parameter values used in the simulations, unless otherwise stated, are: $\Omega_s = 3.7$, $2\,\varepsilon\,\mu = 0.1$. Before using the digital computer to simulate equation (4.1), we apply the Melnikov's method to provide a necessary condition of chaotic motions.

4.6.1 Melnikov's method

Melnikov's method provides a measure of the separation between the stable and unstable manifolds along the unperturbed homoclinic orbit (Guckenheimer and Holmes [1987], Wiggins [1988]). It involves the computation of the Melnikov function $M(\tau_0)$; if $M(\tau_0)$ has simple zeros the stable and unstable manifolds may intersect an infinite number of times and chaotic motions may exist.

Following the procedure of this method, equation (4.1) is written in the form

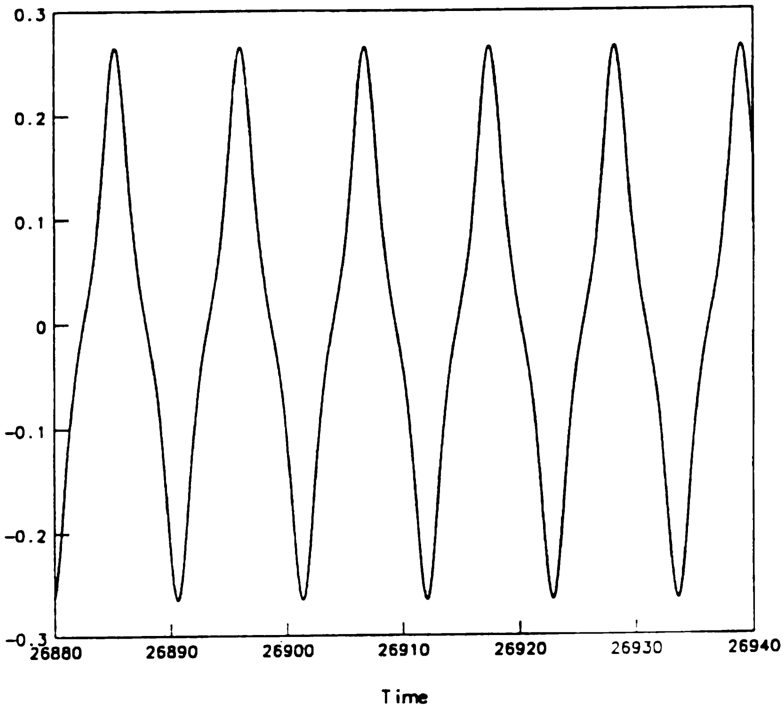

Figure 4.16a Time Trace of the Steady-State Solution Q for $\sigma = -35$; $Q(0) = 0.25$, $\dot{Q}(0) = 0.0$.

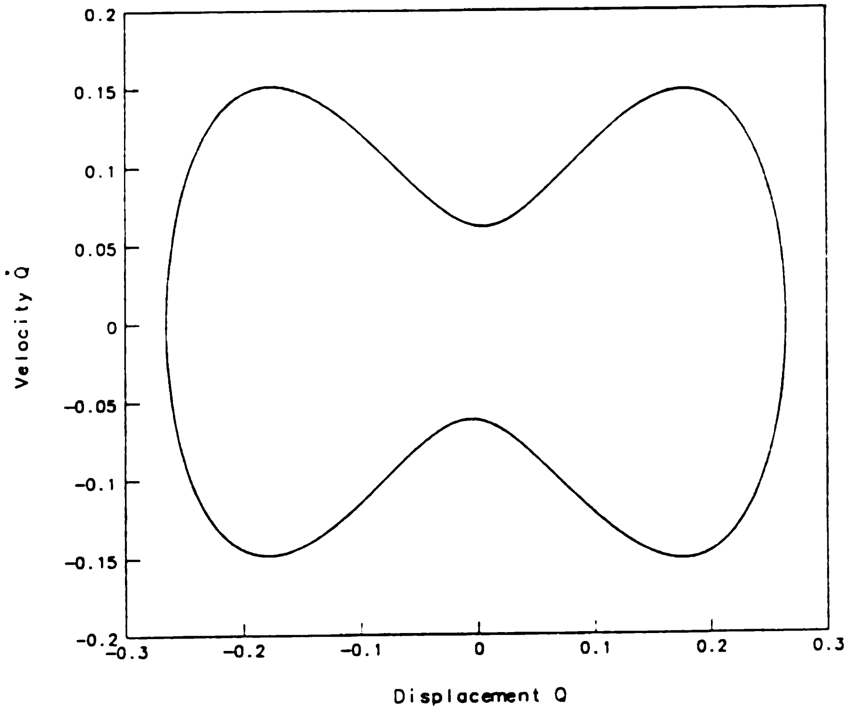

Figure 4.16b Phase Portrait of the Steady-State Solution Q for $\sigma = -35$; $Q(0) = 0.25$, $\dot{Q}(0) = 0.0$.

$$\dot{\mathbf{z}} = \mathbf{f}(\mathbf{z}) + \varepsilon\, \mathbf{g}(\mathbf{z},\tau) + \varepsilon^2\, \mathbf{h}(\mathbf{z},\tau), \quad \mathbf{z} = \begin{bmatrix} Q \\ \dot{Q} \end{bmatrix} = \begin{bmatrix} x_1 \\ x_2 \end{bmatrix} \in \mathbf{R}^2 \tag{4.47}$$

where

$$\mathbf{f}(\mathbf{z}) = \begin{bmatrix} f_1(x_1,x_2) \\ f_2(x_1,x_2) \end{bmatrix} = \begin{bmatrix} x_2 \\ -\dfrac{d\, x_1 x_2^{\,2} + b\, x_1^{\,3} + (\Omega_0^{\,2} - \Omega_s^{\,2})\, x_1}{1 + d\, x_1^{\,2}} \end{bmatrix}$$

$$\mathbf{g}(\mathbf{z},\tau) = \begin{bmatrix} g_1(x_1,x_2,\tau) \\ g_2(x_1,x_2,\tau) \end{bmatrix} = \begin{bmatrix} 0 \\ -\dfrac{2\mu\, x_2 - 2\,\Omega_s \Omega_A \sin(\omega\tau)\, x_1}{1 + d\, x_1^{\,2}} \end{bmatrix}$$

$$\mathbf{h}(\mathbf{z},\tau) = \begin{bmatrix} h_1(x_1,x_2,\tau) \\ h_2(x_1,x_2,\tau) \end{bmatrix} = \begin{bmatrix} 0 \\ \dfrac{(\Omega_A \sin \omega\tau)^2\, x_1}{1 + d\, x_1^{\,2}} \end{bmatrix}.$$

The Melnikov function is given by the formula (Guckenheimer and Holmes [1987], page 187)

$$M(\tau_0) = \int_{-\infty}^{\infty} \left[f_1(x_{10}, x_{20})\, g_2(x_{10}, x_{20}, \tau + \tau_0) - f_2(x_{10}, x_{20})\, g_1(x_{10}, x_{20}, \tau + \tau_0) \right] d\tau \tag{4.48}$$

where (x_{10}, x_{20}) is the unperturbed homoclinic orbit.

For the system presently being studied, it is impossible to find an analytical solution of the unperturbed homoclinic orbit. Therefore, we use the Runge-Kutta method to find an approximation to the unperturbed homoclinic orbit by setting $\varepsilon = 0$ in equation (4.47) with an initial condition very near to (0, 0).

Equation (4.48) can be written as

$$M(\tau_0) = -2\mu\, I_1 + 2\,\Omega_s\, \Omega_A\, [\, I_2(\omega) \cos \omega\tau_0 + I_3(\omega) \sin \omega\tau_0 \,] \tag{4.49}$$

where

$$I_1 = \int_{-\infty}^{\infty} \frac{x_{20}^{\;2}}{1+d\,x_{10}^{\;2}}\,d\tau \tag{4.50}$$

$$I_2(\omega) = \int_{-\infty}^{\infty} \frac{(\sin \omega\tau)\,x_{10}x_{20}}{1+d\,x_{10}^{\;2}}\,d\tau \tag{4.51}$$

$$I_3(\omega) = \int_{-\infty}^{\infty} \frac{(\cos \omega\tau)\,x_{10}x_{20}}{1+d\,x_{10}^{\;2}}\,d\tau \tag{4.52}$$

Then we numerically integrate the equations (4.50) and (4.51) by using Simpson's rule. It is found that $I_1 > 0$ and $I_3(\omega) = 0$ (since the integrand in equation (4.52) is an odd function). Obviously, when $2\,\Omega_s\,\Omega_A\,I_2(\omega) > 2\,\mu\,I_1$, $M(\tau_0)$ has simple zeros (i.e., the stable and unstable manifolds intersect transversely). The ratio of I_1 and $I_2(\omega)$ is plotted as a function of ω in Figure 4.17 for a value of $\Omega_s = 3.70$. The regions above the curve in Figure 4.17 are the parameter values where a homoclinic tangle exists. The influence of the mean spin rates, Ω_s, on this curve can be seen in Figure 4.18. We observe that the possible chaotic motion regions and the lower limit of the curves increase as Ω_s increases.

To add confidence to the results predicted by the Melnikov analysis, we numerical obtain a number of the stable, W^s, and unstable,W^u, manifolds associated with the saddle point of equation (4.47). To generate portion of W^u, points on a small segment along the unstable eigendirection centered at the saddle point are mapped forward in time in the Poincare section. The W^s can be generated in a similar way, with time running backward. For the fixed parameter values $2\varepsilon\mu = 0.1$ and $\omega = 1.54 \approx \omega_0$, Figure 4.19a-c show the stable and the unstable manifolds of the saddle point (0,0) for three different values of $\frac{\Omega_s\Omega_A}{\mu}$. As shown in Figure 4.19b, W^s just intersects W^u tangentially at $\frac{\Omega_s\Omega_A}{\mu} = 1.036$, in comparison with a theoretical value of 1.073. Figure 4.20a-c shows the result for another

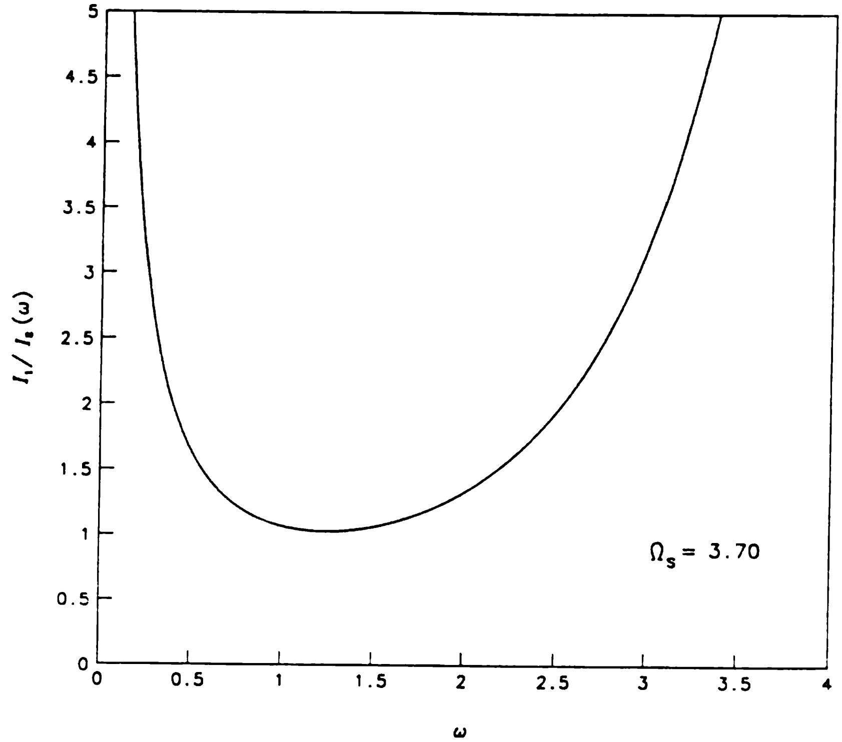

Figure 4.17 Variation of the Ratio $I_1 : I_2(\omega)$ with ω for $\Omega_s = 3.70$.

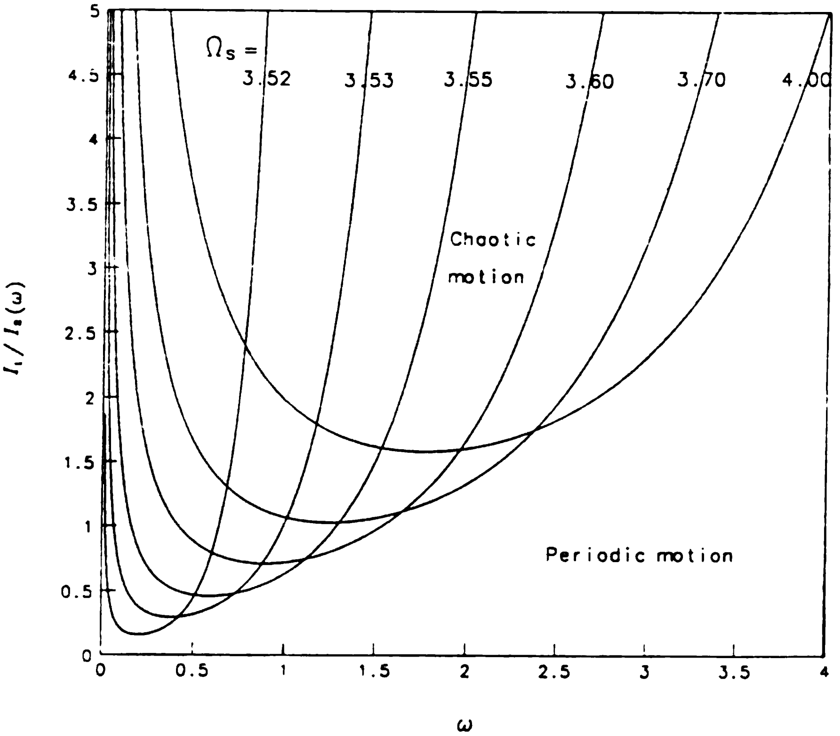

Figure 4.18 Variation of the Ratio $I_1 : I_2(\omega)$ with ω for Ω_s = 3.52, 3.53, 3.55, 3.60, 3.70, 4.0.

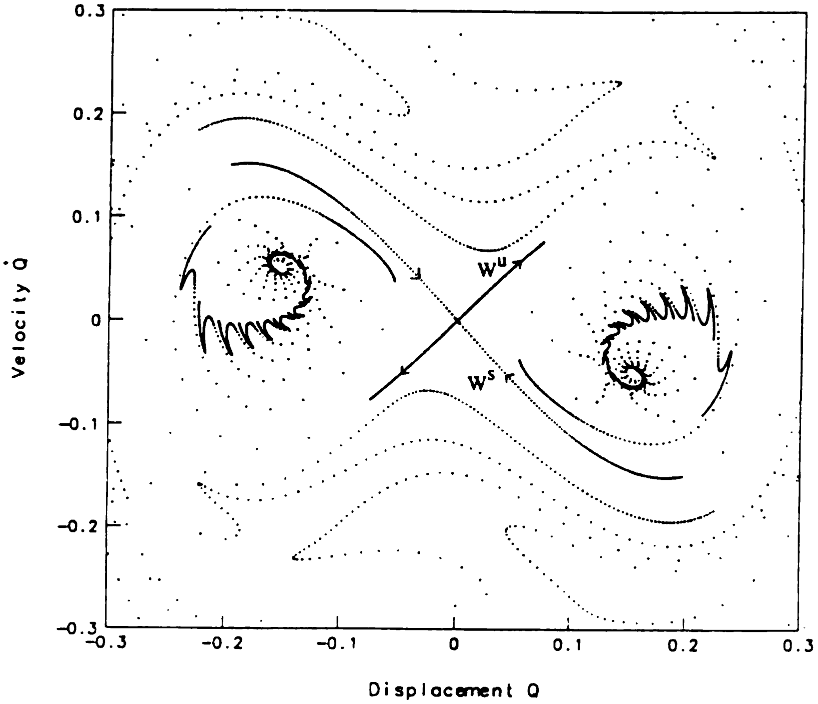

Figure 4.19a Stable Manifold W^S and Unstable Manifold W^u; $\frac{\Omega,\Omega_A}{\mu}$ = 0.74.

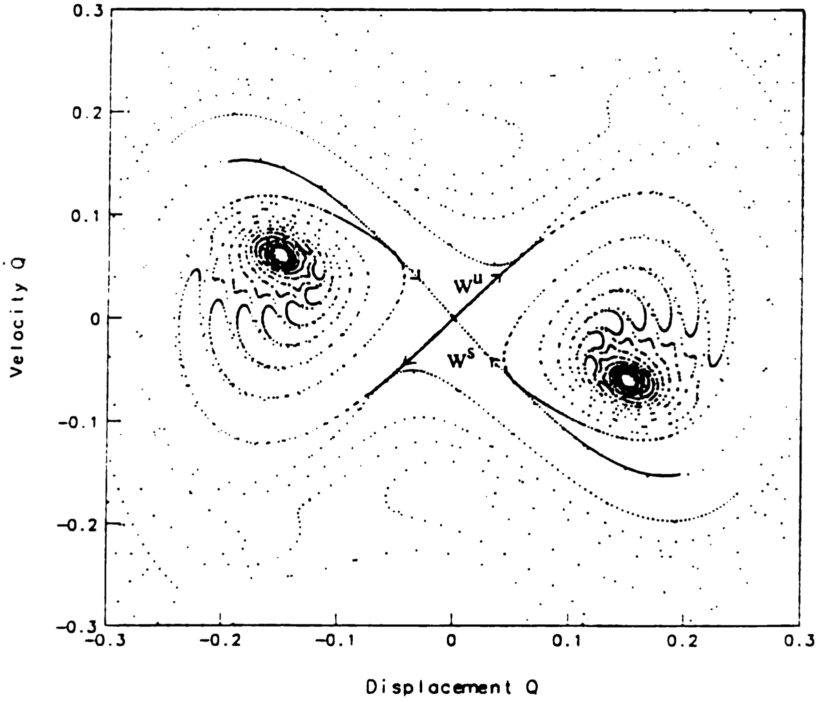

Figure 4.19b Stable Manifold W^S and Unstable Manifold W^u; $\frac{\Omega,\Omega_A}{\mu}$ = 1.036.

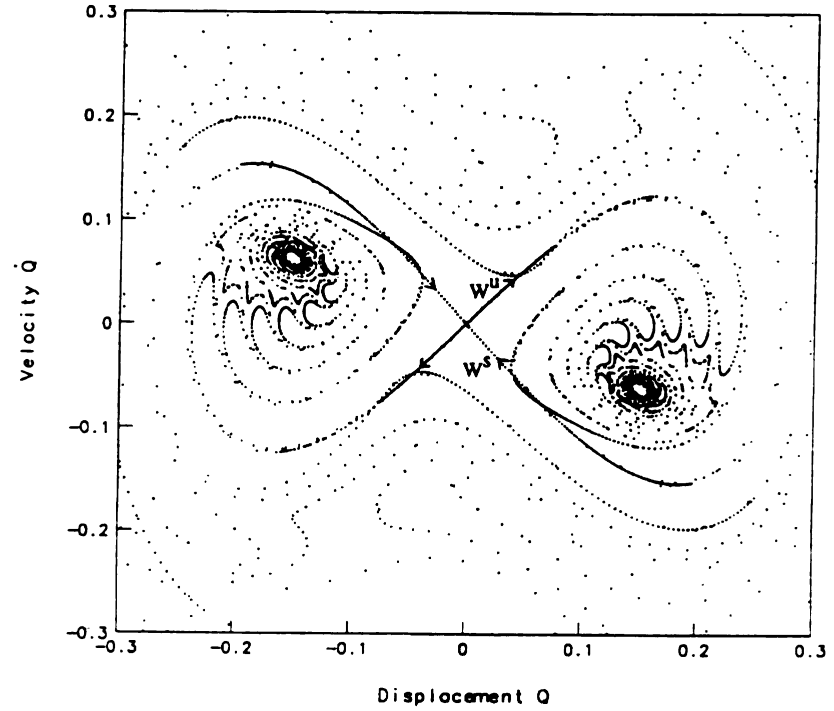

Figure 4.19c Stable Manifold W^s and Unstable Manifold W^u; $\frac{\Omega_s\Omega_A}{\mu} = 1.11$.

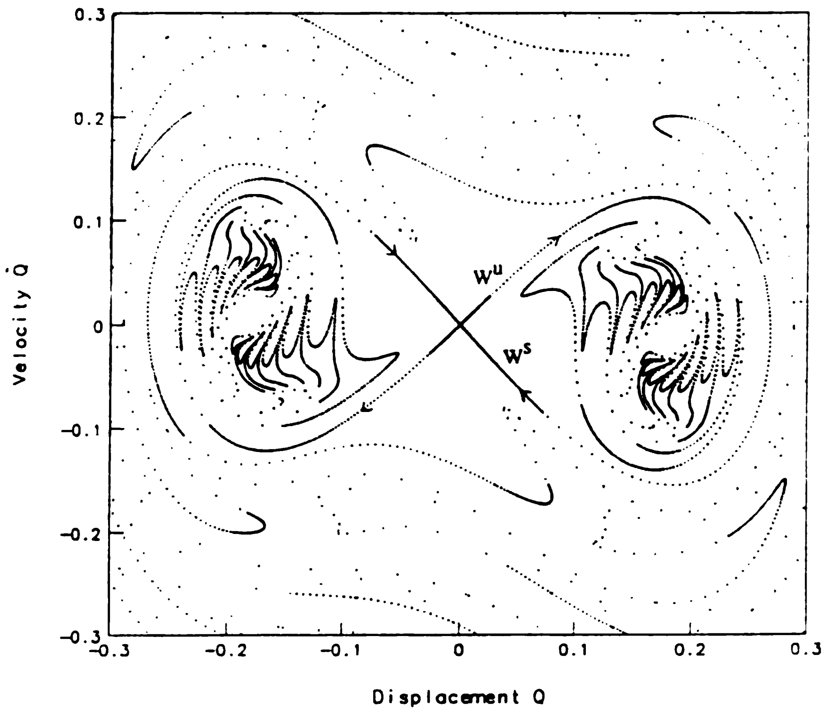

Figure 4.20a Stable Manifold W^s and Unstable Manifold W^u; $\frac{\Omega_s\Omega_A}{\mu} = 1.48$.

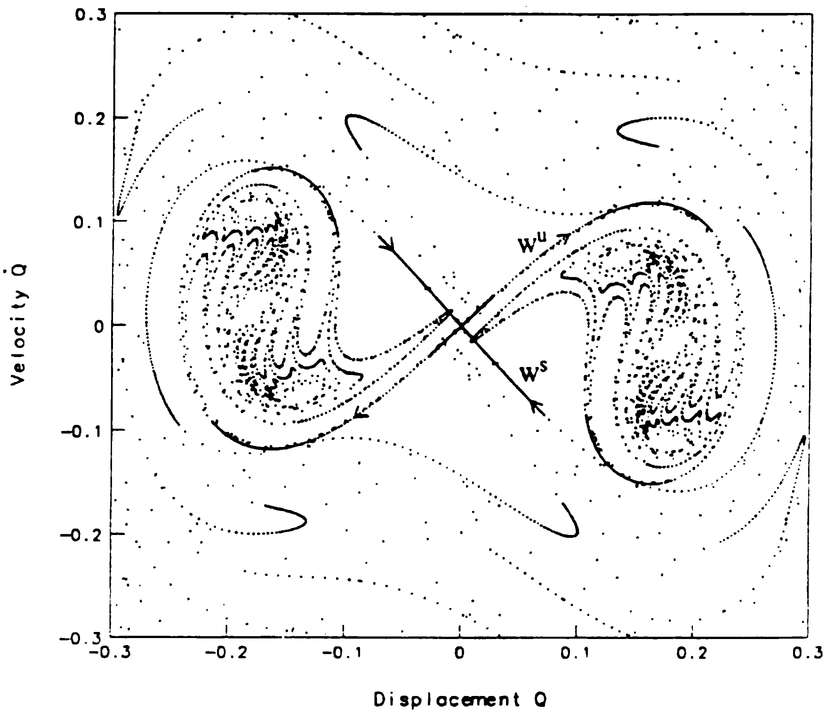

Figure 4.20b Stable Manifold W^s and Unstable Manifold W^u; $\frac{\Omega_s\Omega_A}{\mu} = 2.22$.

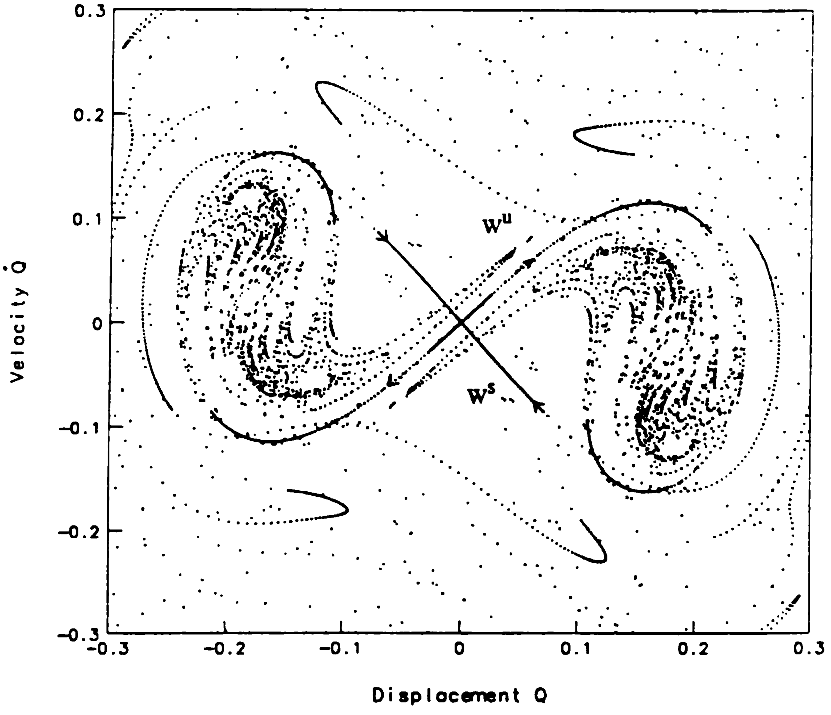

Figure 4.20c Stable Manifold W^s and Unstable Manifold W^u; $\frac{\Omega_s\Omega_A}{\mu} = 2.96$.

set of the fixed parameter values $2\varepsilon\mu = 0.1$ and $\omega = 2.79 \approx 2\,\omega_0$. Note that the first tangency (see Figure 4.20b) appears to occur about $\frac{\Omega_s\Omega_A}{\mu} = 2.22$, compared with the predicted value of 2.54. We conclude that the results obtained by Melnikov's method are good. The slight disagreement between the analytical method and numerical simulations are possibly because the Melnikov's method is a first-order approximation.

In the next two sub-sections, we will vary the value of $\varepsilon\,\Omega_A$ to see what happens to the solution $Q\,(\tau)$ as one crosses the homoclinic bifurcation curve shown in Figure 4.17. To this end equation (4.1) is simulated on a digital computer. After transient motions decayed, the steady-state solution is recorded. The initial conditions used for the simulation, unless otherwise stated, are $Q\,(\tau) = 0.1$ and $\dot{Q}(\tau) = 0.0$. The time step size equal to $\frac{T}{200}$, where $T = \frac{2\pi}{\omega}$ is the forcing period. Note that, for small values of $\varepsilon\,\Omega_A$, the rotating, buckled beam will vibrate about one of the two buckled positions and the initial conditions determine which buckled position the beam will vibrate.

4.6.2 The Primary Resonance: $\omega \approx \omega_0$

Equation (4.1) was simulated on a digital computer for fixed values of $\Omega_s = 3.70$, $2\varepsilon\mu = 0.1$ and $\omega = 1.54$. We present here only the effect of varying the amplitude, $\varepsilon\,\Omega_A$,of the small sinusoidal fluctuation of the rotational speed. The results are shown in Figures 4.21-23 and summarized in Table 4.1.

For values of $\varepsilon\,\Omega_A$ between 0.045 and 0.4605, we see a period doubling sequence. This ends in an almost periodic motion at $\varepsilon\,\Omega_A = 0.04657$. Between 0.0467 and 0.4685 there exists an island of periodic motion motions (12T and 6T) before one again encounter an almost periodic motion at $\varepsilon\,\Omega_A = 0.0469$.

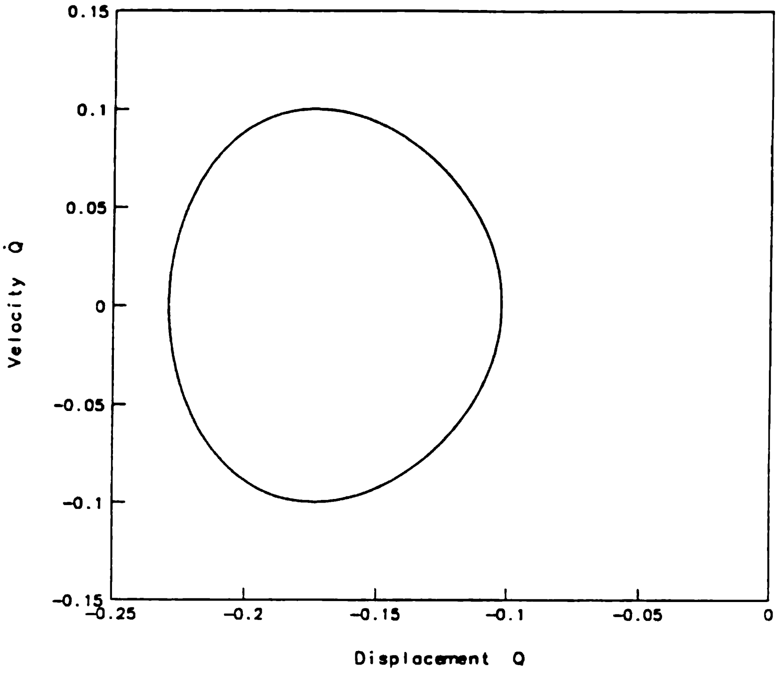

Figure 4.21a Phase Portrait of Period 1 Motion; $\varepsilon^2\Omega_A = 0.035$.

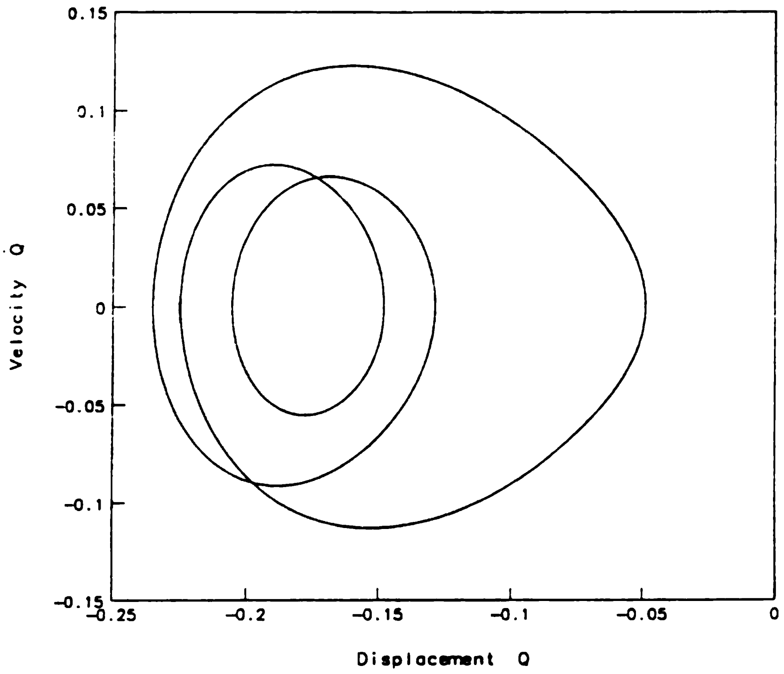

Figure 4.21b Phase Portrait of Period 3 Motion; $\varepsilon^2\Omega_A = 0.045$.

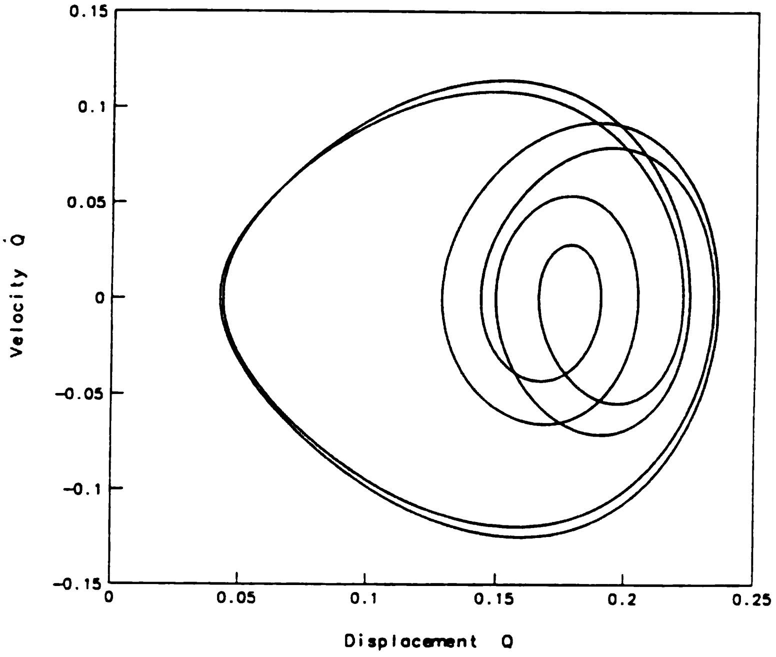

Figure 4.21c Phase Portrait of Period 6 Motion; $\varepsilon^2\Omega_A = 0.046$.

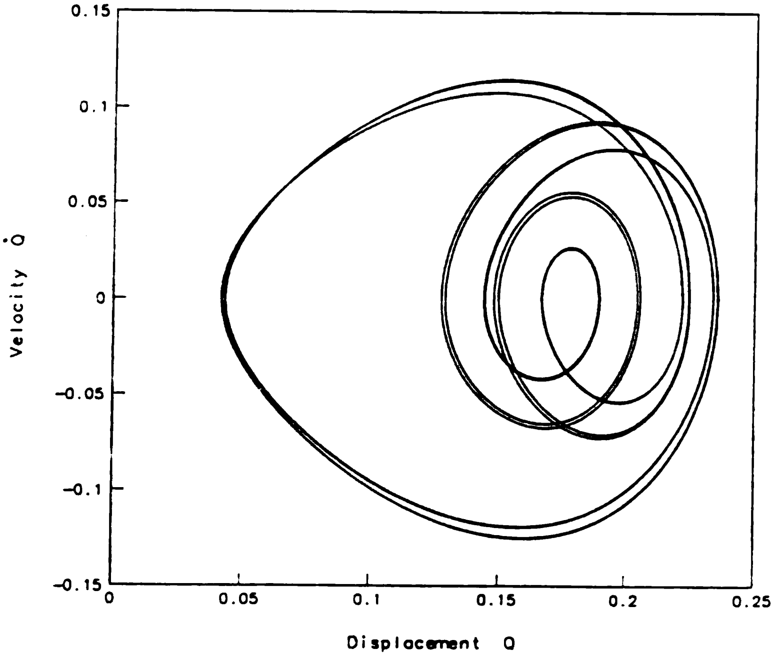

Figure 4.21d Phase Portrait of Period 12 Motion; $\varepsilon^2\Omega_A = 0.04605$.

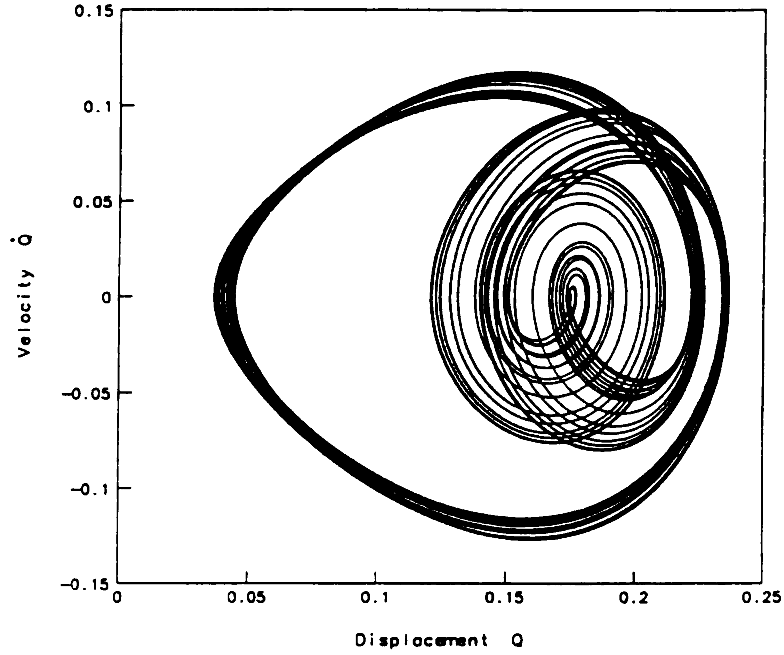

Figure 4.21e Phase Portrait of Almost Periodic Motion; $\varepsilon^2\Omega_A = 0.04657$.

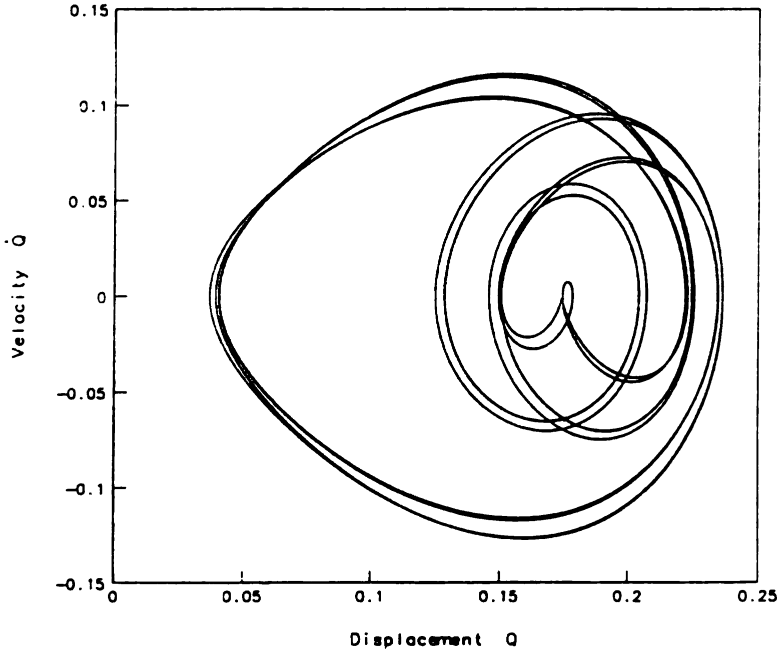

Figure 4.21f Phase Portrait of Period 12 Motion; $\varepsilon^2\Omega_A = 0.0467$.

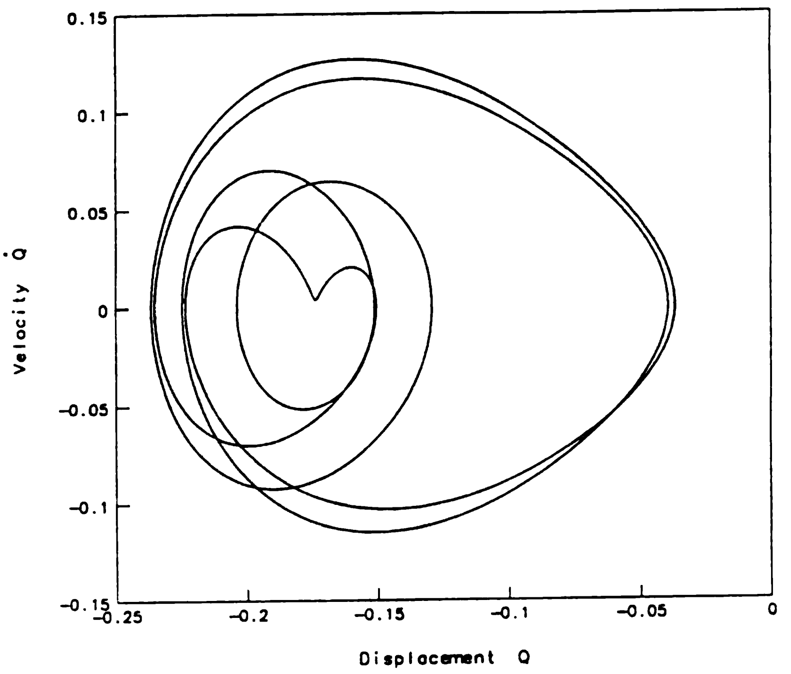

Figure 4.21g Phase Portrait of Period 6 Motion; $\varepsilon^2\Omega_A = 0.0468$.

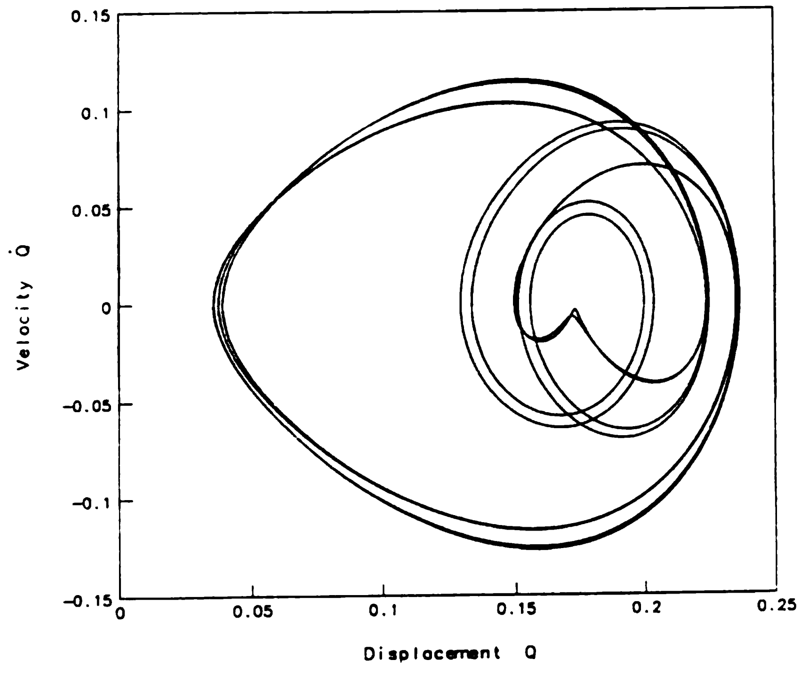

Figure 4.21h Phase Portrait of Period 12 Motion; $\varepsilon^2\Omega_A = 0.04685$.

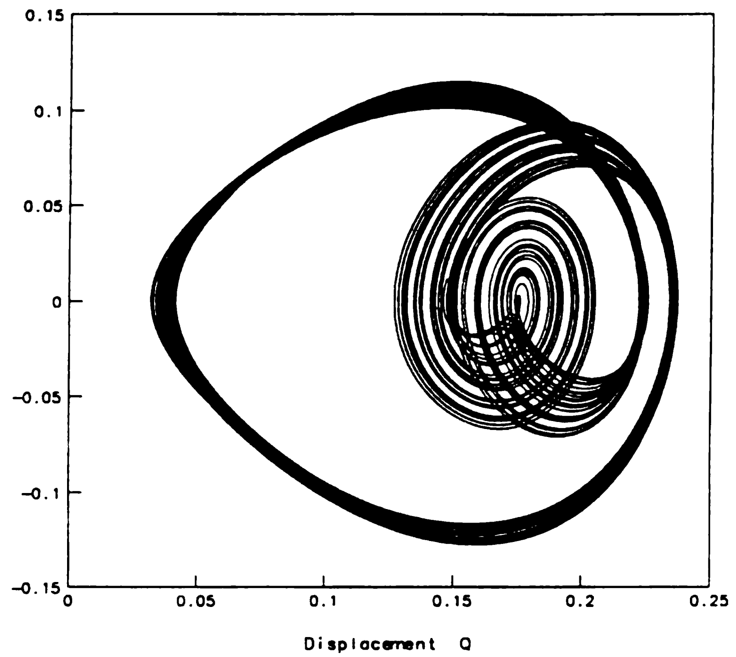

Figure 4.21i Phase Portrait of Almost Periodic Motion; $\varepsilon^2\Omega_A = 0.0469$.

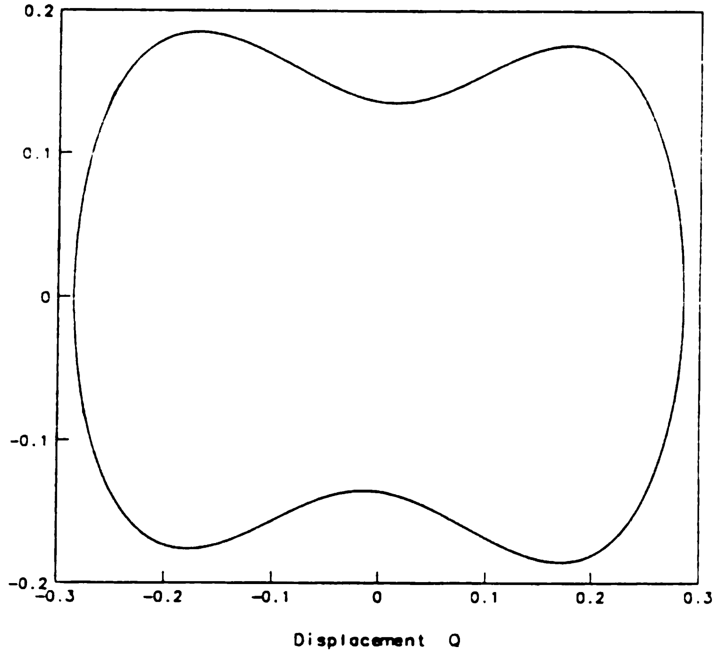

Figure 4.22a Phase Portrait of Period 2 Motion $\varepsilon^2\Omega_A = 0.047$.

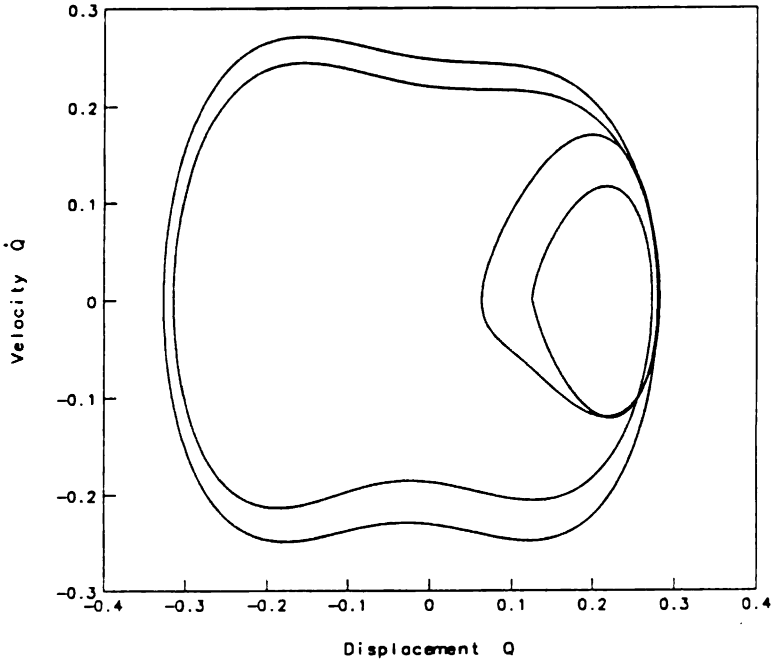

Figure 4.22b Phase Portrait of Period 6 Motion; $\varepsilon^2\Omega_A = 0.0915$.

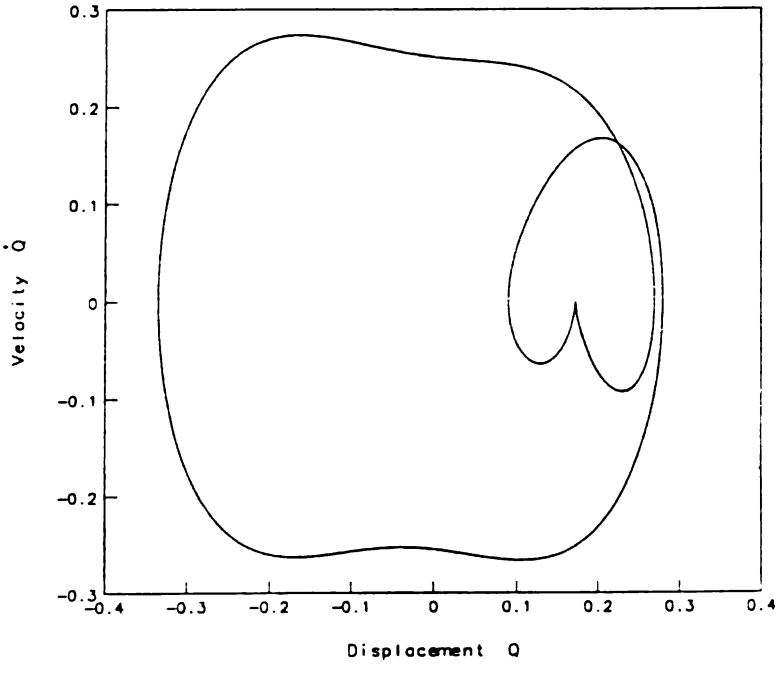

Figure 4.22c Phase Portrait of Period 3 Motion; $\varepsilon^2\Omega_A = 0.115$.

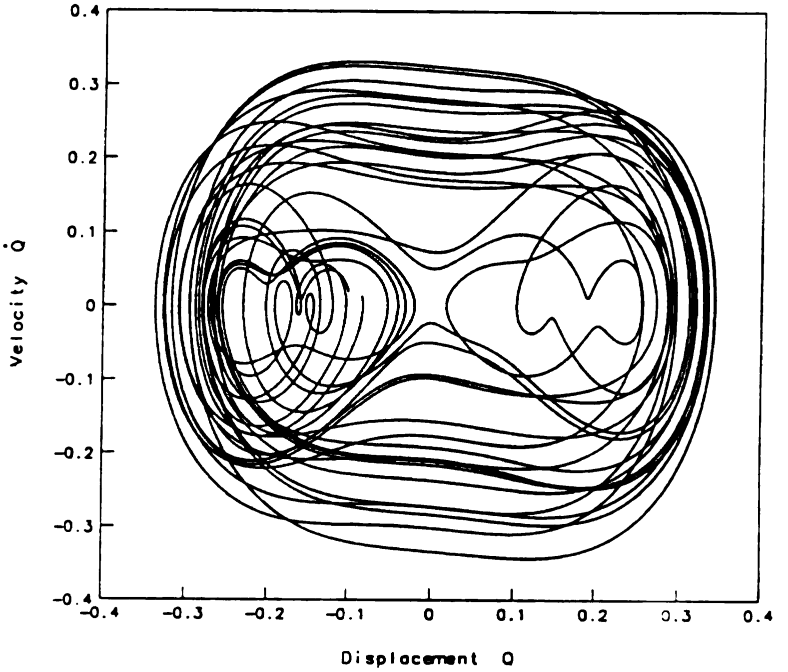

Figure 4.23 Phase Portrait of Chaotic Motion; $\varepsilon^2\Omega_A = 0.12$.

Table 4.1 Summary of Bifurcated and Chaotic Motions for $\omega = 1.54$.

$\varepsilon \Omega_A$	Figure	Type of Motion	Initial Conditions $(Q(0), \dot{Q}(0))$
0.035	Figure 4.21a	1T	(0.10, 0.0)
0.045	Figure 4.21b	3T	(0.10, 0.0)
0.046	Figure 4.21c	6T	(0.10, 0.0)
0.04605	Figure 4.21d	12T	(0.10, 0.0)
0.04657	Figure 4.21e	almost periodic	(0.10, 0.0)
0.0467	Figure 4.21f	12T	(0.05, 0.0)
0.0468	Figure 4.21g	6T	(0.10, 0.0)
0.04685	Figure 4.21h	12T	(0.15, 0.0)
0.0469	Figure 4.21i	almost periodic	(0.15, 0.0)
0.047	Figure 4.22a	2T	(0.10, 0.0)
0.0915	Figure 4.22b	6T	(0.10, 0.0)
0.115	Figure 4.22c	3T	(0.10, 0.0)
0.12	Figure 4.23	chaotic	(0.10, 0.0)

Increasing the value of $\varepsilon \Omega_A$ further, as one might anticipate, the beam will not vibrate about only one of the buckled positions but will snap-through and adopt an orbit enclosing the two buckled positions. A period 2T snap-through motion is easily seen by the time $\varepsilon \Omega_A = 0.047$ in Figure 4.22a. Once again, as we continuously increase $\varepsilon \Omega_A$ beyond some critical value, a period demultiplying bifurcation occurs with period 6T and period 3T, as shown in Figures 4.22b and 4.22c. In these two figures we observe that the beam vibrates in a complex manner, first vibrates about one buckled position and then snap-through between the two buckled positions. It should be stressed that this is a periodic motion. Finally, a chaotic motion occurs with $\varepsilon \Omega_A = 0.12$, as shown in Figure 4.23. The simulations indicate that as the value of $\varepsilon \Omega_A$ is varied, period doubling bifurcations, demultiplying bifurcations and chaotic motions occur.

Another way of showing the results just presented is to use a Poincare map. If the response is periodic, then its Poincare map will only show a finite number of points. However, when the motion becomes chaotic, its Poincare map will contain an infinite number of points and reveal a fractal pattern (i.e., strange attractor). It is also known that the Poincare map of an almost periodic motions is represented by line segments. Figure 4.24h-i depict the Poincare maps corresponding to a selection of the response shown in Figures 4.21, 4.22 and 4.23.

4.6.3 The Subharmonic Resonance: $\omega \approx 2\,\omega_0$

In this sub-section we consider the case of subharmonic resonance (i.e., $\omega \approx 2\,\omega_0$). As in Sub-section 4.6.2, as we continuously change the parameter $\varepsilon\,\Omega_A$, a period doubling bifurcation occurs. For fixed values of $\Omega_s = 3.70$, $2\varepsilon\mu = 0.1$ and $\omega = 2.79$, the results from the numerical simulation are shown in Figures 4.25-26 and summarized in Table 4.2.

Table 4.2 Summary of Bifurcated and Chaotic Motions for $\omega = 2.79$.

$\varepsilon\Omega_A$	Figure	Type of Motion	Initial Conditions $(Q(0), \dot{Q}(0))$
0.07	Figure 4.25a	2T	(0.10, 0.0)
0.08	Figure 4.25b	4T	(0.10, 0.0)
0.0832	Figure 4.25c	8T	(0.10, 0.0)
0.0833	Figure 4.25d	16T	(0.10, 0.0)
0.0834	Figure 4.25e	32T	(0.10, 0.0)
0.0835	Figure 4.26	chaotic	(0.10, 0.0)

Figures 4.25a-e show the phase portraits of the rotating, buckled beam with different values of $\varepsilon\,\Omega_A$. These figures indicate that, as the value of $\varepsilon\,\Omega_A$ is varied, from

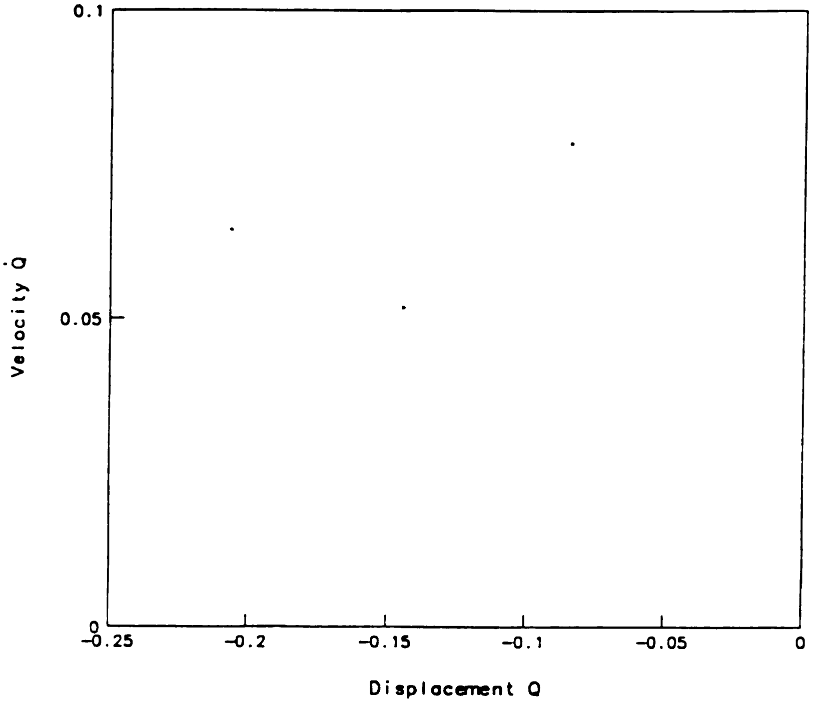

Figure 4.24a Poincare Map of Period 3 Motion; $\varepsilon^2\Omega_A = 0.045$.

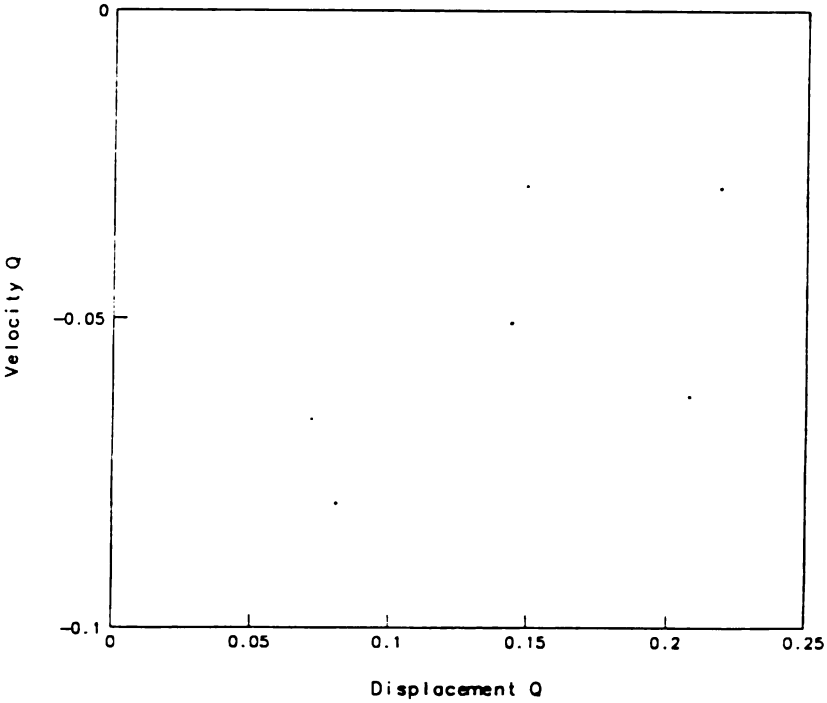

Figure 4.24b Poincare Map of Period 6 Motion; $\varepsilon^2\Omega_A = 0.046$.

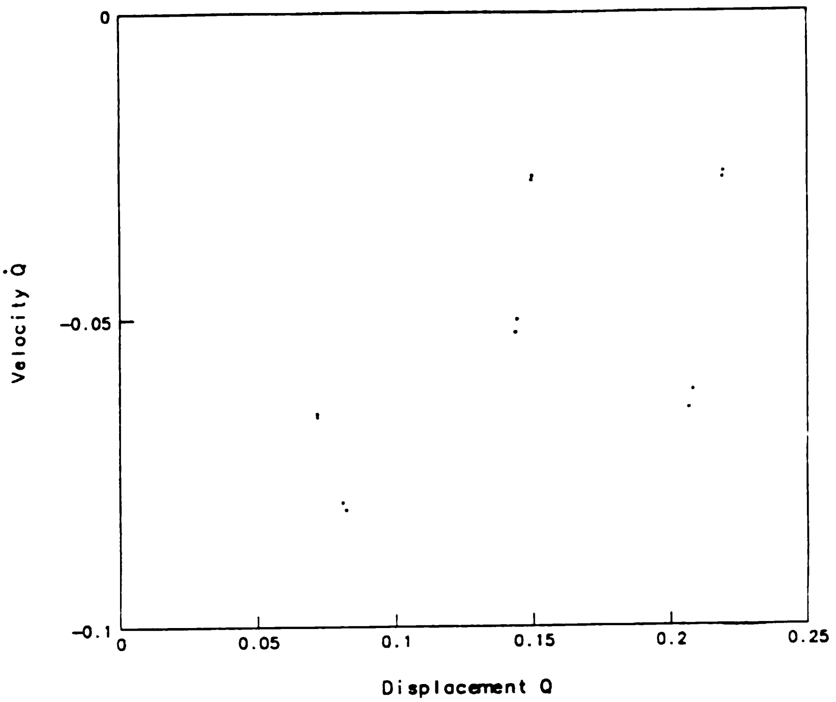

Figure 4.24c Poincare Map of Period 12 Motion; $\varepsilon^2\Omega_A$= 0.04605.

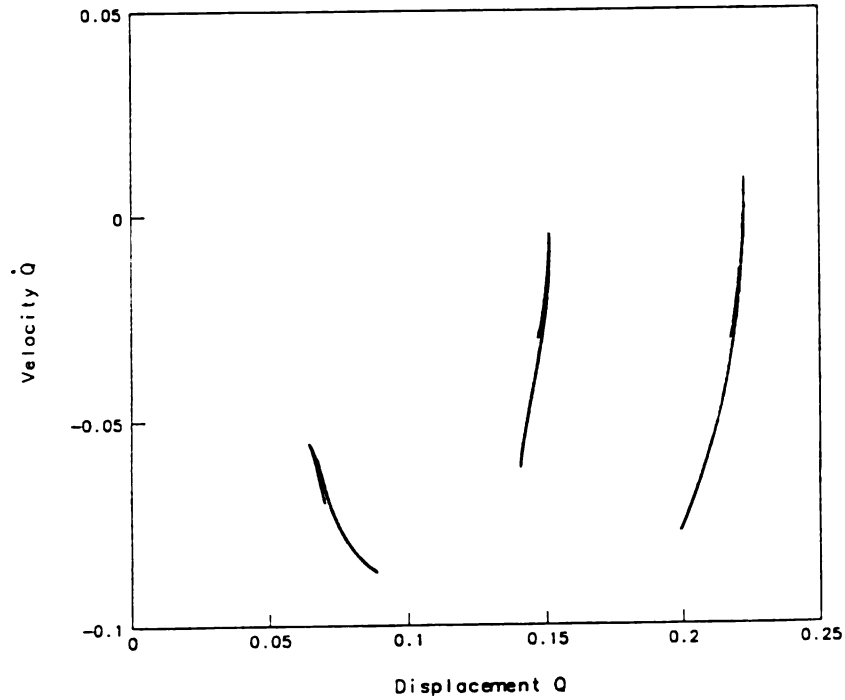

Figure 4.24d Poincare Map of Almost Periodic Motion; $\varepsilon^2\Omega_A$= 0.04657.

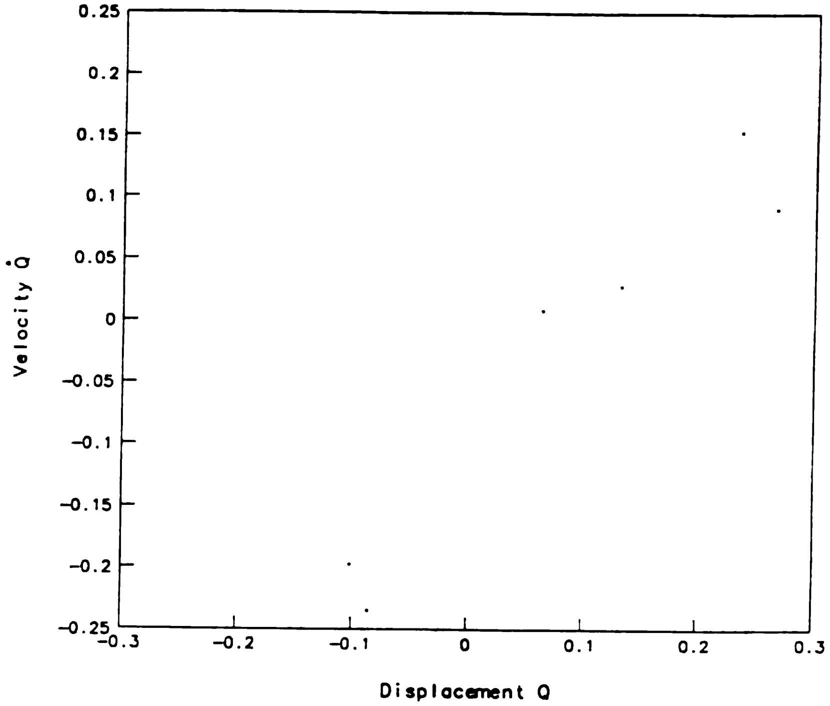

Figure 4.24e Poincare Map of Period 6 Motion; $\varepsilon^2\Omega_A$= 0.0915.

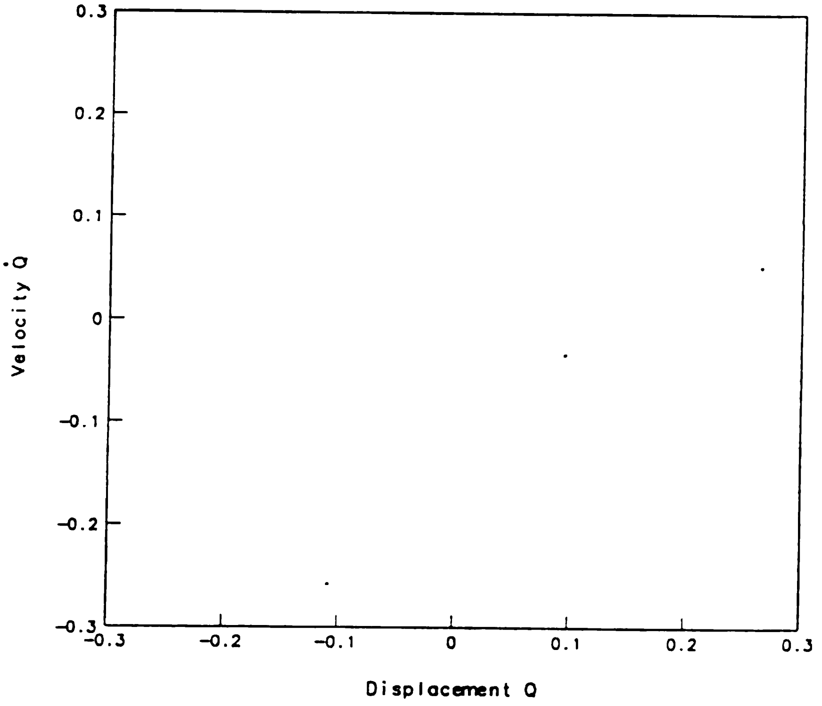

Figure 4.24f Poincare Map of Period 3 Motion; $\varepsilon^2\Omega_A$= 0.115.

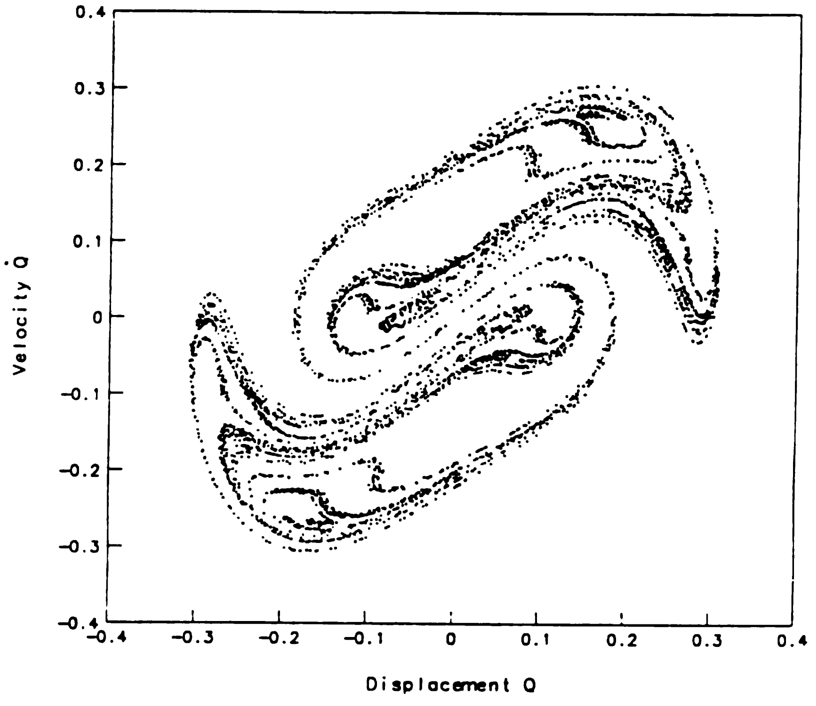

Figure 4.24g Poincare Map of Chaotic Motion; $\varepsilon^2\Omega_A = 0.12$.

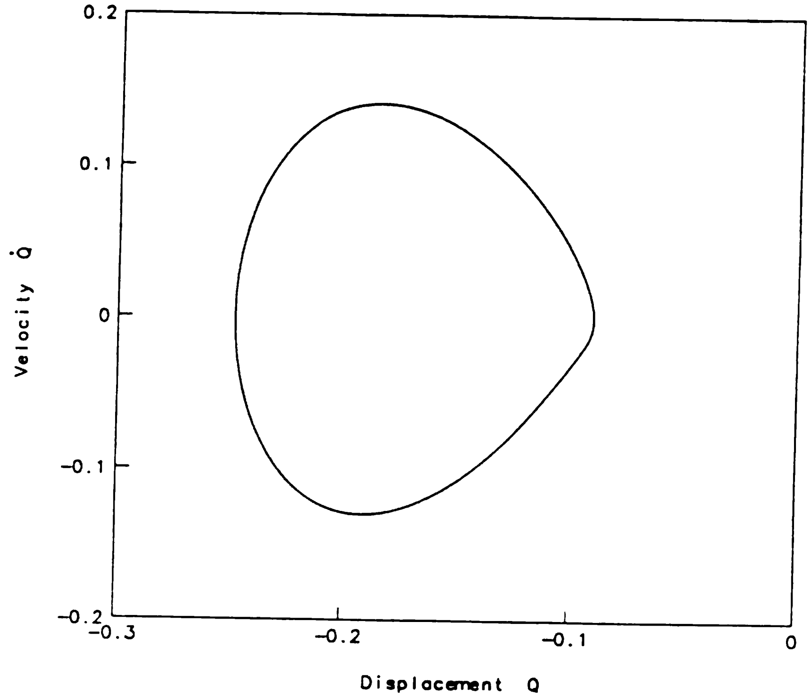

Figure 4.25a Phase Portrait of Period 2 Motion; $\varepsilon^2\Omega_A = 0.07$.

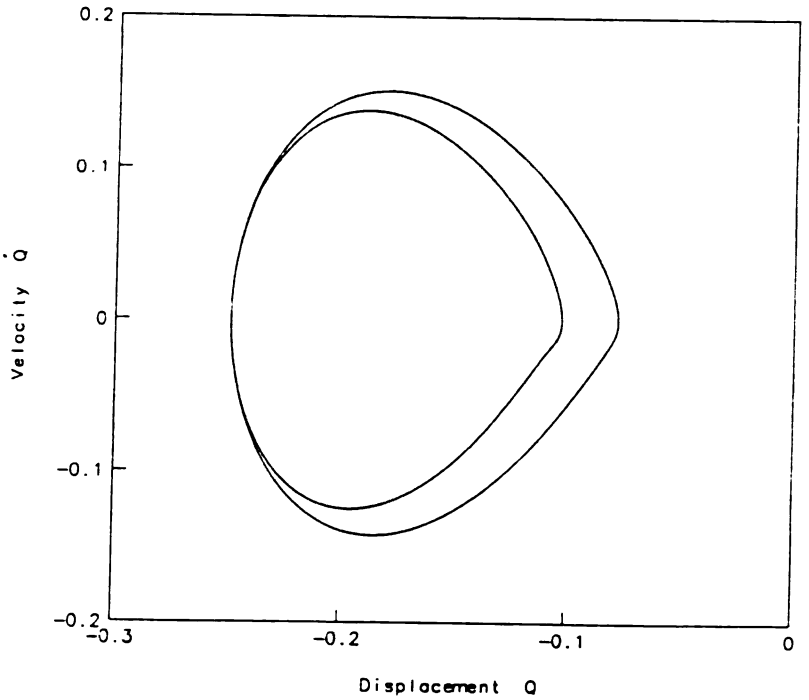

Figure 4.25b Phase Portrait of Period 4 Motion; $\varepsilon^2\Omega_A = 0.08$.

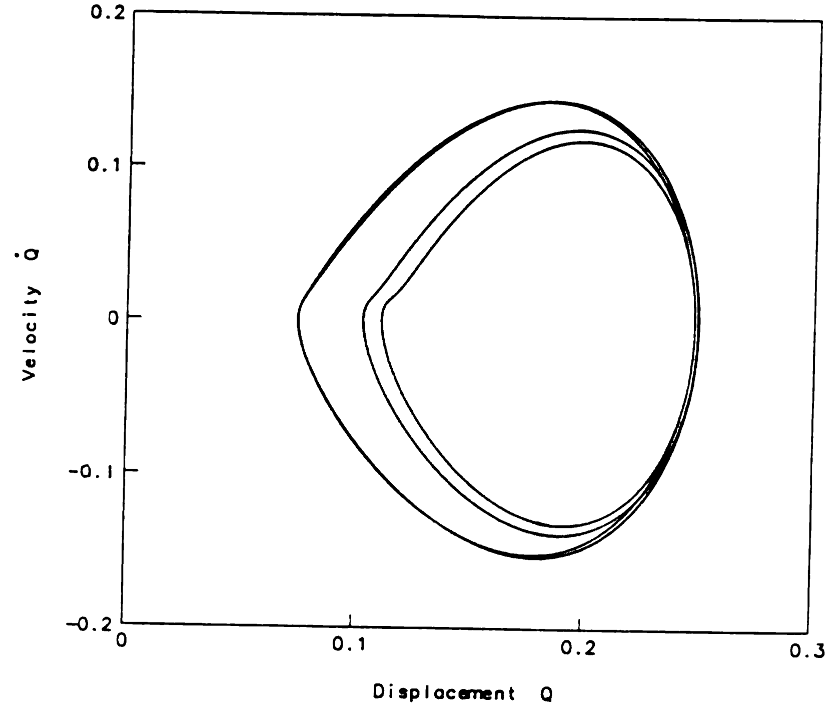

Figure 4.25c Phase Portrait of Period 8 Motion; $\varepsilon^2\Omega_A = 0.0832$.

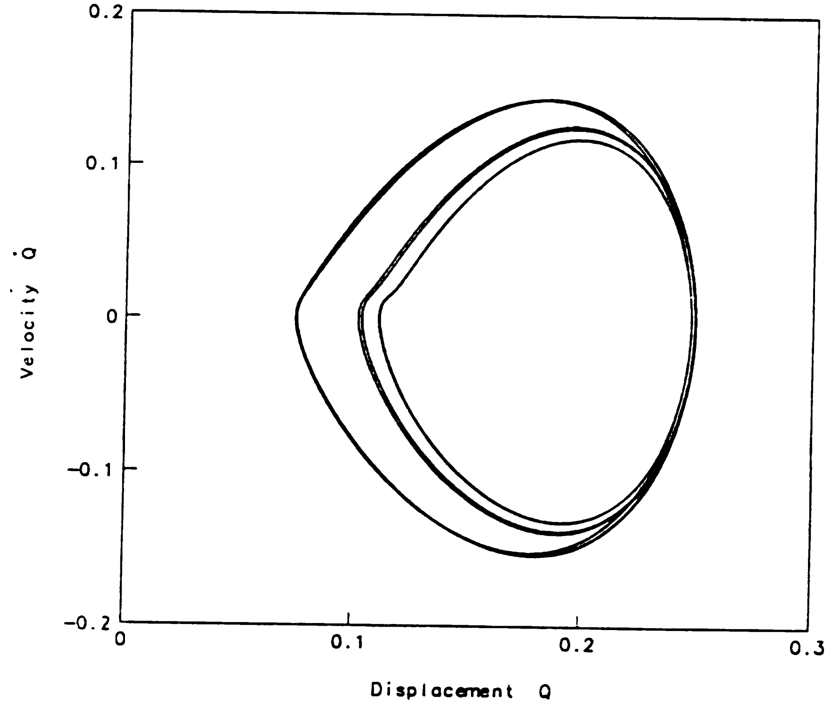

Figure 4.25d Phase Portrait of Period 16 Motion; $\varepsilon^2\Omega_A = 0.0833$.

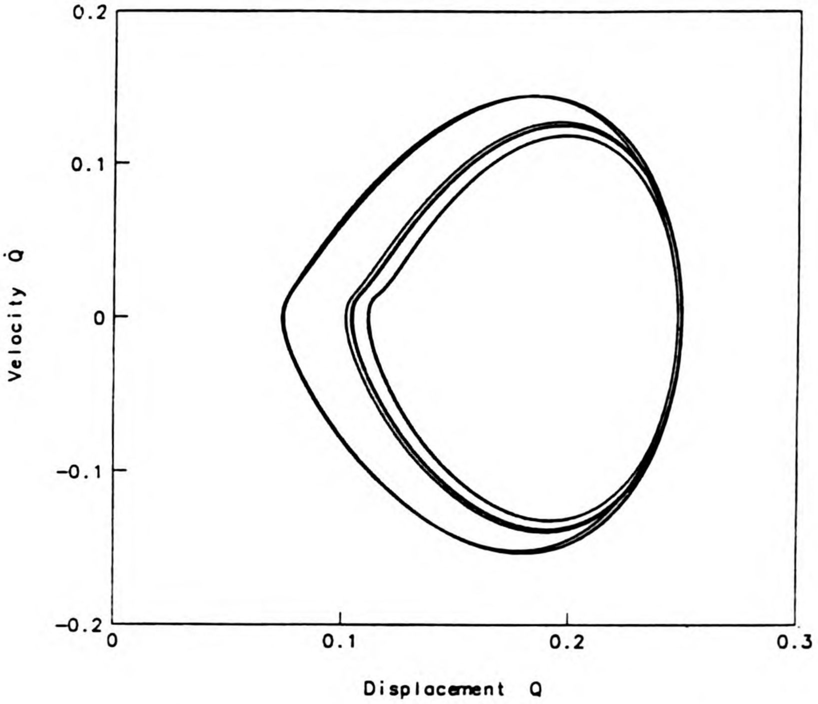

Figure 4.25e Phase Portrait of Period 32 Motion; $\varepsilon^2\Omega_A = 0.0834$.

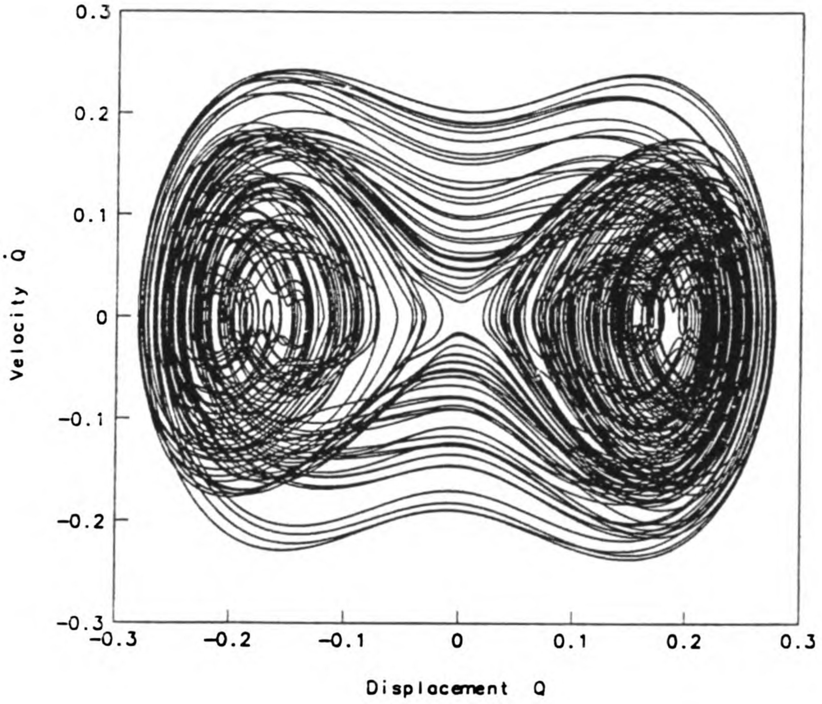

Figure 4.26 Phase Portrait of Chaotic Motion; $\varepsilon^2\Omega_A = 0.0835$.

$\varepsilon\,\Omega_A = 0.07$ to $\varepsilon\,\Omega_A = 0.0834$, the beam undergoes a succession of period doubling bifurcations (from period 2 motion to period 32 motion). Figure 4.26 shows a phase portrait of a chaotic motion with $\varepsilon\,\Omega_A = 0.0835$. The corresponding Poincare map of Figures 4.25 and 4.26 are shown in Figure 4.27. Plots of the displacement versus time for period 4 and chaotic motions are shown in Figures 4.28 and 4.29.

Figure 4.30 shows a summary of the preceding numerical results. Clearly, chaos was observed to occur well above the curve obtained by Melnikov's method. However, this is consistent with the analysis since Melnikov's method gives a necessary, but not sufficient, condition for steady-state chaotic motion to occur. It is also interesting to note that for the resonance $\omega = 1.54 \approx \omega_0$ we found almost periodic motions. No such motion were found for the $\omega = 2.79 \approx 2\,\omega_0$.case. Moreover, the sequence of period doubling bifurcations is different in the two cases as is the strange attractor depicted in the Poincare maps of Figure 4.24i and 4.27f.

4.7 Summary of the Chapter

The method of multiple scales was used to obtain a uniform second order expansion for the response of a rotating buckled beam subjected to subharmonic and primary resonances. For sufficiently small $\varepsilon\,\Omega_A$ values, the beam was found to vibrate about one of the buckled positions with a softening-type, nonlinear behavior. As we increased the $\varepsilon\,\Omega_A$ value beyond some critical value, the beam's orbit encompassed both buckled positions. In the vicinity of the critical value of $\varepsilon\,\Omega_A$, a region was found where the beam will displayed bifurcated and chaotic motions.

Melnikov's method was applied to predict the regions where chaotic motions might exist. Numerical simulations were used to find bifurcated and chaotic motions in the region

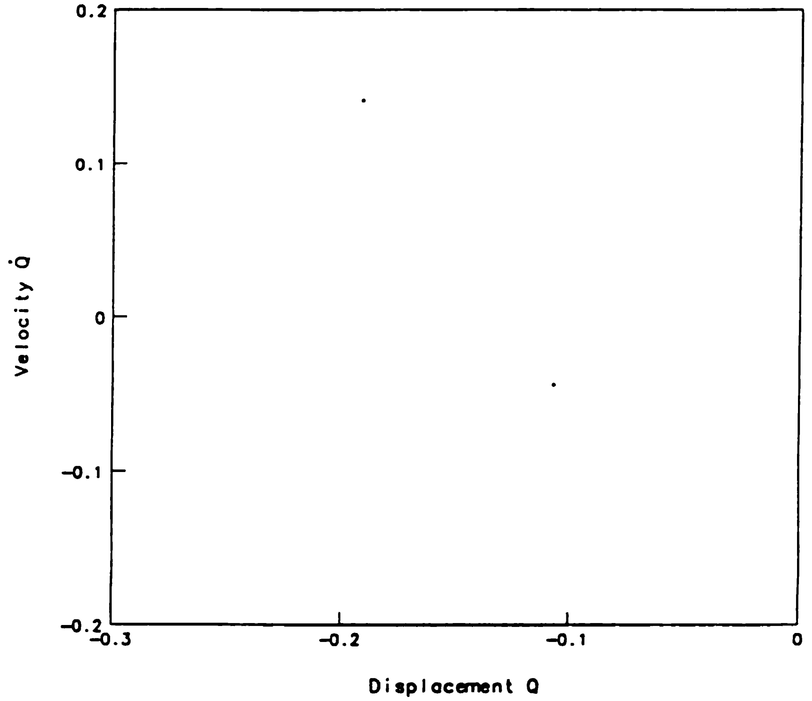

Figure 4.27a Poincare Map of Period 2 Motion; $\varepsilon^2\Omega_A = 0.07$.

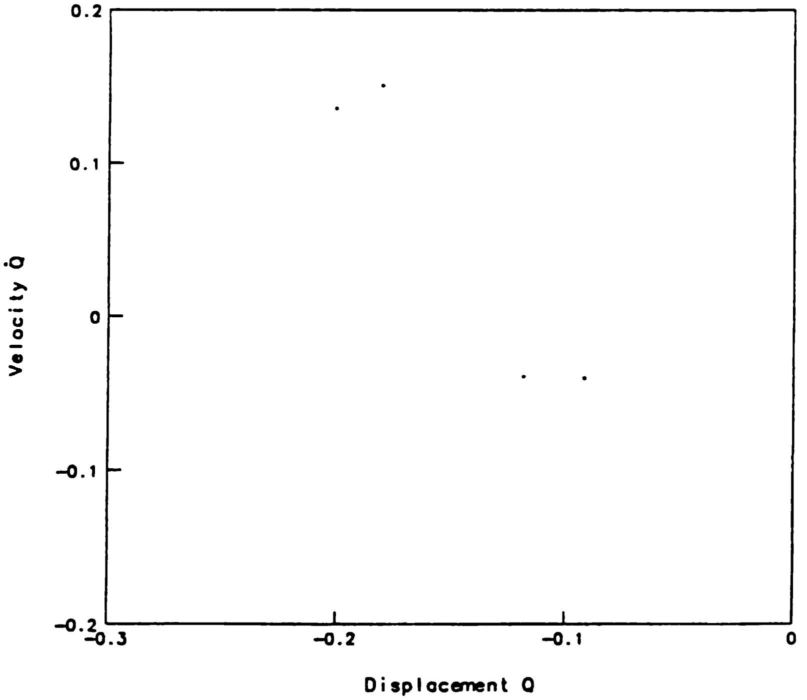

Figure 4.27b Poincare Map of Period 4 Motion; $\varepsilon^2\Omega_A = 0.08$.

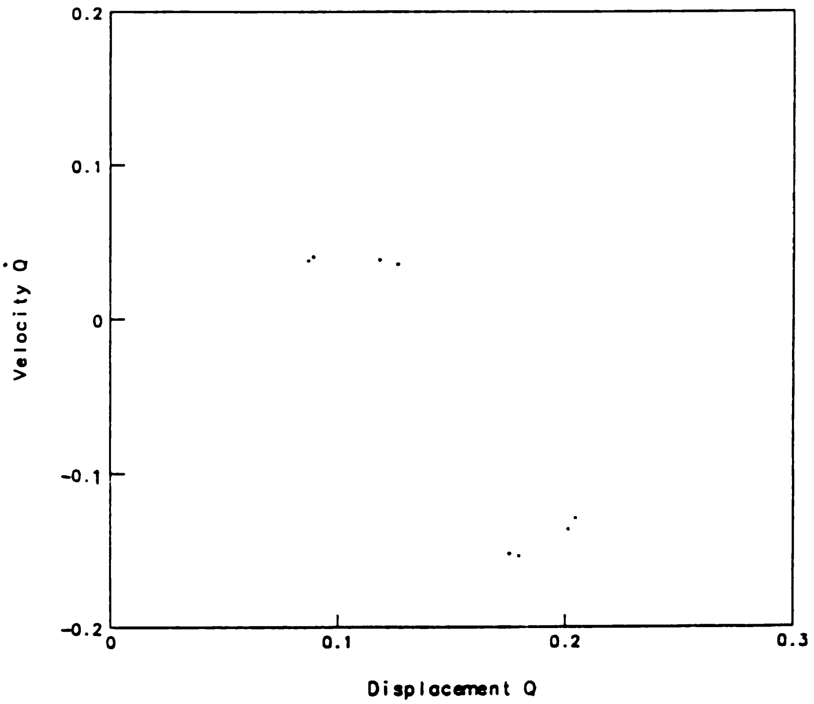

Figure 4.27c Poincare Map of Period 8 Motion; $\varepsilon^2\Omega_A = 0.0832$.

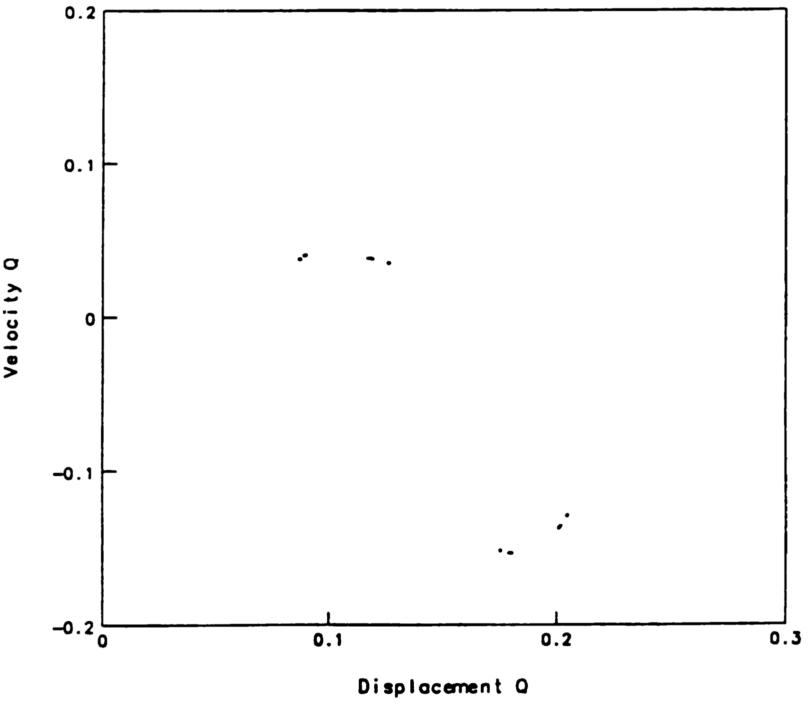

Figure 4.27d Poincare Map of Period 16 Motion; $\varepsilon^2\Omega_A = 0.0833$.

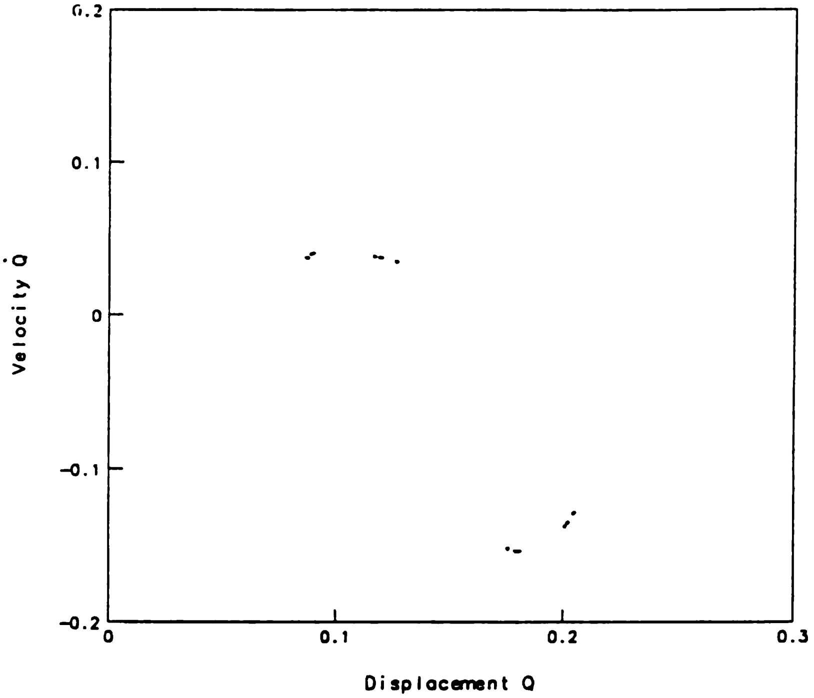

Figure 4.27e Poincare Map of Period 32 Motion; $\varepsilon^2\Omega_A = 0.0834$.

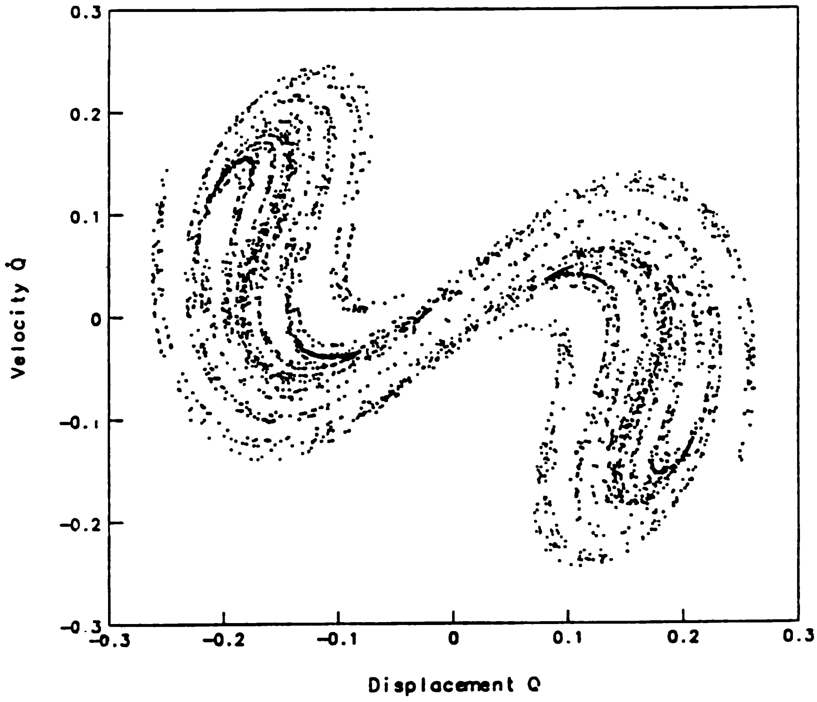

Figure 4.27f Poincare Map of Chaotic Motion; $\varepsilon^2\Omega_A = 0.0835$.

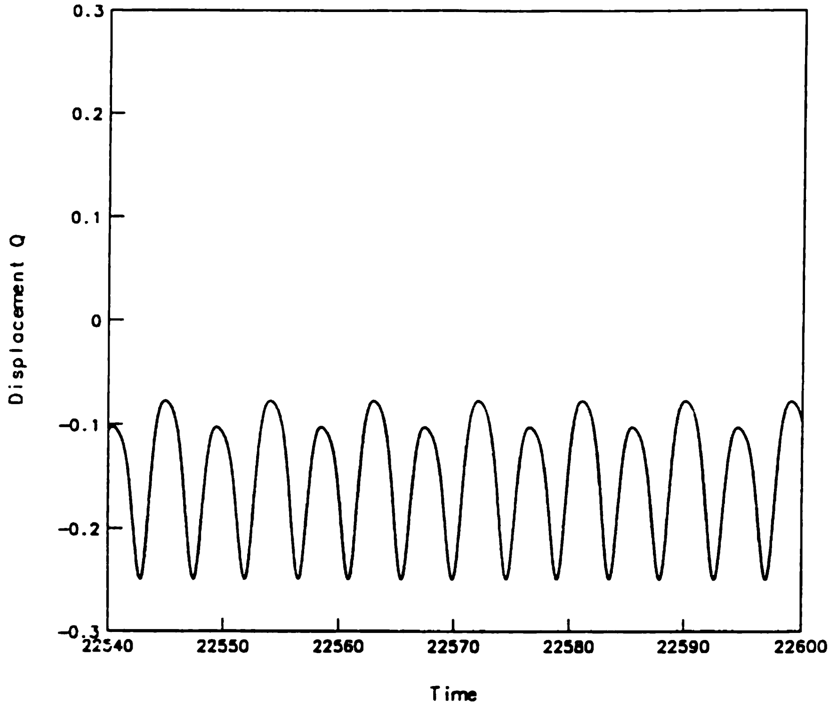

Figure 4.28 Time Trace of Displacement of Period 4 Motion; $\varepsilon^2\Omega_A = 0.08$.

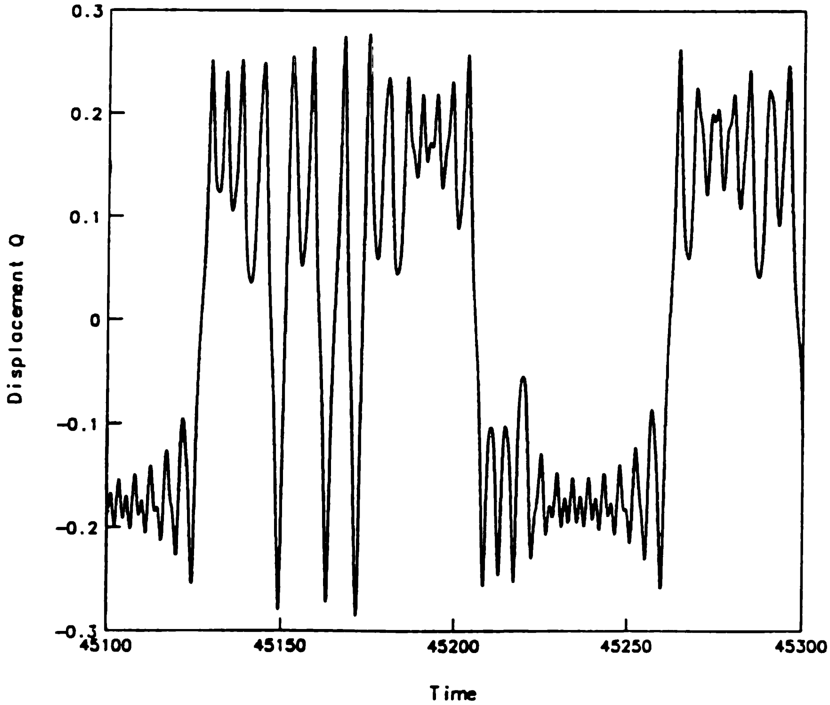

Figure 4.29 Time Trace of Displacement of Chaotic Motion; $\varepsilon^2\Omega_A = 0.0835$.

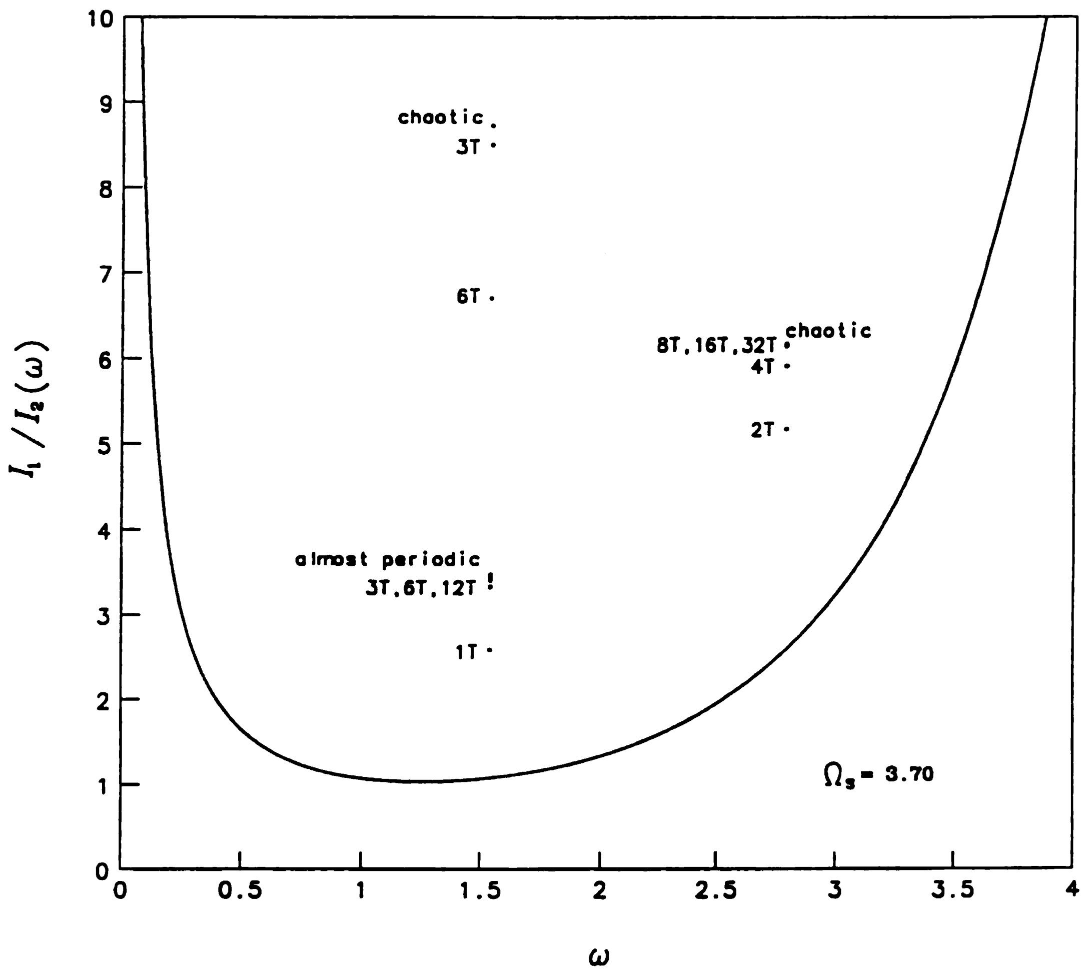

Figure 4.30 Comparison between Melnikov's Method and Numerical Simulations.

of primary and subharmonic resonances. The values of $\varepsilon\,\Omega_A$ for which chaotic motions occurred are much above the homoclinic bifurcation curve, indicating that Melnikov's method gives a lower bound in the parameter space.

CHAPTER 5

ANALYSIS OF A ROTATING, SIMPLY SUPPORTED SHAFT WITH $\Omega_s < \Omega_0$

5.1 Introduction

In this chapter we investigate the nonlinear, non-planar motion of a uniform, initially straight, elastic shaft rotating about its longitudinal axis at a nonconstant spin rate. The shaft is considered to be simply supported and has immovable ends. For a shaft with these end conditions, nonlinearities arise due to mid-line stretching. Two classifications of cross section will be investigated: (a) exactly circular and (b) close to circular. We restrict our investigation to mean spin rates, Ω_s, less than Ω_0 (i.e., pre-critical). The post-critical behaviors of the shaft will be studied in Chapter 6.

The derivation of approximate solutions to the system's nonlinear governing equations of motion are presented in this chapter for the four cases of parametric resonances, viz. $\omega \approx 2\,\omega_1$, $\omega \approx 2\,\omega_2$, $\omega \approx \omega_1 + \omega_2$ and $\omega \approx \omega_2 - \omega_1$. Each case is analyzed firstly in the absence of internal tuning (i.e., ω_2 is assumed to be well removed from $3\omega_1$) and secondly in the presence of internal tuning (i.e., ω_2 is assumed to be closed to $3\omega_1$). We also presents a stability analysis of the steady-state solutions which were obtained by the method of multiple scales for each case. The accuracy of the approximate solutions will be checked by direct numerical integration of the original equations of the motion. The choice of parameters for numerical simulation is based upon an experimental model. The case of $\omega \approx 2\,\omega_1$ with $\omega_2 \approx 3\,\omega_1$ will be given a more detailed discussion.

5.2 Approximate Solutions

Approximate solutions to equations (2.40) and (2.41) are obtained by the method of multiple scales. These approximate solutions will remain uniformly valid for all τ when ε is small. Before beginning the analysis we note that for rotational rates below Ω_0, the internal and external damping terms have the same influence on the shaft and so, with no loss of generality, we will set $\mu_i = 0$. (Note, however, when the rotational speed of the shaft is above Ω_0, internal damping has a destabilizing effects (Tondl [1965]).

Consider equations (2.40) and (2.41) derived in Chapter 2, we seek a first-order solution for small but finite amplitudes in the form

$$U(\tau;\varepsilon) = u_0(T_0,T_1) + \varepsilon\, u_1(T_0,T_1) + \varepsilon^2\, u_2(T_0,T_1) + \cdots\cdots\cdots \tag{5.1}$$

$$V(\tau;\varepsilon) = v_0(T_0,T_1) + \varepsilon\, v_1(T_0,T_1) + \varepsilon^2\, v_2(T_0,T_1) + \cdots\cdots\cdots \tag{5.2}$$

where $T_n = \varepsilon^n\, \tau$.

Note that the small parameter, ε, has a physical interpretation (see Section 2.3 in Chapter 2) and is the square of the slenderness ratio. Unlike the beam case, it is therefore dependent on the system's parameters.

Substituting equations (5.1), (5.2), (3.6) and (3.7) into equations (2.40) and (2.41) and equating coefficients of like powers of ε, we obtain

ε^0:

$$D_0^2 u_0 + (\Omega_0^2 - \Omega_s^2)\, u_0 - 2\,\Omega_s D_0 v_0 = 0 \tag{5.3}$$

$$D_0^2 v_0 + ((1+\delta)\Omega_0^2 - \Omega_s^2) v_0 + 2\Omega_s D_0 u_0 = 0 \tag{5.4}$$

ε^1:

$$\begin{aligned} D_0^2 u_1 + (\Omega_0^2 - \Omega_s^2) u_1 - 2\Omega_s D_0 v_1 &= -2 D_0 D_1 u_0 - \Omega_0^2 u_0^3 \\ &\quad - \Omega_0^2 u_0 v_0^2 + 2\Omega_s D_1 v_0 + 2\Omega_s \mu_e v_0 - 2\mu_e D_0 u_0 \\ &\quad + 2\Omega_A \Omega_s u_0 \sin \omega\tau + \Omega_A \omega v_0 \cos \omega\tau + 2\Omega_A \sin \omega\tau \ D_0 v_0 \end{aligned} \tag{5.5}$$

$$\begin{aligned} D_0^2 v_1 + ((1+\delta)\Omega_0^2 - \Omega_s^2) v_1 + 2\Omega_s D_0 u_1 &= -2 D_0 D_1 v_0 - \Omega_0^2 v_0^3 \\ &\quad - \Omega_0^2 v_0 u_0^2 - 2\Omega_s D_1 u_0 - 2\Omega_s \mu_e u_0 - 2\mu_e D_0 v_0 \\ &\quad + 2\Omega_A \Omega_s v_0 \sin \omega\tau - \Omega_A \omega u_0 \cos \omega\tau - 2\Omega_A \sin \omega\tau \ D_0 u_0 \end{aligned} \tag{5.6}$$

The solution of equations (5.3) and (5.4) can be expressed in the form

$$u_0 = A_1(T_1)\exp(i\omega_1 T_0) + A_2(T_1)\exp(i\omega_2 T_0) + cc \tag{5.7}$$

$$v_0 = \Lambda_1 A_1(T_1)\exp(i\omega_1 T_0) + \Lambda_2 A_2(T_1)\exp(i\omega_2 T_0) + cc \tag{5.8}$$

where

$$\omega_1 = \left[\frac{2\Omega_0^2 + 2\Omega_s^2 + \Omega_0^2\delta - \Omega_0\sqrt{16\Omega_s^2 + 8\Omega_s^2\delta + \Omega_0\delta^2}}{2}\right]^{\frac{1}{2}} \tag{5.9}$$

$$\omega_2 = \left[\frac{2\Omega_0^2 + 2\Omega_s^2 + \Omega_0^2\delta + \Omega_0\sqrt{16\Omega_s^2 + 8\Omega_s^2\delta + \Omega_0^2\delta^2}}{2}\right]^{\frac{1}{2}} \tag{5.10}$$

$$\Lambda_1 = k_1 \, i = -\frac{2\omega_1\Omega_s}{((1+\delta)\Omega_0^2 - \Omega_s^2) - \omega_1^2} i \tag{5.11}$$

$$\Lambda_2 = k_2\, i = -\frac{2\,\omega_2\,\Omega_s}{((1+\delta)\,\Omega_0^2 - \Omega_s^2) - \omega_2^2}\, i \tag{5.12}$$

$i = \sqrt{-1}$

cc denotes the complex conjugate of the preceding terms

A_1 and A_2 are arbitrary complex functions of T_1 which will be determined at the next level of approximation.

In this section we focus on the shaft's behavior close to a main parametric response (i.e., $\omega \approx 2\,\omega_1$) in the presence of the internal resonance, $\omega_2 \approx 3\,\omega_1$. To this end we introduce two detuning parameters,

$$\omega = 2\,\omega_1 + \varepsilon\sigma_1 \tag{5.13}$$

and

$$\omega_2 = 3\,\omega_1 + \varepsilon\sigma_2 \tag{5.14}$$

where σ_1 is known as the external detuning parameter and σ_2 as the internal detuning parameter. We note that ω is an independent variable and that we can control σ_2 by varying Ω_s (see equations (5.9) and (5.10)).

Next, in order to determine the solvability conditions of equations (5.5) and (5.6), we express the form of their particular solution as

$$u_1 = P_{11} \exp(\, i\,\omega_1 T_0\,) + P_{12} \exp(\, i\,\omega_2 T_0\,) \tag{5.15}$$

$$v_1 = P_{21} \exp(i\, \omega_1 T_0) + P_{22} \exp(i\, \omega_2 T_0) \tag{5.16}$$

and substitute equations (5.7), (5.8), (5.13), (5.14), (5.15) and (5.16) into equations (5.5) and (5.6), equate the coefficients of $\exp(i\, \omega_1 T_0)$ and $\exp(i\, \omega_2 T_0)$ to obtain

$$\begin{bmatrix} \Omega_0^2 - \Omega_s^2 - \omega_1^2 & -i\, 2\, \Omega_s \omega_1 \\ i\, 2\, \Omega_s \omega_1 & (1+\delta)\, \Omega_0^2 - \Omega_s^2 - \omega_1^2 \end{bmatrix} \begin{Bmatrix} P_{11} \\ P_{21} \end{Bmatrix} = \begin{Bmatrix} R_{11} \\ R_{21} \end{Bmatrix} \tag{5.17}$$

$$\begin{bmatrix} \Omega_0^2 - \Omega_s^2 - \omega_2^2 & -i\, 2\, \Omega_s \omega_2 \\ i\, 2\, \Omega_s \omega_2 & (1+\delta)\, \Omega_0^2 - \Omega_s^2 - \omega_2^2 \end{bmatrix} \begin{Bmatrix} P_{12} \\ P_{22} \end{Bmatrix} = \begin{Bmatrix} R_{12} \\ R_{22} \end{Bmatrix} \tag{5.18}$$

where R_{ij} are defined in Appendix D.

Since the determinant of the coefficient matrices of (5.17) and (5.18) are zero (this is how ω_1 and ω_2 were originally found), then for there to exist a non-trivial solution of the P_{ij} we must have

$$\begin{vmatrix} R_{11} & -i\, 2\, \Omega_s \omega_1 \\ R_{21} & (1+\delta)\, \Omega_0^2 - \Omega_s^2 - \omega_1^2 \end{vmatrix} = 0 \tag{5.19}$$

$$\begin{vmatrix} R_{12} & -i\, 2\, \Omega_s \omega_2 \\ R_{22} & (1+\delta)\, \Omega_0^2 - \Omega_s^2 - \omega_2^2 \end{vmatrix} = 0 \tag{5.20}$$

At this stage it is convenient to consider two distinct cases, viz., $\delta = 0$ and $\delta \neq 0$ (i.e., symmetrical and unsymmetrical). In the former case the analysis can proceed by considering equations (5.9) to (5.12) from which we find

$$\Lambda_1 = - i$$

$$\Lambda_2 = i$$

$$\omega_1 = \Omega_0 - \Omega_s$$

$$\omega_2 = \Omega_0 + \Omega_s$$

$$\Omega_s = \frac{1}{2}\Omega_0 + \frac{1}{4}\varepsilon\sigma_2$$

Substituting (D1), (D2), (D3) and (D4) in Appendix D into (5.19) and (5.20), we obtain the reduced equations

$$i A_1' + i \mu_e A_1 + 2\Omega_0 A_1^2 \overline{A}_1 + 4\Omega_0 A_1 A_2 \overline{A}_2 = 0 \tag{5.21}$$

$$i A_2' + i \mu_e A_2 + 2\Omega_0 A_2^2 \overline{A}_2 + 4\Omega_0 A_1 A_2 \overline{A}_1 = 0 \tag{5.22}$$

where the prime denotes a partial derivative with respect to T_1. The only steady-state solution of equations (5.21) and (5.22) is $A_1 = A_2 = 0$. Hence for a perfectly circular shaft, it is impossible to excite a main parametric resonance. This is consistent with Kammer and Schlack [1987]. Moreover, the reduced equations are independent of the internal detuning parameter and the above result also hold in the absence of internal resonance. For the other cases of the parametric resonances (i.e., $\omega \approx 2\omega_2$, $\omega \approx \omega_1 + \omega_2$ and $\omega \approx \omega_2 - \omega_1$), it can also be shown that no non-trivial steady-state solutions exist.

We now return to equations (5.19) and (5.20) and consider the cross section of the shaft to be close to circular (i.e., $\delta \neq 0$ and the shaft possesses unequal principal moments of inertia). For clarity we will further subdivide the study by first investigating parametric response in the absence of the internal detuning and then investigating the influence of the internal resonance.

5.3 Assuming ω_2 Well Separated from $3\omega_1$

In this sub-section we assume ω_2 is well removed from $3\omega_1$ (i.e., no internal tuning). The approximate solutions are obtained by the method of multiple scales for four cases, viz. $\omega \approx 2\,\omega_1$, $\omega \approx 2\,\omega_2$, $\omega \approx \omega_1 + \omega_2$ and $\omega \approx \omega_2 - \omega_1$.

5.3.1 The case of $\omega \approx 2\omega_1$

Following the same procedure as was used in Section 5.2., we obtain the reduced equations

$$i\,A_1' + i\,G_{13}\,e^{i\sigma_1 T_1}\,\bar{A}_1 + i\,G_{15}\,\mu_e\,A_1 + G_{16}\,A_1^2\,\bar{A}_1 + G_{17}\,A_1\,A_2\,\bar{A}_2 = 0 \tag{5.23}$$

$$i\,A_2' + i\,G_{23}\,\mu_e\,A_2 + G_{25}\,A_2^2\,\bar{A}_2 + G_{24}\,A_1\,A_2\,\bar{A}_1 = 0 \tag{5.24}$$

where G_{ij} are defined in Appendix E.

To solve equations (5.23) and (5.24), we write A_1 and A_2 in the polar form

$$A_1 = \frac{1}{2}\,a_1\,e^{\,i\beta_1} \tag{5.25}$$

$$A_2 = \frac{1}{2}\,a_2\,e^{\,i\beta_2} \tag{5.26}$$

where a_1, a_2, β_1 and β_2 are real.

Substituting equations (5.25) and (5.26) into equations (5.23) and (5.24) and separating real and imaginary parts yields

$$a_1' = -G_{13}\, a_1 \cos\gamma - G_{15}\, \mu_e\, a_1 \tag{5.27}$$

$$a_1\gamma' = a_1\sigma_1 + 2\, G_{13}\, a_1 \sin\gamma - \tfrac{1}{2}\, G_{16}\, a_1^3 - \tfrac{1}{2}\, G_{17}\, a_1\, a_2^2 \tag{5.28}$$

$$a_2' = -G_{23}\, \mu_e\, a_2 \tag{5.29}$$

$$a_2\ \beta_2' = \tfrac{1}{4}\, G_{24}\, a_1^2\, a_2 + \frac{1}{4}\, G_{25}\, a_2^3 \tag{5.30}$$

where $\gamma = \sigma_1 T_1 - 2\,\beta_1$. (5.31)

Of particular interest are the steady-state solutions which correspond to $a_1' = a_2' = \gamma' = 0$. This gives rise to two solution sets: $a_1 = 0$ and $a_2 = 0$, $a_1 \neq 0$ and $a_2 = 0$. In the second set we can evaluate a_1 by noting that

$$\cos\gamma = -\frac{\mu_e}{G_{13}} \tag{5.32}$$

$$\sin\gamma = \frac{1}{4\, G_{13}}\left(G_{16}\, a_1^2 - 2\,\sigma_1\right) \tag{5.33}$$

Squaring and adding equations (5.32) and (5.33), we obtain

$$a_1^2 = \frac{2\left[\sigma_1 \pm 2\left(G_{13}^2 - \mu_e^2\right)^{\frac{1}{2}}\right]}{G_{16}} \tag{5.34}$$

Reconstructing the first order approximate solutions of equations (2.40) and (2.41), using equations (5.7), (5.8), (5.25), (5.26) and (5.31), we have

$$u_0 = a_1 \cos\left(\frac{\omega\tau - \gamma}{2}\right) \tag{5.35}$$

$$v_0 = -k_1 a_1 \sin\left(\frac{\omega\tau - \gamma}{2}\right) \tag{5.36}$$

The parameter values used for numerical results in this and subsequent sections, unless otherwise stated, are:

$$\Omega_A = 5760,\ \mu_e = 250,\ \delta = 1.0,\ \Omega_0 = \pi^2 \text{ and } \varepsilon = (\tfrac{1}{240})^2.$$

Figure 5.1 shows a typical frequency response curve for a mean spin rate $\Omega_s = 7.0$. This shows the variation of the steady-state amplitude a_1 as a function of the frequency of the oscillating component of the spin. Both stable and unstable solutions are shown. Dashed lines denote unstable solutions and solid lines indicate stable solutions. The stability of the steady-state solutions can be ascertained by adding small perturbation to the steady-state solutions and checking if this perturbation grows or decays. For the trivial solution this results in an unstable solution for $-\sigma_u < \sigma < \sigma_u$ where

$$\sigma_u = 2\left[\, G_{13}^2 - \mu_e^2 \,\right]^{\frac{1}{2}} \tag{5.37}$$

It can be proved that the upper branch of the non-trivial solution is always stable, whereas the lower branch is always unstable. The general form of this curve is the same as would be obtained by an analysis of Duffing's equation with a parametric forcing term.

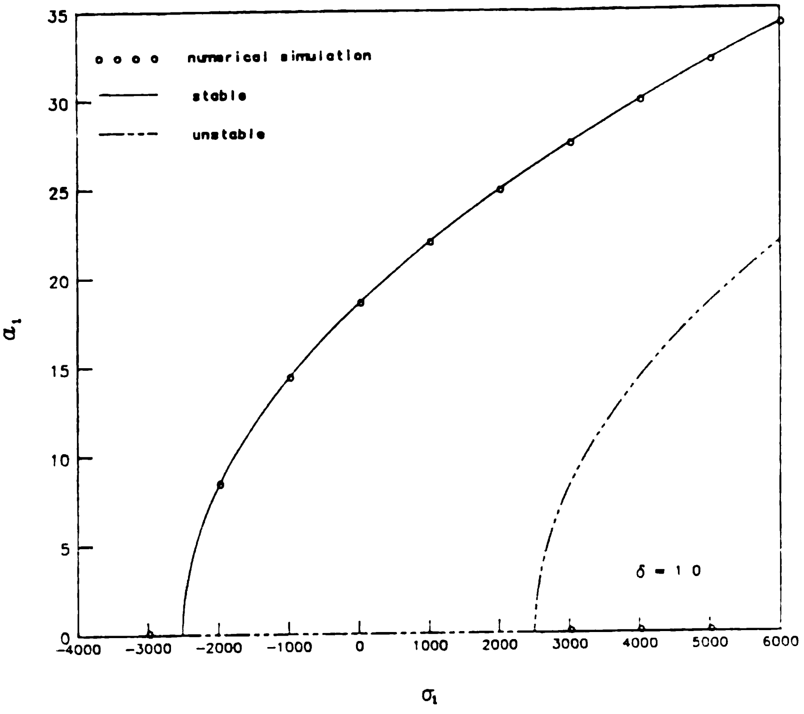

Figure 5.1 Variation of the Steady-State Amplitude, a_1, with σ_1; Ω_s =7.0, δ = 1.0.

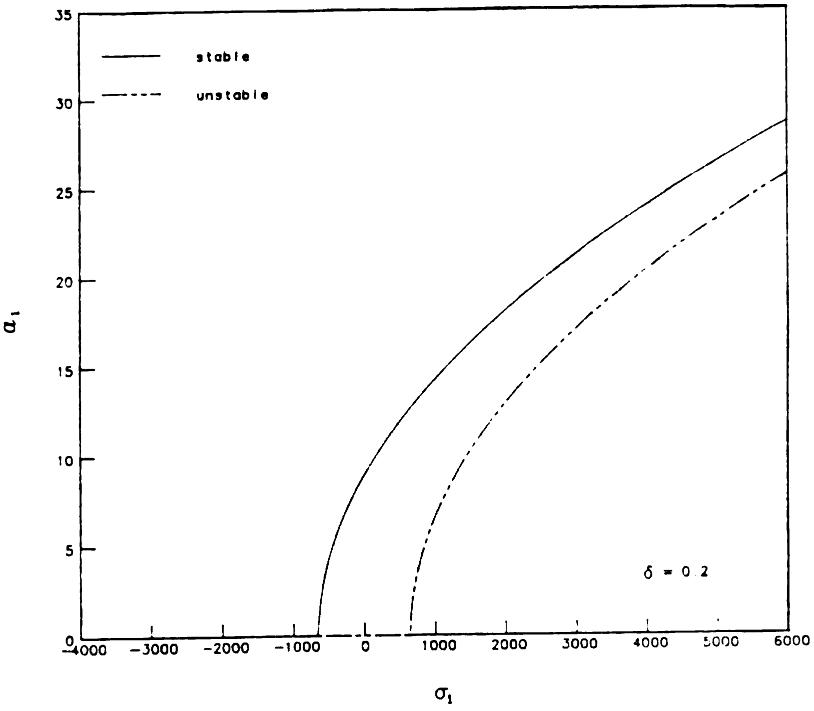

Figure 5.2 Variation of the Steady-State Amplitude, a_1, with σ_1; Ω_s =7.0, δ = 0.2.

Figure 5.2 shows another frequency response curve with δ equal to 0.2. Comparing Figure 5.1 with Figure 5.2, we observe that the width of the instability region of the trivial solution and the amplitude a_1 both increase as the δ value increases.

The results obtained using the method of multiple scales can be checked by numerically integrating the original equations (2.40) and (2.41). The results of such an integration are also shown in Figure 5.1 and the comparison is very good in all the cases tested. The response of the rotating shaft can be shown in various projections of the five dimensional $(U, \dot{U}, V, \dot{V}, \tau)$ extended space. Hence, we plot the motion of the shaft in a (U,V) projection to get a better visualization, as shown in Figure 5.3. The result is a relatively simple elliptic orbit. Later, in Section 5.4, we will see how the structure of this orbit becomes much more complex when the condition of internal resonances is added.

5.3.2 The case of $\omega \approx 2\,\omega_2$

In this sub-section the frequency ω is taken to be closed to $2\omega_2$ and hence the external detuning parameter, σ_2, is redefined as

$$\omega = 2\,\omega_2 + \varepsilon\,\sigma_1 \tag{5.38}$$

Following the procedure used in Section 5.2, the solvability conditions of equations (5.5) and (5.6) are now

$$i\,A_1' + i\,G_{15}\,\mu_e\,A_1 + G_{16}\,A_1^2\,\overline{A}_1 + G_{17}\,A_1\,A_2\,\overline{A}_2 = 0 \tag{5.39}$$

$$i\,A_2' + i\,G_{23}\,\mu_e\,A_2 + G_{25}\,A_1^2\,\overline{A}_2 + i\,G_{22}\,e^{i\sigma_1 T_1}\,\overline{A}_2 + G_{24}\,A_1\,\overline{A}_1\,A_2 = 0 \tag{5.40}$$

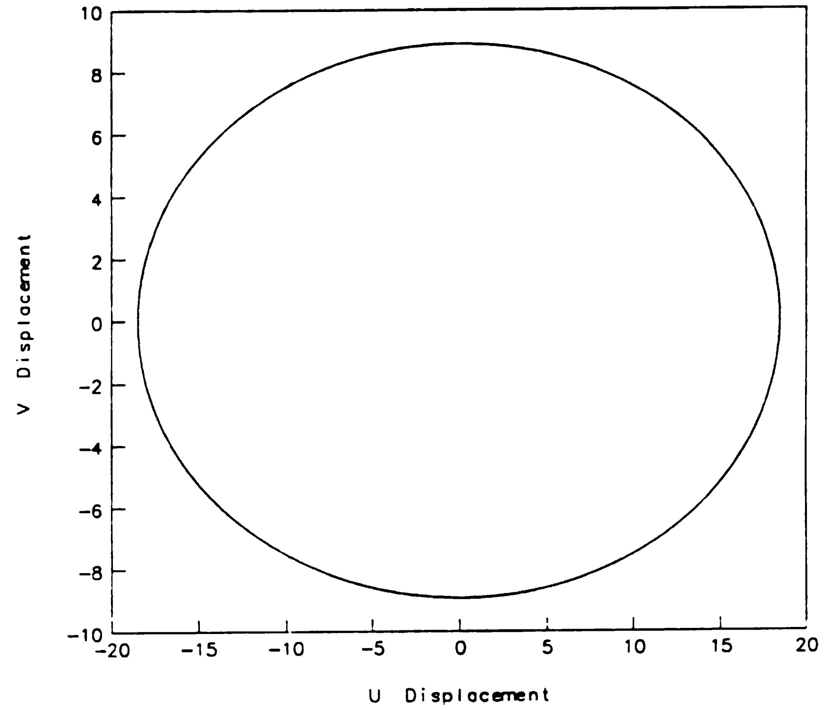

Figure 5.3 Orbit in (U,V) Projection; Ω_s =7.0, δ = 1.0.

To solve equations (5.39) and (5.40) for A_1 and A_2, it is again convenient to introduce the polar forms given in equations (5.25) and (5.26). Substituting equations (5.25) and (5.26) into equations (5.39) and (5.40) and separating the result into real and imaginary parts, it follows that

$$a_1' = -G_{15}\,\mu_e\,a_1 \tag{5.41}$$

$$a_1\,\beta_1' = G_{16}\,a_1^3 + \frac{1}{4}G_{17}a_1\,a_2^2 \tag{5.42}$$

$$a_2' = -G_{23}\,\mu_e\,a_2 - G_{22}\,a_2\cos\gamma \tag{5.43}$$

$$a_2\gamma_1' = a_1\sigma_1 + 2\,G_{22}\,a_2\sin\gamma - \frac{1}{2}G_{24}a_2\,a_1^2 - \frac{1}{2}G_{25}\,a_2^3 \tag{5.44}$$

where $\gamma = \sigma_1\,T_1 - 2\;\beta_1$. (5.45)

Once more, it is possible to simplify these equations should only the steady-state responses be sought. For such a case, equations (5.41) to (5.44) reduced to

$$G_{15}\,\mu_e\,a_1 = 0 \tag{5.46}$$

$$a_1\beta_1' = G_{16}\,a_1^3 + \frac{1}{4}G_{17}a_1\,a_2^2 \tag{5.47}$$

$$G_{23}\,\mu_e\,a_2 + G_{22}\,a_2\cos\gamma = 0 \tag{5.48}$$

$$a_1\sigma_1 + 2\,G_{22}\,a_2\sin\gamma - \frac{1}{2}G_{24}a_2\,a_1^2 - \frac{1}{2}G_{25}\,a_2^3 = 0 \tag{5.49}$$

For non-zero damping there are two possible solution sets to these equations: either $a_1 = 0$ and $a_2 = 0$ or $a_1 = 0$ and $a_2 \neq 0$. In the second set we can evaluate a_2 by noting that

$$\cos\gamma = -\frac{G_{15}}{G_{22}}\,\mu_e \tag{5.50}$$

$$\sin\gamma = \frac{1}{4G_{22}}[G_{25}a_2^2 - 2\sigma_1] \tag{5.51}$$

Squaring and adding equations (5.50) and (5.51), we obtain

$$a_2^2 = \frac{2\left[\sigma_1 \pm 2\left(G_{22}^2 - \mu_e^2\right)^{\frac{1}{2}}\right]}{G_{25}} \tag{5.52}$$

Then the first approximations to the solutions of the original equations of motion have the form

$$u_0 = a_2 \cos\left(\frac{\omega\tau - \gamma}{2}\right)$$

$$v_0 = -k_2 a_2 \sin\left(\frac{\omega\tau - \gamma}{2}\right)$$

A typical frequency response curve is shown in Figure 5.4 with $\Omega_s = 7.0$. Once again, numerical simulations show very good agreement with the approximate solutions.

5.3.3 The case of $\omega \approx \omega_2 + \omega_1$

In this sub-section we investigate the combination resonance and hence the external detuning parameter will be defined by

$$\omega = \omega_1 + \omega_2 + \varepsilon\sigma_1 \tag{5.53}$$

The solvability conditions are

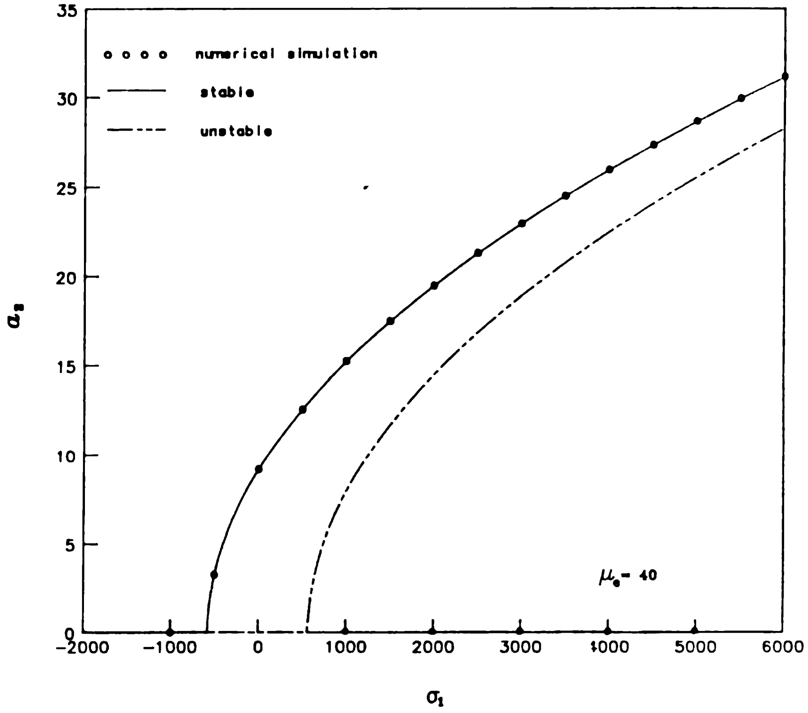

Figure 5.4 Variation of the Steady-State Amplitudes, a_2, with σ_1; $\Omega_s = 7.0$, $\delta = 1.0$.

$$i A_1' + i G_{15} \mu_e A_1 + G_{16} A_1^2 \overline{A}_1 + i G_{13} e^{i \sigma_1 T_1} \overline{A}_2 + G_{17} A_1 A_2 \overline{A}_2 = 0 \tag{5.54}$$

$$i A_2' + i G_{23} \mu_e A_2 + G_{25} A_2^2 \overline{A}_2 + i G_{22} e^{i \sigma_1 T_1} \overline{A}_1 + G_{24} A_1 \overline{A}_1 A_2 = 0 \tag{5.55}$$

Substituting the usual polar forms (5.25) and (5.26) of A_1 and A_2 into equations (5.54) and (5.55) and following the normal procedure, yields

$$a_1' = - G_{15} \mu_e a_1 - G_{13} a_2 \cos\gamma_1 \tag{5.56}$$

$$a_1 \beta_1' = - G_{13} a_2 \sin\gamma_1 + \frac{1}{4} G_{16} a_1^3 + \frac{1}{4} G_{17} a_1 a_2^2 \tag{5.57}$$

$$a_2' = - G_{23} \mu_e a_2 - G_{22} a_1 \cos\gamma_1 \tag{5.58}$$

$$a_2 \beta_2' = - G_{22} a_1 \sin\gamma_1 + \frac{1}{4} G_{24} a_2 a_1^2 + \frac{1}{4} G_{25} a_2^3 \tag{5.59}$$

where $\gamma_1 = \sigma_1 T_1 - \beta_1 - \beta_2$. (5.60)

For the steady-state motions (i.e., $a_1' = a_2' = \gamma_1' = 0$) we find

$$G_{15} \mu_e a_1 + G_{13} a_2 \cos\gamma_1 = 0 \tag{5.61}$$

$$G_{23} \mu_e a_2 + G_{22} a_1 \cos\gamma_1 = 0 \tag{5.62}$$

$$\begin{aligned} \sigma_1 + G_{22} \frac{a_1}{a_2} \sin\gamma_1 - \frac{1}{4} G_{24} a_1^2 - \frac{1}{4} G_{25} a_2^2 + G_{13} \frac{a_2}{a_1} \sin\gamma_1 \\ - \frac{1}{4} G_{16} a_1^2 - \frac{1}{4} G_{17} a_2^2 = 0 \end{aligned} \tag{5.63}$$

By eliminating $\cos\gamma_1$ in equations (5.61) and (5.62), one obtains the following linear relationship between a_1 and a_2

$$a_2 = K a_1 \tag{5.64}$$

where $K = \left[\frac{G_{22}}{G_{13}}\right]^{\frac{1}{2}}$.

Substituting equation (5.64) into equations (5.61) and (5.63) yields

$$a_1^2 = \frac{4\left\{\sigma_1 \pm C_2\left[1-\left(\frac{K\,\mu_e}{G_{22}}\right)^{\frac{1}{2}}\right]\right\}}{C_1} \tag{5.65}$$

where

$$C_1 = G_{24} + G_{16} + K^2\,(G_{25} + G_{17})$$

$$C_2 = G_{22}/K + G_{13}\,K.$$

Hence, the steady-state solution has the form

$$u_0 = a_1 \cos[(\omega_1 + \varepsilon\,\overline{\beta}_1)\tau - \theta_1] + a_2 \cos[(\omega_2 + \varepsilon\,\overline{\beta}_2)\tau - \theta_2] \tag{5.66}$$

$$v_0 = -k_1\,a_1 \sin[(\omega_1 + \varepsilon\,\overline{\beta}_1)\tau - \theta_1] - k_2\,a_2 \sin[(\omega_2 + \varepsilon\,\overline{\beta}_2)\tau - \theta_2] \tag{5.67}$$

where

$$\overline{\beta}_1 = -G_{13}\frac{a_2}{a_1}\sin\gamma_1 + \frac{1}{4}G_{16}\,a_1^2 + \frac{1}{4}G_{17}\,a_2^2$$

$$\overline{\beta}_2 = -G_{22}\frac{a_1}{a_2}\sin\gamma_1 + \frac{1}{4}G_{24}a_1^2 + \frac{1}{4}G_{25}a_2^2$$

$\gamma_1 = \theta_1 + \theta_2$, θ_1 and θ_2 are constants depending on the initial conditions.

A typical frequency response plot (equation (5.65)) is shown in Figure 5.5. This curve is similar to the two cases already presented in Sections 5.3.1 and 5.3.2.

When ω_2 and ω_1 are incommensurate, the resulting response is non-periodic. A clear way to demonstrate this is to plot the trajectory of the steady-state response obtained by numerically integrating equations (2.40) and (2.41) in a (U,V) projection, this is shown in Figure 5.6a and the corresponding result obtained by the method of multiple scales (equations (5.66) and (5.67)) is shown in Figure 5.6b. A comparison between these two figures shows remarkable agreement.

5.3.4 The case of $\omega \approx \omega_2 - \omega_1$

In this sub-section we consider ω near to be the difference between ω_1 and ω_2 and we introduce the external detuning parameter as

$$\omega = \omega_2 - \omega_1 + \varepsilon\sigma_1 \tag{5.68}$$

The solvability conditions of this case are

$$i A_1' + i G_{15}\mu_e A_1 + G_{16} A_1^2 \overline{A}_1 + i G_{12} e^{-i\sigma_1 T_1} A_2 + G_{17} A_1 A_2 \overline{A}_2 = 0 \tag{5.69}$$

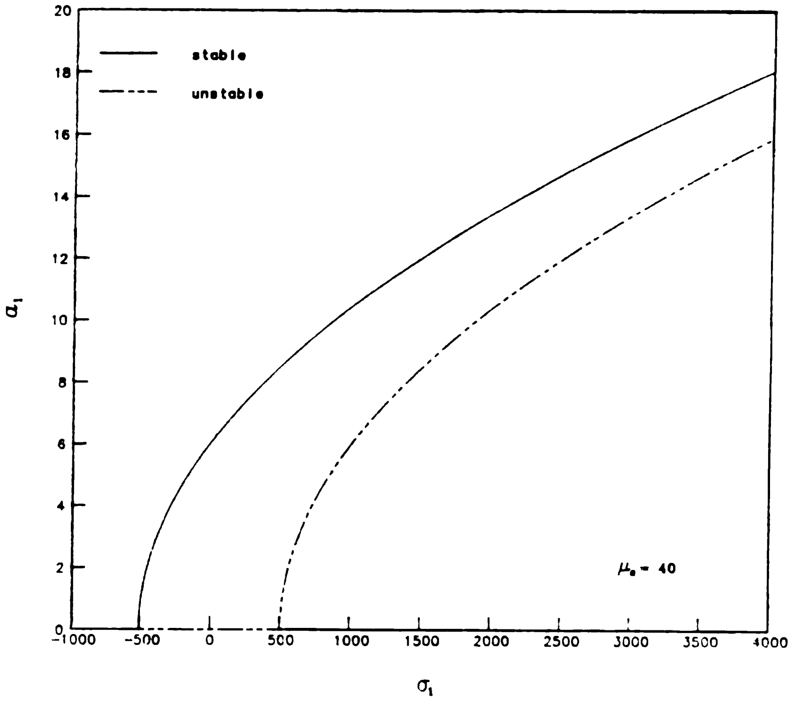

Figure 5.5 Variation of the Steady-State Amplitude, a_1, with σ_1; $\Omega_s = 7.0$, $\delta = 1.0$.

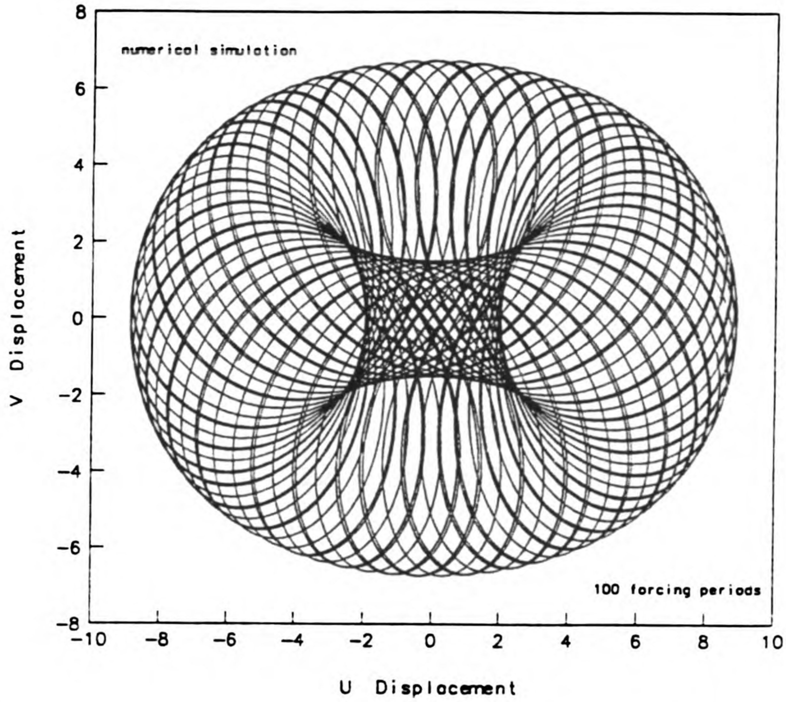

Figure 5.6a Trajectory obtained by Numerical Simulation in (U,V) Projection; $\Omega_s = 7.0$, $\delta = 1.0$.

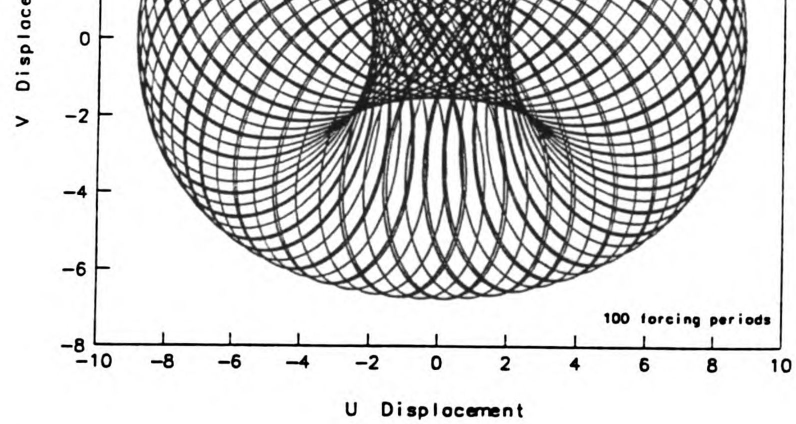

Figure 5.6b Trajectory obtained by MMS in (U,V) Projection; $\Omega_s = 7.0$, $\delta = 1.0$.

$$i A_2' + i G_{23} \mu_e A_2 + G_{25} A_2^2 \overline{A}_2 + i G_{22} e^{i \sigma_1 T_1} A_1 + G_{24} A_1 \overline{A}_1 A_2 = 0 \tag{5.70}$$

To solve equations (5.69) and (5.70) it is convenient to express the A_1 and A_2 terms in their polar form as defined in equations (5.25) and (5.26). Separating the resulting equations into real and imaginary parts, yields

$$a_1' = - G_{15} \mu_e a_1 - G_{12} a_2 \cos\gamma_1 \tag{5.71}$$

$$a_1 \beta_1' = - G_{12} a_2 \sin\gamma - \frac{1}{4} G_{16} a_1^3 - \frac{1}{4} G_{17} a_1 a_2^2 \tag{5.72}$$

$$a_2' = - G_{23} \mu_e a_2 - G_{22} a_1 \cos\gamma_1 \tag{5.73}$$

$$a_2 \beta_2' = - G_{22} a_1 \sin\gamma_1 + \frac{1}{4} G_{24} a_2 a_1^2 + \frac{1}{4} G_{25} a_2^3 \tag{5.74}$$

where $\gamma_1 = \sigma_1 T_1 - \beta_1 - \beta_2$. (5.75)

For the steady-state motions (i.e., $a_1' = a_2' = \gamma_1' = 0$) we find

$$G_{15} \mu_e a_1 + G_{12} a_2 \cos\gamma_1 = 0 \tag{5.76}$$

$$G_{23} \mu_e a_2 + G_{22} a_1 \cos\gamma_1 = 0 \tag{5.77}$$

$$\begin{aligned} &\sigma_1 + G_{22} \frac{a_1}{a_2} \sin\gamma_1 + \frac{1}{4} G_{24} a_1^2 + \frac{1}{4} G_{25} a_2^2 \\ &\quad + G_{12} \frac{a_2}{a_1} \sin\gamma_1 - \frac{1}{4} G_{16} a_1^2 - \frac{1}{4} G_{17} a_2^2 = 0 \end{aligned} \tag{5.78}$$

Following the same procedure as was employed in Sub-section 5.3.3, a linear relationship between a_1 and a_2 is found in the form

$$a_2 = K a_1 \tag{5.79}$$

where $K = \left[\frac{G_{22}}{G_{12}}\right]^{\frac{1}{2}}$.

It can be found that G_{22} always less than zero. Hence the trivial solution is the only steady-state solution for this case of resonance.

5.4 Assuming $\omega_2 \approx 3\omega_1$

The condition of internal tuning is now introduced. The nearness of ω_2 to $3\omega_1$ is quantified by σ_2 and this is controlled primarily by changing Ω_s (see equations (5.9) and (5.10)). For example, if δ equal to 1 and Ω_s equal to 5.46309, ω_2 will be very close to $3\omega_1$. This section comprises three cases, two for the case of principal parametric resonance and one for the case of combination resonance. Since many of the points discussed and techniques utilized are common to all three cases, the first is presented in most detail.

5.4.1 The case of $\omega \approx 2\omega_1$

Following the method of the multiple scales, the reduced equations for this case are found to be

$$\begin{aligned} & i A_1' + i G_{12} e^{i(\sigma_2-\sigma_1)T_1} A_2 + i G_{13} e^{i\sigma_1 T_1} \overline{A}_1 + G_{14} e^{i\sigma_2 T_1} \overline{A}_1^2 A_2 \\ & \quad + i G_{15} \mu_e A_1 + G_{16} A_1^2 \overline{A}_1 + G_{17} A_1 A_2 \overline{A}_2 = 0 \end{aligned} \tag{5.80}$$

$$\begin{aligned} & i A_2' + i G_{22} e^{i(\sigma_2-\sigma_1)T_1} A_1 + G_{26} e^{-i\sigma_2 T_1} A_1^3 + i G_{23} \mu_e A_2 \\ & \quad + G_{25} A_2^2 \overline{A}_2 + G_{24} A_1 A_2 \overline{A}_1 = 0 \end{aligned} \tag{5.81}$$

To solve equations (5.80) and (5.81), it is again convenient to introduce the polar forms given in equations (5.25) and (5.26). Substituting equations (5.25) and (5.26) into equations (5.80) and (5.81) and separating the result into real and imaginary parts yields

$$a_1' = -G_{13}\,a_1\cos\gamma_1 - G_{15}\,\mu_e\,a_1 - G_{12}\,a_2\cos\gamma_2 - \frac{1}{4}G_{14}\,a_1^2\,a_2\,\sin(\gamma_1+\gamma_2) \tag{5.82}$$

$$\begin{aligned} a_1\gamma_1' = {} & a_1\sigma_1 + 2\,G_{13}\,a_1\sin\gamma_1 - \frac{1}{2}G_{16}\,a_1^3 + 2\,G_{12}\,a_2\,\sin\gamma_2 \\ & - \frac{1}{2}G_{14}\,a_1^2\,a_2\cos(\gamma_1+\gamma_2) - \frac{1}{2}G_{17}\,a_1\,a_2^2 \end{aligned} \tag{5.83}$$

$$a_2' = -G_{22}\,a_1\cos\gamma_2 - G_{23}\,\mu_e\,a_2 + \frac{1}{4}G_{26}\,a_1^3\sin(\gamma_1+\gamma_2) \tag{5.84}$$

$$\begin{aligned} a_2\left(\gamma_2' - \frac{1}{2}\gamma_1'\right) = {} & a_2\left(\sigma_2 - \frac{3}{2}\sigma_1\right) + G_{22}\,a_1\sin\gamma_2 + \frac{1}{4}G_{24}\,a_1^2\,a_2 \\ & + \frac{1}{4}G_{25}\,a_2^3 + \frac{1}{4}G_{26}\,a_1^3\cos(\gamma_1+\gamma_2) \end{aligned} \tag{5.85}$$

where

$$\gamma_1 = \sigma_1\,T_1 - 2\,\beta_1 \tag{5.86}$$

$$\gamma_2 = (\sigma_1 - \sigma_2)\,T_1 + \beta_2 - \beta_1 \tag{5.87}$$

The steady-state solutions of equations (2.40) and (2.41) correspond to the fixed points of the reduced equations (5.84) to (5.87), which result from $a_1' = a_2' = \gamma_1' = \gamma_2' = 0$. Once again we have two possible solution sets: a trivial set $a_1 = 0$ and $a_2 = 0$ and a non-trivial set $a_1 \neq 0$ and $a_2 \neq 0$. The nonlinear transcendental equations governing the non-trivial set are

$$G_{13}\,a_1\cos\gamma_1 + G_{15}\,\mu_e\,a_1 + G_{12}\,a_2\cos\gamma_2 + \frac{1}{4}G_{14}\,a_1^2\,a_2\,\sin(\gamma_1+\gamma_2) = 0 \tag{5.88}$$

$$a_1\sigma_1 + 2\,G_{13}\,a_1 \sin\gamma_1 - \tfrac{1}{2}G_{16}\,a_1^3 + 2\;G_{12}\,a_2\;\sin\gamma_2$$
$$-\tfrac{1}{2}G_{14}\,a_1^2\,a_2\cos(\gamma_1+\gamma_2) - \tfrac{1}{2}G_{17}\,a_1\,a_2^2 = 0 \tag{5.89}$$

$$G_{22}\,a_1\cos\gamma_2 + G_{23}\,\mu_e\,a_2 - \frac{1}{4}G_{26}\,a_1^3\sin(\gamma_1+\gamma_2) = 0 \tag{5.90}$$

$$a_2(\sigma_2 - \tfrac{3}{2}\sigma_1) + G_{22}\,a_1\sin\gamma_2 + \tfrac{1}{4}G_{24}\,a_1^2\,a_2$$
$$+\frac{1}{4}G_{25}\,a_2^3 + \tfrac{1}{4}G_{26}\,a_1^3\cos(\gamma_1+\gamma_2) = 0 \tag{5.91}$$

Equations (5.88) to (5.91) can be solved numerically to determine the non-trivial steady state solutions a_1, a_2, γ_1 and γ_2. The first order approximate solutions to the equations (2.40) and (2.41) can now be reconstructed using equations (5.25), (5.26), (5.86), (5.87), (5.13),(5.14), (5.7) and (5.8) to yield

$$u_0 = a_1\cos\left(\frac{\omega}{2}\tau - \frac{\gamma_1}{2}\right) + a_2\cos\left(\frac{3\omega}{2}\tau + \gamma_2 - \frac{\gamma_1}{2}\right) \tag{5.92}$$

$$v_0 = -\,k_1\,a_1\sin\left(\frac{\omega}{2}\tau - \frac{\gamma_1}{2}\right) - k_2\,a_2\sin\left(\frac{3\omega}{2}\tau + \gamma_2 - \frac{\gamma_1}{2}\right) \tag{5.93}$$

Figure 5.7 shows the variation of the steady-state modal amplitudes, a_1 and a_2, as functions of the external detuning parameter σ_1 (i.e., frequency response curve). Parameters were chosen to be representative of a physical system and a value of $\Omega_s = 5.46309$ was chosen such that we have perfect internal tuning ($\sigma_2 = 0$). The results of a stability analysis are also shown on this figure. Stable solutions are denoted by a solid line, unstable solutions by a dotted or chained line.

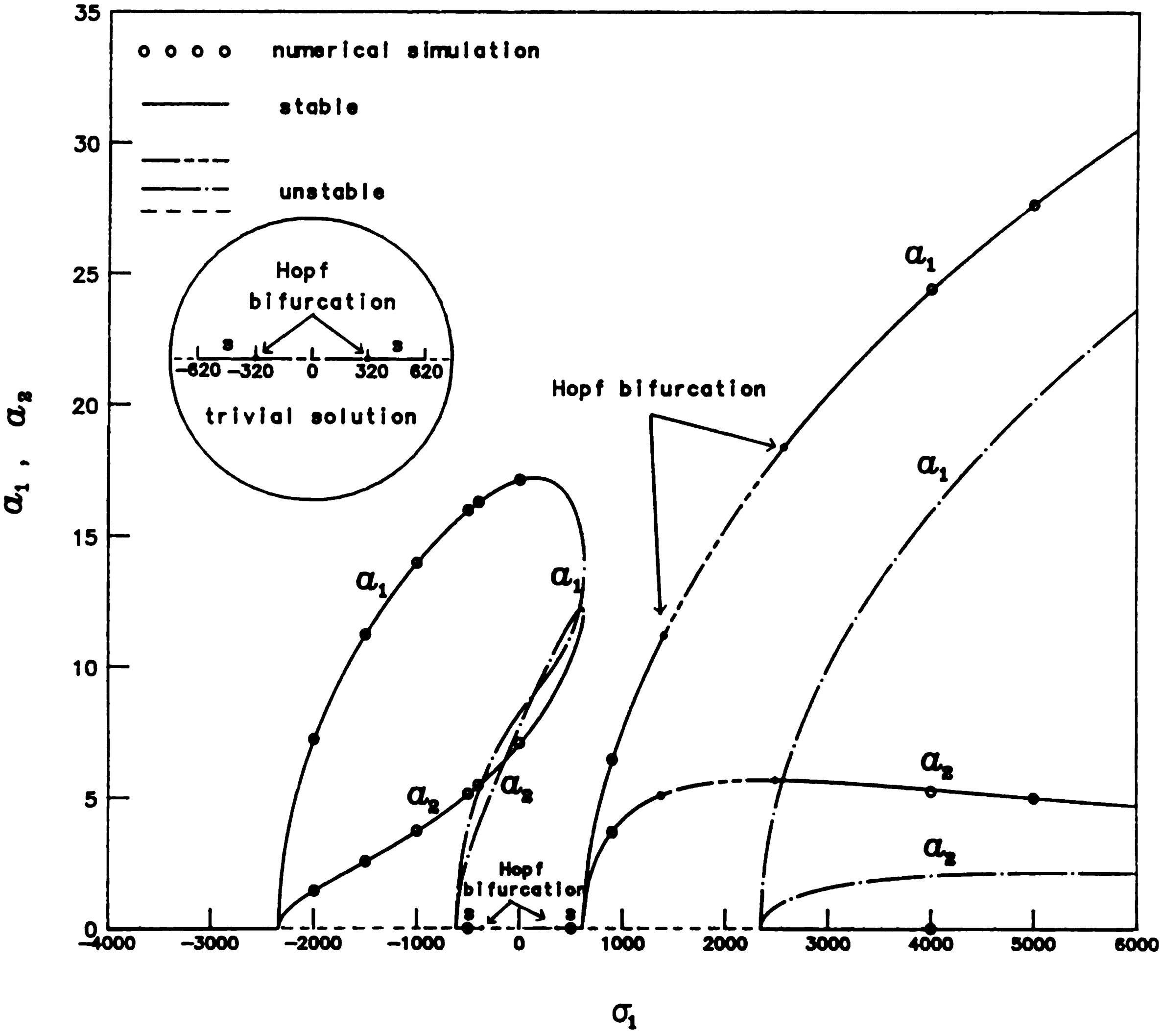

Figure 5.7 Variation of the Steady-State Amplitudes, a_1 and a_2, with σ_1; $\sigma_2 = 0.0$, ($\Omega_s = 5.46309$), $\delta = 1.0$.

In Figure 5.7, it is interesting to note that there is a region in the vicinity of σ_1 equal to 2000 over which neither the trivial nor the non-trivial unstable solutions are stable. By investigating the form of the eigenvalues we find that the non-trivial solutions have undergone a Hopf bifurcation. Hence, the amplitudes and phases are not constant but vary with time (i.e., quasi-periodic motions). To better demonstrate this point, we have numerically integrated the equations of motion (2.40) and (2.41) for a value of σ_1= 1300 and compared this to the results obtained for the value of σ_1= 1500. Based on the predictions of the approximate solution (see Figure 5.7) the former should yield a stable steady state solution where the latter should give rise to a quasi-periodic motion. The results are presented in Figures 5.8a and 5.8b respectively, in the form of an orbit plots of U versus V. Both figures show the solutions after all transients have decayed and are plotted for a length of time corresponding to 100 cycles of the forcing term. Clearly the orbit in Figure 5.8a is periodic whereas the orbit depicted in Figure 5.8b shows a slow amplitude variation. If this orbit where plotted for a longer period of time, more of the (U,V) space would become populated. This is typical of quasi-periodic motions.

With reference to Figure 5.7, it was initially thought that the trivial solutions were unstable for values of $|\sigma_1| < 2360$. However, upon closer inspection we find that the solutions re-stabilize over regions of $320 < |\sigma_1| < 620$. Moreover, at $|\sigma_1| < 320$ the trivial solutions undergo a Hopf bifurcation and so we can predict the motion between $|\sigma_1| < 320$ will be quasi-periodic. Hence, there is a region in the vicinity of σ_1 equal to 0 over which non-trivial steady-state motions and amplitude modulated motions are coexist. The motion adopted depends on the choice of the initial conditions. Figures 5.9a and 5.9b show the orbits corresponding two different initial conditions with σ_1 equal to 0.

Next, we present a collection of results which show how the steady state solutions vary as a function of the system parameters. For clarity, we have not shown the stability of

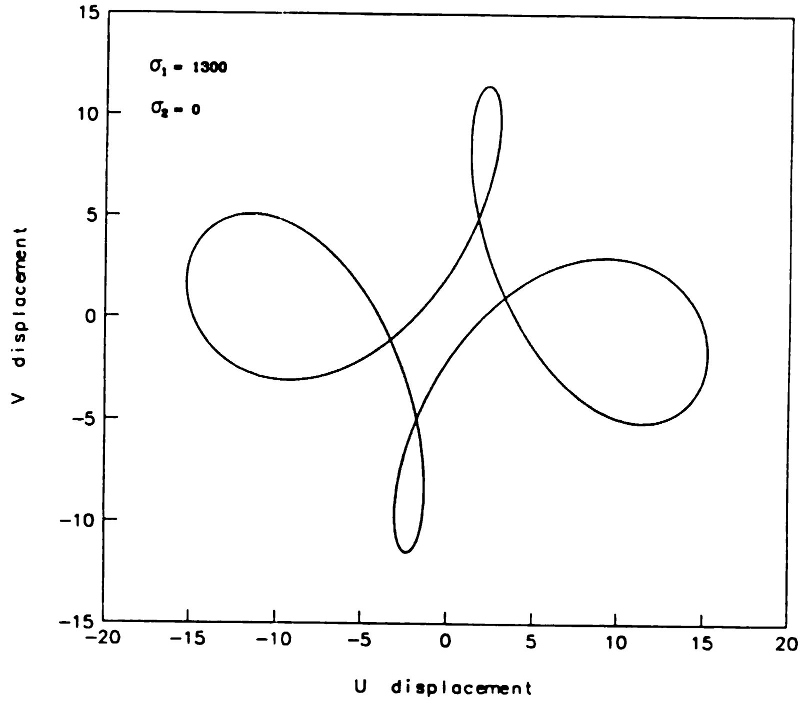

Figure 5.8a Orbit in (U,V) Projection; σ_1 =1300, σ_2 =0.0.

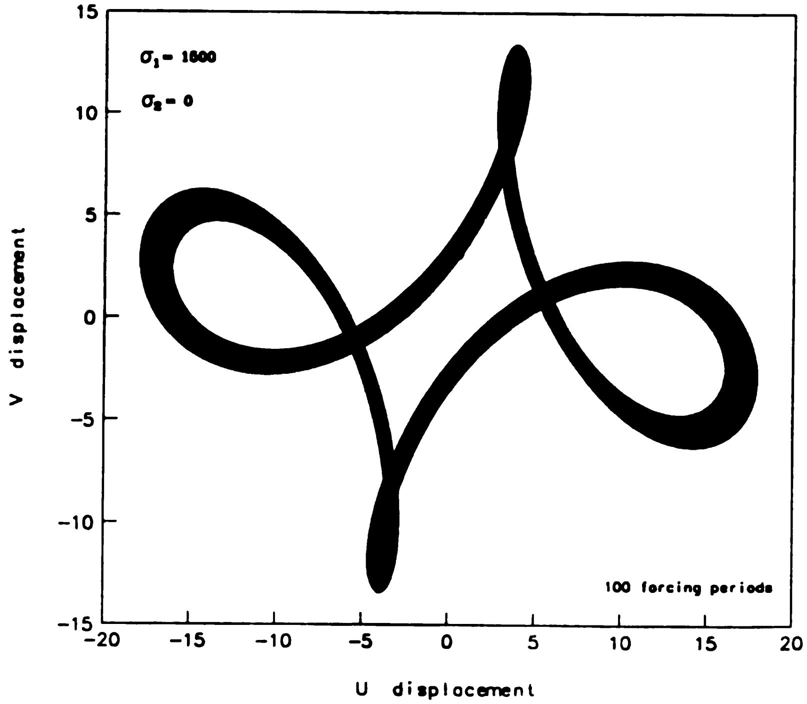

Figure 5.8b Orbit in (U,V) Projection; σ_1 =1500, σ_2 =0.0.

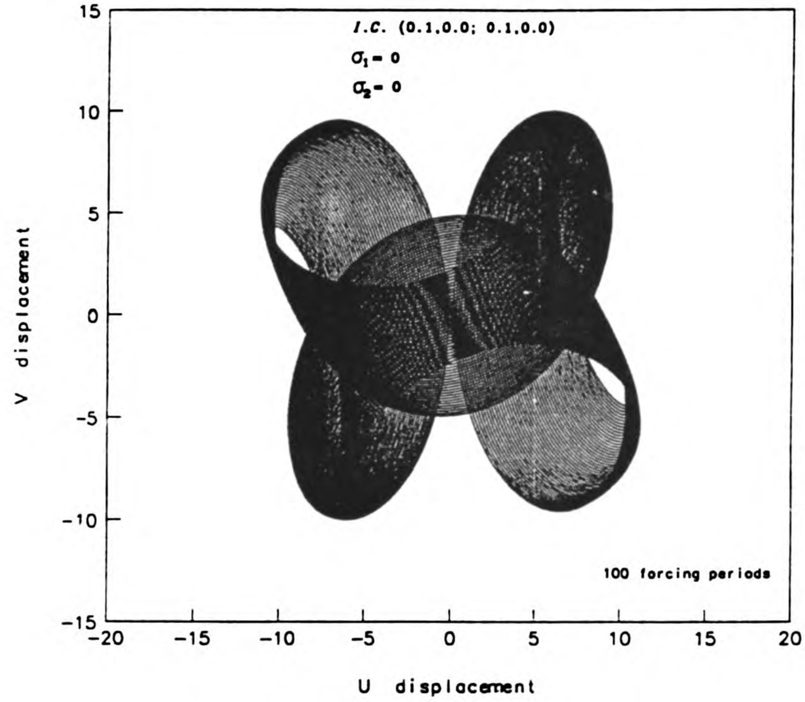

Figure 5.9a Orbit in (U,V) Projection; $\sigma_1 = 0.0$, $\sigma_2 = 0.0$, $U(0) = 0.1, \dot{U}(0) = 0.0; V(0) = 0.1, \dot{V}(0) = 0.0$.

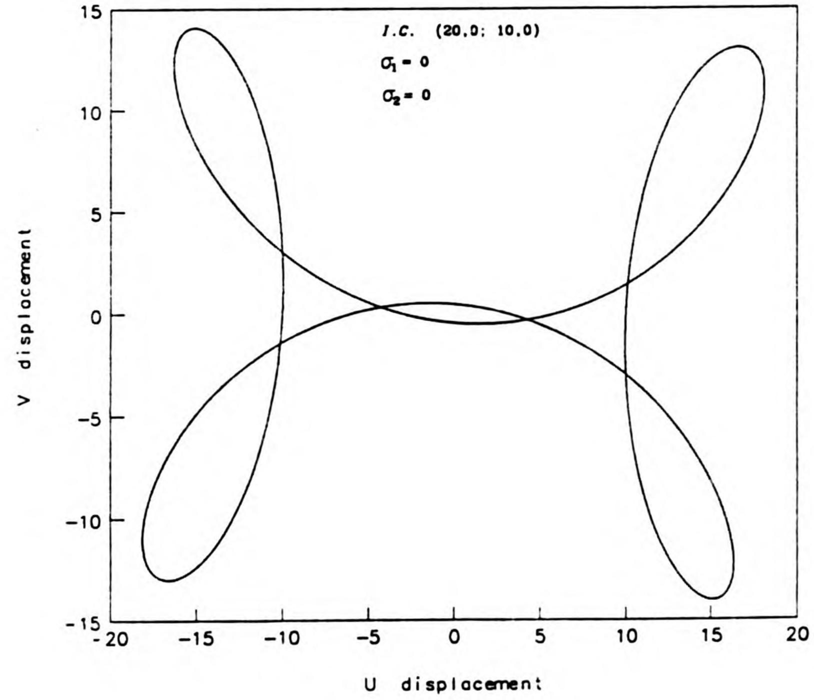

Figure 5.9b Orbit in (U,V) Projection; $\sigma_1 = 0.0$, $\sigma_2 = 0.0$, $U(0) = 20, \dot{U}(0) = 0.0; V(0) = 10, \dot{V}(0) = 0.0$.

the solutions. Figures 5.10a and 5.10b show the frequency response curves for two different Ω_A values. For a small Ω_A value (Figure 5.10a), the four branches in the frequency response curve are well separated from each other. In Figure 5.10b the value of Ω_A has been increased slightly and a more complex combination of solutions exists, many of which have been checked by direct numerical integration of equations (2.40) and (2.41). Figures 5.11a-h show the trends association with changing the internal tuning. Clearly we see that as the magnitude of the detuning, σ_2, becomes large the form of the response curve reverts to that of Figure 5.1. This is to be expected as large $|\sigma_2|$ corresponds to a lack of internal resonance, hence the case described in Section 5.3.1 is recovered. Figures 5.12a-c show frequency response curves with different δ values (at a small μ_e= 40). Obviously, both the amplitude, a_1 and a_2, increase as the δ value increases. It should be note that no distinction is made between stable and unstable solutions in Figures 5.10 to 5.12.

Figure 5.13 shows an orbit with σ_1 equal to 900. Because of the presence of internal resonance, the orbit is no longer an ellipse (c.f. the form of Figure 5.3). The corresponding time histories of the steady-state solution in x and y directions obtained by directly numerically integrating equations (2.40) and (2.41) are shown in Figures 5.14a and 5.14b. Figure 5.15 shows the corresponding spectrum of the time history of the U coordinate, which is obtained by using the Fast Fourier Transform (FFT) algorithm. In all the cases we checked, the numerical simulation results were indistinguishable from the results obtained using the method of multiple scales.

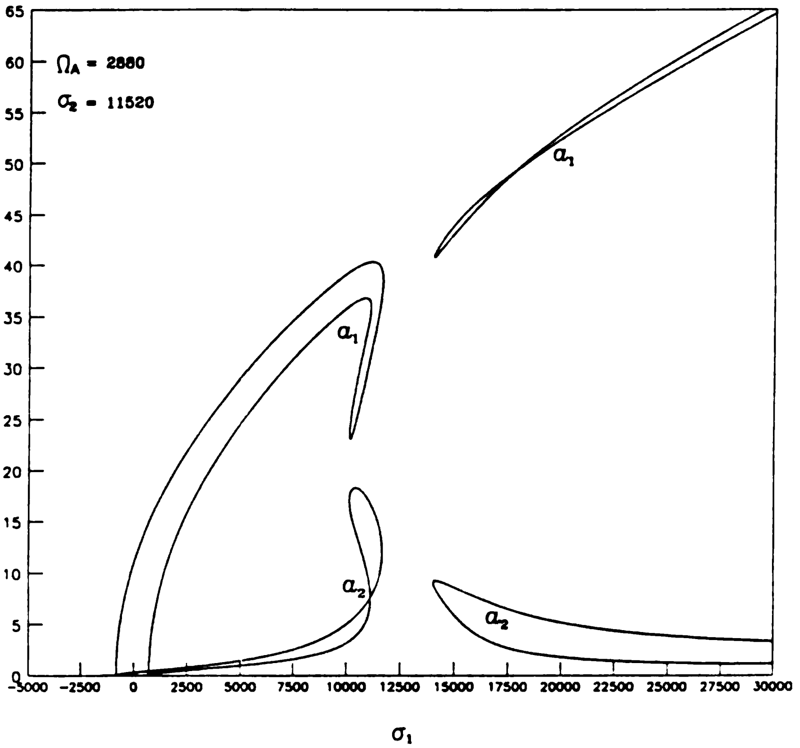

Figure 5.10a Variation of the Steady-State Amplitudes, a_1 and a_2, with σ_1; $\Omega_A = 2880$, $\sigma_2 = 11520$.

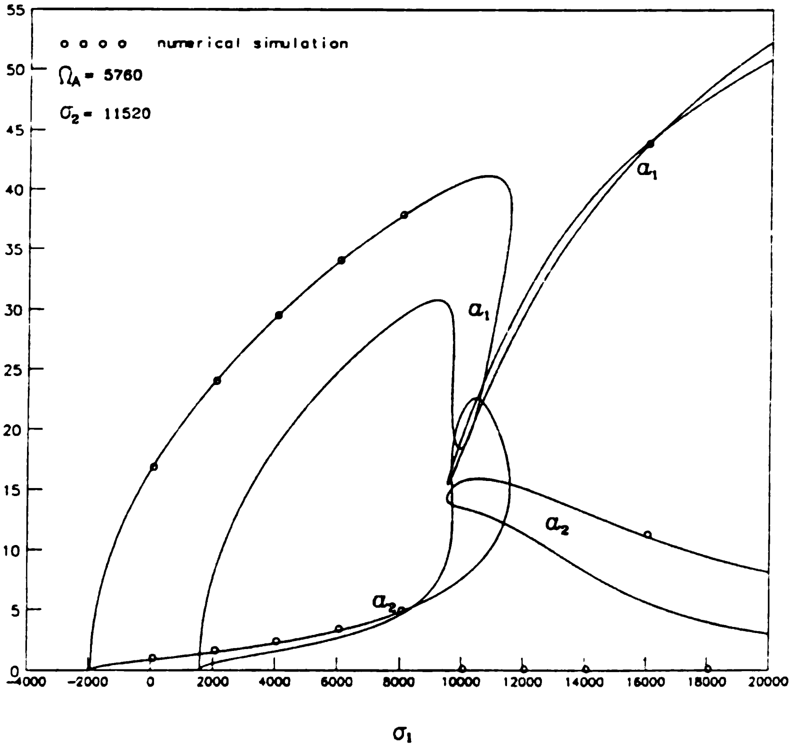

Figure 5.10b Variation of the Steady-State Amplitudes, a_1 and a_2, with σ_1; $\Omega_A = 5760$, $\sigma_2 = 11520$.

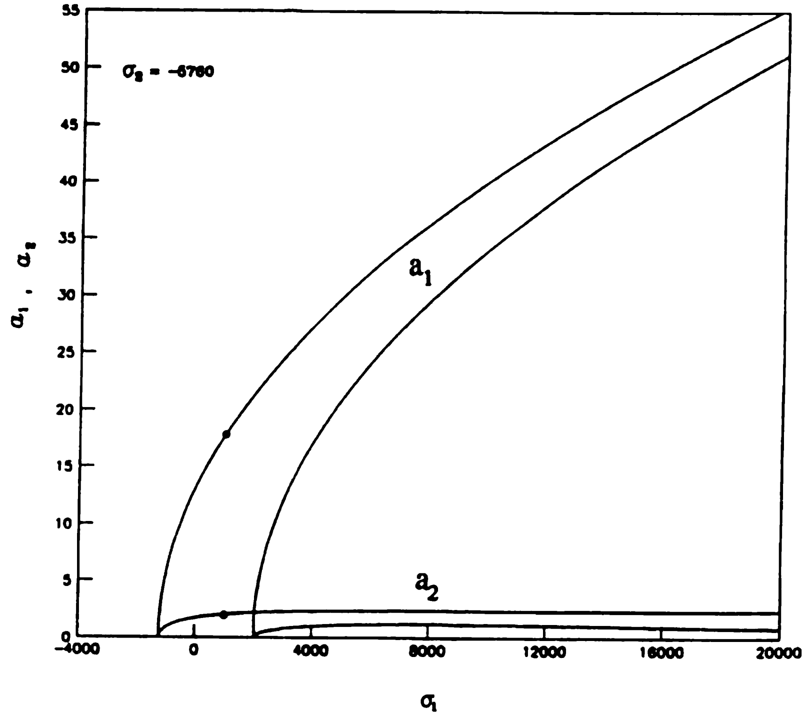

Figure 5.11a Variation of the Steady-State Amplitudes, a_1 and a_2, with σ_1; $\Omega_A = 5760$, $\sigma_2 = -5760$.

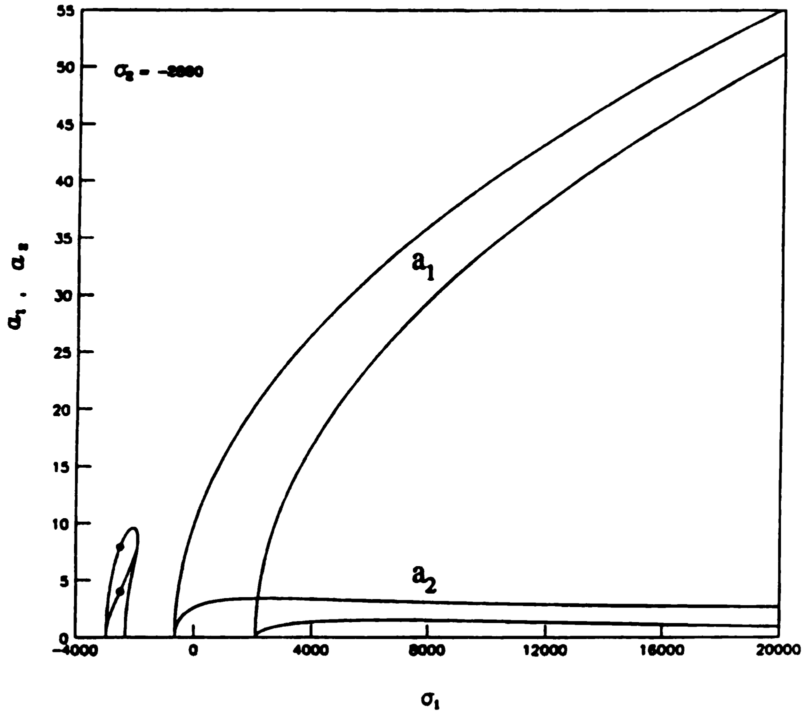

Figure 5.11b Variation of the Steady-State Amplitudes, a_1 and a_2, with σ_1; $\Omega_A = 5760$, $\sigma_2 = -2880$.

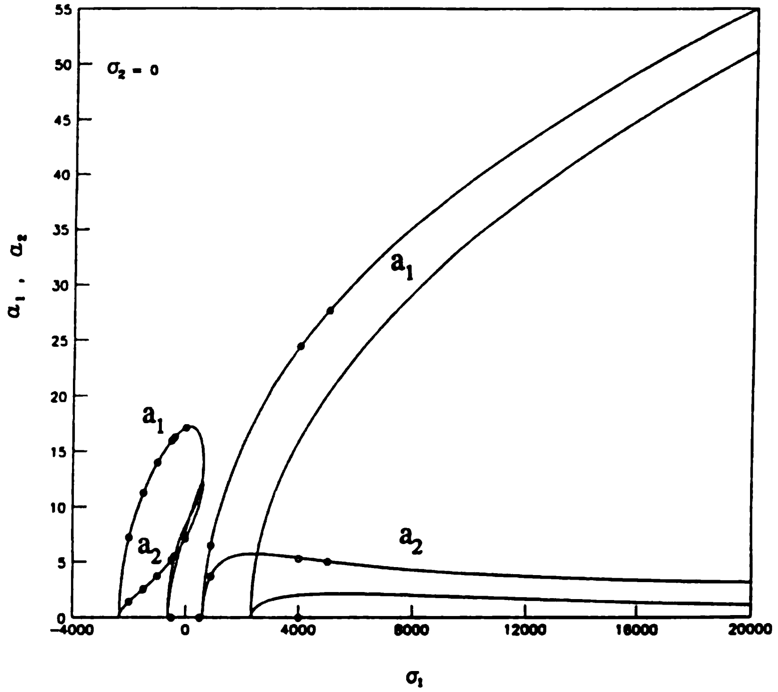

Figure 5.11c Variation of the Steady-State Amplitudes, a_1 and a_2, with σ_1; $\Omega_A = 5760$, $\sigma_2 = 0$.

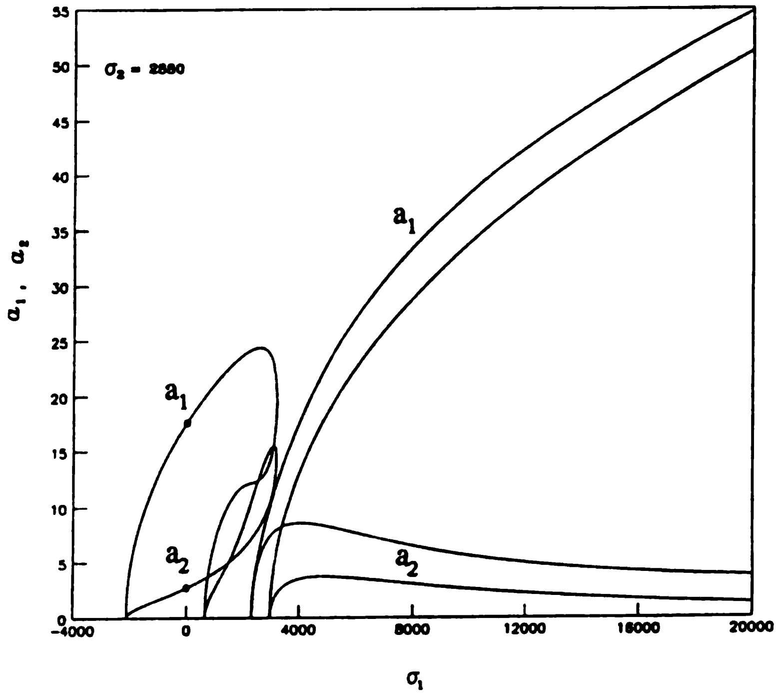

Figure 5.11d Variation of the Steady-State Amplitudes, a_1 and a_2, with σ_1; $\Omega_A = 5760$, $\sigma_2 = 2880$.

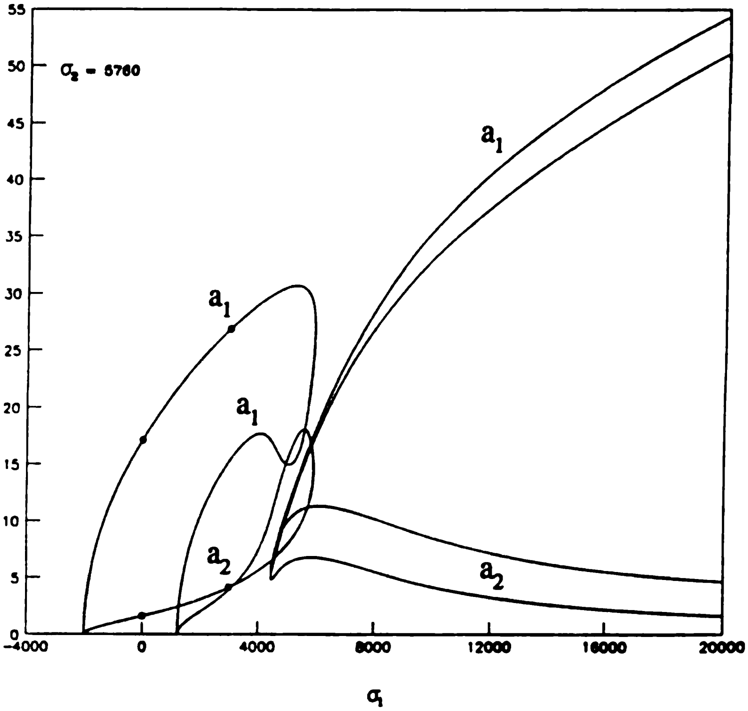

Figure 5.11e Variation of the Steady-State Amplitudes, a_1 and a_2, with σ_1; $\Omega_A = 5760$, $\sigma_2 = 5760$.

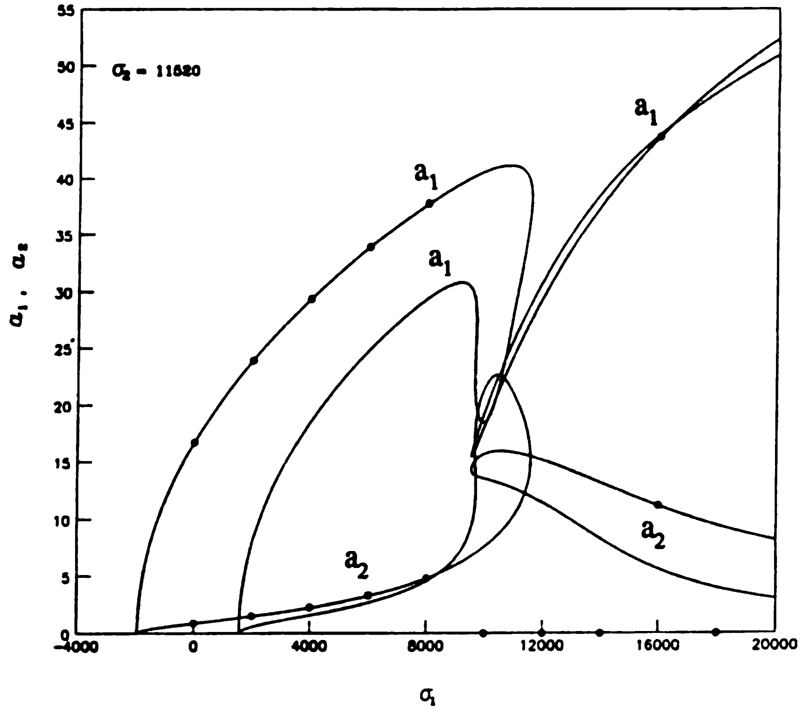

Figure 5.11f Variation of the Steady-State Amplitudes, a_1 and a_2, with σ_1; $\Omega_A = 5760$, $\sigma_2 = 11520$.

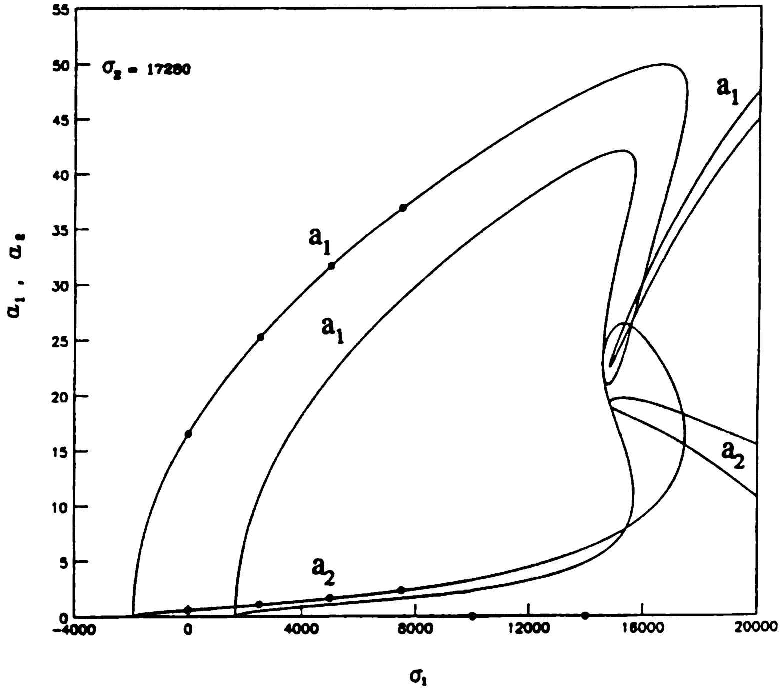

Figure 5.11g Variation of the Steady-State Amplitudes, a_1 and a_2, with σ_1; $\Omega_A = 5760$, $\sigma_2 = 17280$.

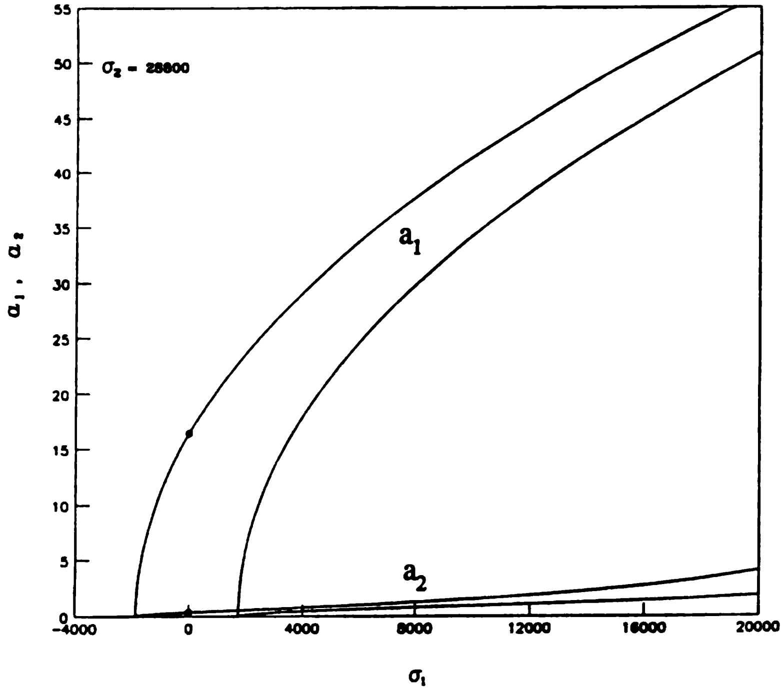

Figure 5.11h Variation of the Steady-State Amplitudes, a_1 and a_2, with σ_1; $\Omega_A = 5760$, $\sigma_2 = 28800$.

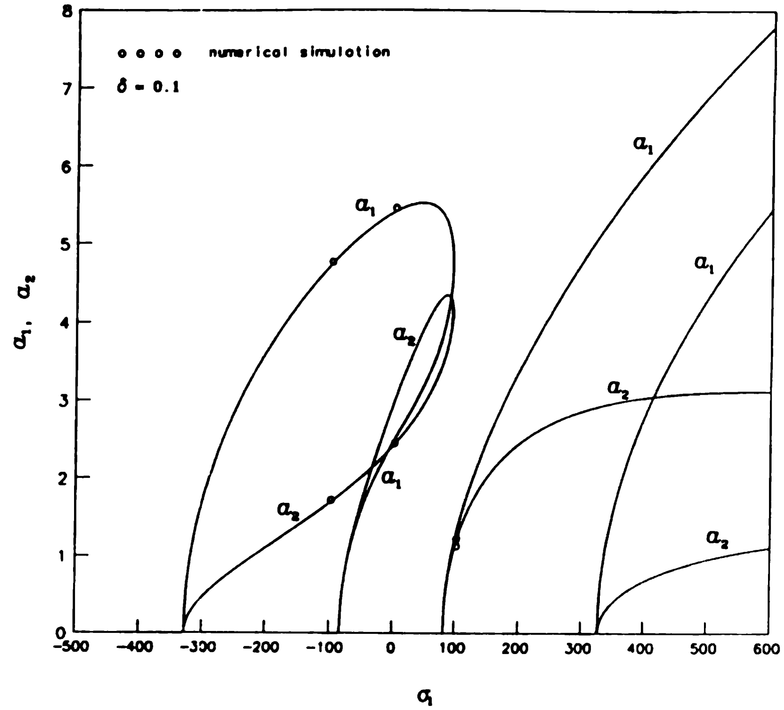

Figure 5.12a Variation of the Steady-State Amplitudes, a_1 and a_2, with σ_1; $\Omega_A = 5760$, $\sigma_2 = 0$, $\delta = 0.1$.

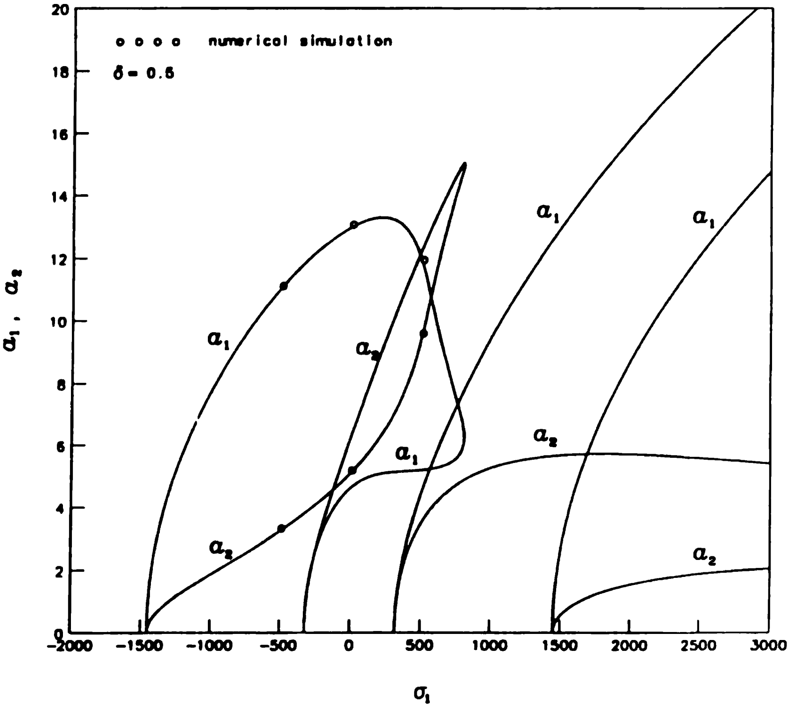

Figure 5.12b Variation of the Steady-State Amplitudes, a_1 and a_2, with σ_1; $\Omega_A = 5760$, $\sigma_2 = 0$, $\delta = 0.5$.

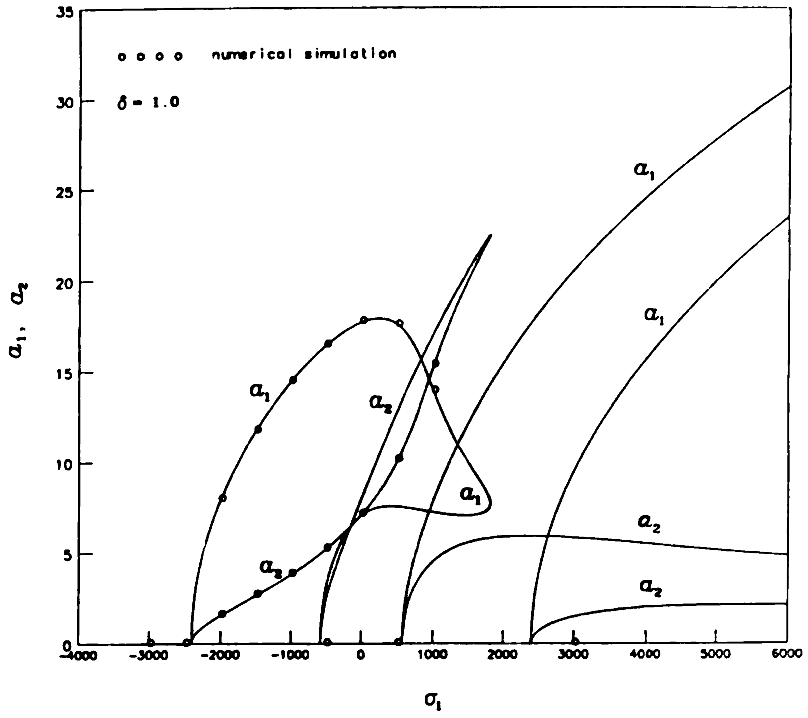

Figure 5.12c Variation of the Steady-State Amplitudes, a_1 and a_2, with σ_1; $\Omega_A = 5760$, $\sigma_2 = 0$, $\delta = 1.0$.

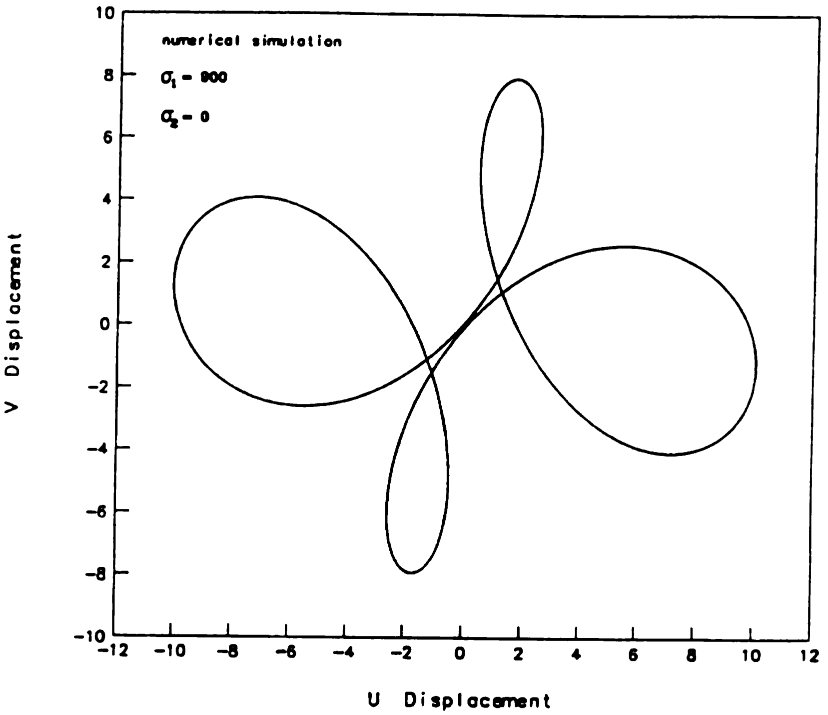

Figure 5.13 Orbit in (U,V) Projection; σ_1 =900, σ_2 =0.0.

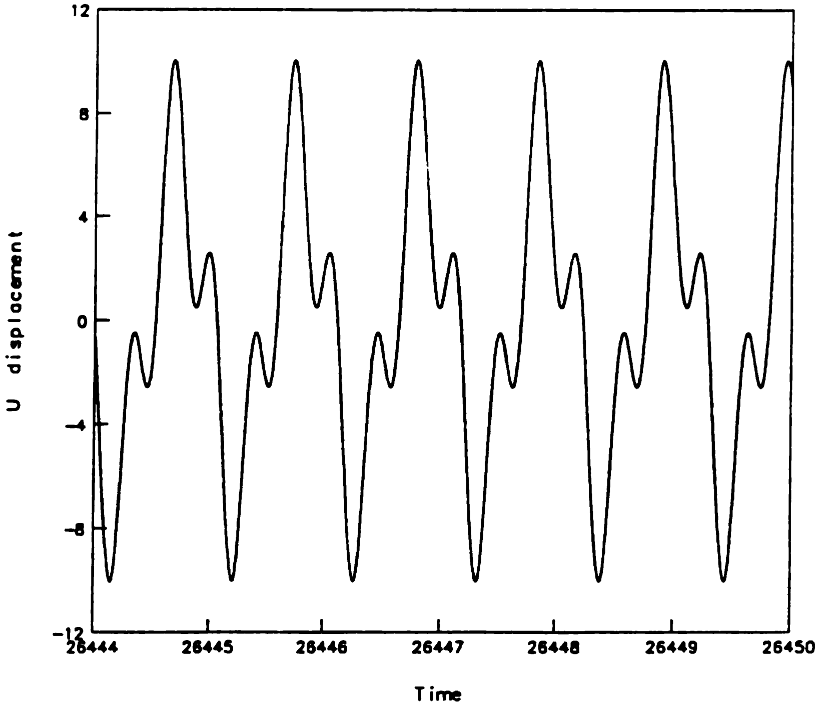

Figure 5.14a Time History of Steady-State Solution U; σ_1 =900, σ_2 =0.0.

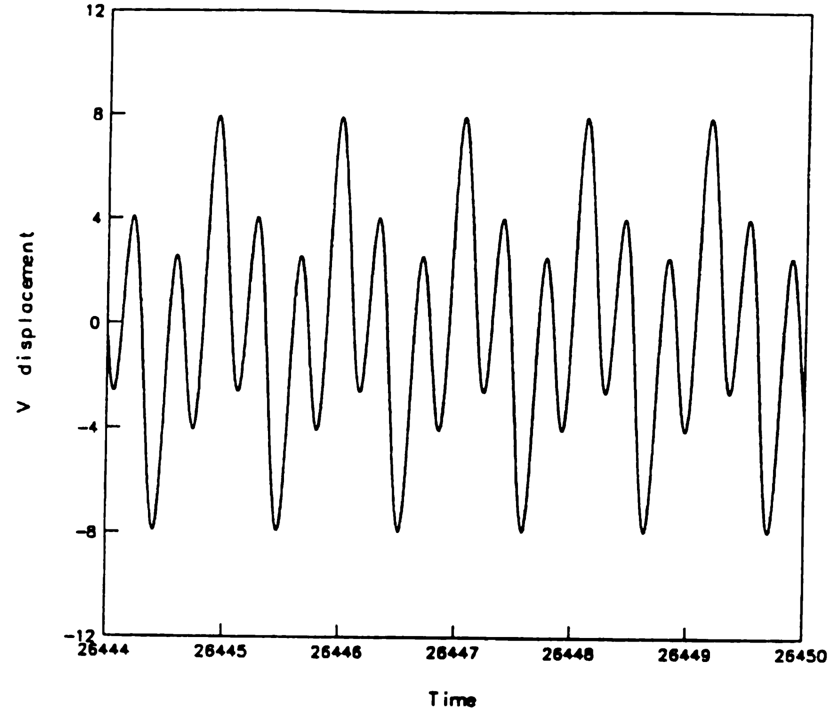

Figure 5.14b Time History of Steady-State Solution V; σ_1 =900, σ_2 =0.0.

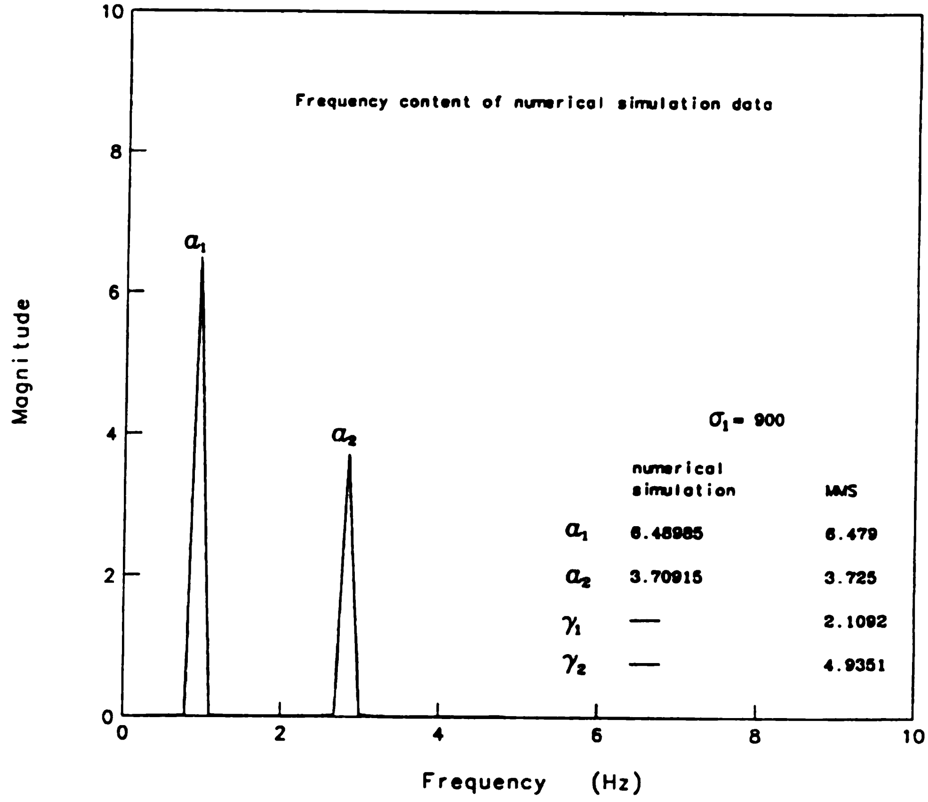

Figure 5.15 Spectrum of the Steady-State Solution U; σ_1 =900, σ_2 =0.0.

5.4.2 The case of $\omega \approx 2\,\omega_2$

The solvability conditions of this case are

$$i A_1' + G_{14} e^{i\sigma_2 T_1} \overline{A}_1^2 A_2 + i G_{15} \mu_e A_1 + G_{16} A_1^2 \overline{A}_1 + G_{17} A_1 A_2 \overline{A}_2 = 0 \tag{5.94}$$

$$i A_2' + i G_{22} e^{i\sigma_1 T_1} \overline{A}_2 + G_{26} e^{-i\sigma_2 T_1} A_1^3 + i G_{23} \mu_e A_2 + G_{25} A_2^2 \overline{A}_2 + G_{24} A_1 A_2 \overline{A}_1 = 0 \tag{5.95}$$

Substituting equations (5.25) and (5.26), the polar forms of A_1 and A_2, into equation (5.94) and (5.95) and separating the results into real and imaginary parts, yields

$$a_1' = -G_{15} \mu_e a_1 - \tfrac{1}{4} G_{14} a_1^2 a_2 \sin \gamma_1 \tag{5.96}$$

$$a_1(2\gamma_1' + \gamma_2') = a_1(2\sigma_1 + \sigma_2) - \tfrac{3}{2} G_{16} a_1^3 - \tfrac{3}{2} G_{14} a_1^2 a_2 \cos \gamma_1 - \tfrac{3}{2} G_{17} a_1 a_2^2 \tag{5.97}$$

$$a_2' = -G_{22} a_2 \cos\gamma_2 - G_{23} \mu_e a_2 + \tfrac{1}{4} G_{26} a_1^3 \sin \gamma_1 \tag{5.98}$$

$$a_2 \gamma_2' = a_2 \sigma_1 + G_{22} a_2 \sin\gamma_2 - \tfrac{1}{2} G_{24} a_1^2 a_2 - \tfrac{1}{2} G_{26} a_1^3 \cos \gamma_1 - \tfrac{1}{2} G_{25} a_2^3 \tag{5.99}$$

where

$$\gamma_1 = \sigma_2 T_1 + \beta_2 - 3\beta_1 \tag{5.100}$$

$$\gamma_2 = \sigma_1 T_1 - 2\beta_2. \tag{5.101}$$

These are the reduced equations for the case of $\omega \approx 2\,\omega_2$ with $\omega_2 \approx 3\,\omega_1$. Of particular interest are the steady-state case which correspond to $a_1' = a_2' = \gamma_1' = \gamma_2' = 0$. Equations (5.96) to (5.99) then reduce to

$$a_1\,(G_{15}\,\mu_e + \tfrac{1}{4}\,G_{14}\,a_1\,a_2\,\sin\,\gamma_1) = 0 \tag{5.102}$$

$$a_1[(\,2\,\sigma_1 + \sigma_2\,) - \tfrac{3}{2}\,G_{16}\,a_1{}^2 - \tfrac{3}{2}\,G_{14}\,a_1{}^2\,a_2\cos\,\gamma_1 - \tfrac{3}{2}\,G_{17}\,a_2{}^2] = 0 \tag{5.103}$$

$$G_{22}\,a_2\cos\gamma_2 + G_{23}\,\mu_e\,a_2 - \tfrac{1}{4}\,G_{26}\,a_1{}^3\sin\,\gamma_1 = 0 \tag{5.104}$$

$$a_2\,\sigma_1 + 2\,G_{22}\,a_2\sin\gamma_2 - \tfrac{1}{2}\,G_{24}\,a_1{}^2\,a_2 - \tfrac{1}{2}\,G_{26}\,a_1{}^3\cos\,\gamma_1 - \tfrac{1}{2}\,G_{25}\,a_2{}^3 = 0 \tag{5.105}$$

This gives rise to three possible sets of solutions to these equations:

(1) $a_1 = 0$ and $a_2 = 0$

(2) $a_1 = 0$ and $a_2 \neq 0$

(3) $a_1 \neq 0$ and $a_2 \neq 0$

We first consider possibility (2) viz. $a_1 = 0$ and $a_2 \neq 0$. For this case equation (5.104) and (5.105) reduce to

$$G_{23}\,\mu_e\,a_2 + G_{22}\,a_2\cos\gamma_1 = 0 \tag{5.106}$$

$$a_1\sigma_1 + 2\,G_{22}\,a_2\sin\gamma_1 - \frac{1}{2}\,G_{24}a_2\,a_1{}^2 - \frac{1}{2}\,G_{25}\,a_2{}^3 = 0 \tag{5.107}$$

Equations (5.106) and (5.107) are exactly equal to equations (5.48) and (5.49) (i.e., the no internal resonance case) and so are not discussed again here.

For possibility (3), we solved the roots (i.e., non-trivial steady-state solutions) of equations (5.102) to (5.105) using numerical routine DNEQNF from the IMSL library. This routine use a modified Powell hybrid method to find the roots. Although a great many initial estimates of the solutions were used. The routine only found the trivial solutions. The reason may be because the basin of attraction of the non-trivial steady-state solutions is extremely small and/or irregular. This is consistent with the results obtained by directly numerically integrating the original equations (2.40) and (2.41) in which all trajectories of the cases tested eventually approach the trivial solution or possibility (2).

5.4.3 The case of $\omega \approx \omega_2 + \omega_1$

The solvability conditions of this case are

$$\begin{aligned} & i A_1' + i G_{13} e^{i\sigma_1 T_1} \overline{A}_2 + G_{14} e^{i\sigma_2 T_1} \overline{A}_1^2 A_2 \\ & \quad + i G_{15} \mu_e A_1 + G_{16} A_1^2 \overline{A}_1 + G_{17} A_1 A_2 \overline{A}_2 = 0 \end{aligned} \tag{5.108}$$

$$\begin{aligned} & i A_2' + i G_{22} e^{i\sigma_1 T_1} \overline{A}_1 + G_{26} e^{-i\sigma_2 T_1} A_1^3 + i G_{23} \mu_e A_2 \\ & \quad + G_{25} A_2^2 \overline{A}_2 + G_{24} A_1 A_2 \overline{A}_1 = 0 \end{aligned} \tag{5.109}$$

Substituting the usual polar forms of A_1 and A_2 into equation (5.108) and (5.109) and following the normal procedure, yields

$$a_1' = - G_{13} a_2 \cos\gamma_1 - G_{15} \mu_e a_1 - \frac{1}{4} G_{14} a_1^2 a_2 \sin \gamma_2 \tag{5.110}$$

$$a_1(\gamma_1'+\gamma_2')=a_1(\sigma_1+\sigma_2)-G_{16}\,a_1^3+G_{13}\,a_2\ \sin\gamma_2$$
$$-G_{14}\,a_1^2\,a_2\cos\gamma_2-\ G_{17}\,a_1\,a_2^2 \tag{5.111}$$

$$a_2'=-\,G_{22}\,a_1\cos\gamma_1-G_{23}\,\mu_e\,a_2+\frac{1}{4}G_{26}\,a_1^3\sin\gamma_2 \tag{5.112}$$

$$a_2\left(\frac{3}{4}\gamma_1'-\frac{1}{4}\gamma_2'\right)=a_2\left(\frac{3}{4}\sigma_1-\frac{1}{4}\sigma_2\right)+G_{22}\,a_1\sin\gamma_1-\frac{1}{4}G_{24}\,a_1^2\,a_2$$
$$-\frac{1}{4}G_{25}\,a_2^3-\frac{1}{4}G_{26}\,a_1^3\cos\gamma_2 \tag{5.113}$$

where

$$\gamma_1=\sigma_1\,T_1-\beta_2-\ \beta_1 \tag{5.114}$$

$$\gamma_2=\sigma_2\,T_1-3\,\beta_1+\ \beta_2. \tag{5.115}$$

Two possibilities of the steady-state solutions exists: either a_1 and a_2 are zero, or neither one is zero. The steady-state solution has the form

$$u_0=a_1\cos\left[\frac{\omega\tau-(\gamma_1+\gamma_2)}{4}\right]+a_2\cos\left[\frac{3\omega\tau-(\gamma_2-3\gamma_1)}{4}\right] \tag{5.116}$$

$$v_0=-k_1\,a_1\sin\left[\frac{\omega\tau-(\gamma_1+\gamma_2)}{4}\right]-k_2\,a_2\sin\left[\frac{3\omega\tau-(\gamma_2-3\gamma_1)}{4}\right] \tag{5.117}$$

Figure 5.16 shows a typical frequency response curve obtained by finding the roots of the steady-state form of equations (5.110) to (5.113). The approximate solutions to the full equations of motion can be checked by directly numerically integrating equations (2.40) and (2.41). The comparison is good in all the cases tested. Figures 5.17a and 5.17b show the orbits of the shaft obtained by numerical integration of equations (2.40) and (2.41) and by the method of multiple scales (equations (5.116) and (5.117)), respectively. Note that,

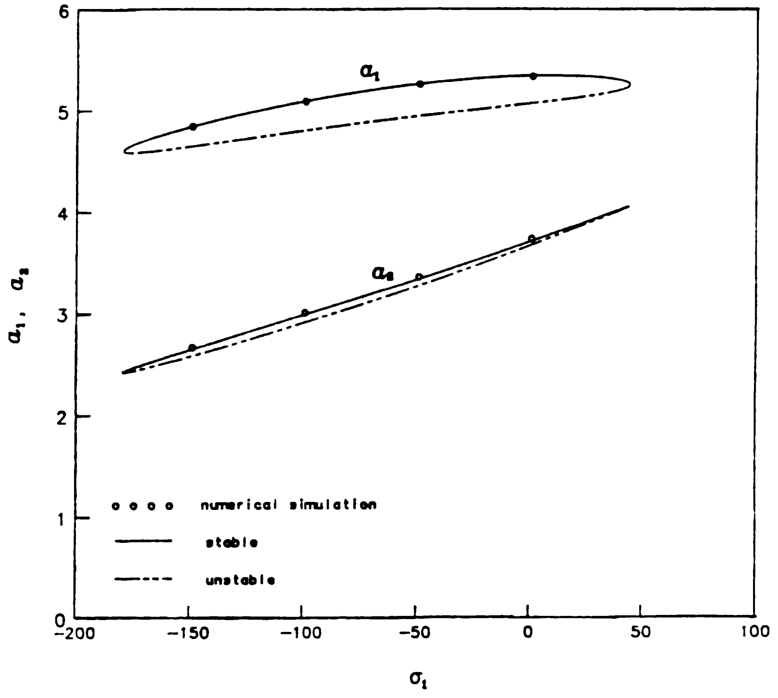

Figure 5.16 Variation of the Steady-State Amplitudes, a_1 and a_2, with σ_1; $\sigma_2 = 0$, $\delta = 1.0$.

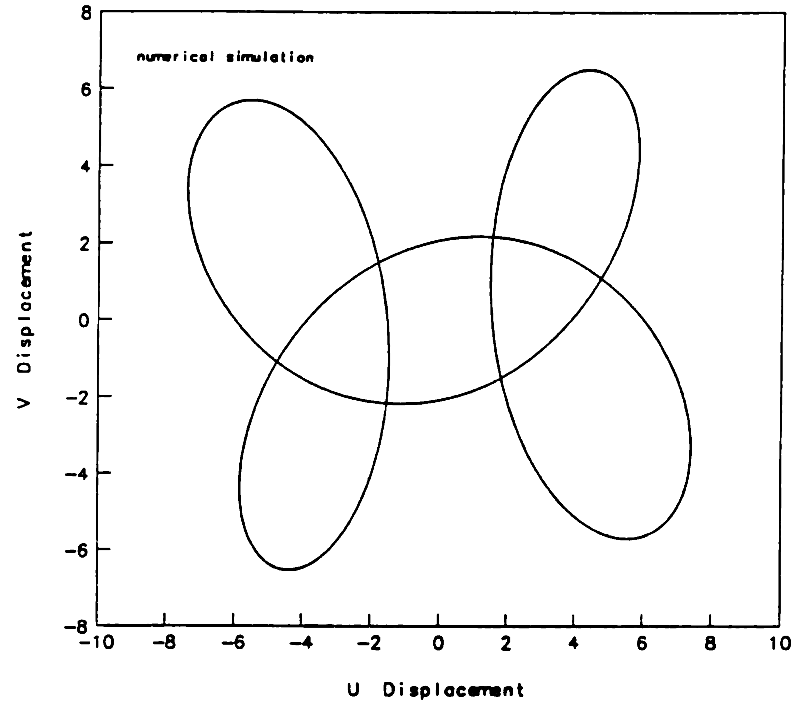

Figure 5.17a Orbit obtained by Numerical Simulation in (U,V) Projection; $\sigma_2 = 0$, $\delta = 1.0$.

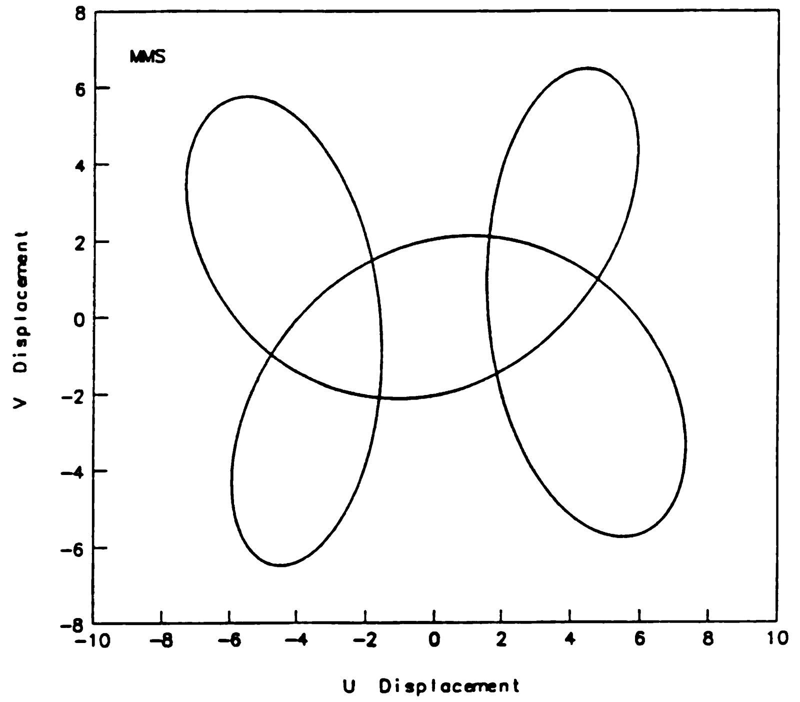

Figure 5.17b Orbit obtained by MMS in (U,V) Projection; $\sigma_2 = 0$, $\delta = 1.0$.

because of the condition of perfect internal resonance (i.e., ω_1 and ω_2 are commensurate), the orbits are fixed in the rotating frame.

The final resonance case $\omega \approx \omega_2 - \omega_1$, with internal resonance, reduces to the case of $\omega \approx 2\omega_1$, which has covered in Section 5.4.1.

5.5 Summary of the Chapter

This chapter has been concerned with a theoretical investigation of the nonlinear dynamics of a perfectly balanced shaft rotating at a nonconstant speed. The nonconstant speed gives rise to time-dependent coefficients in the equations of motion. Four cases of parametric resonances, viz. $\omega \approx 2\omega_1$, $\omega \approx 2\omega_2$, $\omega \approx \omega_1 + \omega_2$ and $\omega \approx \omega_2 - \omega_1$ were considered. Each case was analyzed firstly in the absence of internal tuning (i.e., ω_2 is assumed to be well removed from $3\omega_1$) and secondly in the presence of internal tuning (i.e., ω_2 is assumed to be closed to $3\omega_1$). The investigation was restricted to the pre-buckled case (i.e., $\Omega_s < \Omega_0$) and approximate solutions were obtained using the method of multiple scales.

No parametric resonances were possible in the case of a perfectly balanced symmetrical shaft either with or without internal resonances. However, for a shaft that is close to circular, it was found that parametric resonances occur. In the absence of internal resonance we observed a single frequency response with a period twice that of the excitation. This resulted in an elliptic orbit of the shaft in the rotating frame. When the internal resonance is present, the response of the shaft contains two frequencies and the frequency response curve is much more complex than that of the former case. In the later case, we found the existence of such phenomena as non-existence of steady-state motions, coexistence of steady-state motions and amplitude modulate motions and re-stabilization of the trivial solutions.

CHAPTER 6

ANALYSIS OF A ROTATING, SIMPLY SUPPORTED SHAFT WITH $\Omega_s > \Omega_0$

6.1 Introduction

The source of the nonconservative forces which act on rotating shafts becomes particularly important as one passes beyond the critical speed. These forces can be divided into two categories. The first category contains forces defined as external frictional forces. These are caused by contact of the rotating shaft with fixed components. The second category contains forces defined as internal frictional forces. These have two fundamental components: hysteresis forces and structural damping forces. The former arise as a result of the rate of deformation in the elastic shaft, whereas the latter arise as a result of micro-shifts between individual parts of the rotor structure. As was pointed out by Tondl [1965], when the rotational speed of the shaft is above Ω_0, internal frictional forces, under certain circumstances, can cause instabilities, whereas external frictional forces always assist in damping the vibrations.

The influence of the internal damping on the shaft's response is one of the effects we shall study in this chapter. A number of the results are based on numerical integration studies since it is extremely hard to obtain even a first order approximate solution to the complex differential equations which govern the shaft's motion. However, some analytical results have been obtained for the post buckled behavior of a perfectly circular shaft subjected to a nonconstant spin rate. The analysis begins by converting the governing equations from Cartesian coordinates to polar coordinates. This allows one to find the buckled, or equilibrium position that the shaft will adopt when it is spun at a constant rate. It is motions about this buckled position which we then go on to investigate. A shift in the coordinate system is undertaken and approximate solutions are sought to the resulting coupled, differential equations, under the influence of the small speed fluctuations. In particular, we look at the frequency, ω, of speed fluctuations being close to the whirl speed, $\overline{\omega}$.

We also report on findings related to almost circular shafts. Unlike the pre-buckled case, where Ω_s could be altered in order to obtain an internal resonance condition of $\omega_2 \approx 3\omega_1$, this can not be accomplished for the post-buckled case. This results from the fact that $\omega_2 >> \omega_1$, for all $\Omega_s > \Omega_0$. A limited amount of analysis is reported which shows the type of response that might be expected and numerical simulations are completed to investigate period doubling bifurcations and chaotic motions for the case of $\omega \approx \omega_1$ and $\omega \approx 2\omega_1$.

6.2 Exactly Circular Cross Section

In this section we investigate the post-critical behavior of shafts with exactly circular cross section (i.e., $\delta = 0$). The influence of internal damping will be considered at two different orders of magnitude.

6.2.1 Equilibrium Position

In order to find the buckled positions of the shaft, it is convenient to introduce the polar coordinates R and ϕ, defined by the relation

$$U + i V = R e^{i\phi} \tag{6.1}$$

where U and V are nondimensional modal displacements.

Substituting equation (6.1) and $\delta = 0$ into equations (2.40) and (2.41) and separating real and imaginary parts yields

$$\ddot{R} + 2\varepsilon\mu_e\dot{R} + \varepsilon\mu_i\dot{R} + (\Omega_0^2 - \Omega^2)R - 2\Omega R\dot{\phi} - R\dot{\phi}^2 + \varepsilon\Omega_0^2 R^3 = 0 \qquad (6.2)$$

$$R\ddot{\phi} + R\dot{\Omega} + 2\varepsilon\mu_e(\Omega R + R\dot{\phi}) + \varepsilon\mu_i R\dot{\phi} + 2\Omega\dot{R} + 2\dot{R}\dot{\phi} = 0 \qquad (6.3)$$

Defining $\overline{R}$ and $\overline{\phi}$ to be the equilibrium solution set of equations (6.2) and (6.3), they can be found by noting that $\Omega = \Omega_s$ and by setting all time derivatives equal to zero. Hence we have

$$(\Omega_0^2 - \Omega_s^2)\overline{R} + \varepsilon\Omega_0^2\overline{R}^3 = 0 \qquad (6.4)$$

$$2\varepsilon\mu_e\Omega_s\overline{R} = 0 \qquad (6.5)$$

The trivial solution $\overline{R} = 0$ corresponds to the undeformed configuration of the shaft and is always a solution. The non-trivial solution exists only when $\Omega_s > \Omega_0$ and $\mu_e = 0$ (i.e., no external damping) and is given by

$$\overline{R} = \left[\frac{(\Omega_s^2 - \Omega_0^2)}{\varepsilon\Omega_0^2}\right]^{\frac{1}{2}} \qquad (6.6)$$

However, in practice there will always be damping and in such a case there is another possible solution set in which $\ddot{R} = \dot{R} = 0$, $R = \overline{R}$ and $\ddot{\phi} = 0$, $\overline{\phi} = -\overline{\omega}$, where $\overline{\omega}$ is defined

to represent the fact that the shaft whirls at a speed different from the rotational speed of the shaft (i.e., nonsynchronous whirling).

Equations (6.2) and (6.3) now become

$$(\Omega_0^2-\Omega_s^2)\,\overline{R}+2\,\Omega_s\,\overline{R}\,\overline{\omega}-\overline{R}\,\overline{\omega}^2+\varepsilon\,\Omega_0^2\,\overline{R}^3=0 \tag{6.7}$$

$$2\,\varepsilon\,\mu_e\,(\overline{R}\,\Omega_s-\overline{R}\,\overline{\omega})-\varepsilon\,\mu_i\,\overline{R}\,\overline{\omega}=0 \tag{6.8}$$

From equation (6.8), we have

$$\overline{\omega}=\frac{2\mu_e\,\Omega_s}{2\,\mu_e+\mu_i} \qquad (\,\overline{R}\neq 0\,) \tag{6.9}$$

Substituting equation (6.9) into equation (6.7), we have

$$\overline{R}=\left[\frac{(\Omega_s-\overline{\omega})^2-\Omega_0^2}{\varepsilon\,\Omega_0^2}\right]^{\frac{1}{2}} \tag{6.10}$$

Noting that we want $\overline{R}$ to be real, we can solve equation (6.10) to find the value of Ω_s at which a non-trivial value of $\overline{R}$ just appears. Calling this value of Ω_s, Ω_s^*, it is found to be

$$\Omega_s^*=\Omega_0+\frac{2\,\mu_e\Omega_0}{\mu_i} \tag{6.11}$$

This is the first critical speed at which the trivial solution loses its stability and bifurcates into a stable periodic solution which whirls at a speed different from the rotational speed of the shaft (for stability details see, for example, Tondl [1965], page 20). Also, from equation (6.11), we found that if $\mu_i = 0$, then $\Omega_s^* \to \infty$. This means that, for a symmetrical and perfectly balanced shaft, if we assume $\mu_i = 0$, whirling motions will never occur.

6.2.2 Coordinate Transformation

Before employing the method of multiple scales to obtain approximate solutions for the motion about the buckled position, we first transfer the coordinates of equations (6.2) and (6.3) such that the new coordinates describe the motion about the buckled position.

Let the new coordinates be q and $\dot{\varphi}$, such that

$$R = \bar{R} + q \tag{6.12}$$

and

$$\phi = -\bar{\omega}\tau + \varphi + \phi_0 \tag{6.13}$$

where ϕ_0 is a constant depending on the initial conditions.

Substituting equations (6.12) and (6.13) into equations (6.2) and (6.3) and setting $\Omega = \Omega_s + \varepsilon\,\Omega_A \sin\omega\tau$, we obtain

$$\begin{aligned} &\ddot{q} + 2\left[(\Omega_s - \bar{\omega})^2 - \Omega_0^2\right] q - 2(\Omega_s - \bar{\omega})(q + \bar{R})\dot{\varphi} - (q + \bar{R})\dot{\varphi}^2 \\ &\quad + 3\varepsilon\,\Omega_0^2 q^2 \bar{R} + \varepsilon\,\Omega_0^2 q^3 + \varepsilon(2\mu_e + \mu_i)\dot{q} = 2\varepsilon(q + \bar{R})\Omega_A\,\dot{\varphi}\sin\omega\tau \\ &\quad + 2\varepsilon(\Omega_s - \bar{\omega})\Omega_A(\bar{R} + q)\sin\omega\tau + \varepsilon^2\Omega_A^2(q + \bar{R})\sin\omega\tau^2 \end{aligned} \tag{6.14}$$

$$\begin{aligned}(q+\overline{R})\ddot{\varphi}+2\dot{q}\dot{\varphi}+2(\Omega_s-\overline{\omega})\dot{q}+\varepsilon(q+\overline{R})\dot{\varphi}(2\mu_e+\mu_i)\\ +2\varepsilon\mu_e q(\Omega_s-\overline{\omega})-\varepsilon\mu_i q\overline{\omega}=-\varepsilon\Omega_A\omega(q+\overline{R})\cos\omega\tau\\ -2\varepsilon\Omega_A\dot{q}\sin\omega\tau-2\varepsilon^2\mu_e\Omega_A(q+\overline{R})\sin\omega\tau\end{aligned}\qquad(6.15)$$

Note that these equations describes the response of a shaft about the buckled positions to combined parametric and external excitations.

We will now seek a first order approximate solution to the two equations. Before presenting this, we note that when the shaft operates above the first critical speed (i.e., $\Omega_s > \Omega_s^*$), internal damping has a destabilizing effect (i.e., it acts as a source of energy to the system). We therefore might expect the internal damping to play a very important role in the final form of the approximate solutions. This is indeed the case and it is necessary to assume two different orderings for the size of μ_i. In the analysis to follow we will consider two cases: (a) the internal damping appears at the same order as nonlinearity and (b) the internal damping appears in the lowest order of the perturbation equations.

6.2.3 A First-order Approximate Solution with $\mu_i = O(1)$

In this sub-section we assume the internal damping will appear when the nonlinearities appear. We seek a first-order uniform expansion by using the method of multiple scales in the form

$$q(\tau;\varepsilon)=\varepsilon\, q_1(T_0,T_1)+\varepsilon^2 q_2(T_0,T_1)+\varepsilon^3 q_3(T_0,T_1)+\cdots\cdots\qquad(6.16)$$

$$\varphi(\tau;\varepsilon)=\varepsilon\,\varphi_1(T_0,T_1)+\varepsilon^2\varphi_2(T_0,T_1)+\varepsilon^3\varphi_3(T_0,T_1)+\cdots\cdots\qquad(6.17)$$

Substituting equations (6.16), (6.17), (3.6) and (3.7) into equations (6.14) and (6.15) and equating coefficients of like powers of ε, we obtain

ε^1:

$$D_0^2 q_1 - 2(\Omega_s - \bar{\omega})\bar{R} D_0^2 \varphi_1 + 2\left[(\Omega_s - \bar{\omega})^2 - \Omega_0^2\right] q_1$$
$$= 2\ (\Omega_s - \bar{\omega})\,\Omega_A \bar{R} \sin \omega\tau \qquad (6.18)$$

$$\bar{R} D_0^2 \varphi_1 + 2(\Omega_s - \bar{\omega}) D_0 q_1 = -\Omega_A\, \omega\, \bar{R} \cos \omega\tau\ . \qquad (6.19)$$

The solutions of equations (6.18) and (6.19) can be expressed in the form

$$q_1 = q_{1h} + q_{1p} \qquad (6.20)$$

$$\bar{R}\varphi_1 = p_1 = p_{1h} + p_{1p} \qquad (6.21)$$

where

$$q_{1h} = A_1(T_1) + A_2(T_1)\exp(i\omega_1 T_0) + cc \qquad (6.22)$$

$$p_{1h} = \Lambda_1 A_1(T_1) + \Lambda_2 A_2(T_1)\exp(i\omega_1 T_0) + cc \qquad (6.23)$$

$$q_{1p} = 0 \qquad (6.24)$$

$$p_{1p} = \frac{\Omega_A \bar{R}}{\omega}\cos \omega\tau \qquad (6.25)$$

and

$$\omega_1 = \left[\, 6(\Omega_s - \overline{\omega})^2 - 2\,\Omega_0^{\,2} \,\right]^{\frac{1}{2}}$$

$$\Lambda_1 = \frac{(\Omega_s - \overline{\omega})^2 - \Omega_0^{\,2}}{\Omega_s - \overline{\omega}}\,\tau$$

$$\Lambda_2 = \frac{2(\Omega_s - \overline{\omega})}{\omega_2}\,i$$

cc stands for the complex conjugate of the preceding terms.

In equations (6.13) and (6.14), the excitation comes from two parts: (a) parametric and (b) direct forcing. If the analysis is continued to the next order we can shown that the A_1 and A_2 decay to zero and thus the direct forcing term only influences p_{1p} which in turn only effects the whirling speed of the shaft, and not the radius of the whirl. Therefore, for a perfectly circular shaft with a very small value of internal damping μ_i, the orbit of the whirling cannot be parametrically excited.

6.2.4 A First-order Approximate Solution with $\mu_i = O\,(\frac{1}{\varepsilon})$

In this sub-section we investigate the effect of internal damping on the response of a perfectly circular shaft rotating at nonconstant speed. We first order the internal damping so that it will appear in the lowest-order perturbation equations. To this end we introduce $\hat{\mu}_i$, such that $\hat{\mu}_i = \varepsilon\, \mu_i$.

Substituting equations (6.16), (6.17), (3.6) and (3.7) into equations (6.14) and (6.15) and equating coefficients of like powers of ε, we obtain

ε^1:

$$D_0^2 q_1 - 2(\Omega_s - \bar{\omega})\bar{R} D_0 \varphi_1 + \hat{\mu}_i D_0 q_1 + 2\left[(\Omega_s - \bar{\omega})^2 - \Omega_0^2\right] q_1 = 2\ (\Omega_s - \bar{\omega})\,\Omega_A \bar{R} \sin \omega\tau \tag{6.26}$$

$$\bar{R} D_0^2 \varphi_1 + 2(\Omega_s - \bar{\omega}) D_0 q_1 + \hat{\mu}_i \bar{R} D_0 \varphi_1 - \hat{\mu}_i q_1 \bar{\omega} = -\Omega_A\, \omega\, \bar{R} \cos \omega\tau \tag{6.27}$$

The solutions of equations (6.26) and (6.27) can be expressed in the form

$$q_1 = q_{1h} + q_{1p} \tag{6.28}$$

$$\bar{R}\varphi_1 = p_1 = p_{1h} + p_{1p} \tag{6.29}$$

By investigating the eigenvalues of equations (6.26) and (6.27) we find that the homogeneous solutions will be damped out (i.e., q_{1h} and $p_{1h} \rightarrow 0$). The particular solutions can be found as follow

$$q_{1p} = A_{1p} \sin(\omega\tau + \alpha_1) \tag{6.30}$$

$$p_{1p} = A_{2p} \cos(\omega\tau - \alpha_2) \tag{6.31}$$

where

$$A_{1p}=\sqrt{H_1^{\,2}+H_2^{\,2}}, \qquad \alpha_1=\tan^{-1}\frac{H_1}{H_2}$$

$$A_{2p}=\sqrt{H_3^{\,2}+H_4^{\,2}}, \qquad \alpha_2=\tan^{-1}\frac{H_3}{H_4}$$

and

H_1, H_2, H_3 and H_4 are defined in Appendix F.

Hence, the steady state solutions have the form

$$U=R\cos\phi=\left[\bar{R}+\varepsilon A_{1p}\sin(\omega\tau+\alpha_1)\right]\cos\left[-\bar{\omega}t+\varepsilon\frac{A_{2p}}{\bar{R}}\cos(\omega\tau-\alpha_2)+\phi_0\right] \tag{6.32}$$

$$V=R\sin\phi=\left[\bar{R}+\varepsilon A_{1p}\sin(\omega\tau+\alpha_1)\right]\sin\left[-\bar{\omega}t+\varepsilon\frac{A_{2p}}{\bar{R}}\cos(\omega\tau-\alpha_2)+\phi_0\right] \tag{6.33}$$

where ϕ_0 depends on the initial conditions. Note that both the amplitude and frequency parts in equations (6.32) and (6.33) have a small oscillation term with frequency ω and the amplitudes A_{1p} and A_{2p} which depend on $\hat{\mu}_i$, μ_e, Ω_s, Ω_A and ω.

6.2.5 Numerical Results

In this sub-section we present the numerical results using the set of parameter values: $\Omega_s = 10.1$, $\mu_e = 173$ and $\varepsilon = (\frac{1}{240})^2$. The original differential equations (2.40) and (2.41) are simulated on a digital computer. After transient motions decay, the steady-state solutions are recorded and compared to those predicted by the method of multiple scales (equations (6.32) and (6.33)).

We first demonstrate the effect of internal damping μ_i on the symmetrical shaft response. Figures 6.1a-c show the orbits of the shaft for three different values of μ_i with $\omega = \overline{\omega}$. From Figure 6.1a we observe that the shaft has a nonsynchronous whirling motion with a circular orbit if the value of μ_i is very small (note that U and V are rotating coordinates). However, for larger values of μ_i, this circular orbit will change to a "circular" orbit with a overhang. Note that the the size of the overhang and the radius of the orbit increase as the value of μ_i increases.

Figures 6.2a-i depict the results from both the numerical simulations and the method of multiple scales for a selection of different ω values, viz. $\omega = n\,\overline{\omega}$, $n = 1, \frac{3}{2}, 2, 3$. From these figures, we observe that the approximate solutions and the numerical solutions are in close agreement. It should be noted that the phase angle constant ϕ_0 in equations (6.32) and (6.33) depends on the initial conditions, which in turn fixes the orientation of the overhang. Also, from these figures we observe that if n is a integer, the number of overhangs is equal to n. If n is a irrational number, then the response of the shaft is non-periodic. The corresponding results for such a case are shown in Figures 6.3a-b where $\omega = \sqrt{2}\,\overline{\omega}$. In this case the simulations represent approximately 10 cycles of ω.

6.3 Close to Circular Cross Section

In this section we consider the shaft to have close to a circular section (i.e., $\delta \neq 0$). Employing the same procedure as was used in the Section 6.2, the post-critical behavior of the shaft is investigated.

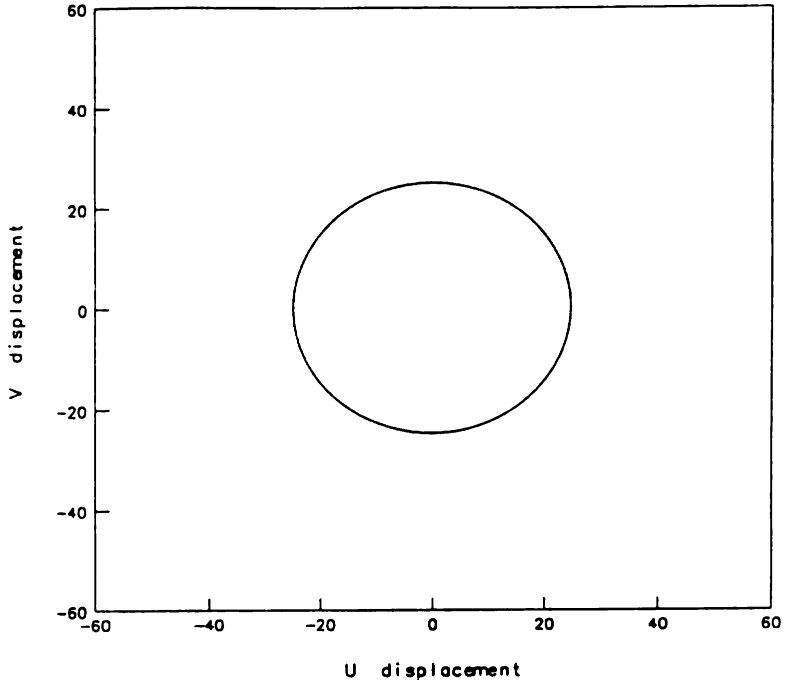

Figure 6.1a Orbit in (U,V) Projection; $\mu_i = 200\pi^2$, $\omega = \overline{\omega}$.

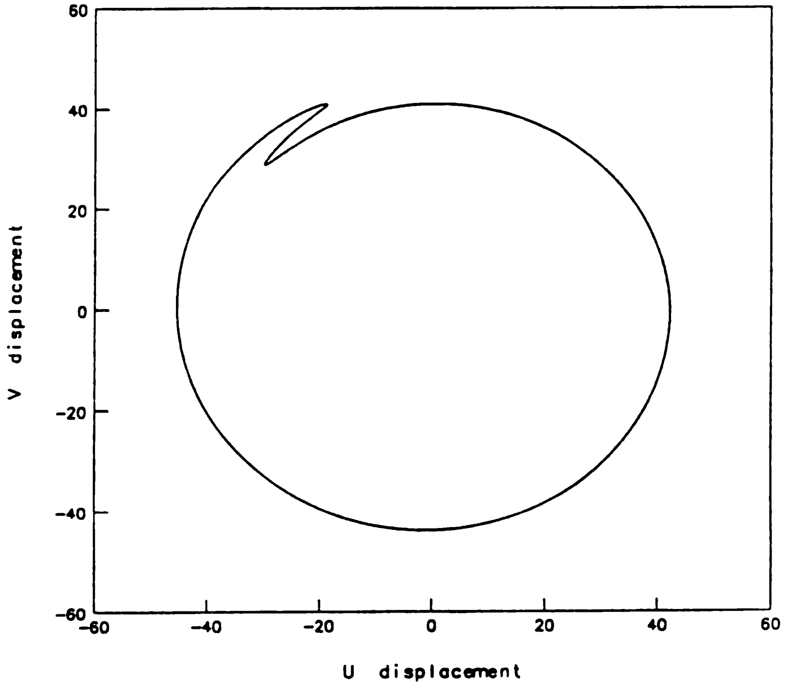

Figure 6.1b Orbit in (U,V) Projection; $\mu_i = 500\pi^2$, $\omega = \overline{\omega}$.

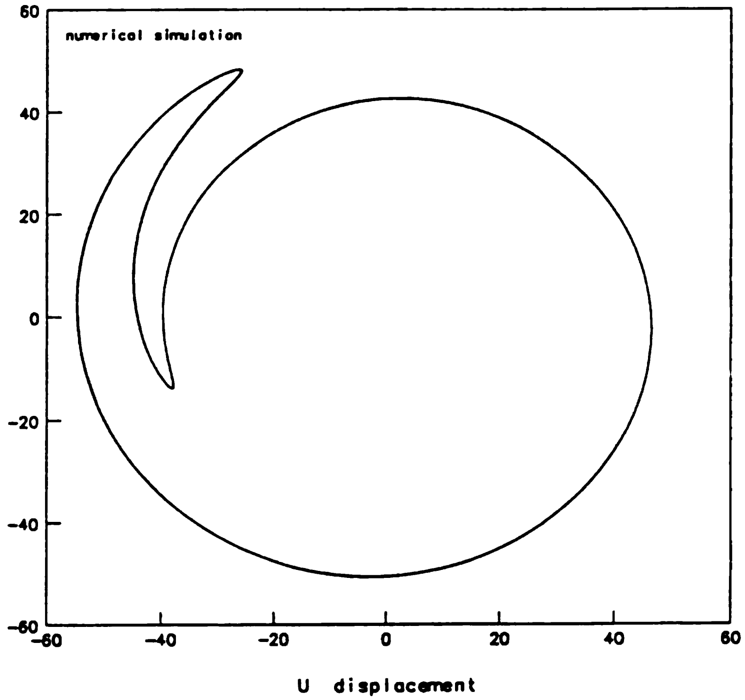

Figure 6.1c Orbit in (U,V) Projection; $\mu_i = 1000\pi^2$, $\omega = \overline{\omega}$.

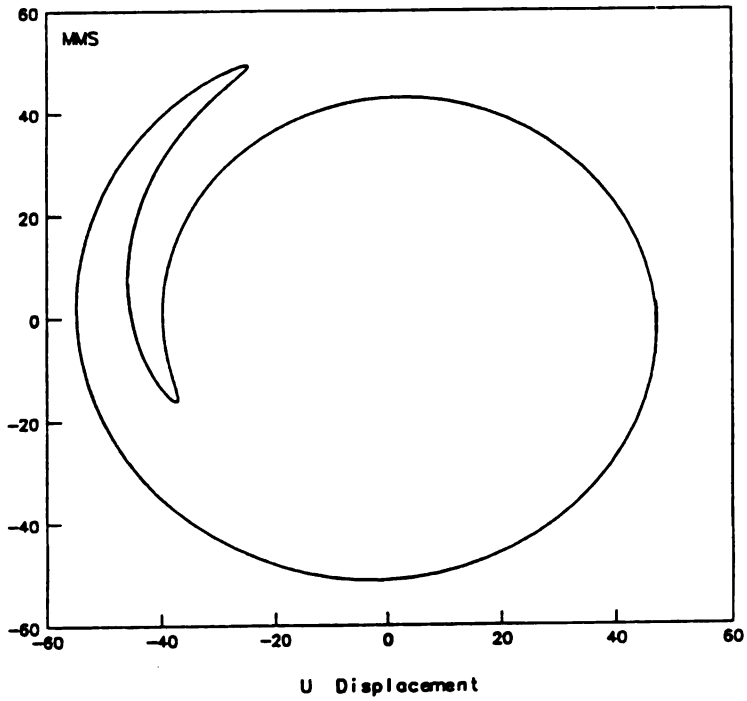

Figure 6.2a Orbit obtained by MMS in (U,V) Projection; $\mu_i = 1000\pi^2$, $\omega = \overline{\omega}$.

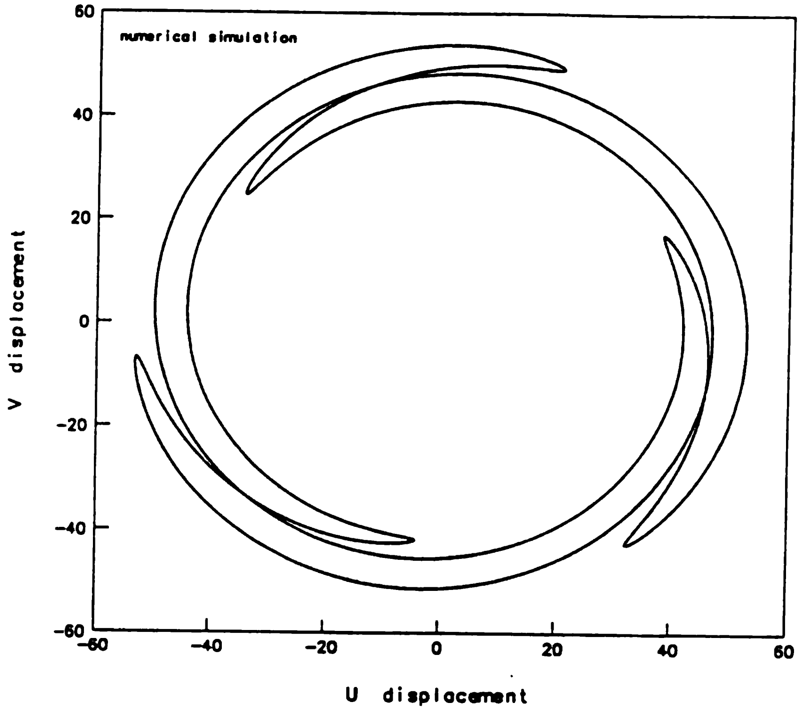

Figure 6.2b Orbit obtained by Numerical Simulation in(U,V) Projection; $\mu_i = 1000\pi^2$, $\omega = \frac{3}{2}\overline{\omega}$.

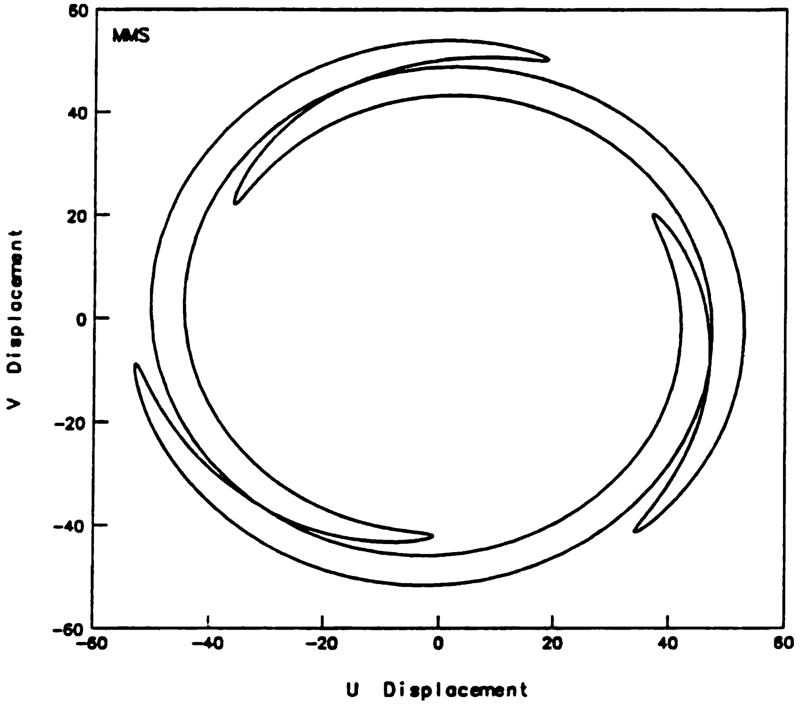

Figure 6.2c Orbit obtained by MMS in (U,V) Projection; $\mu_i = 1000\pi^2$, $\omega = \frac{3}{2}\overline{\omega}$.

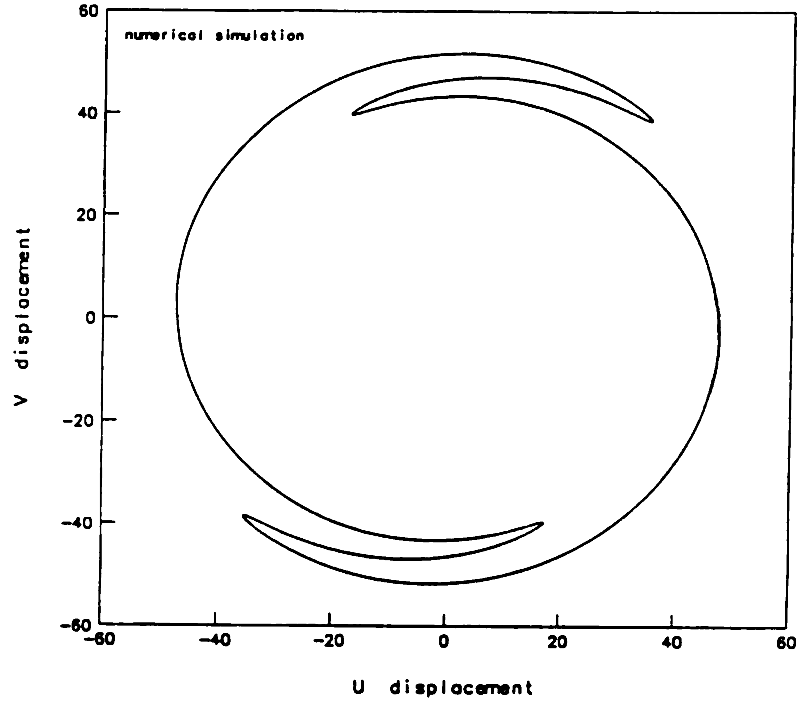

Figure 6.2d Orbit obtained by Numerical Simulation in (U,V) Projection; $\mu_i = 1000\pi^2$, $\omega = 2\bar{\omega}$.

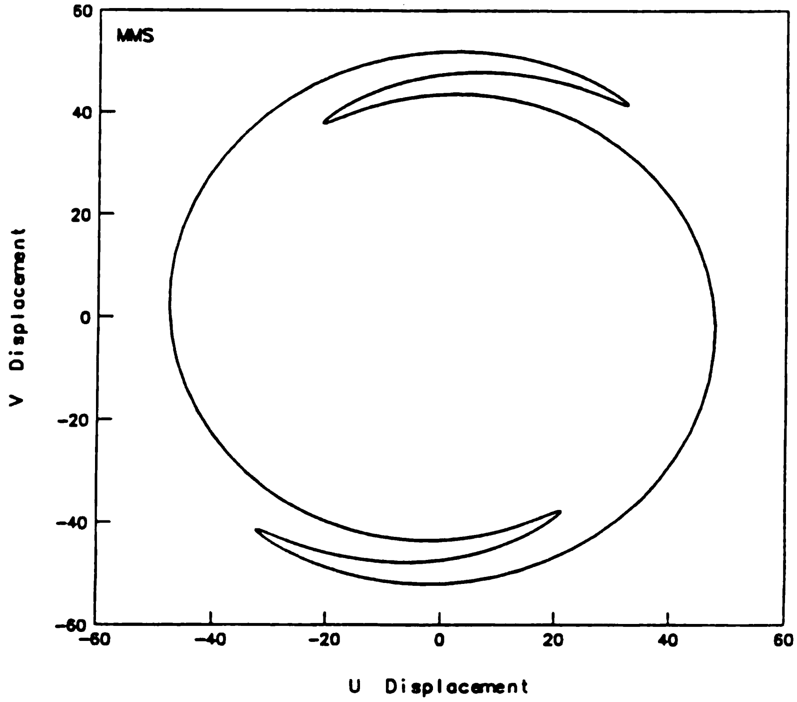

Figure 6.2e Orbit obtained by MMS in (U,V) Projection; $\mu_i = 1000\pi^2$, $\omega = 2\bar{\omega}$.

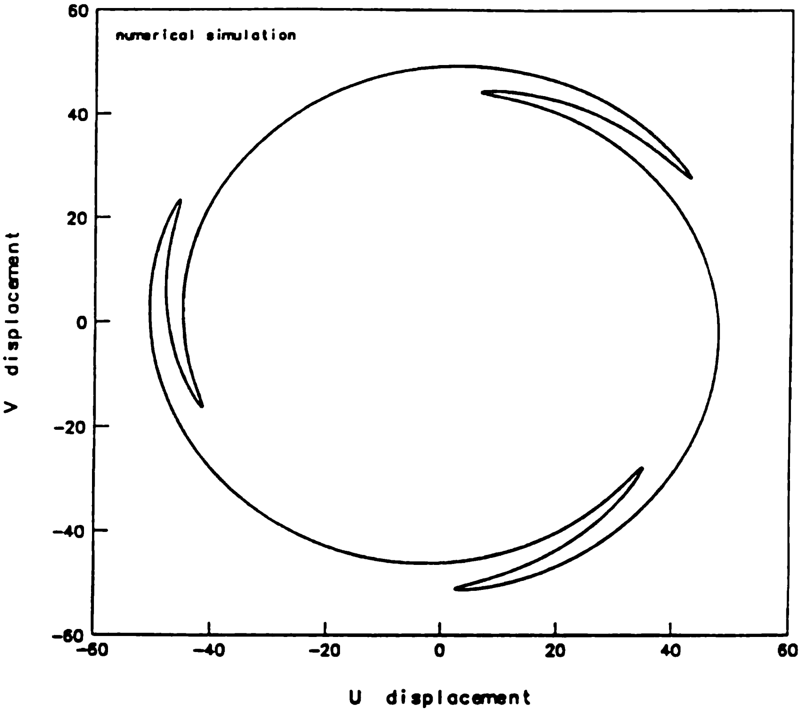

Figure 6.2f Orbit obtained by Numerical Simulation in (U,V) Projection; $\mu_i = 1000\pi^2$, $\omega = 3\bar{\omega}$.

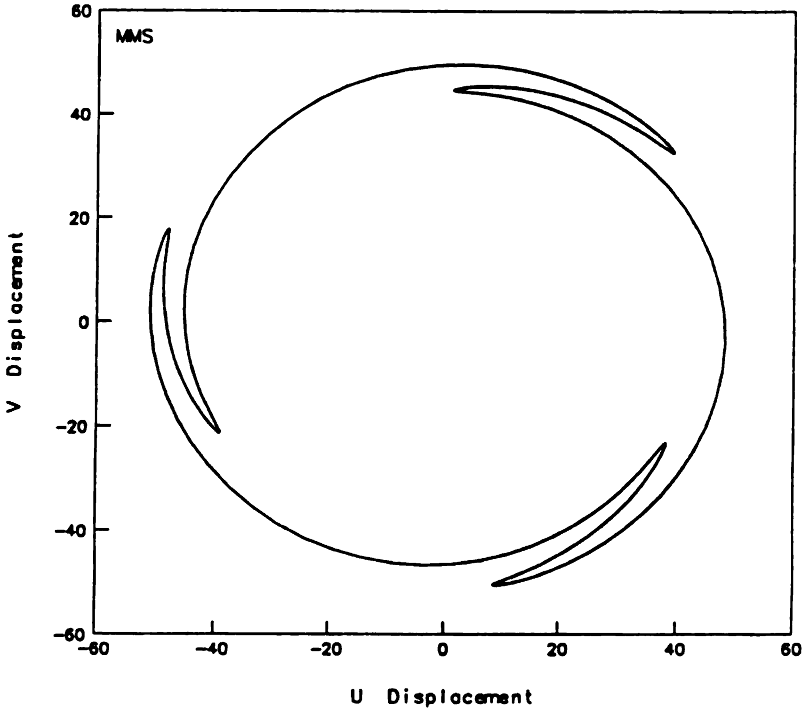

Figure 6.2g Orbit obtained by MMS in (U,V) Projection;$\mu_i = 1000\pi^2$, $\omega = 3\bar{\omega}$.

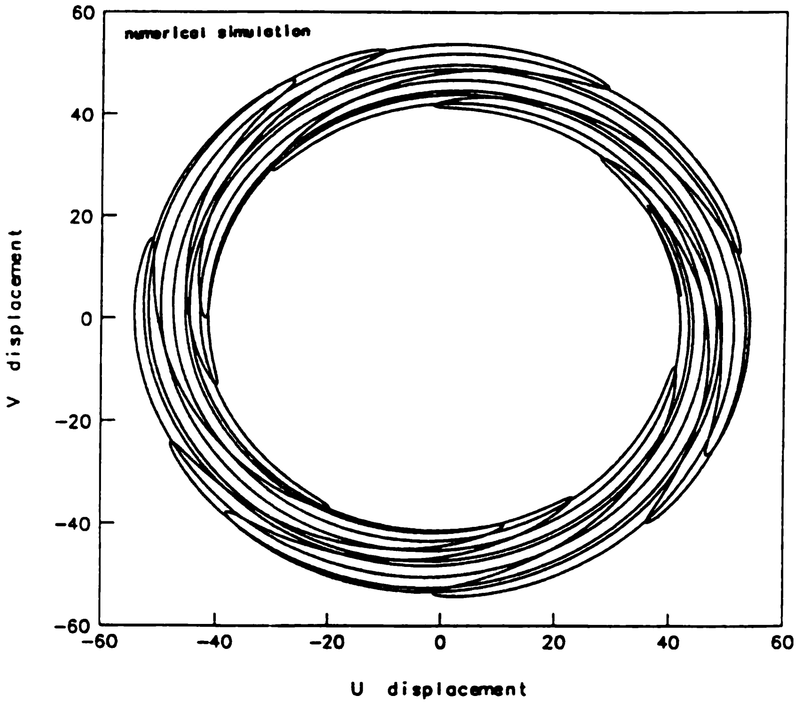

Figure 6.3a Orbit obtained by Numerical Simulation in (U,V) Projection; $\mu_i = 1000\pi^2$, $\omega = \sqrt{2}\,\overline{\omega}$.

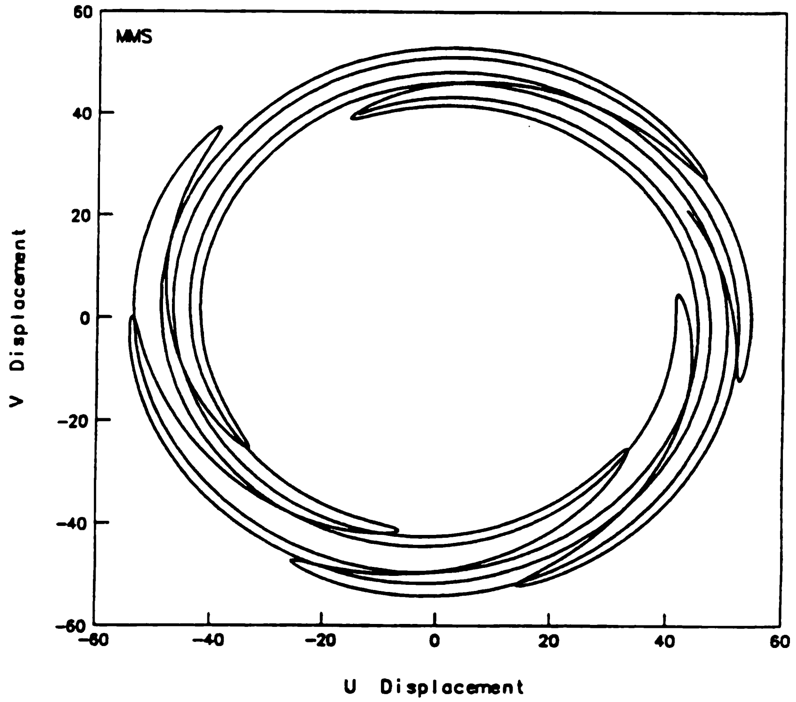

Figure 6.3b Orbit obtained by MMS in (U,V) Projection; $\mu_i = 1000\pi^2$, $\omega = \sqrt{2}\,\overline{\omega}$.

6.3.1 Equilibrium Position

We first transform the equations (2.40) and (2.41) into polar form, by substituting equation (6.1) into equations (2.40) and (2.41) and separating real and imaginary parts to find

$$\begin{aligned}&\ddot{R}+2\varepsilon\mu_e\dot{R}+\varepsilon\mu_i\dot{R}+(\overline{\Omega}_0{}^2-\Omega^2)R-2\Omega R\dot{\phi}-R\dot{\phi}^2\\&\quad+\varepsilon\Omega_0{}^2R^3+\Omega_d R\cos 2\phi=0\end{aligned} \tag{6.34}$$

$$\begin{aligned}&R\ddot{\phi}+R\dot{\Omega}+2\varepsilon\mu_e(\Omega R+R\dot{\phi})+\varepsilon\mu_i R\dot{\phi}+2\Omega\dot{R}\\&\quad+2\dot{R}\dot{\phi}-\Omega_d R\sin 2\phi=0\end{aligned} \tag{6.35}$$

where

$$\overline{\Omega}_0{}^2=\frac{2+\delta}{2}\,\Omega_0{}^2 \tag{6.36}$$

and

$$\Omega_d=\frac{-\delta}{2}\,\Omega_0{}^2. \tag{6.37}$$

Setting $\Omega=\Omega_s$ and all time derivatives in equation (6.34) and (6.35) equal to zero, we find the equations govern the steady-states $\overline{R}$ and $\overline{\phi}$ to be

$$(\overline{\Omega}_0{}^2-\Omega_s{}^2)\overline{R}+\varepsilon\Omega_0{}^2\overline{R}^3=-\Omega_d\overline{R}\cos 2\overline{\phi} \tag{6.38}$$

$$2\varepsilon\mu_e\overline{R}\Omega_s=\Omega_d\overline{R}\sin 2\overline{\phi} \tag{6.39}$$

Three equilibrium positions can be found, either $\overline{R} = 0$ or

$$\overline{R}_{1,2} = \left[\frac{\Omega_s^{\,2} - \overline{\Omega}_0^{\,2} \pm \sqrt{\Omega_d^{\,2} - (2\,\varepsilon\,\mu_e\,\Omega_s)^2}}{\varepsilon\,\Omega_0^{\,2}} \right]^{\frac{1}{2}}, \quad \overline{R}_1 > \overline{R}_2 \tag{6.40}$$

$$\overline{\phi} = \tan^{-1}\left[\frac{-2\,\varepsilon\,\mu_e\,\Omega_s}{\Omega_s^{\,2} - \overline{\Omega}_0^{\,2} + \varepsilon\,\Omega_0^{\,2}\,\overline{R}^2} \right] \tag{6.41}$$

Note that $\overline{R}_{1,2}$ and $\overline{\phi}$ are independent of the value of μ_i.

Again, we can find the values of Ω_s, say $\Omega^*_{1,2}$, where equation (6.40) just begins to generate real, positive values of $\overline{R}$. They are

$$\Omega^*_{1,2} = \left[\overline{\Omega}_0^{\,2} - 2\,\varepsilon^2\,\mu_e^{\,2} \pm \sqrt{(\overline{\Omega}_0^{\,2} - 2\,\varepsilon^2\,\mu_e^{\,2})^2 - (\overline{\Omega}_0^{\,4} - \Omega_d^{\,2})} \right]^{\frac{1}{2}} \text{ and } \quad \Omega^*_1 < \Omega^*_2 \,. \tag{6.42}$$

For $\Omega_s < \Omega^*_1$ only one stable trivial solution exists. For $\Omega^*_1 < \Omega_s < \Omega^*_2$, two solutions exist: the unstable trivial solution and a single stable non-trivial solution. For $\Omega^*_2 < \Omega_s$, there are three solutions: one stable non-trivial solution (i.e., $\overline{R}_1$), one non-trivial solution (i.e., $\overline{R}_2$) and one trivial solution. The stabilities of the latter two depend on μ_i and μ_e (see Ariaratnam [1965] for details). For Ω_s sufficiently close to Ω_0, we only need to consider one stable non-trivial solution (i.e., $\overline{R}_1$).

6.3.2 Coordinate Transformation

Once more, we transfer the coordinates of equations (6.36) and (6.37) such that the new coordinates describe the motion about the buckled position (i.e., $\overline{R} = \overline{R}_1$).

Let the new coordinates be q and φ, such that

$$R = \overline{R} + q \tag{6.43}$$

and

$$\phi = \overline{\phi} + \varphi \tag{6.44}$$

Substituting equations (6.43) and (6.44) into equations (6.36) and (6.37), we obtain

$$\begin{aligned}
&\ddot{q} + \varepsilon(2\mu_e + \Omega_0{}^2\mu_i)\dot{q} - 2\Omega_s(q+\overline{R})\dot{\varphi} - (q+\overline{R})\dot{\varphi}^2 \\
&\quad + 2\left[\Omega_s{}^2 - \overline{\Omega}_0{}^2 + \sqrt{\Omega_d{}^2 - (2\varepsilon\mu_e\Omega_s)^2}\,\right]q + \varepsilon\,\Omega_0{}^2 q^2(q+3\overline{R}) \\
&\quad + \Omega_d(q+\overline{R})\left[\cos 2\overline{\phi}\,(-\frac{(2\varphi)^2}{2} + \cdots\cdots) - \sin 2\overline{\phi}\,(2\varphi - \frac{(2\varphi)^3}{3} + \cdots\cdots)\right] \\
&\quad = 2\varepsilon\Omega_A\Omega_s(q+\overline{R})\sin\omega\tau + 2\varepsilon\,\Omega_A\dot{\varphi}(q+\overline{R})\sin\omega\tau + \varepsilon^2\,\Omega_A{}^2(q+\overline{R})\sin\omega\tau^2
\end{aligned} \tag{6.45}$$

$$\begin{aligned}
&(q+\overline{R})\ddot{\varphi} + 2\Omega_s\dot{q} + 2\dot{\varphi}\,\dot{q} + \varepsilon(2\mu_e + \mu_i)(q+\overline{R})\dot{\varphi} - 2\left[\Omega_d{}^2 - (2\varepsilon\mu_e\Omega_s)^2\right]^{\frac{1}{2}}(\overline{R}+q)\varphi \\
&\quad + \Omega_d(q+\overline{R})\left[\sin 2\overline{\phi}\,(-\frac{(2\varphi)^2}{2} + \cdots\cdots) + \cos 2\overline{\phi}\,(-\frac{(2\varphi)^3}{3} + \cdots\cdots)\right] = \\
&\quad - \varepsilon\,\Omega_A\,\omega(q+\overline{R})\cos\omega\tau - 2\varepsilon\,\Omega_A\dot{q}\,\sin\omega\tau - 2\varepsilon^2\mu_e\Omega_A(q+\overline{R})\sin\omega\tau
\end{aligned} \tag{6.46}$$

6.3.3 Approximate Solutions

Assume a first-order expansion in the form

$$q(\tau;\varepsilon) = \varepsilon\, q_1(T_0,T_1) + \varepsilon^2 q_2(T_0,T_1) + \varepsilon^3 q_3(T_0,T_1) + \cdots\cdots \tag{6.47}$$

$$\varphi(\tau;\varepsilon) = \varepsilon\, \varphi_1(T_0,T_1) + \varepsilon^2 \varphi_2(T_0,T_1) + \varepsilon^3 \varphi_3(T_0,T_1) + \cdots\cdots \tag{6.48}$$

Substituting equations (6.47) and (6.48) into equations (6.45) and (6.46) and equating coefficients of like powers of ε, we obtain

ε^1:

$$\begin{aligned} &D_0{}^2 q_1 - 2\,\Omega_s \bar{R}\, D_0 \varphi_1 + 2\Big[\,\Omega_s{}^2 - \bar{\Omega}_0{}^2 + \sqrt{\Omega_d{}^2 - (2\varepsilon\mu_e\Omega_s)^2}\,\Big] q_1 \\ &\quad = 2\,\Omega_A\,\Omega_s\,\bar{R}\,\sin\omega\tau \end{aligned} \tag{6.49}$$

$$\bar{R}\, D_0{}^2 \varphi_1 + 2\,\Omega_s D_0 q_1 + 2\left[\Omega_d{}^2 - (2\varepsilon\mu_e\Omega_s)^2\right]^{\frac{1}{2}}\ \bar{R}\varphi_1 = -\,\Omega_A \bar{R}\,\omega\cos\omega\tau \tag{6.50}$$

The solutions of equations (6.49) and (6.50) can be expressed in the form

$$q_1 = q_{1h} + q_{1p} \tag{6.51}$$

$$\bar{R}\varphi_1 = p_1 = p_{1h} + p_{1p} \tag{6.52}$$

where

$$q_{1h} = A_1(T_1)\exp(\,i\omega_1 T_0) + A_2(T_1)\exp(\,i\omega_2 T_0) + cc$$

$$p_{1h} = \Lambda_1 A_1(T_1) \exp(i\omega_1 T_0) + \Lambda_2 A_2(T_1) \exp(i\omega_2 T_0) + cc$$

$$q_{1p} = A_{1p} \sin \omega\tau$$

$$p_{1p} = A_{2p} \cos \omega\tau$$

and

$$\Lambda_1 = -\frac{2\,\Omega_s\,\omega_1}{2\left[\Omega_d^{\,2} - 2\,(\varepsilon\mu_e\Omega_s)^2\right]^{\frac{1}{2}} - \omega_1^{\,2}}$$

$$\Lambda_2 = -\frac{2\,\Omega_s\,\omega_2}{2\left[\Omega_d^{\,2} - 2\,(\varepsilon\mu_e\Omega_s)^2\right]^{\frac{1}{2}} - \omega_2^{\,2}}$$

$$\omega_1 = \left[\frac{6\,\Omega_s^{\,2} + 4\left[\Omega_d^{\,2} - (2\,\varepsilon\mu_e\Omega_s)^2\right]^{\frac{1}{2}}(1 - 8\,\Omega_s^{\,2}) - 2\overline{\Omega}_0^{\,2} - (6\,\Omega_s^{\,2} - 2\,\overline{\Omega}_0^{\,2})^2}{2}\right]^{\frac{1}{2}}$$

$$\omega_2 = \left[\frac{6\,\Omega_s^{\,2} + 4\left[\Omega_d^{\,2} - (2\,\varepsilon\mu_e\Omega_s)^2\right]^{\frac{1}{2}}(1 + 8\,\Omega_s^{\,2}) - 2\overline{\Omega}_0^{\,2} + (6\,\Omega_s^{\,2} - 2\,\overline{\Omega}_0^{\,2})^2}{2}\right]^{\frac{1}{2}}$$

A_{1p} and A_{2p} are depend on Ω_s, Ω_A, ω, Ω_d, $\overline{\Omega}_0$, $\overline{R}$ and μ_e and cc stands for the complex conjugate of the preceding terms.

Note that A_1 and A_2 are arbitrary complex functions of T_1 which can be determined at the next level of approximation. However, due to the complexity of these equations it was found impossible to proceed with analysis beyond this point. Instead, we employed numerical simulation techniques to explore the bifurcated and chaotic motions of this case.

6.3.4 Numerical Results

Equations (2.40) and (2.41) were simulated on a digital computer. The parameter values used, unless otherwise stated, were:

$$\Omega_s = 9.9,\ \delta = 1.0,\ \mu_e = 256,\ \mu_i = 200\pi^2 \text{ and } \varepsilon = (\tfrac{1}{240})^2.$$

Before investigating the shaft's response to a parametric excitation, we calculate the buckled positions of the unperturbed case (i.e., $\varepsilon\Omega_A = 0$). From equation (6.1) we can express these positions as

$$\overline{U} = \overline{R}_1 \cos\overline{\phi} \tag{6.53}$$

and

$$\overline{V} = \overline{R}_1 \sin\overline{\phi} \tag{6.54}$$

Substituting the above parameter values into equations (6.40), (6.41), (6.53) and (6.54), we find $\overline{U} = \pm 18.8489$ and $\overline{V} = \mp 0.017$. Obviously, there is a big difference between $\overline{U}$ and $\overline{V}$. Hence, we next try another value of $\delta = 0.01$ (i.e., the shaft has very slight asymmetry) and we find $\overline{U} = \pm 18.6468$ and $\overline{V} = \mp 1.69855$. The value of $\overline{U}$ is still much larger than the value of $\overline{V}$. This suggests that, for an unsymmetrical, buckled shaft, its post-buckled behavior may be similar to that of a rotating buckled beam. We will see that this is the case in some of the numerical simulations to follow.

We now use numerical integration to find the trajectory of the free response of the rotating, unsymmetrical shaft by setting $\varepsilon\Omega_A = 0$ in equations (2.40) and (2.41). Figures 6.4a-b show trajectories of the free response depicted in a (U,V) projection for two different μ_i values with $\delta = 0.5$. In both cases the orbits approach the right hand buckled position. A different choice of the initial conditions would cause the trajectory to go to the other buckled position. Comparing Figure 6.4a with Figure 6.4b, we observe that the rate at which the trajectory of the free response approaches the buckled position depends on μ_i.

We will next consider $\varepsilon\Omega_A \neq 0$ and show that the shaft will vibrate about one of the buckled positions or encompass the two buckled positions. The following sub-sections will consider the cases of $\omega \approx 2\omega_1$ and $\omega \approx \omega_1$.

6.3.4.1 The Case of $\omega \approx 2\omega_1$

We first use numerical simulation to observe the trend of the frequency response curve. Equations (2.40) and (2.41) are simulated on a digital computer for fixed $\Omega_s = 9.9$, $\Omega_A = 5760$, $\mu_e = 256$, $\mu_i = 200$, $\delta = 1.0$, $\varepsilon = (\frac{1}{240})^2$ (and hence $\omega_1 = 0.4885$) and ω is varied. The results are depicted in a (U,V) projection in Figure 6.5. From this figure we observe that the magnitudes of the displacement U and V increase as ω decreases. That means the nonlinearities are of a softening type.

Next, instead of varying ω, we present the effect of varying Ω_A on the shaft's response with $\omega = 0.947 \approx 2\omega_1$. The results of the numerical simulation are shown in Figures 6.6 and 6.7 and are summarized in Table 6.1.

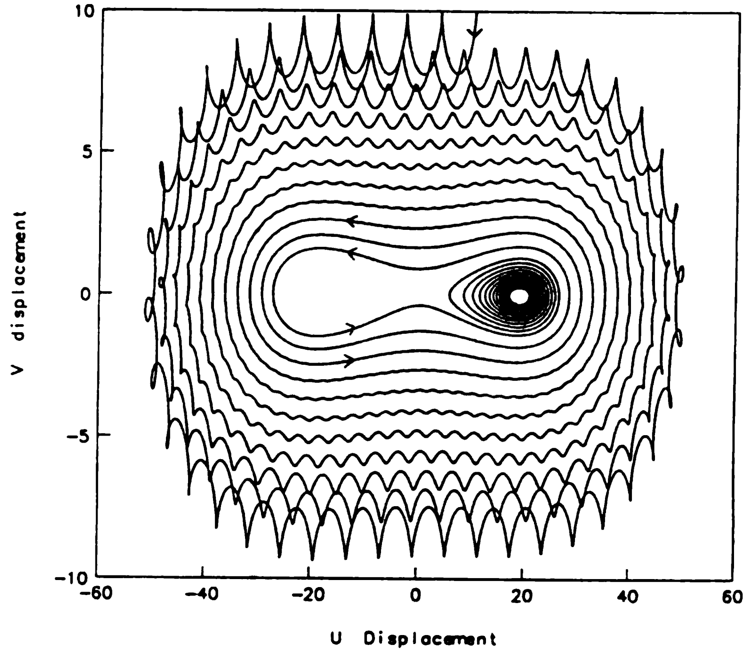

Figure 6.4a Trajectory of the Free Response in (U,V) Projection; $\mu_i = 20\pi^2$, $\delta = 0.5$.

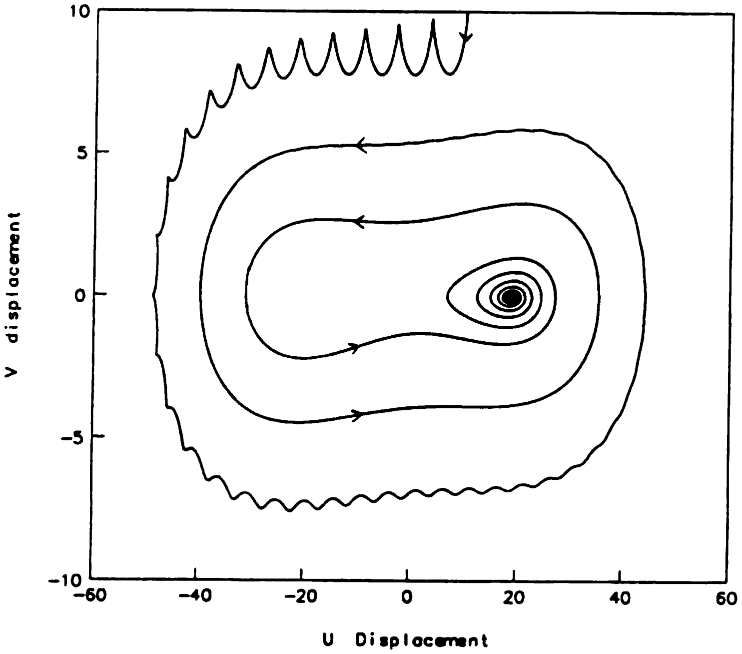

Figure 6.4b Trajectory of the Free Response in (U,V) Projection; $\mu_i = 200\pi^2$, $\delta = 0.5$.

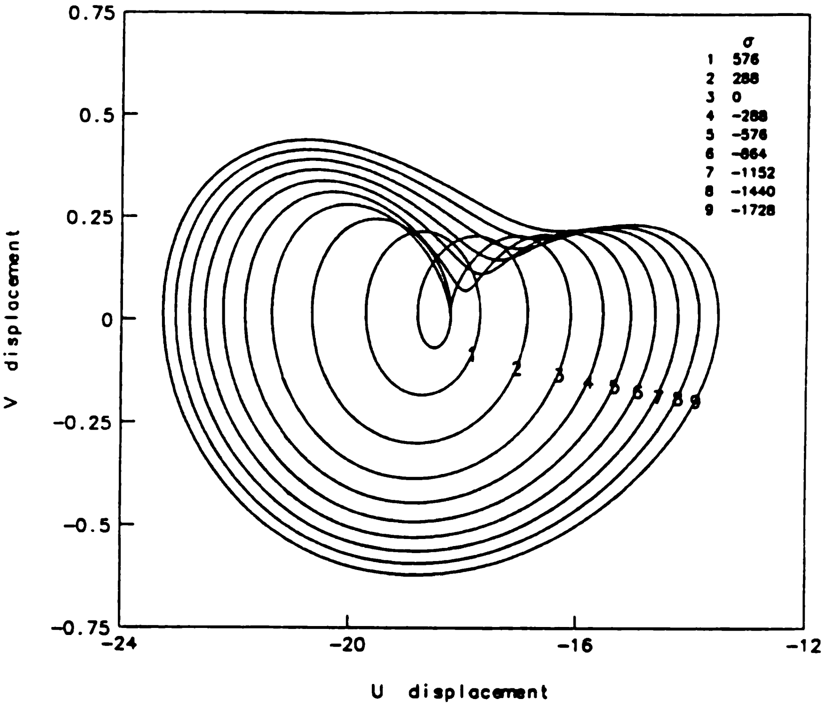

Figure 6.5 Orbit obtained by Numerical Simulation in (U,V) Projection; $\omega = 2\,\omega_1 + \varepsilon\,\sigma$, σ from 576 to -1728.

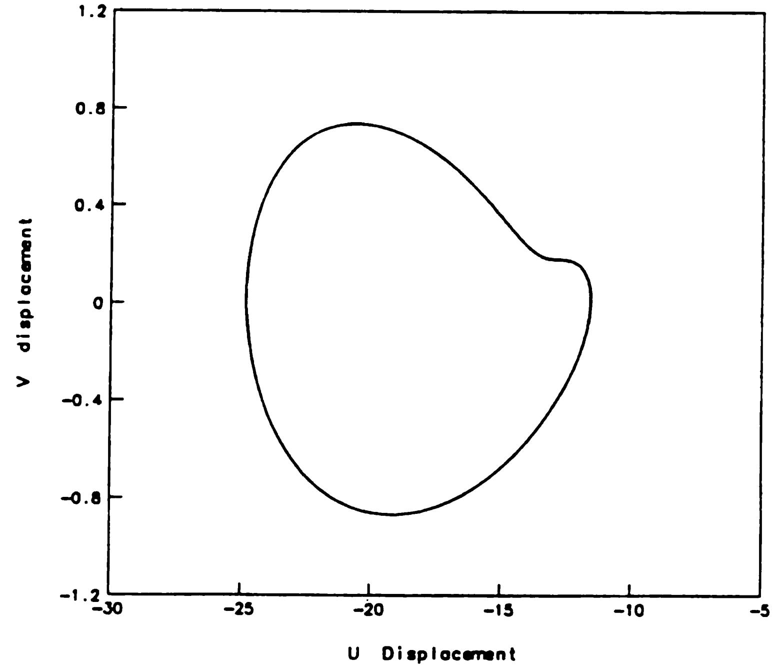

Figure 6.6a Orbit of Period 2 Motion in (U,V) Projection; $\Omega_A = 864$, $\omega = 0.947$.

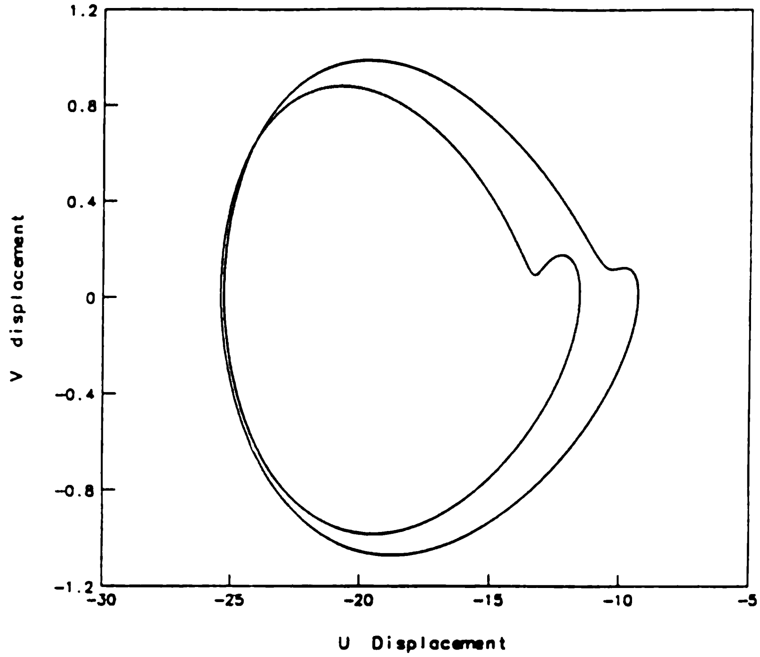

Figure 6.6b Orbit of Period 4 Motion in (U,V) Projection; Ω_A =1296, ω =0.947.

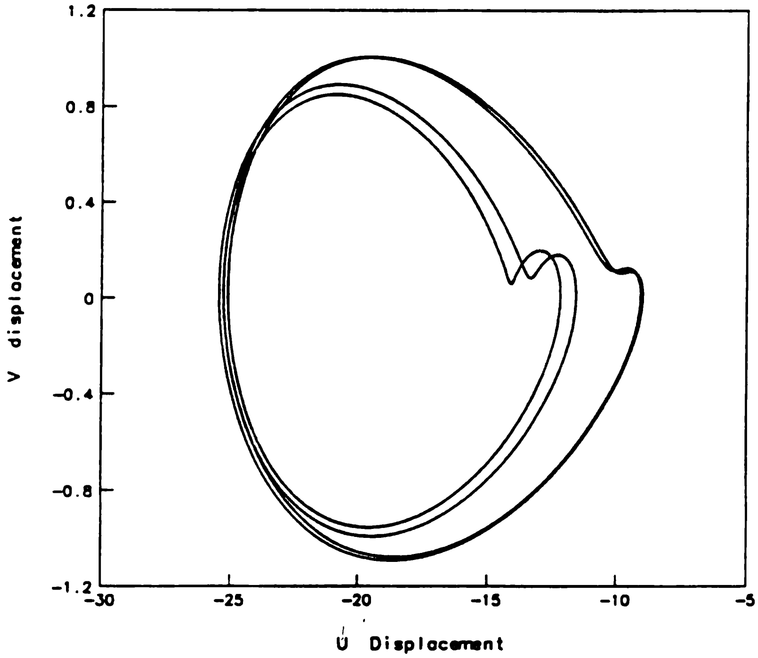

Figure 6.6c Orbit of Period 8 Motion in (U,V) Projection; Ω_A = 1340, ω =0.947.

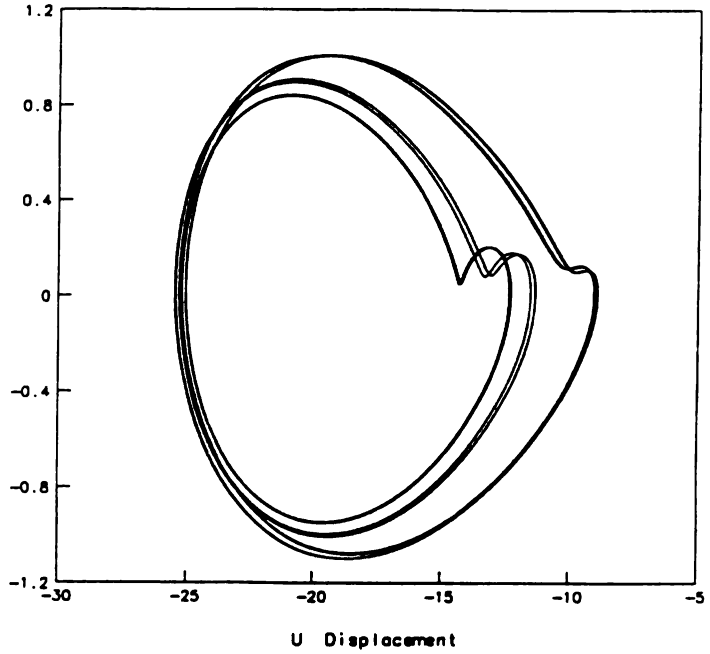

Figure 6.6d Orbit of Period 16 Motion in (U,V) Projection; $\Omega_A = 1350$, $\omega = 0.947$.

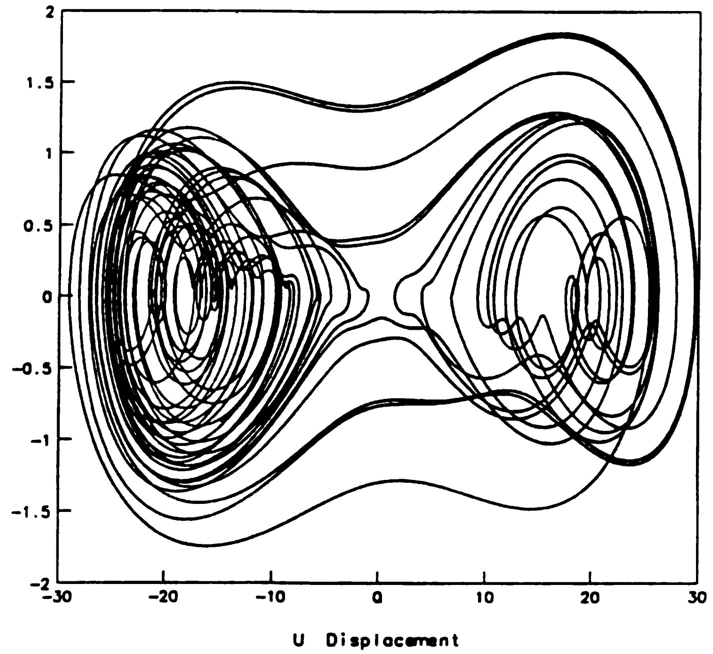

Figure 6.7 Orbit of Chaotic Motion in (U,V) Projection; $\Omega_A = 1440$, $\omega = 0.947$.

Table 6.1 Summary of Bifurcated and Chaotic Motions for $\omega = 0.947$.

Ω_A	Figure	Type of Motion	Initial Conditions $(U(0),\dot{U}(0); V(0),\dot{V}(0))$
864	Figure 6.6a	2T	(1.0, 0.0; 1.0, 0.0)
1296	Figure 6.6b	4T	(1.0, 0.0; 1.0, 0.0)
1340	Figure 6.6c	8T	(1.0, 0.0; 1.0, 0.0)
1350	Figure 6.6d	16T	(1.0, 0.0; 1.0, 0.0)
1440	Figure 6.7	chaotic	(1.0, 0.0; 1.0, 0.0)

Figures 6.6a-d show a period doubling bifurcation depicted on a (U,V) projection. This series of bifurcations, if continued, would lead to chaos. The simulation indicates that at $\Omega_A = 1440$, a chaotic motion occurs as shown in Figure 6.7. In this case it is convenient to describe the response of the shaft by projecting the trajectories on to the $(U,\dot{U})$ and $(V,\dot{V})$ planes and sample the values once per forcing period (as in a Poincare map). Figures 6.8a-b depict the points in the $(U,\dot{U})$ and $(V,\dot{V})$ planes corresponding to the motion shown in Figure 6.7. Note that Figure 6.8a is similar to Figure 4.24h in Chapter 4, and the motion in the U direction dominates the shaft's response.

6.3.4.2 The Case of $\omega \approx \omega_1$

In this sub-section, we consider the case of $\omega = \omega_1 = 0.4885$. A period doubling bifurcation can occur as one varies the value of Ω_A. The results of numerical simulation are summarized in Table 6.2 and plotted in Figures 6.9-13.

For a small value of Ω_A, the shaft vibrates about one of the buckled positions. Figure 6.9 shows the limit-cycle attractor around the left buckled position with $\Omega_A = 288$.

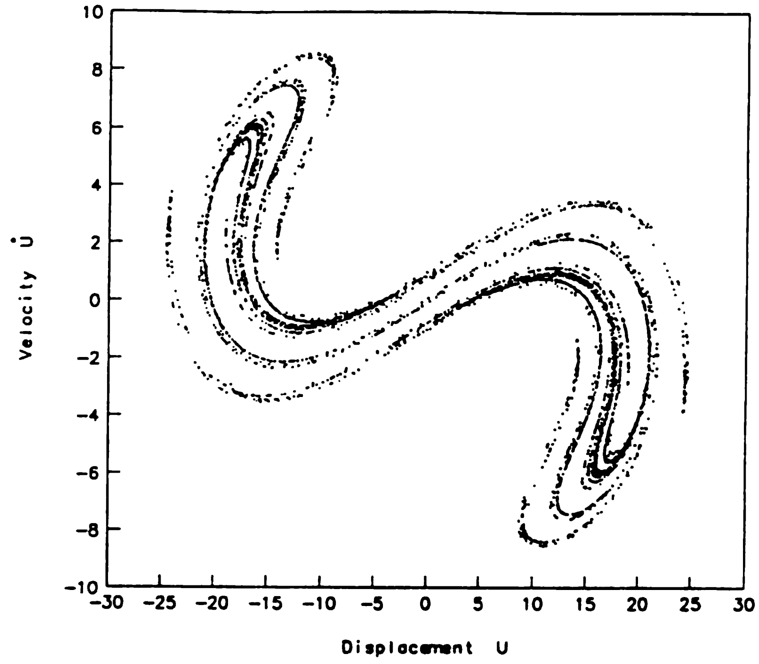

Figure 6.8a Map of Figure 6.7 in $(U,\dot{U})$ Projection; $\Omega_A = 1440$, $\omega = 0.947$.

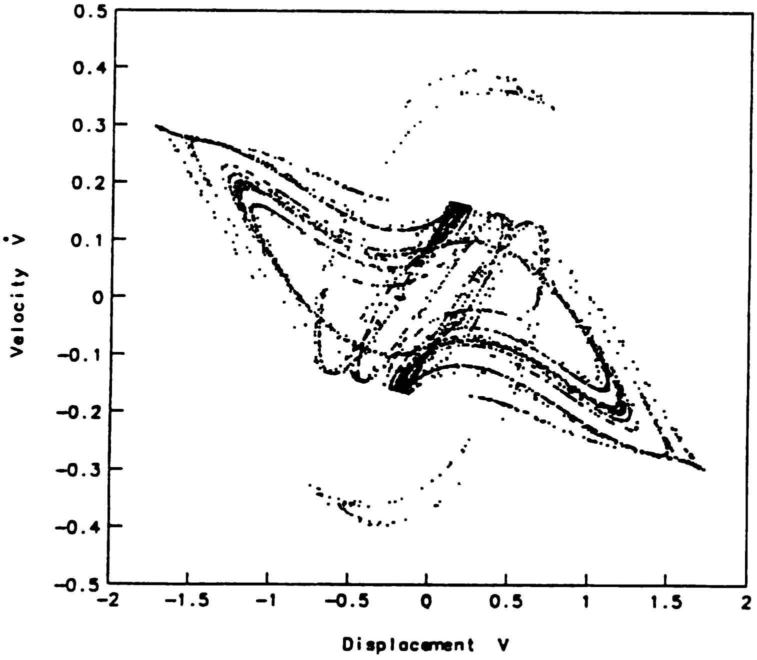

Figure 6.8b Map of Figure 6.7 in $(V,\dot{V})$ Projection; $\Omega_A = 1440$, $\omega = 0.947$.

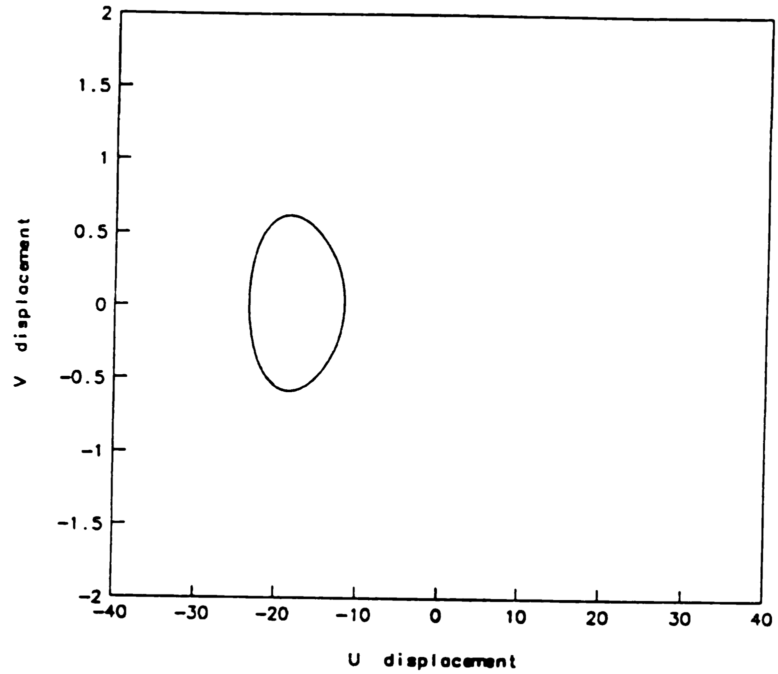

Figure 6.9 Orbit of Period 1 Motion in (U,V) Projection; $\Omega_A = 288$, $\omega = 0.4885$.

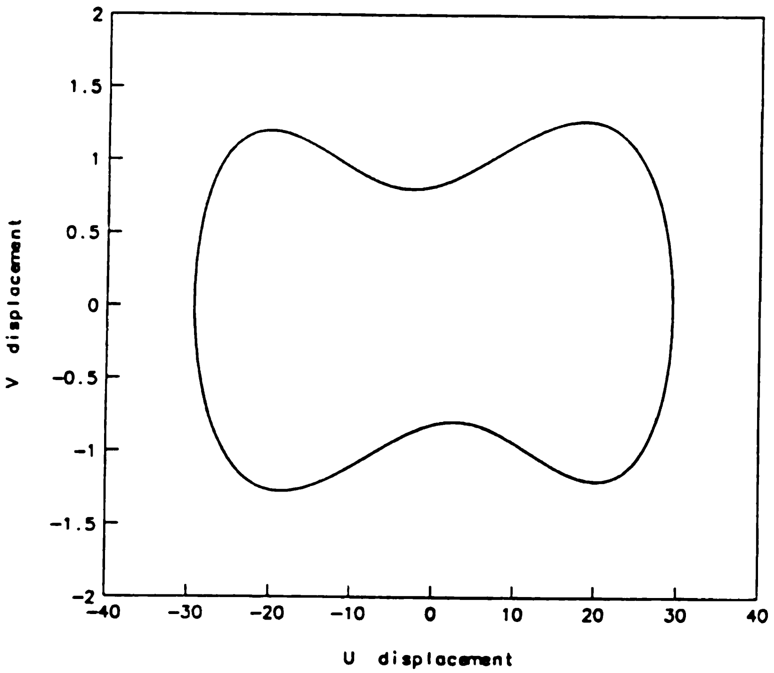

Figure 6.10a Orbit of Period 2 Motion in (U,V) Projection; $\Omega_A = 576$, $\omega = 0.4885$.

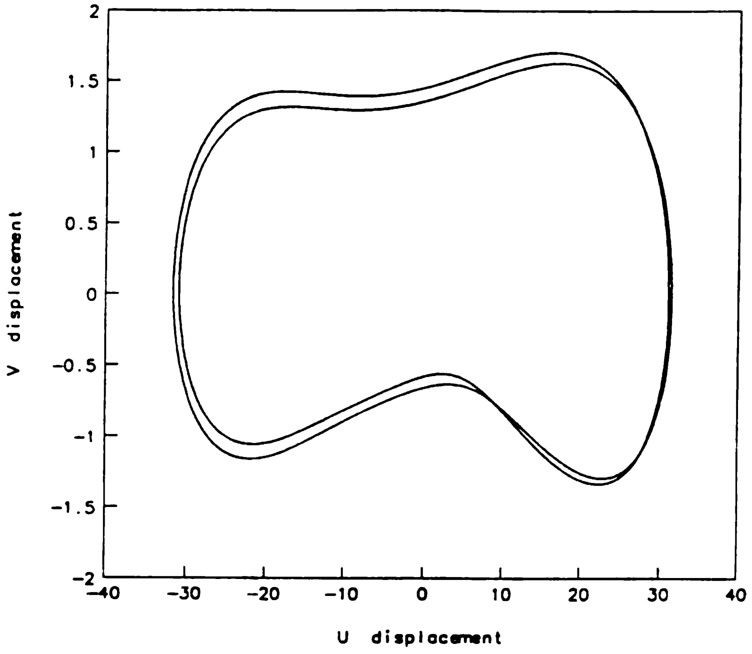

Figure 6.10b Orbit of Period 4 Motion in (U,V) Projection; $\Omega_A = 1100$, $\omega = 0.4885$.

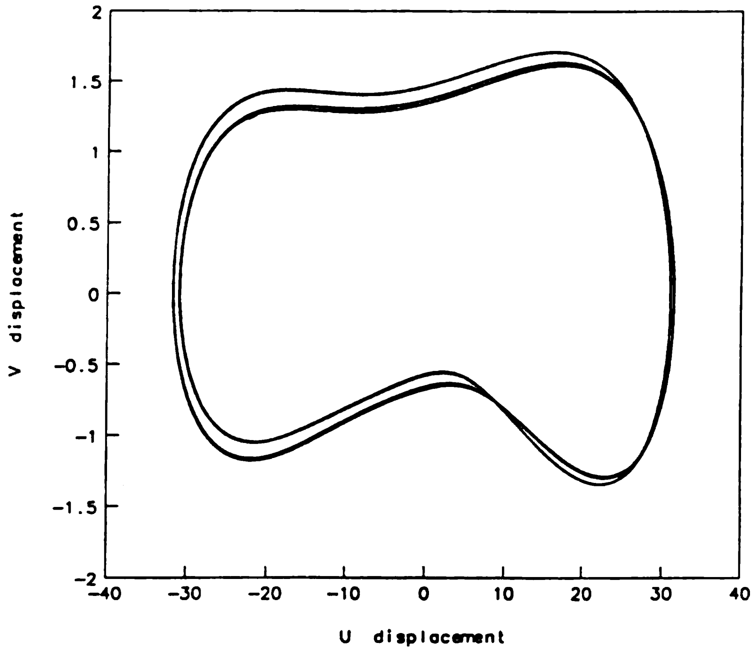

Figure 6.10c Orbit of Period 8 Motion in (U,V) Projection; $\Omega_A = 1110$, $\omega = 0.4885$.

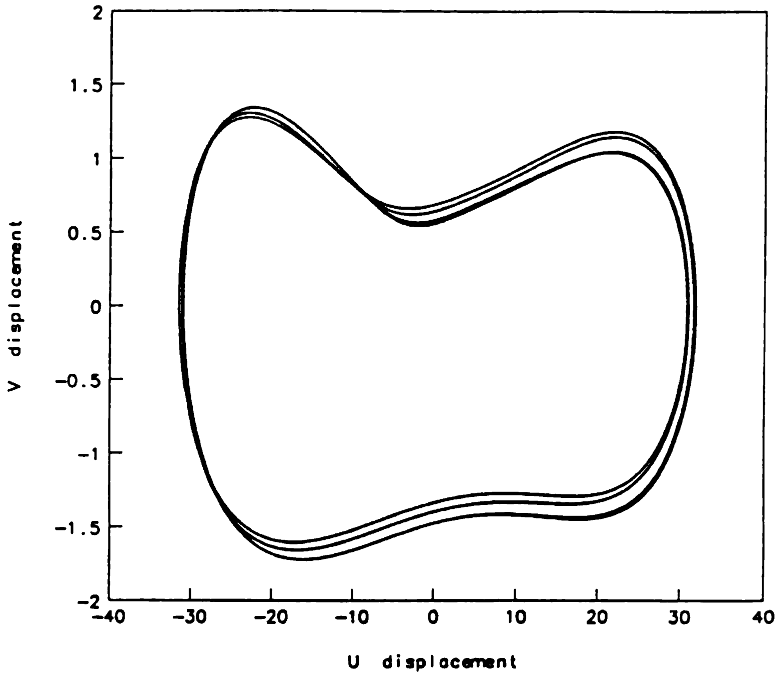

Figure 6.10d Orbit of Period 16 Motion in (U,V) Projection; $\Omega_A = 1116$, $\omega = 0.4885$.

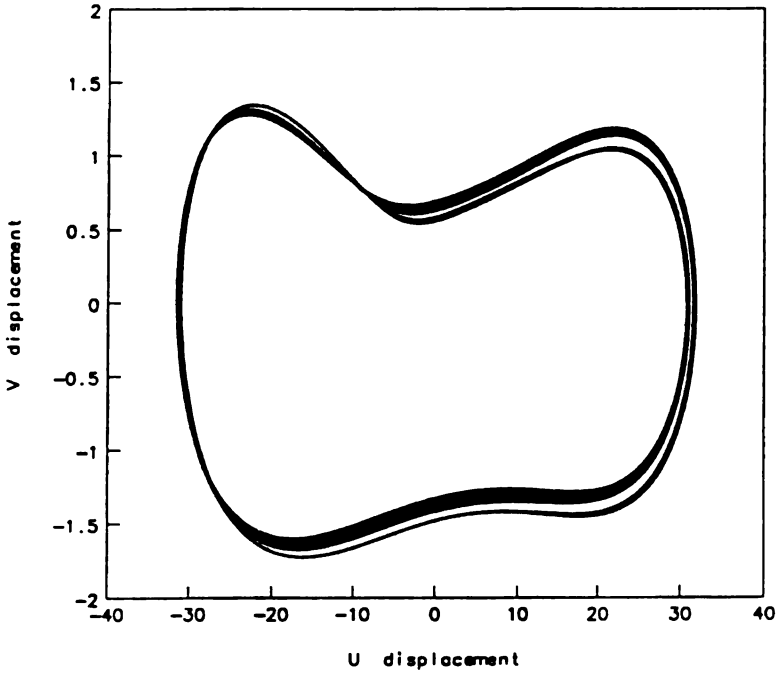

Figure 6.11 Orbit of Almost Periodic Motion in (U,V) Projection; $\Omega_A = 1120$, $\omega = 0.4885$.

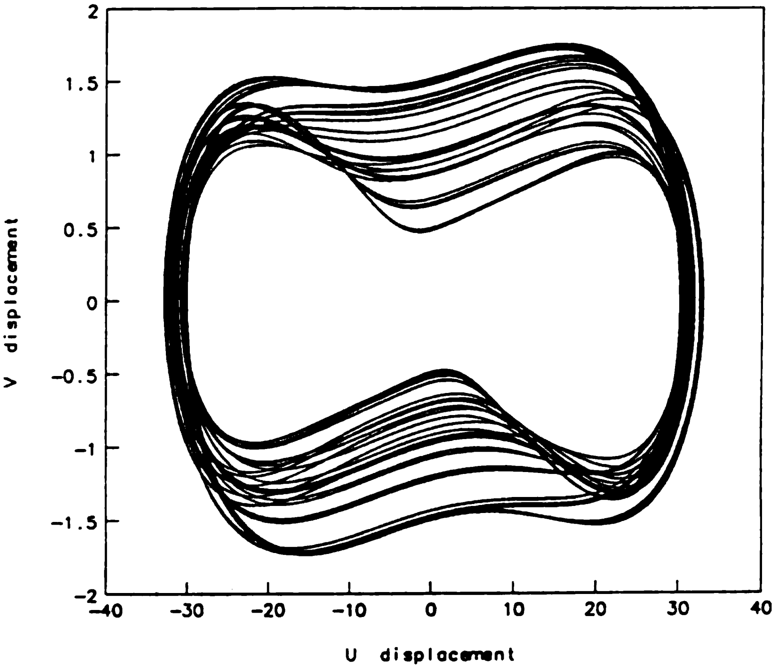

Figure 6.12 Orbit of Chaotic Motion in (U,V) Projection; $\Omega_A = 1152$, $\omega = 0.4885$.

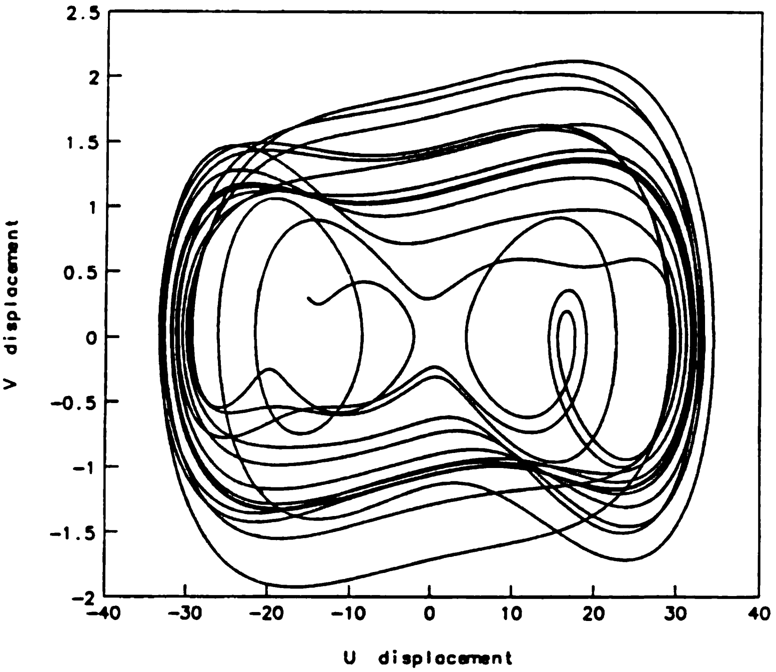

Figure 6.13 Orbit of Chaotic Motion in (U,V) Projection; $\Omega_A = 1440$, $\omega = 0.4885$.

Table 6.2 Summary of Bifurcated and Chaotic Motions for $\omega = 0.4885$.

Ω_A	Figure	Type of Motion	Initial Conditions $(U(0),\dot{U}(0); V(0),\dot{V}(0))$
288	Figure 6.9	1T	(10.0, 0.0; 20.0, 0.0)
576	Figure 6.10a	2T	(10.0, 0.0; 20.0, 0.0)
1100	Figure 6.10b	4T	(10.0, 0.0; 20.0, 0.0)
1110	Figure 6.10c	8T	(10.0, 0.0; 20.0, 0.0)
1116	Figure 6.10d	16T	(10.0, 0.0; 20.0, 0.0)
1120	Figure 6.11	almost periodic	(10.0, 0.0; 20.0, 0.0)
1152	Figure 6.12	chaotic	(10.0, 0.0; 20.0, 0.0)
1440	Figure 6.13	chaotic	(10.0, 0.0; 20.0, 0.0)

However, for larger values of Ω_A, this attractor becomes unstable and gives rise to yet another new, larger limit-cycle attractor that encircles both buckled positions, as shown in Figure 6.10a. As we continue to increase the value of the Ω_A, this large outer trajectory bifurcates, as shown in Figures 6.10b-d. This cascading of period-doubling bifurcations will ultimately lead to a chaotic motion. However, before chaos is observed an almost periodic motion is found for a $\Omega_A = 1120$, see Figure 6.11 which represents approximately 100 forcing periods. The trajectories of the chaotic motion associated with $\Omega_A = 1152$ and 1440 are shown in Figures 6.12 and 6.13, respectively. Clearly the chaos in Figure 6.12 is not as well developed as in Figure 6.13, but it is certainly more than simple quasi-periodic motion. Again, the trajectories in Figures 6.12 and 6.13 are projected on to the $(U,\dot{U})$ and $(V,\dot{V})$ planes and sampled once per forcing period. The results are shown in Figures 6.14a-b and 6.15a-b, respectively. Note that the points in Figures 6.14a-b appear to lie on a set of curves. However, the points in Figures 6.15a-b reveal a fractal-like pattern (i.e., strange attractor) and Figure 6.15a is similar to Figure 4.27f of the rotating beam case.

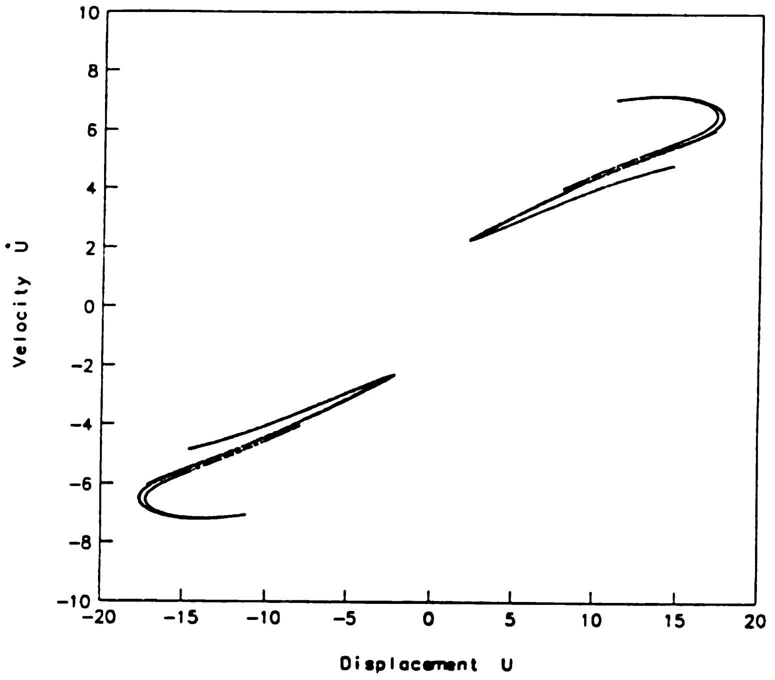

Figure 6.14a Map of Figure 6.12 in $(U,\dot{U})$ Projection; $\Omega_A = 1152$ $\omega = 0.4885$.

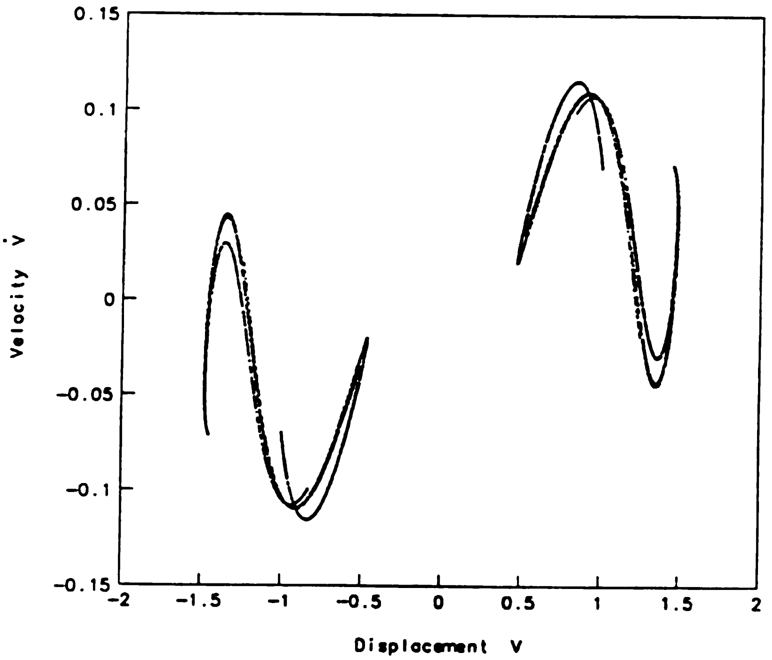

Figure 6.14b Map of Figure 6.12 in $(V,\dot{V})$ Projection; $\Omega_A = 1152$, $\omega = 0.4885$.

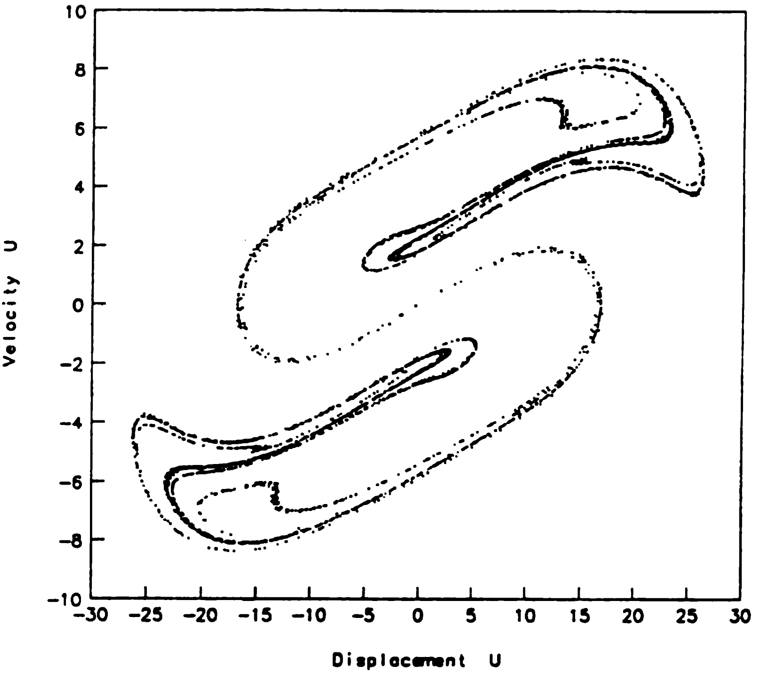

Figure 6.15a Map of Figure 6.13 in $(U,\dot{U})$ Projection;$\Omega_A = 1440$, $\omega = 0.4885$.

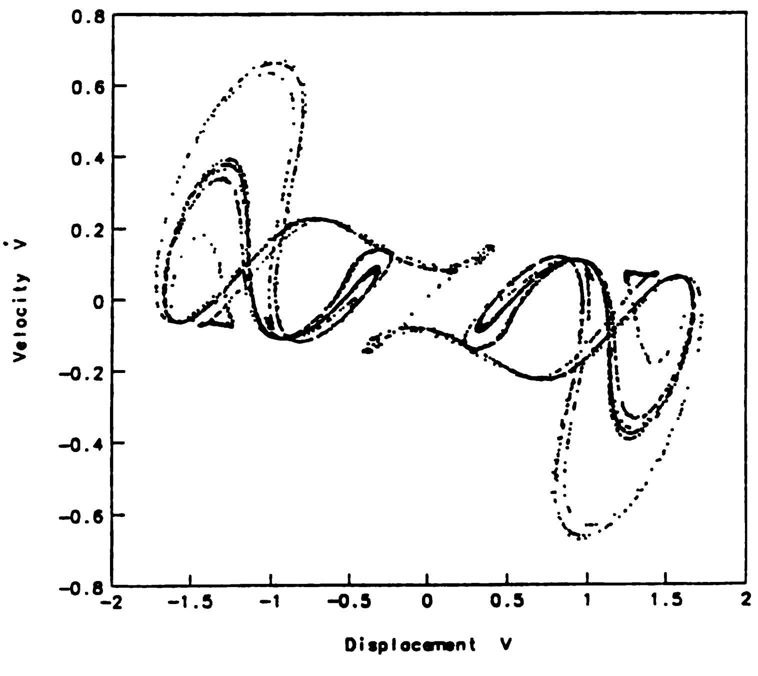

Figure 6.15b Map of Figure 6.13 in $(V,\dot{V})$ Projection;$\Omega_A = 1440$, $\omega = 0.4885$.

6.4 Summary of the Chapter

In Chapter 6, we have investigated the post-critical behavior of a perfectly balanced shaft by applying the method of the multiple scales and employing numerical simulations. When the rotational speed of a symmetrical shaft is over the first critical speed, the shaft will whirl with a circular orbit at a speed different from the rotational speed. The radius of the orbit depends on Ω_s, μ_e and μ_i. No parametric resonances about the orbit of the whirling were possible in the case of a symmetrical shaft with small internal damping. However, the orbit of the whirling will be distorted (i.e., a circular orbit with a overhang) in the case of a larger value of internal damping.

When the rotational speed of an unsymmetrical shaft is greater than the corresponding first critical speed, the straight equilibrium position is unstable and the shaft buckles. Due to the complexity of the equations, no approximate solution were found for this case. However, bifurcated and chaotic motions were found numerically to exist in unsymmetrical, buckled shafts. The motions in the U direction dominated the shaft's response. Therefore, for an unsymmetrical, buckled shaft, its post-buckled behavior seems to be similar to that of a rotating, buckled beam.

CHAPTER 7

EXPERIMENTAL WORK

7.1 Introduction

The purpose of this chapter is to present an experimental investigation of a physical model (i.e., a rotating beam) whose motion is governed by the differential equations which have been analyzed in Chapters 3 and 4. The results of this experimental study confirm the presence of the majority of the phenomena which were theoretically predicted to exist.

In Section 7.2, the details for developing the experimental apparatus are described. Attention is focused on the measurement techniques of the motor's speed and beam's response. The experimental procedures and corresponding results of both pre-buckled and post-buckled cases are described in Section 7.3 and 7.4, respectively.

7.2 Experimental Setup

The laboratory test equipment consisted of:

1. AND AD-3525 FFT Analyzer.
2. WAVETEK 2M Hz Variable Phase Synthesizer, Model 650.
3. PM6666 Philips 120Mhz Programmable Timer/Counter.
4. Stanford Dual Channel Low-Pass Filter, Model SR640.
5. PM 3365 Philips Oscilloscope.
6. Measurement Group Signal Conditioning Amplifier, Model 2210.

7. ALLEN-BRADLEY Bulletin 1326 AC Servo Motor.
8. Wendon Slip Ring, Part Number WSD-1750-102.
9. Analog Devices AD-650 Frequency-to-Votlage Converter.
10. Hewlett-Packard 6235A Triple Output Power Supply.
11. MASSCOMP 5550 Lab. Workbench 2.1.

The instrumentation schematic is shown in Figure 7.1.

The experimental model consisted of a spring steel beam with a length of 175 mm. and 0.508 mm. x 12.7 mm. cross section rigidly clamped at one end which is driven by an AC servo motor. The beam's first natural frequency was experimentally found to be 13.50 Hz by simply striking the beam and studying the frequency at which it responded. The damping ratio of the beam was found to be approximately 0.01 from a transient decay test. The experimental system was rigidly mounted on an aluminum plate which was vertically hung on the wall in order to negate the effect of gravity. Details of the mechanical construction of the experimental system is shown in Figure 7.2.

The experimental model was driven by an AC servo motor. The speed of the motor was precisely controlled by a feedback system. The speed of the motor, Ω (t), was set by the voltage output from a high accuracy signal generator. In all the experiments, the value of the DC offset of the signal generator was set equal to 8 Vdc. An encoder attached to the motor generated pulses at a rate of 1,000 per revolution. We then used two techniques to monitor the rotational speed. Firstly, we used a counter to measure the frequency of the pulses from the encoder and hence to measure the mean spin rate, Ω_s. A control box was used to adjust the voltage of the DC signal to obtain a desired mean spin rate. After obtaining the desired mean spin rate, we superposed a small sinusoidal signal on the DC signal to generate a periodic perturbation in the spin rate. Next, a Frequency-to-Votlage

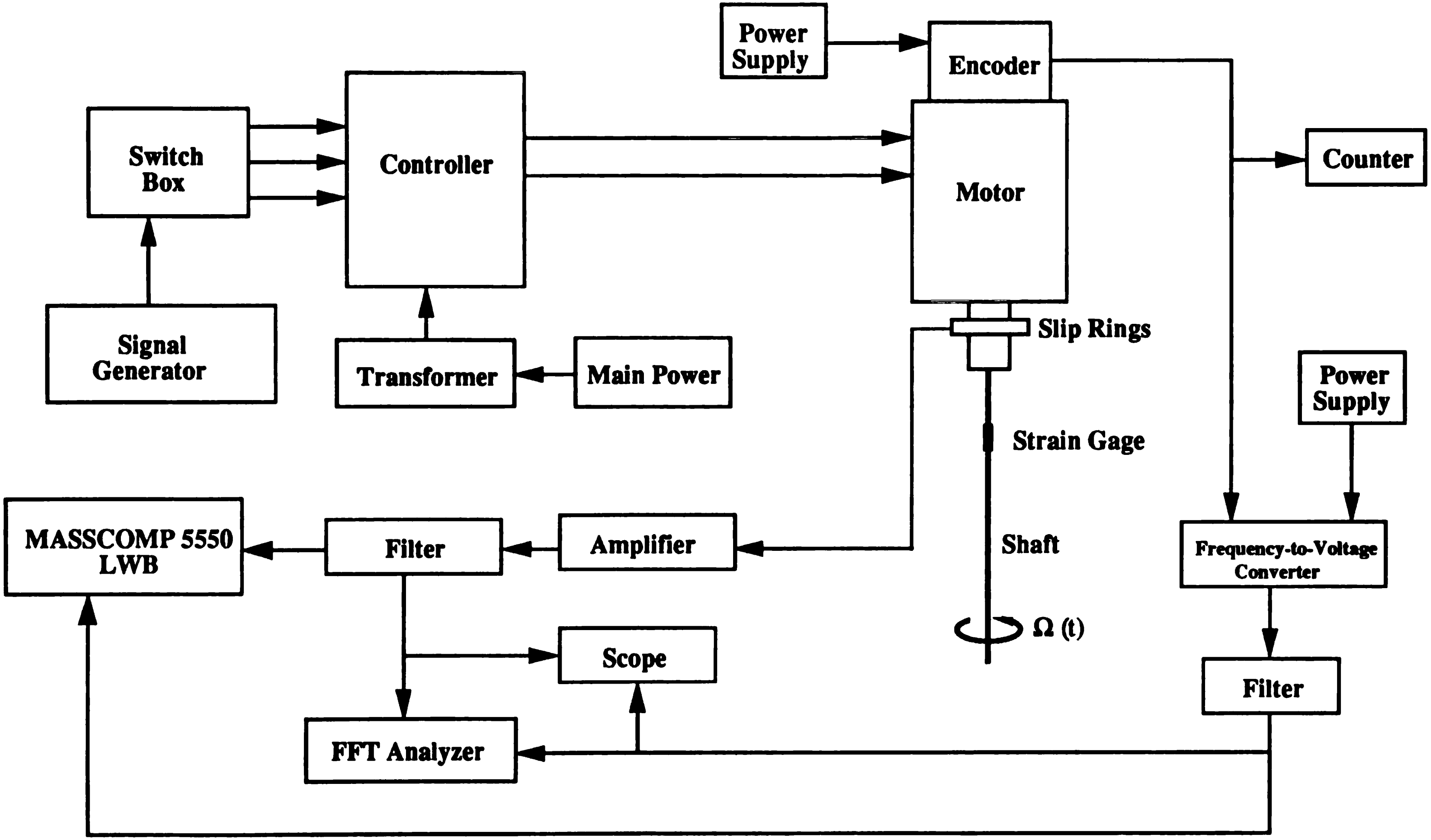

Figure 7.1 Schematic Diagram of the Experimental Apparatus.

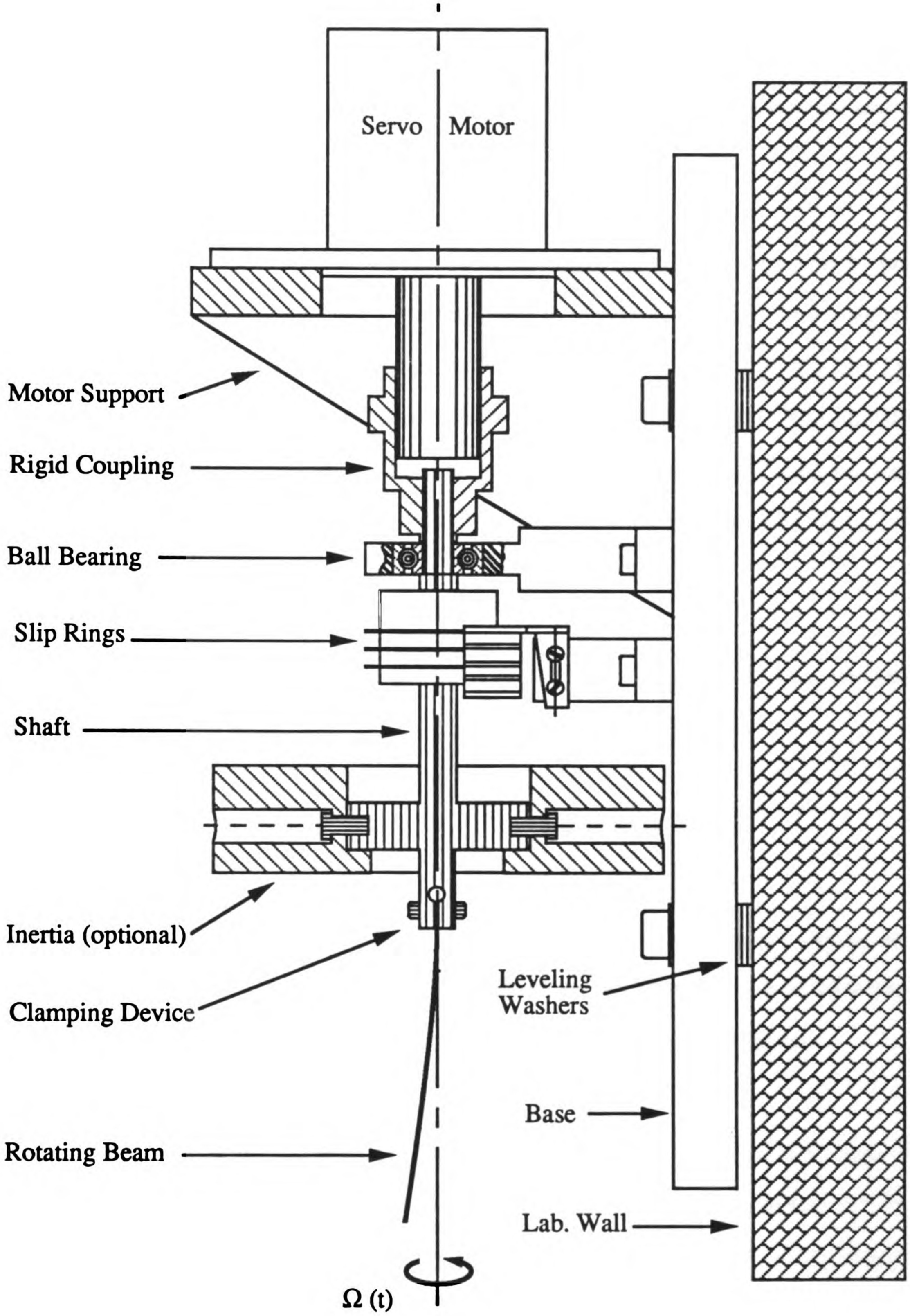

Figure 7.2 Mechanical Construction of the Experimental System.

converter was designed and built to convert the frequency of the pulse from the encoder into an analog voltage signal. This analog signal was monitored on an oscilloscope and a FFT analyzer.

The amplitude of the beam's response was measured by a strain gage which was cemented near the clamped end of the beam and wired to form a half-bridge for the signal conditioning amplifier. The signal of the strain gage was transmitted to the amplifier by slip rings. Low-pass filters were used to filter out noise of the signals. The cut-off frequency was set equal to 30 Hz for all the experiments. A two-channel FFT analyzer was used to monitor and record the response of the beam and the rotational speed of the motor in the time and frequency domain .

We now present the experimental results of the two cases: (a) $\Omega_s < \Omega_0$ and (b) $\Omega_s > \Omega_0$ in the following sections.

7.3 The Case of $\Omega_s < \Omega_0$

Based on the theoretical work described in Chapter 3, we would expect an instability to occur close to $\omega = 2\omega_0$. Using the result of Chapter 3, this will be in the neighborhood of $2\sqrt{\Omega_0^2 - \Omega_s^2}$ where Ω_0 is experimentally found to be 13.50 Hz.

Figures 7.3a-c present the results obtained by completing an incremental frequency sweep over the range $2\omega_0$, while holding the mean rotational speed Ω_s constant at 9.04 Hz, 10.55 Hz, and 11.0 Hz, respectively. The amplitude, $\varepsilon\Omega_A$, for all cases was set equal to $0.025\Omega_s$. The "amplitude" term as it was plotted in Figures 7.3a-c corresponds to the root mean square value of the signal from the strain gage. Representative examples of the

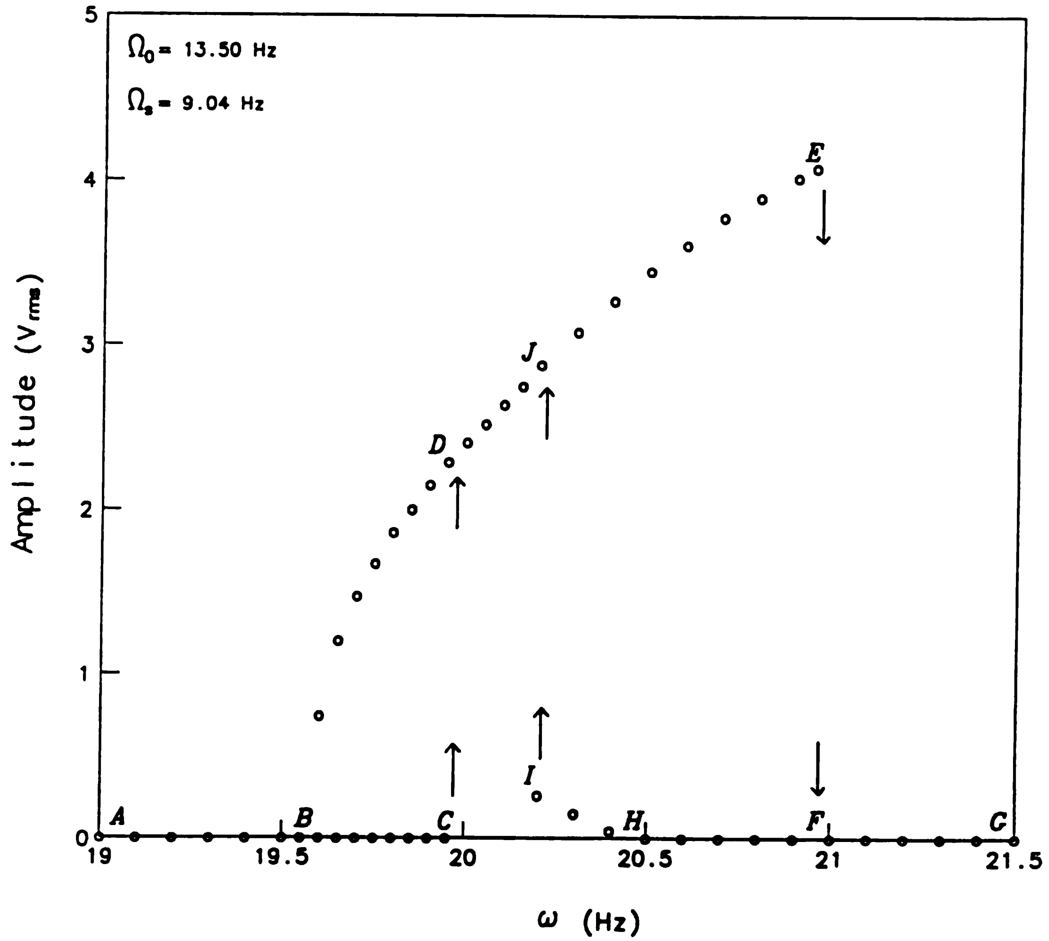

Figure 7.3a Frequency Response Curve for Ω_s = 9.04 Hz.

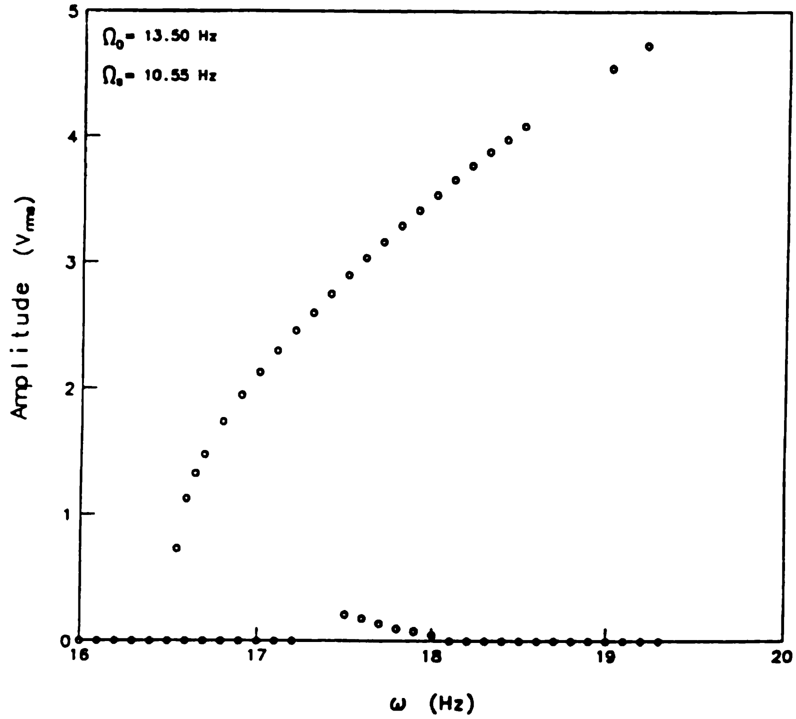

Figure 7.3b Frequency Response Curve for Ω_s = 10.55 Hz.

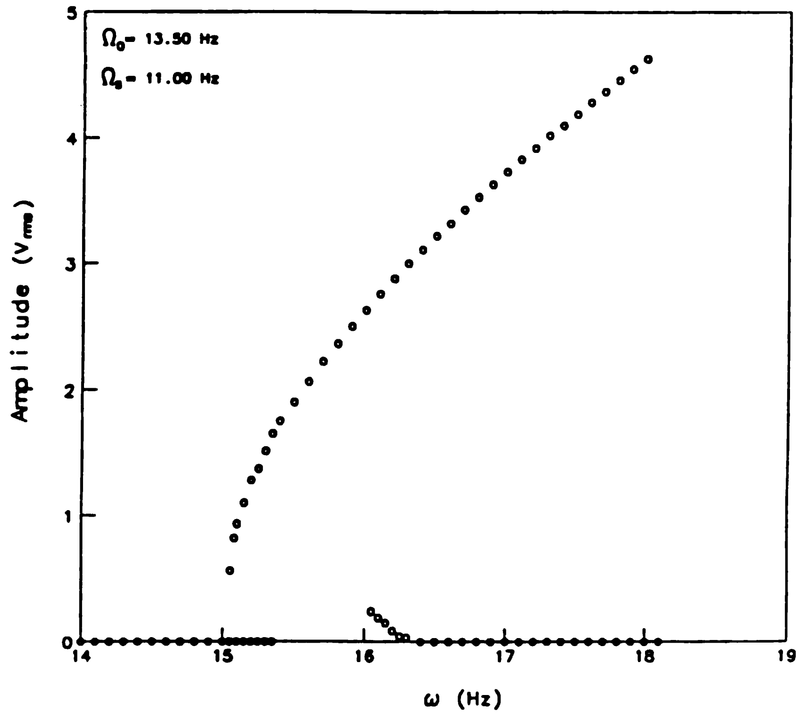

Figure 7.3c Frequency Response Curve for Ω_s = 11.00 Hz.

time traces obtained from the strain gage and from the signal representing the fluctuating part of the motor speed, are shown in Figure 7.4 along with their associated Fourier transforms in Figure 7.5, respectively.

In general, the form of the experimental response curves depicted in Figures 7.3a-b agree well with the theoretical predictions, as presented in Figure 3.1. The trivial solution, an amplitude of zero, becomes unstable over a region close to $2\omega_0$ and the resulting response is of a nonlinear hardening type. There is also a range over which we can observe multi-valued solutions. However, the type of behavior in the vicinity of the point where the trivial solutions go unstable, is slightly different from that predicted by the theory. The theory is based on a perfectly balanced, initially straight beam. In practice this is hard to achieve and the introduction of small imperfections lead to imperfect bifurcations (see, for example, Golubitsky and Schaeffer [1984], page 6).

To better explain the results depicted in Figure 7.3a, consider the points A, B, C, D, E, F, G, H, I, and J as shown on this figure. First, we sweep the frequency, ω, up. The experiment is started at a frequency corresponding to point A on Figure 7.3a. As ω is increased, the trivial attractor is stable through point B until point C is reached. As ω is increased further, the beam jump from point C to point D (i.e., the beam moves to the non-trivial attractor), after which the amplitude of the beam's motion is increased with increasing ω until point E is reached. As ω is increased further, the beam jump from point E to point F (i.e., the beam returns to the trivial attractor again). Next, we sweep ω down. The experiment is started at point G, the beam stay at the trivial attractor through point F until point H is reached. As ω is decreased further, a small amplitude motion takes place until point I is reached. As ω is decreased further, a jump of the beam takes place from point I to point J, after which the amplitude is decreased with decreasing ω until point B is reached. As ω is decreased further, the beam returns once more to the trivial attractor. The

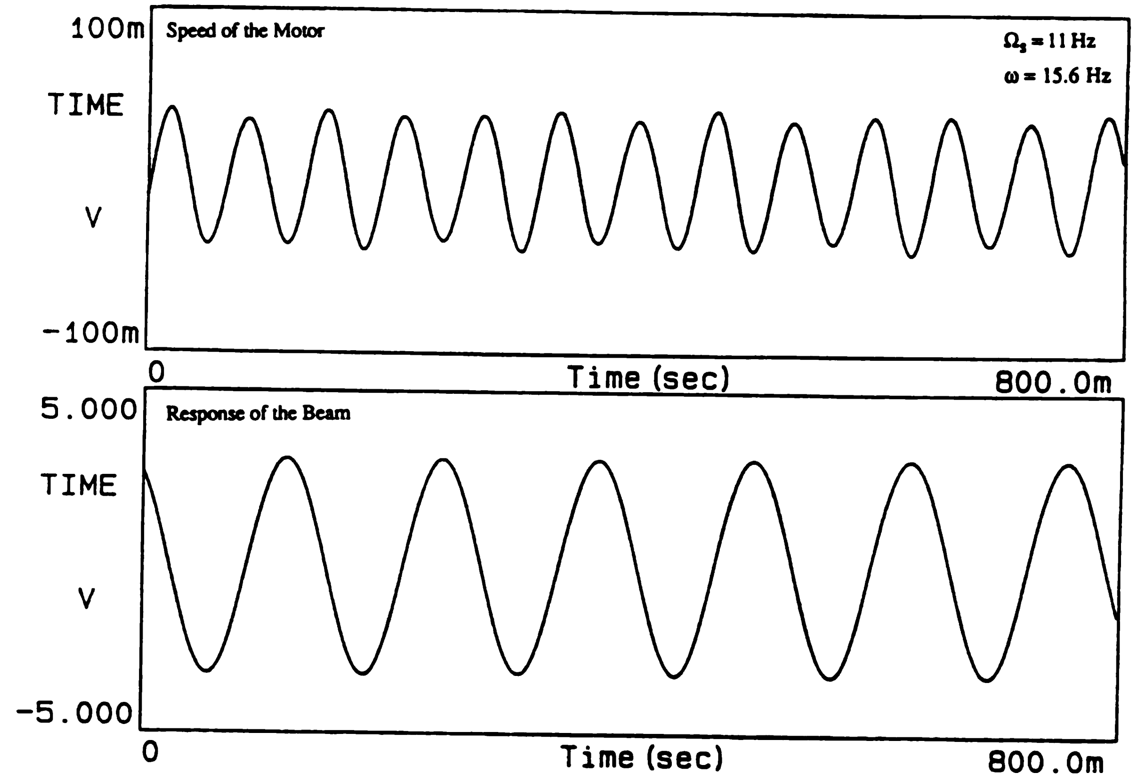

Figure 7.4 Time Traces of the Fluctuation of Motor Speed and Beam Displacement.

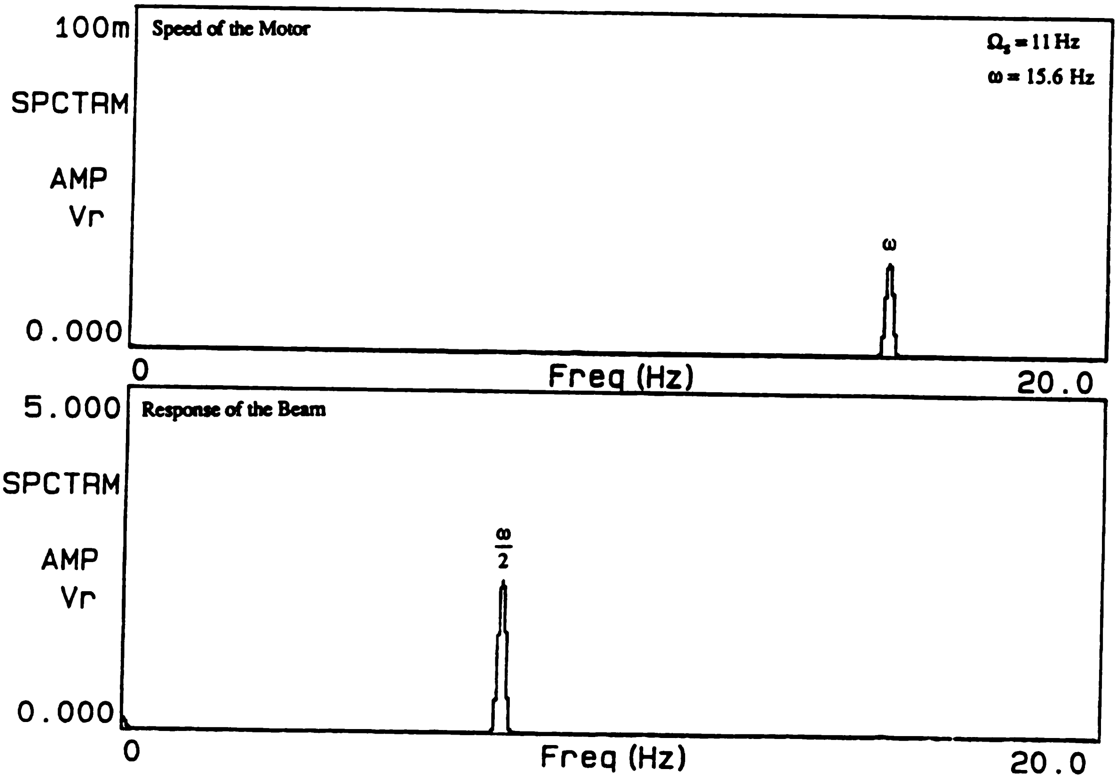

Figure 7.5 Spectrum of the Fluctuation of Motor Speed and Beam Displacement.

maximum amplitude corresponding to point E is attainable only when approached by sweeping up. Figures 7.3b and 7.3c show the same trends, but the influence of the imperfect bifurcation decreases as the spin rate, Ω_s, increases.

Figure 7.6 presents the results from measuring the rms value of the strain gage while slowly varying the amplitude $\varepsilon\Omega_A$ of the small fluctuation. The mean spin rate, Ω_s, for this experiment was set equal to 9.04 Hz and ω was fixed at 20.1 Hz. Once again, the general trends as predicted by the theory are the same (cf. Figure 7.6 to Figure 3.3b). We also note the influence of the imperfect bifurcation.

7.4 The Case of $\Omega_s > \Omega_0$

In this section we investigate the post-buckled behavior (i.e., $\Omega_s > \Omega_0$) of the experimental model. For this case the straight equilibrium position of the beam is unstable and the beam buckles due to centrifugal effects.

We present the results of two experiments which were carried out on the physical model. These experiments investigate the beam's response as functions of the frequency ω of the small sinusoidal oscillation. The mean rotational speed Ω_s is held constant at: (1) 13.58 Hz and (2) 13.70 Hz. It is hard to experimentally measure ω_0, the natural frequency of the beam vibrating about the buckled position. However, we do have experimental values for Ω_0 and, of course Ω_s, and therefore we can use the equations in Appendix C to obtain a "theoretical" value of ω_0 based on experimental measurements. Hence, we find $\omega_0 = 4.4$ Hz when $\Omega_s = 13.58$ Hz and $\omega_0 = 4.9$ Hz when $\Omega_s = 13.70$ Hz. We complete experiments over the range of $\omega = 2$ Hz to 12 Hz and thus we will cover resonances at ω_0 and $2\omega_0$.

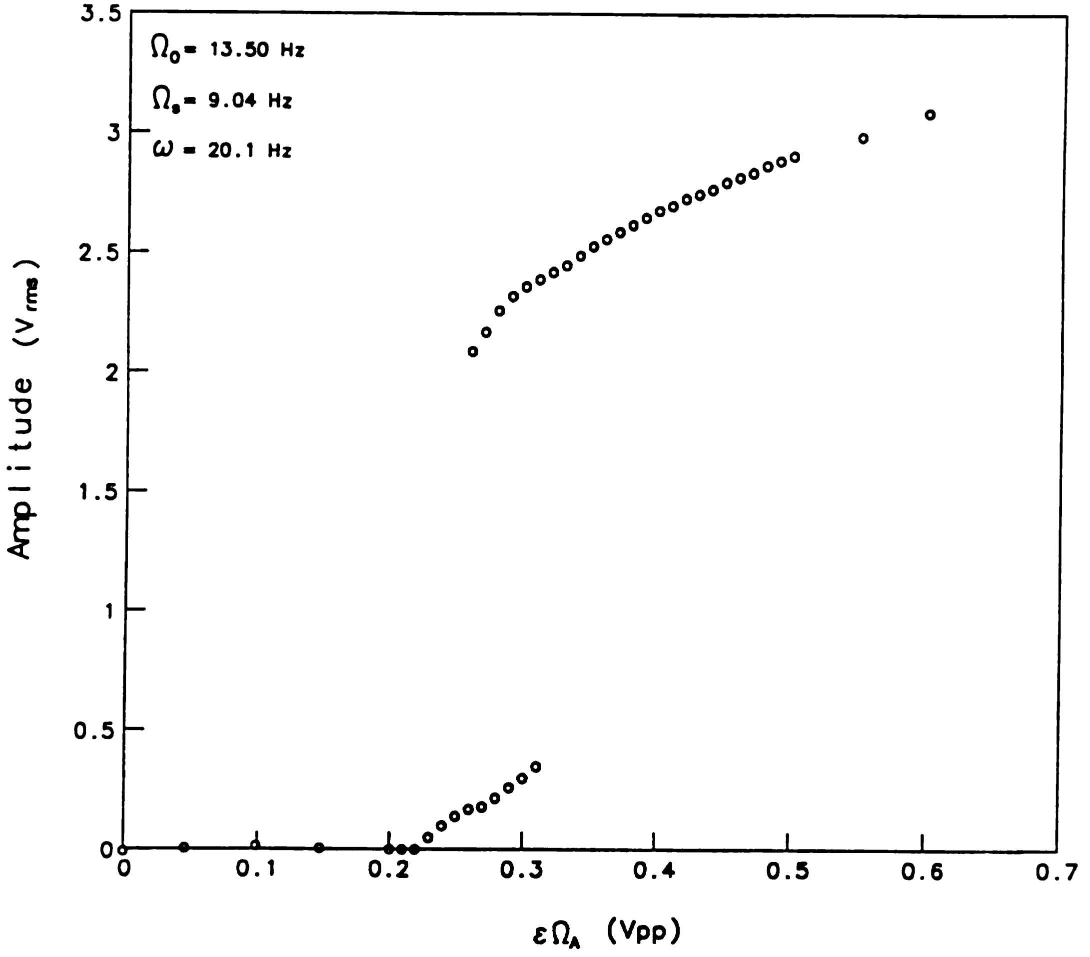

Figure 7.6 Variation of the amplitude of beam displacement with $\varepsilon\Omega_A$.

The results of the experiments are presented as amplitude frequency plots in Figures 7.7a-b. In Figures 7.8-7.17 we present a selection of both the time trace and its corresponding spectrum for different values of ω with $\Omega_s = 13.58$ Hz.

The theory and the numerical simulations presented in Chapter 4 predict that for forcing frequencies, ω, well above $2\omega_0$ we will only see a small amplitude, directly forced response, i.e., the beam will respond at ω. Figure 7.8, which shows the time trace of the beam response at a value of $\omega = 11$ Hz, is consistent with this. To theoretical make a comparison with the results obtained using the method of multiple scales we have plotted the response depicted in Figure 7.8 as a trivial response i.e., zero amplitude, on Figures 7.6. At first this may seem contradictory, however, it is the resonant response at $\frac{\omega}{2}$ that we are interested in. As is often the case in nonlinear studies, it is difficult to plot a standard response curve (i.e. amplitude of response verse forcing frequency) since the response may contain many frequencies in addition to the forcing frequency. As stated, we have chosen to plot the amplitude of the $\frac{\omega}{2}$ component on Figures 7.6a-b. This will then be consistent with, for example Figure 4.1, as presented in the theoretical section.

As we decrease the forcing frequency, we reach a bifurcation point at 10 Hz (see Figure 7.7a), below which a subharmonic response is found. Figure 7.9 depicts the time trace and its spectrum for the case where $\omega = 8$ Hz. When we decrease the frequency below this value we find a period four motion is introduced (see Figure 7.10). This was not predicted by the method of multiple scales but it was by the numerical simulations of the equation of motion, see, for example, Figure 4.28 in Chapter 4.

Further decreasing the value of ω below 7.8 Hz we enter into a region of chaotic response. Time traces and spectrums recorded in this region are presented in Figure 7.11.

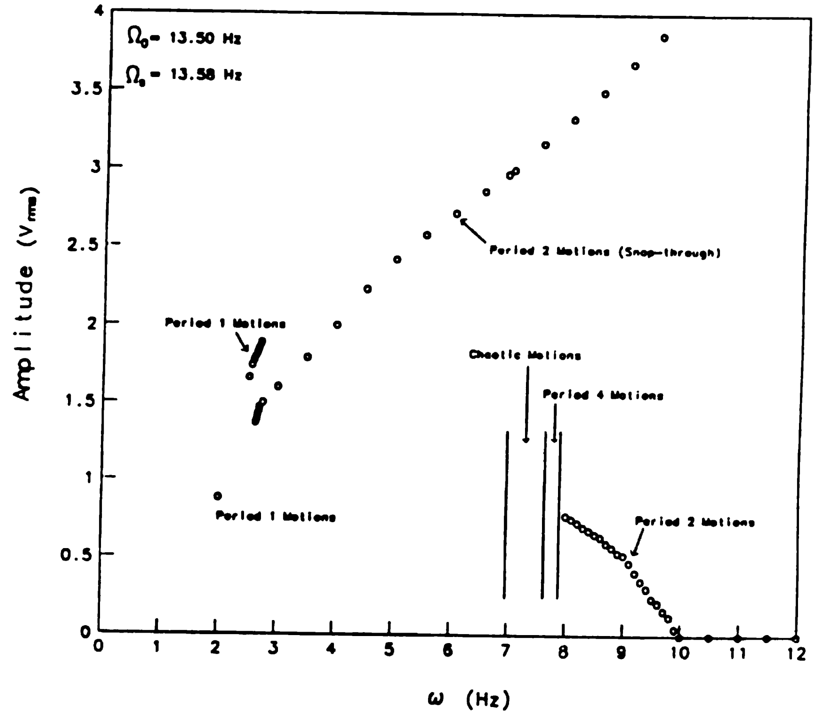

Figure 7.7a Frequency Response Curve for $\Omega_s = 13.58$ Hz.

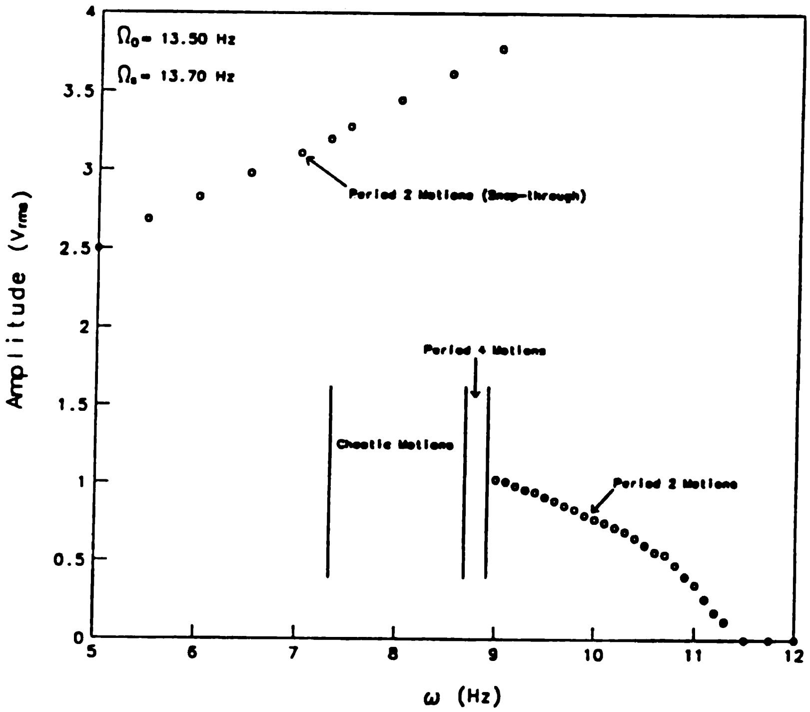

Figure 7.7b Frequency Response Curve for $\Omega_s = 13.70$ Hz.

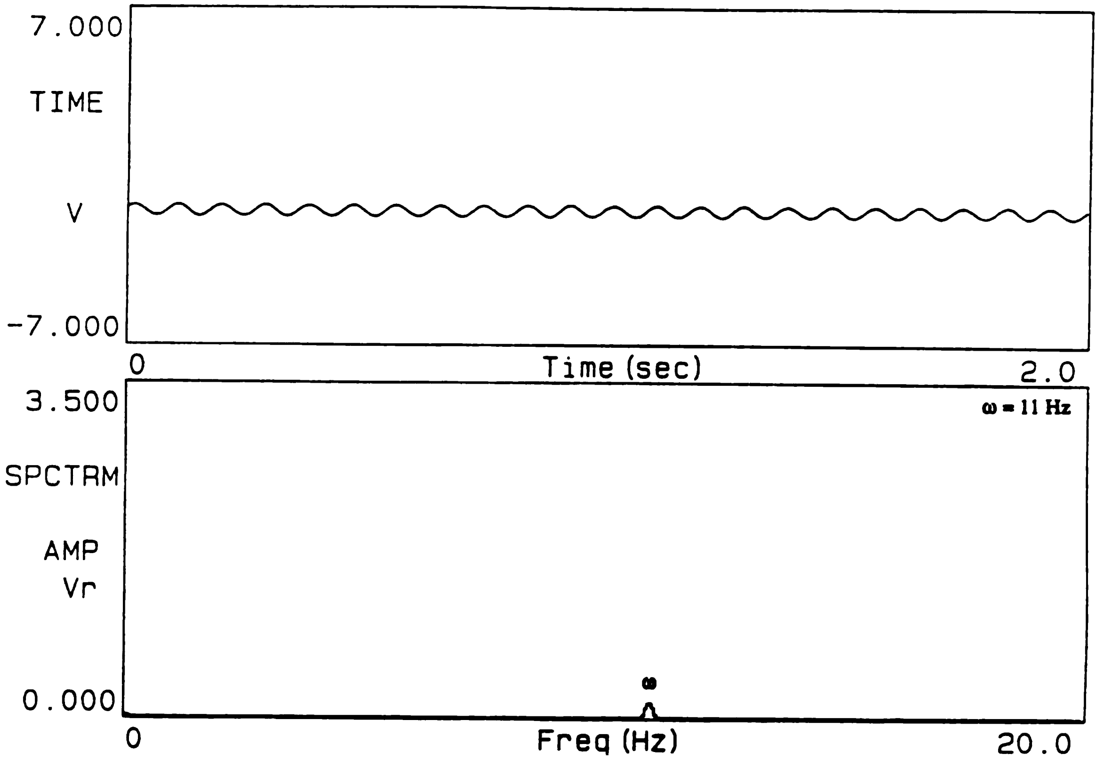

Figure 7.8 Time Trace and Spectrum of Beam Displacement for ω = 11 Hz.

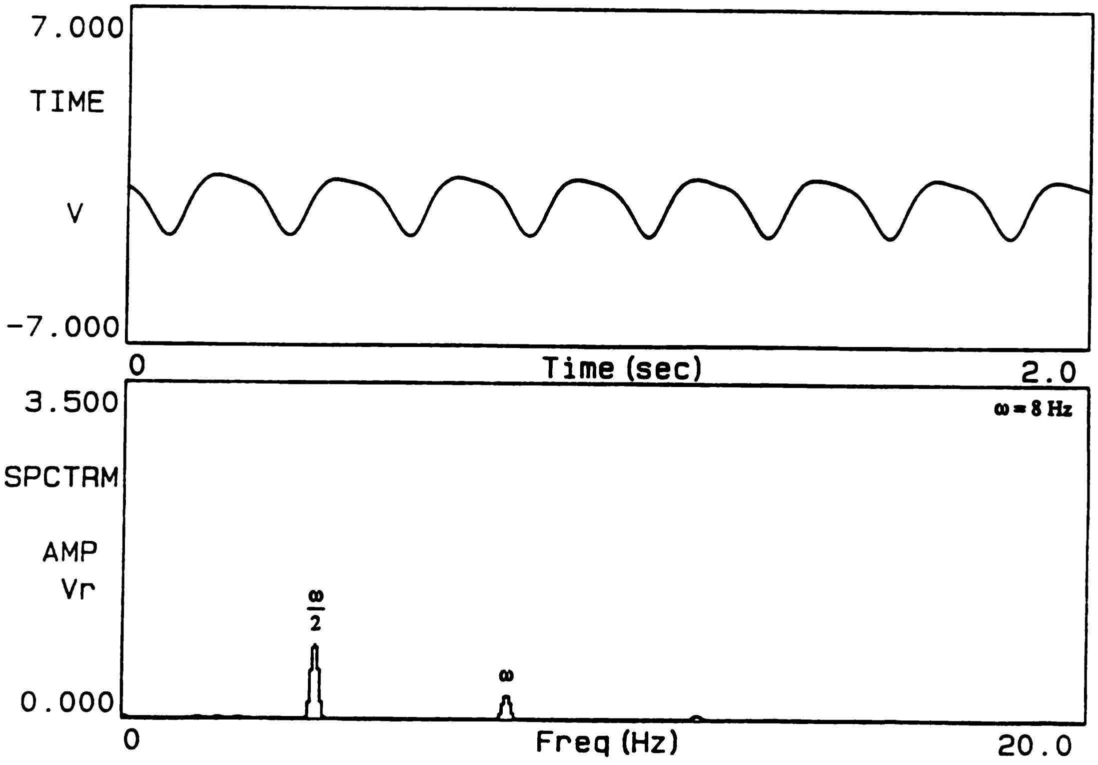

Figure 7.9 Time Trace and Spectrum of Beam Displacement for ω = 8 Hz.

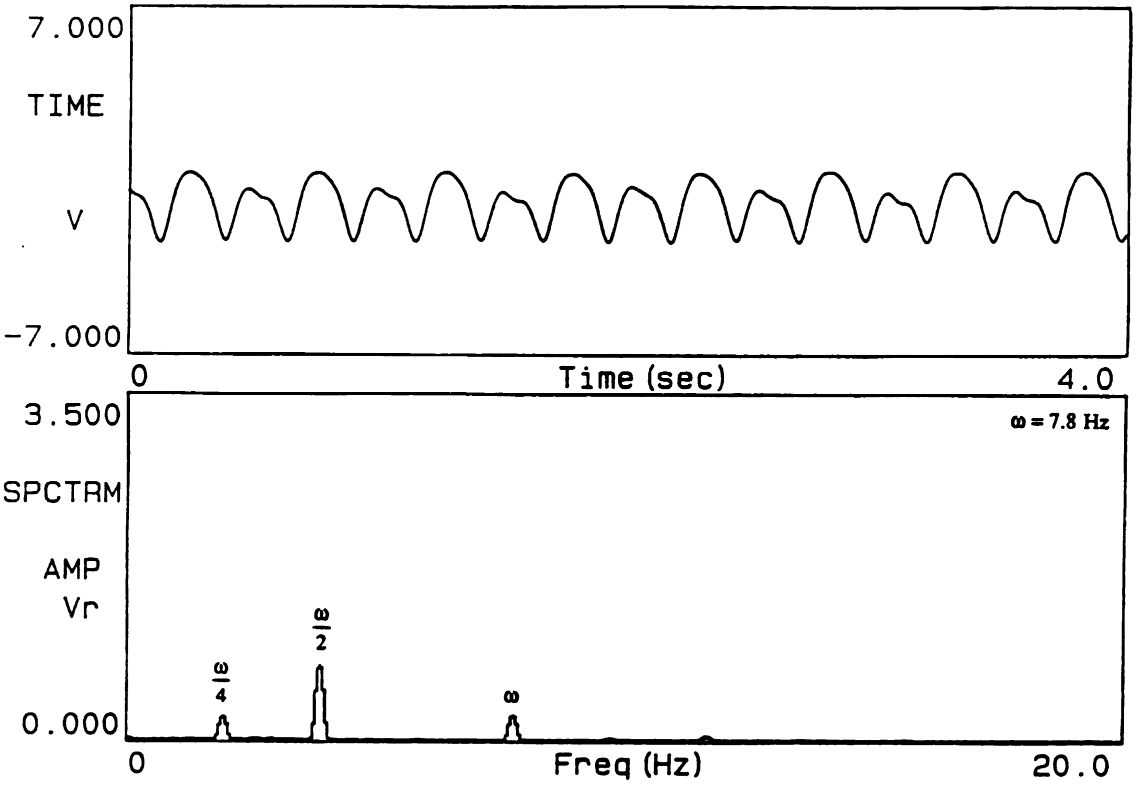

Figure 7.10 Time Trace and Spectrum of Beam Displacement for ω = 7.8 Hz.

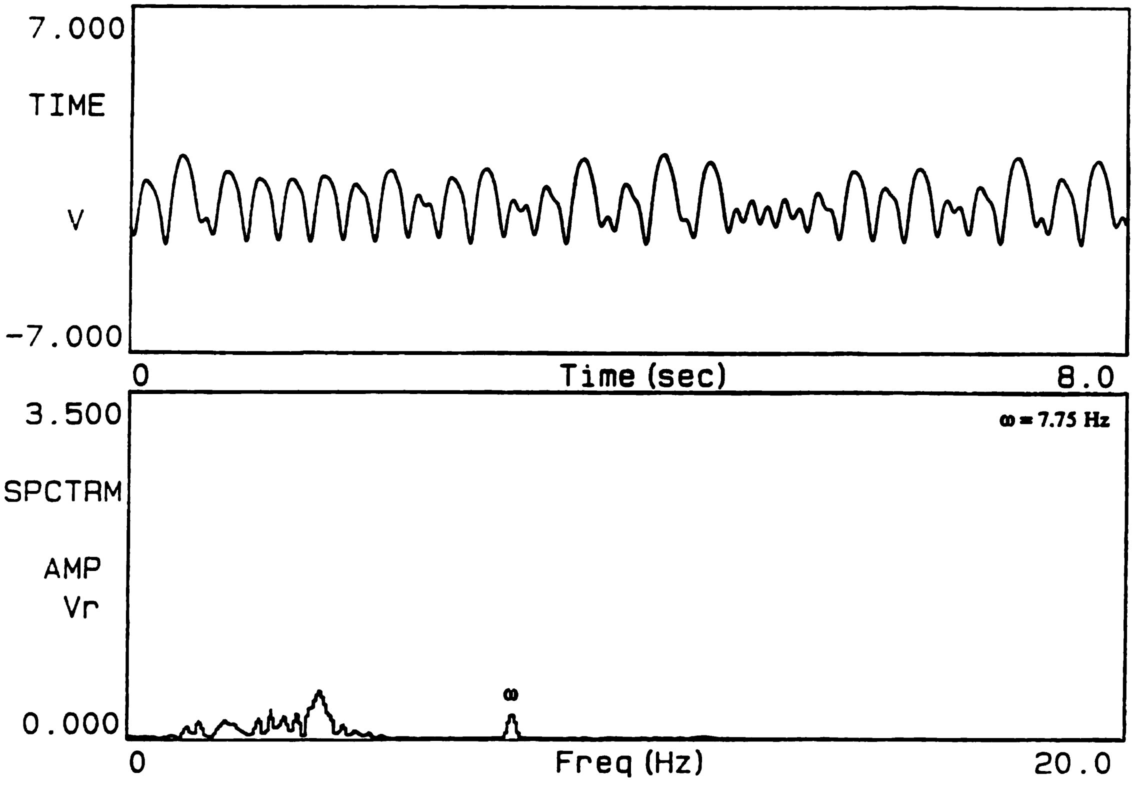

Figure 7.11 Time Trace and Spectrum of Beam Displacement for ω = 7.75 Hz.

To better demonstrate the chaotic motions, another two time traces also presented for $\omega =$ 7.1 Hz and 7.0 Hz, as shown in Figures 7.12. Once again this is consistent with the numerical simulation completed in Chapter 4.

For values of ω below 7 Hz a period two motion remains but now the motion encompasses both buckled positions. This motion was described as "snap-through" in Chapter 4 and, as was found in the numerical simulations, is of a hardening type of nonlinear response. This can be seen in Figure 7.7a which clearly shows the amplitude of the snap-through motion decreases as ω is decreased, but increases if we increase ω. Hence, for 10 Hz > ω > 7 Hz multiple steady-states exist. Time trace and its spectrum, are presented for such a case with $\omega = 8.0$ Hz in Figure 7.13. Comparing this with Figure 7.9, which was also obtained at $\omega = 8$ Hz; clearly shows the existence of multiple solutions.

The system having adopted the snap-through motion, can maintain this type of response over a very wide range of ω. Indeed the motion was recorded right down to approximately a ω of 2.65 Hz, at which time the motion changed to having a period of one. Figures 7.14 and 7.15 show time traces and spectrums associated with the transition. From these figures, we also observed that the third and fourth harmonics appeared. The period one motion was found to exist over a region of $\omega = 2.5$ Hz to 2.71 Hz, at which point the period two motion was then once more adopted.

One other type of motion was found to exist for $\omega = 2$ Hz, as shown in Figures 7.16. This corresponds to a main resonance response, i.e., $\omega \approx \omega_0$. It was extremely difficult to experimentally obtain more data for this type of response as the snap-through motion would intermittently occur. Indeed some chaotic motion was also observed in this region. Figure 7.17 shows time trace and spectrum of a chaotic motion for $\omega = 2.64$ Hz.

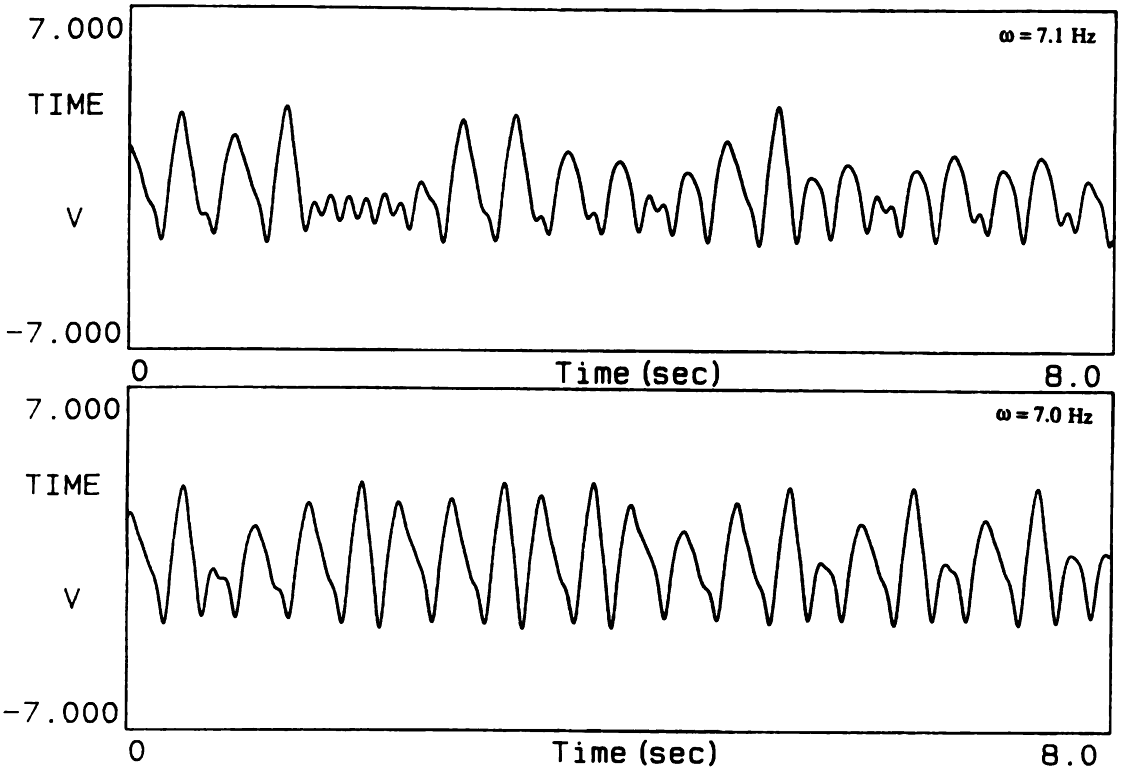

Figure 7.12 Time Trace of Beam Displacement for ω = 7.1 Hz and 7.0 Hz.

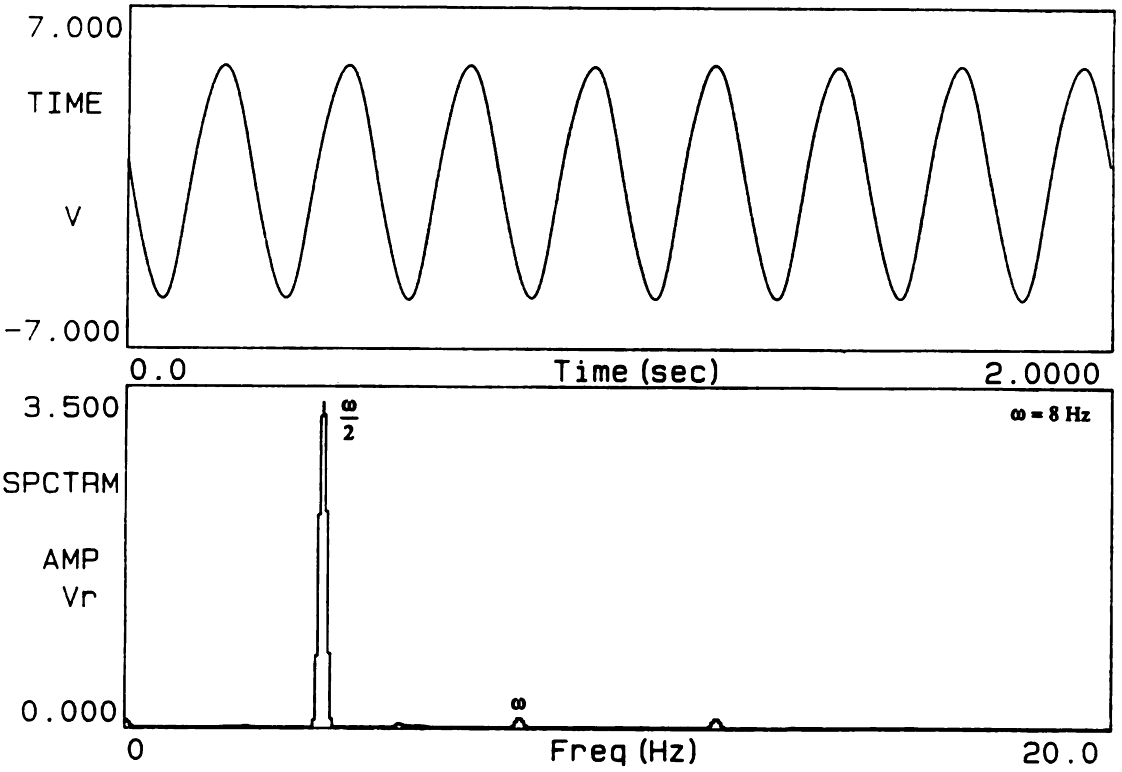

Figure 7.13 Time Trace and Spectrum of Beam Displacement for ω = 8 Hz.

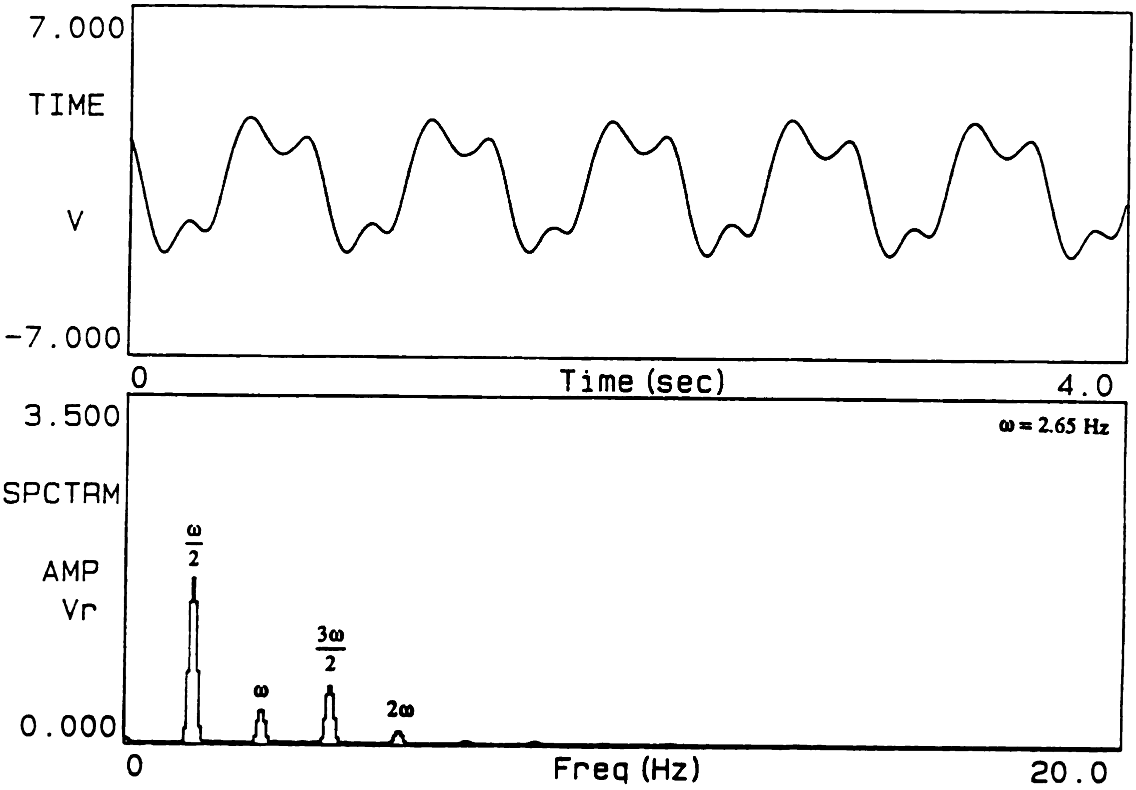

Figure 7.14 Time Trace and Spectrum of Beam Displacement for ω = 2.65 Hz.

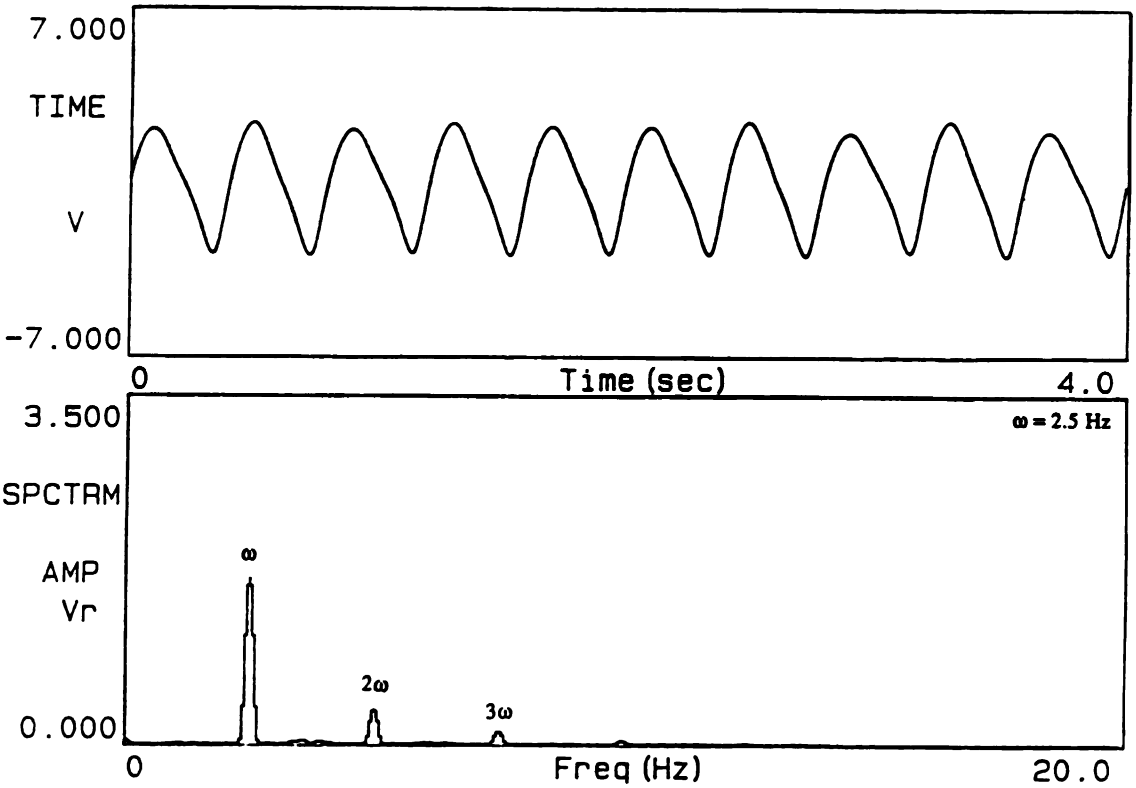

Figure 7.15 Time Trace and Spectrum of Beam Displacement for ω = 2.5 Hz.

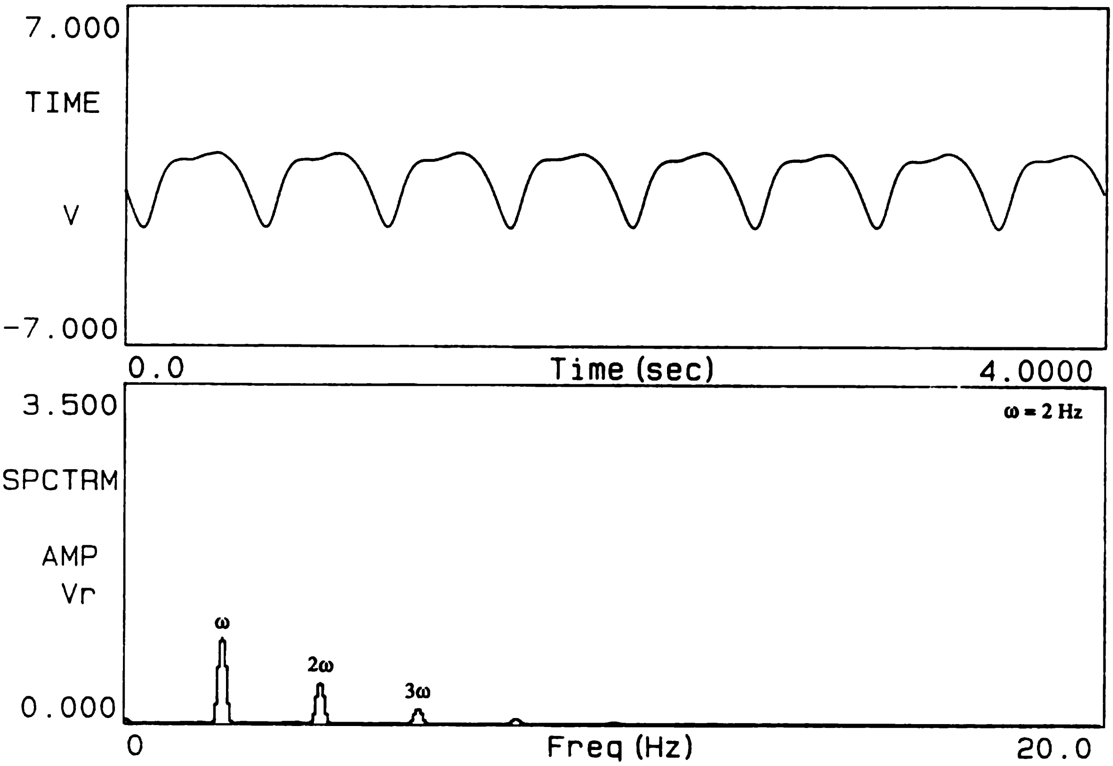

Figure 7.16 Time Trace and Spectrum of Beam Displacement for ω = 2 Hz.

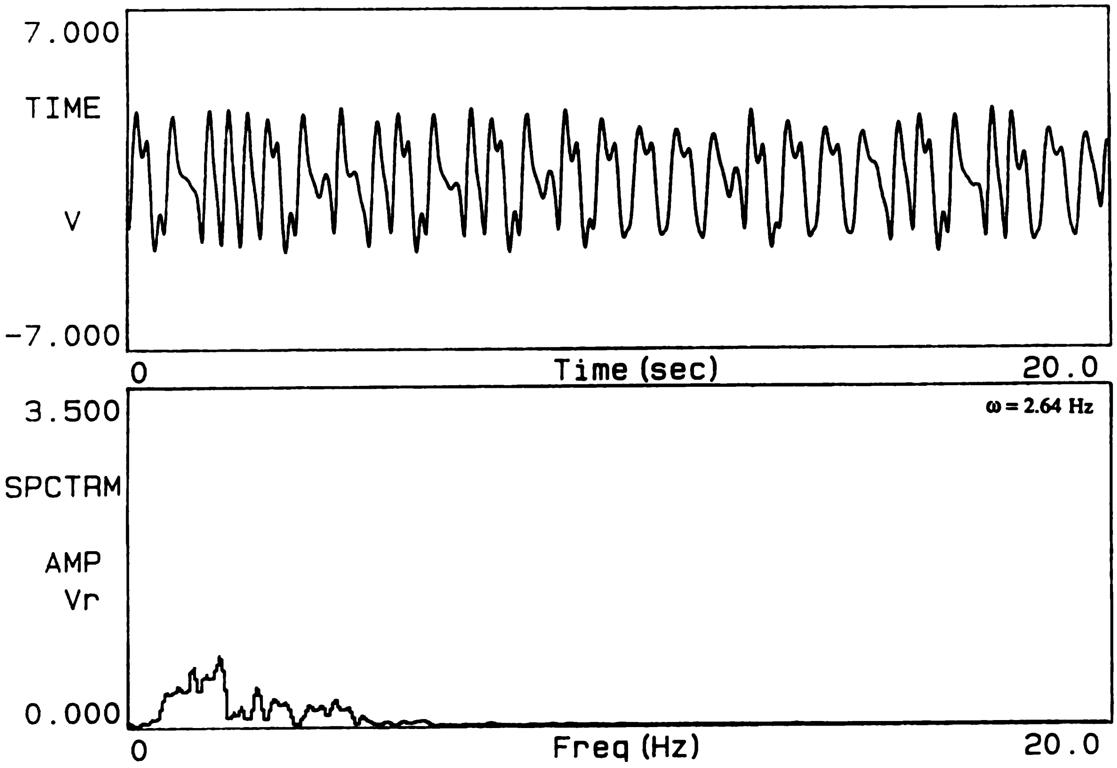

Figure 7.17 Time Trace and Spectrum of Beam Displacement for ω = 2.64 Hz.

7.5 Summary of the Chapter

We have conducted a series of experiments on a rotating cantilever beam for two cases: (a) $\Omega_s < \Omega_0$ and (b) $\Omega_s > \Omega_0$. The results of the experiments of both cases show qualitative agreement with the perturbation solutions and/or the numerical simulations. For the pre-buckled case, we observed regions of imperfect bifurcations. For the post-buckled case, we observed bifurcated and chaotic motions.

CHAPTER 8

SUMMARY AND CONCLUDING REMARKS

8.1 Summary of the Dissertation

The effects of a nonconstant spin rate on the nonlinear dynamic response of shafts has been investigated. The analytical study was based on equations of motion which were derived in Chapter 2. These partial differential equations were quite general in nature, but were reduced to ordinary differential equations for two particular cases, upon which the remainder of the dissertation was based. The first case investigated the behavior of a cantilevered beam rotating about its longitudinal axis, the motion in this case being modeled by a single, second order, nonlinear differential equation with time dependent coefficients. The second case was concerned with the dynamics of a circular shaft, simply supported at either end. For this case, two coupled, nonlinear, second order differential equations were used to model the behavior. Time dependent coefficients were once again present.

In each of the two cases the investigation focused firstly on the system's behavior for spin rates below the critical speed and secondly, on their behavior above the critical speed. The general approach was to seek approximate solutions to the governing equations of motion using the method of multiple scales. The accuracy of these solutions was checked using direct numerical integration.

In Chapter 3, the pre-buckled behavior of a fixed-free beam was investigated. It was clearly demonstrated that a principal parametric resonance can occur at mean spin rates well below the first critical speed of the beam. For this type of resonance, the nonlinearities were of a hardening type. In Chapter 4 the post-buckled behavior of a cantilevered beam was investigated. For sufficiently small $\varepsilon \Omega_A$ values, the beam was found to vibrate about one of the buckled positions with a softening-type, nonlinear behavior. As we increased the $\varepsilon \Omega_A$ value beyond some critical value, the beam's orbit encompassed both buckled positions. In the vicinity of the critical value of $\varepsilon \Omega_A$, a region was found where the beam displayed bifurcated and chaotic motions. Melnikov's method was applied to predict the regions where chaotic motions might exist. Numerical simulations were used to find bifurcated and chaotic motions in the regions of primary and subharmonic resonances. The values of $\varepsilon \Omega_A$ for which chaotic motions occurred were found to be much above the homoclinic bifurcation curve, indicating that in this case, Melnikov's method gave a very conservative lower bound for the transition to chaos.

The case of the pre-buckled shaft was consider in Chapter 5. Four cases of parametric resonances, viz. $\omega \approx 2\omega_1$, $\omega \approx 2\omega_2$, $\omega \approx \omega_1 + \omega_2$ and $\omega \approx \omega_2 - \omega_1$ were considered. Each case was analyzed firstly in the absence of internal tuning (i.e., ω_2 was assumed to be well removed from $3\omega_1$) and secondly in the presence of internal tuning (i.e., ω_2 was assumed to be closed to $3\omega_1$). It was shown that no parametric resonances exist for the case of a perfectly balanced, symmetrical shaft. However, for a shaft that is close to circular, it was found that parametric resonances can occur. In the presence of an internal resonance, the shaft's behavior became much more complex. Such phenomena as non-existence of steady-state motions, coexistence of steady-state motions, amplitude modulate motions, and re-stabilization of the trivial solutions were all found to exist. They were confirmed by direct numerical integration of the full equations of motion.

In Chapter 6 the case of the post-buckled shaft was studied. The analysis began by finding the equilibrium position assuming a constant spin rate. The conditions for nonsynchronous whirl were obtained and it was shown that even when a nonconstant spin rate was imposed on the perfectly circular shaft, no resonances occurred if the internal damping was small. However, the orbit of the whirling will become distorted (i.e., a circular orbit with a overhang) for larger values of internal damping. In the case of the almost circular shaft, no approximate solutions to the governing equations were found, on account of the complexity of the problem. However, numerical studies showed the existence of bifurcated and chaotic motions for the case of $\omega \approx \omega_1$ and $\omega \approx 2\,\omega_1$.

The results from an experimental investigation of the cantilevered beam case were presented in Chapter 7. The results of the experiments showed good qualitative agreement with the perturbation solution for all the cases tested. When the beam buckled, bifurcated and chaotic motions were observed.

8.2 Discussion and Future Work

(1) The coupled nonlinear, partial differential equations derived in Chapter 2 were reduced to ordinary differential equations by assuming that the first mode motion dominated the shaft's motion. At least for the case of a rotating beam, the experimental results indicate that such an assumption is valid. Preliminary experimental results, not reported in this thesis, show that a similar assumption would seem to be valid for the shaft case.

(2) Although the approximate steady-state solutions obtained by the method of multiple scales have been shown to be very accurate in a number of cases, the method does have its limitations. For example, when a steady-state motion is found to loss its stability, the method of multiple scales gives no indication as to the specific details of the resulting motion, although the manner that the eigenvalues pass into the positive half plane do give an indication of the type of response we might expect. Related to this is that no information

regarding domains of attraction can readily be obtained from the method. Also, close to regions where degenerate bifurcations occur, the method of multiple scales can not give details of the motion likely to be observed. A possible qualitative approach (e.g., bifurcation theories) might be an alternate way to gain insight into these problems.

Another practical weakness of this, and other perturbation methods, is that carrying out the expansion to higher orders is very cumbersome, especially for multiple degree of freedom systems. In practice one seldom goes beyond the third order unless the algebraic manipulations are performed by a computer. Even then, there are limitations.

(3) In this thesis, the spin rate was expressed as the sum of a steady-state part and a relatively small sinusoidally varying component. However, from an engineering viewpoint a more complex periodic spin rate would be more physically realistic. If this were modeled as a summation of sinusoidal terms (e.g., by a Fourier series), there would be the possibility of multiple resonances occurring simultaneously. This would be an interesting extension to the current work.

(4) In Section 4.6 we observed that Melnikov's method was very conservative in predicting the transition to chaos. Moon [1987] used a different criterion based on the heuristic idea that chaos may occur when periodic orbits become large enough to touch the homoclinic orbit. It would be interesting to apply his ideas to the current problem.

(5) The mathematical models used in the present study did not incorporate the effect of mass unbalance. Since this is a practical consideration, it would be useful to extend the analysis to include this and thus study the interaction between nonconstant spin rates and mass unbalance. Indeed, the experimental results presented in Chapter 7 show that imperfect bifurcation occurred. It is believed that this could be explained by incorporating

mass unbalance and other imperfections in general.

(6) The straight equilibrium position of a rotating beam is stable when $\Omega_s < \Omega_0$ and unstable when $\Omega_s > \Omega_0$. However, when Ω_s is very close to Ω_0, the straight equilibrium position is marginally stable. The stability of the straight equilibrium position will change periodically if we superpose a relatively small sinusoidally varying component on Ω_s. This corresponds to the problem of a system with a periodically disappearing separatrix. The method of the multiple scales cannot capture the nonlinear dynamics of the beam under this condition. This may be investigated by using averaging and elliptic functions (see Coppola and Rand [1990]).

(7) Chapter 7 reported on the experimental investigations completed on a cantilevered beam. This work should be extended to cover the shaft case.

APPENDICES

Appendix A

If φ is the rotation of an element of the beam about the y axis, then the slope of the rotation can be expressed as

$$\tan\varphi = \frac{u'}{1+w'} \tag{A.1}$$

where $(\,)' = \dfrac{\partial(\,)}{\partial S}$ and S is the undeformed arc length.

Differentiating equation (A.1) we obtain

$$\varphi' = \frac{(1+w')\,u'' - u'\,w''}{1+u'^2+w'^2} \tag{A.2}$$

The elongation rate

$$\varepsilon(S,t) = \left[(1+w')^2 + u'^2\right]^{\frac{1}{2}} - 1 \tag{A.3}$$

is the measure of the axial deformation of the neutral axis. For a beam with a movable end (e.g., cantilevered beam) the axial deformation of the neutral axis is negligible, i.e., $\varepsilon(S,t) = 0$. Hence

$$w' = -\tfrac{1}{2}u'^2, \quad w'' = -u'u'' \tag{A.4}$$

Substituting equation (A.4) into equation (A.2) yields

$$\varphi' = \frac{u''(1+\frac{1}{2}u'^2)}{1+u'^2+\frac{1}{4}u'^4} \approx u''(1+\frac{1}{2}u'^2) \tag{A.5}$$

Appendix B

Here we want to determine the function w(z,t) so that it can be eliminated from equation (2.19). Note that

$$ds^2 = dx_1^2 + dx_2^2 \tag{B.1}$$

$$x_1(z,t) = u(z,t) \tag{B.2}$$

$$x_2(z,t) = z + w(z,t) \tag{B.3}$$

therefore,

$$dx_2^2 = \left[\left(\frac{\partial s}{\partial z}\right)^2 - \left(\frac{\partial u}{\partial z}\right)^2\right] dz^2 \tag{B.4}$$

An expression for $\left(\frac{\partial s}{\partial z}\right)^2$ is obtained from equation (2.8) by rearranging terms to get

$$\left(\frac{\partial s}{\partial z}\right)^2 = 1 + 2\,\varepsilon_{zz}(z,t) \tag{B.5}$$

Assuming $\varepsilon_{zz}(z,t) << \frac{1}{2}$, we can get

$$\left(\frac{\partial s}{\partial z}\right)^2 \cong 1 \tag{B.6}$$

The use of equation (B.6) in equation (B.4) and integrating with respect to z shows that

$$x_2(z,t) \cong \int_0^z \left[1 - u'^2(\xi,t)\right]^{\frac{1}{2}} d\xi + C_1(t) \tag{B.7}$$

The end displacement condition is that $x_2(0,t) = 0$, hence

$$x_2(z,t) \cong \int_0^z \left[1 - u'^2(\xi,t)\right]^{\frac{1}{2}} d\xi \tag{B.8}$$

Finally, we combine equations (B.3) and (B.8) to obtain the formula for w(z,t):

$$w(z,t) \cong \int_0^z \left[1 - u'^2(\xi,t)\right]^{\frac{1}{2}} d\xi - z \tag{B.9}$$

In keeping with the first order approximation policy used herein, we expand the integrand of equation (B.9) in a binomial series, to obtain

$$\left[1 - u'^2(\xi,t)\right]^{\frac{1}{2}} = 1 - \frac{1}{2}\left[u'^2(\xi,t)\right] - \cdots\cdots \tag{B.10}$$

This shows that

$$w(z,t) \cong -\frac{1}{2} \int_0^z \left[u'^2(\xi,t)\right] d\xi \quad . \tag{B.11}$$

Appendix C

$$\alpha_1 = \frac{d\,s}{1+d\,s^2}\,, \qquad \alpha_2 = \frac{d}{1+d\,s^2}$$

$$\mu = \frac{c}{2\,\varepsilon\,(1+d\,s^2)}\,, \qquad {\omega_0}^2 = \frac{2\,b\,s^2}{1+d\,s^2}$$

$$\gamma_1 = \frac{3\,b\,s}{1+d\,s^2}\,, \qquad \gamma_2 = \frac{b}{1+d\,s^2}$$

$$g_1 = \frac{2\,\Omega_s\,\Omega_A\,s}{1+d\,s^2}\,, \qquad g_2 = \frac{2\,\Omega_s\,\Omega_A}{1+d\,s^2}$$

$$g_3 = \frac{{\Omega_A}^2\,s}{1+d\,s^2}\,, \qquad g_4 = \frac{{\Omega_A}^2}{1+d\,s^2}\,.$$

Appendix D

$$\begin{aligned} R_{11} = {} & 2\,(i\,\omega_1 - \Lambda_1\,\Omega_s)\,\mu_e\,A_1 + i\,e^{i\varepsilon\sigma_1 T_0}\,\Omega_A\,\Omega_s\,\bar{A}_1 + (3 + \Lambda_1^2 + 2\,\Lambda_1\,\bar{\Lambda}_1)\,\Omega_0^2\,A_1^2\,\bar{A}_1 \\ & + e^{i\varepsilon(\sigma_2-\sigma_1)T_0}\,(2\,\Lambda_2\,\omega_1 - i\,\Omega_s)\,\Omega_A A_2 + e^{i\varepsilon\sigma_2 T_0}\,(3 + \bar{\Lambda}_1^{\,2} + 2\,\bar{\Lambda}_1\,\Lambda_2)\,\Omega_0^2\,\bar{A}_1^2\,A_2 \\ & + (6 + 2\,\Lambda_1\,\Lambda_2 + 2\,\Lambda_1\bar{\Lambda}_2 + 2\,\Lambda_2\,\bar{\Lambda}_2)\,\Omega_0^2 A_1\,A_2\,\bar{A}_2 + 2\,(i\,\omega_1 - \Lambda_1\,\Omega_s)\,A_1' \end{aligned} \tag{D1}$$

$$\begin{aligned} R_{21} = {} & 2\,(i\,\Lambda_1\omega_1 + \Omega_s)\,\mu_e\,A_1 + i\,e^{i\varepsilon\sigma_1 T_0}\,\bar{\Lambda}_1\Omega_A\,\Omega_s\bar{A}_1 \\ & + (3\,\Lambda_1^2\,\bar{\Lambda}_1 + \bar{\Lambda}_1 + 2\,\Lambda_1)\,\Omega_0\,A_1^2\,\bar{A}_1 + -e^{i\varepsilon(\sigma_2-\sigma_1)T_0}\,(2\,\omega_1 + i\,\Lambda_2\Omega_s)\,\Omega_A A_2 \\ & + e^{i\varepsilon\sigma_2 T_0}\,(3\bar{\Lambda}^2\Lambda_2 + \Lambda_2 + 2\,\bar{\Lambda}_1)\,\Omega_0^2\,\bar{A}_1^2\,A_2 \\ & + (6\,\Lambda_1\,\Lambda_2\bar{\Lambda}_2 + 2\,\Lambda_1 + 2\,\bar{\Lambda}_2 + 2\,\Lambda_2)\,\Omega_0^2 A_1\,A_2\,\bar{A}_2 + 2\,(i\Lambda_1\,\omega_1 + \Omega_s)\,A_1' \end{aligned} \tag{D2}$$

$$\begin{aligned} R_{12} = {} & 2\,(i\,\omega_2 - \Lambda_2\,\Omega_s)\,\mu_e\,A_2 + (3 + \Lambda_2^2 + 2\,\Lambda_2\,\bar{\Lambda}_2)\,\Omega_0^2\,A_2^2\,\bar{A}_2 \\ & + e^{i\varepsilon(\sigma_1-\sigma_2)T_0}\left(\frac{-2\,\Lambda_1\,\omega_2}{3} + i\,\Omega_s\right)\Omega_A A_1 + e^{-i\varepsilon\sigma_2 T_0}\,(1 + \bar{\Lambda}_1^{\,2})\,\Omega_0^2\,A_1^3 \\ & + (6 + 2\,\Lambda_1\,\Lambda_2 + 2\,\Lambda_1\bar{\Lambda}_1 + 2\,\Lambda_2\,\bar{\Lambda}_1)\,\Omega_0^2 A_1\,A_2\,\bar{A}_1 + 2\,(i\,\omega_2 - \Lambda_2\,\Omega_s)\,A_2' \end{aligned} \tag{D3}$$

$$\begin{aligned} R_{22} = {} & 2\,(i\,\Lambda_2\,\omega_2 + \Omega_s)\,\mu_e\,A_2 + (3\Lambda_2^2\bar{\Lambda}_2 + \bar{\Lambda}_2 + 2\,\Lambda_2)\,\Omega_0^2\,A_2^2\,\bar{A}_2 \\ & + e^{i\varepsilon(\sigma_1-\sigma_2)T_0}\left(\frac{2\,\omega_2}{3} + i\,\Lambda_1\Omega_s\right)\Omega_A A_1 + e^{-i\varepsilon\sigma_2 T_0}\,(\Lambda_1 + \Lambda_1^3)\,\Omega_0^2\,A_1^3 \\ & + (6\Lambda_1\bar{\Lambda}_1\Lambda_2 + 2\,\Lambda_2 + 2\,\bar{\Lambda}_1 + 2\,\Lambda_1)\,\Omega_0^2 A_1\,A_2\,\bar{A}_1 + 2\,(i\,\Lambda_2\omega_2 + \Omega_s)\,A_2' \end{aligned} \tag{D4}$$

Appendix E

$$\begin{aligned}K_{11} = K_{15} = {} & (2\,i\,\omega_1 - 2\,\Lambda_1\,\Omega_s)\,(\Omega_0{}^2 - \omega_1{}^2) + 2\,\Omega_s{}^2\,(\,i\,\omega_1 + \Lambda_1\,\Omega_s\,) \\ & +2\,\Omega_0{}^2\delta\,(\,i\,\omega_1 - \Lambda_1\,\Omega_s\,)\end{aligned}$$

$$\begin{aligned}K_{12} = {} & 2\,\Lambda_2\,\omega_1\Omega_A\,(\Omega_0{}^2 - \omega_1{}^2) + i\,\Omega_A\,\Omega_s\,(\,\Omega_s{}^2 - \Omega_0{}^2 - 3\,\omega_1{}^2) \\ & + 2\,\Omega_0{}^2\ \Omega_A\,\delta\,(\,\Lambda_2\,\omega_1 - i\,\Omega_s\,)\end{aligned}$$

$$\begin{aligned}K_{13} = {} & 2\,i\,\Omega_s\Omega_A\,(\Omega_0{}^2 - \omega_1{}^2) - \Omega_A\,\Omega_s{}^2\,(\,2\,\overline{\Lambda}_1\,\omega_1 + i\,\Omega_s\,) \\ & + i\,\Omega_0{}^2\ \Omega_A\ \Omega_s\,\delta\end{aligned}$$

$$\begin{aligned}K_{14} = {} & (\Omega_0{}^4 + \Omega_0{}^4\,\delta - \Omega_0{}^2\,\omega_1{}^2 - \Omega_0{}^2\Omega_s{}^2)(\,3 + \overline{\Lambda}_1{}^2 + 2\,\overline{\Lambda}_1\,\Lambda_2\,) \\ & + 2\,i\,\Omega_0{}^2\,\omega_1\,\Omega_s\,(\,\Lambda_2 + 2\,\overline{\Lambda}_1 + 3\,\overline{\Lambda}_1{}^2\,\Lambda_2\,)\end{aligned}$$

$$\begin{aligned}K_{16} = {} & (\,\Omega_0{}^4 + \Omega_0{}^4\,\delta - \Omega_0{}^2\,\omega_1{}^2 - \Omega_0{}^2\Omega_s{}^2\ )(\,3 + \overline{\Lambda}_1{}^2 + 2\,\overline{\Lambda}_1\,\Lambda_1\,) \\ & + 2\,i\,\Omega_0{}^2\,\omega_1\,\Omega_s\,(\,\overline{\Lambda}_1 + 2\,\Lambda_1 + 3\,\Lambda_1{}^2\,\overline{\Lambda}_1\,)\end{aligned}$$

$$\begin{aligned}K_{21} = K_{23} = {} & 2\,i\,\omega_2\,(\Omega_0{}^2 - \omega_2{}^2) - 2\,\Lambda_2\,\Omega_s\ (\Omega_0{}^2 + \omega_2{}^2) \\ & +2\,\Omega_s{}^2\,(\,i\,\omega_2 + \Lambda_2\,\Omega_s\,) + 2\,\Omega_0{}^2\delta\,(\,i\,\omega_2 - \Lambda_2\,\Omega_s\,)\end{aligned}$$

$$\begin{aligned}K_{22} = {} & -\frac{2}{3}\,\Lambda_1\,\omega_2\,\Omega_A\,(\Omega_0{}^2 - \omega_2{}^2) + \frac{i}{3}\,\Omega_A\,\Omega_s\,(\,3\,\Omega_0{}^2 + \omega_2{}^2) \\ & - \Omega_A\,\Omega_s{}^2\,(\,\frac{4}{3}\Lambda_1\omega_2 + i\,\Omega_s\,) - \ \Omega_0{}^2\ \Omega_A\,\delta\,(\,\frac{2}{3}\Lambda_1\,\omega_2 - i\,\Omega_s\,)\end{aligned}$$

$$\begin{aligned}K_{24} = {} & 2\,(\,\Omega_0{}^4 + \Omega_0{}^4\,\delta - \Omega_0{}^2\,\omega_2{}^2 - \Omega_0{}^2\Omega_s{}^2\ )(\,3 + \Lambda_1\overline{\Lambda}_1 + \Lambda_1\Lambda_2 + \overline{\Lambda}_1\,\Lambda_2\,) \\ & + 4\,i\,\Omega_0{}^2\,\omega_2\,\Omega_s\,(\,\Lambda_1 + \Lambda_2 + \overline{\Lambda}_1 + 3\,\Lambda_1\Lambda_2\,\overline{\Lambda}_1\,)\end{aligned}$$

$$\begin{aligned}K_{25} = {} & (\Omega_0{}^4 + \Omega_0{}^4\,\delta - \Omega_0{}^2\,\omega_2{}^2 - \Omega_0{}^2\Omega_s{}^2)(\,3 + \Lambda_2{}^2 + 2\,\overline{\Lambda}_2\,\Lambda_2\,) \\ & + 2\,i\,\Omega_0{}^2\,\omega_1\,\Omega_s\,(\,\overline{\Lambda}_2 + 2\,\Lambda_2 + 3\,\Lambda_2{}^2\,\overline{\Lambda}_2\,)\end{aligned}$$

Appendix F

Let

$$h_1 = 2\left[(\Omega_s - \overline{\omega})^2 - \Omega_0{}^2\right] - \omega^2$$

$$h_2 = \hat{\mu}\,\omega$$

$$h_3 = 2(\Omega_s - \overline{\omega})\omega$$

$$h_4 = \omega^2$$

$$h_5 = \hat{\mu}_i \overline{\omega}$$

$$h_6 = 2\Omega_A(\Omega_s - \overline{\omega})\overline{R}$$

and

$h_7 = -\,\Omega_A \overline{R}\omega$, then

$$H_5 = (h_1h_2)^2 + h_4{}^2(h_1{}^2 + h_2{}^2) + 2(h_2h_3)^2 + h_2{}^4 + h_3{}^4 + 2h_1h_4h_3{}^2$$

$$H_1 = \frac{h_7h_3(h_2{}^2 + h_3{}^2 + h_1h_4) + h_6(h_1h_2{}^2 + h_3{}^2h_4 + h_1h_4{}^2)}{H_5}$$

$$H_2 = \frac{h_7h_3h_2(h_1 - h_4) - h_6h_2(h_2{}^2 + h_3{}^2 + h_4{}^2)}{H_5}$$

$$H_3 = \frac{h_7h_2(h_1{}^2 + h_2{}^2 + h_3{}^2) + h_6h_2h_3(h_4 - h_1)}{H_5}$$

$$H_4 = \frac{-h_7(h_1h_3{}^2 + h_1{}^2h_4 + h_2{}^2h_4) + h_6h_3(h_2{}^2 + h_3{}^2 + h_1h_4)}{H_5} \, .$$

BIBLIOGRAPHY

BIBLIOGRAPHY

Ariaratnam, S. T., 1965, "The Vibration of Unsymmetrical Rotating Shafts," *Journal of Applied Mechanics*, pp. 157-162.

Ariaratnam, S. T. and Sri Namachchivaya, N., 1986, "Periodically Perturbed Nonlinear Gyroscopic Systems," *Journal of Structure Mechanics*, Vol. 14, pp 153-175.

Atanackovic, Teodor M., 1984, "Estimates of Maximum Deflection for a Rotating Rod," *Q. J. Mech. Appl. Math.*, Vol. 37, pp. 515-523.

Atanackovic, Teodor M., 1986, "Buckling of Rotating Compressed Rods," *Acta Mechanica,* Vol. 60, pp. 49-66.

Atluri, S., 1973, "Nonlinear Vibrations of a Hinged Beam Including Nonlinear Inertia Effects," *Journal of Applied Mechanics*, pp. 121-126.

Bauer, H. F., 1980, "Vibration of a Rotating Uniform Beam, Part I: Orientation in the Axis of Rotation," *Journal of Sound and Vibration,* Vol. 72, No.2, pp. 177-189.

Bolotin, V. V., 1963, *Nonconservative Problems of the Theory of Elastic Stability,* New York: The Macmillan Company.

Brosens, P. J. and Crandall, S. H., 1961, " Whirling of Unsymmetrical Rotors," *Journal of Applied Mechanics*, Vol. 28, Trans. ASME, Vol. 83, Series E, pp 355-362.

Coppola, V. T. and Rand R. H., 1990, "*Chaos in a System with a Periodically Disappearing Separatrix,*" Pre-print.

Crandall, S. H. and Brosens, P. J., 1961, " On the Stability of Rotation of a Rotor with Rotationally Unsymmetric Inertia and Stiffness Properties," *Journal of Applied Mechanics*, Vol. 28, Trans. ASME, Vol. 83, Series E, pp 567-570.

Crandall, S. H., 1980, "Physical Explanations of the Destabilizing Effects of Damping in Rotating Parts," *Rotordynamic Instability Problems in High Performance Turbo Machinery,* NASA CP 2133, pp. 369-382.

Day, William B., 1987, "Asymptotic Expansions in Nonlinear Rotordynamics," *Quarterly of Applied Mathematics*, Vol. XLIV, No. 4, pp 779-792.

Dimentberg, F. M., 1961, *Flexural Vibrations of Rotating Shafts,* London: Butterworths.

Ehrich, F. F., 1964, "Shaft Whirl Induced by Rotor Internal Damping," *Journal of Applied Mechanics,* pp. 279-282.

Foote, W. R., Poritsky, H. and Slade, J. J. Jr., 1943, "Critical Speeds of a Rotor with Unequal Shaft Flexibilities, Mounted in Bearings of Unequal Flexibility-I," *Journal of Applied Mechanics*, Vol. 65, pp A77-A84.

Genin, Joseph and Maybee, John S., 1970, "External and Material Damped Three Dimensional Rotor System," *Int. J. Non-Linear Mechanics*, Vol. 5, pp. 287-297.

Genta, G., 1988, "Whirling of Unsymmetrical Rotors:A Finite Element Approach Based on Complex Co-Ordinates," *Journal of Sound and Vibration,* Vol. 124, No. 1, pp. 27-53.

Golubitsky, Martin and Schaeffer, David G., 1985, *Singularities and Groups in Bifurcation Theory,* New York: Springer-Verlag Inc.

Grammel, R., 1929, "Kritische Drehzahl und Kreiselwirkung," *Z Ver. dtsch. Ing.*, No. 32.

Guckenheimer, J. and Holmes, P., 1983, *Nonlinear Oscillations, Dynamical Systems and Bifurcations of Vector Fields,* New York: Springer-Verlag Inc.

Gunter, E. J. Jr., 1967, " The Influence of Internal Friction on the Stability of High Speed Rotors," *Journal of Engineering for Industry,* pp. 683-688.

Gunter, E. J. Jr. and Trumpler, P. R., 1969, " The Influence of Internal Friction on the Stability of High Speed Rotors with Anisotropic Supports," *Journal of Engineering for Industry,* pp. 1105-1113.

Ho, C. H., Scott, R. A., and Eisley, J. G., 1975, "Non-planar, Non-linear Oscillations of a Beam - I. Forced Motions," *International Journal of Non-linear Mechanics*, Vol. 10, pp. 113-127.

Hull, E. H., 1961, "Shaft Whirling as Influenced by Stiffness Asymmetry," *Journal of Engineering for Industry*, pp. 219-226.

Inagaki, T., Kanki, H. and Shiraki, K., 1980, "Response Analysis of a General Asymmetric Rotor-Bearing System," *Journal of Mechanical Design*, Vol. 102, pp.147-157.

Ishida, Y., Ikeda, T., Yamamoto, T. and Akita, T.,1986, "Internal Resonance in a Rotating Shaft System," *Bulletin of JSME*, Vol. 29, No. 251, pp. 1564-1571.

Ishida, Y., Ikeda, T., and Yamamoto, T., 1987, "Transient Vibration of a Rotating Shaft with Nonlinear Spring Characteristics during Acceleration through a Major Critical Speed," *JSME International Journal*, Vol. 30, No. 261, pp 458-466.

Ishida, Y., Ikeda, T., Yamamoto, T., and Murakami, S., 1989, "Nonstationary Vibration of a Rotating Shaft with Nonlinear Spring Characteristics During Acceleration Through a Critical Speed," *JSME International Journal*, Vol. 32, No. 4, pp. 575-584.

Ishida, Y., Ikeda, T., and Yamamoto, T., 1990, "Nonlinear Forced Oscillations Caused by Quartic Nonlinearity in a Rotating Shaft System," *Journal of Vibration and Acoustics*, Vol. 112, pp. 288-297.

Iwatsubo, T., Kanki, H., and Kawai, R., 1972, "Vibration of Asymmetric Rotor Through Critical Speed with Limited Power Supply," *Journal Mechanical Engineering Science*, Vol. 14, No. 3, pp 184-194.

Jeffcott, H. H., 1919, "The Lateral Vibration of Loaded Shafts in the Neighborhood of a Whirl Speed: The Effect of Want of Balance," *Philosophical Magazine*, Ser. 6, 37, 304.

Kammer, D. C. and Schlack, A. L. Jr., 1987, "Effects of Nonconstant Spin Rate on the Vibration of a Rotating Beam," *Journal of Applied Mechanics*, Vol. 54, pp. 305-310.

Kimball, A. L., 1924, "Internal Friction Theory of Shaft Whirling," *General Electric Review*, Vol. 27, No. 4, pp. 244-251.

Krousgrill, C. M. and Bajaj, A. K., 1987, "Complex Nonlinear Dynamics of a Rotating System." *Developments in Mechanics, 20th Midwestern Mech. Conference*, Vol. 14, pp. 832-838.

Kulla, P., 1972, "Dynamics of Spinning Bodies Containing Elastic Rods," *Journal of Spacecraft and Rockets*, Vol. 9, pp. 246-253.

Laurenson, Robert M., 1976, "Modal Analysis of Rotating Flexible Structures," *AIAA Journal*, Vol. 14, No. 16, pp. 1444-1450.

Lewis, F. M., 1932, "Vibration During Acceleration Through a Critical Speed." ASME *Journal of Applied Mechanics,* Vol. 54, pp 235-261.

Mazzilli, C. E. N., 1989, "Subcritical Large-Amplitude Vibrations of Imperfect Rotating Shafts," *Appl. Mech. Rev.*, Vol. 42, No. 11, pp. 157-160.

Meirovitch, L. and Nelson, H. D., 1966, "On the High-Spin Motion of a Satellite Containing Elastic Parts," *Journal of Spacecraft and Rockets,* Vol. 3, pp. 1597-1602.

Moon, F. C., 1987, *Chaotic Vibrations*, New York: John Wiley & Sons.

Nayfeh, Ali Hasan. and Mook, Dean T., 1979, *Nonlinear Oscillations.*, New York: John Wiley & Sons.

Nayfeh, Ali Hasan, 1981, *Introduction to Perturbation Techniques*, New York: John Wiley & Sons.

Newkirk, B. L. and Taylor, N. D., 1925, "Shaft Whirling Due to Oil Action in Journal Bearing," *General Electric Review,* Vol. 28, No. 8.

Nonami, K. and Miyashita, M., 1978, "Problem of Rotor Passing Through Critical Speed with Gyroscopic Effect," *Bulletin of the JSME*, Vol. 21, No. 151, pp 56-63.

Nonami, K. and Miyashita, M., 1979 "Problem of Rotor Passing Through Critical Speed with Gyroscopic Effect," *Bulletin of the JSME*, Vol. 22, No. 169, pp 911-918.

Odeh, F. and Tadjbakhsh, I., 1965, "A Nonlinear Eigenvalue Problem for Rotating Rods," *Arch. Rational Mech. Analysis*, Vol. 20, pp. 81-94.

Rankine, W. J. Mc.Q, 1869, "Centrifugal Whirling of Shafts," *Engineer,* 9 April, XXVI.

Robe, T. R. and Kane, T. R., "Dynamics of an Elastic Satellite, I, II, III," *International Journal of Solids and Structures,* Vol. 3, pp. 333-352, 691-703, 1031-1051.

Shaw, Jinsiang , 1989, "*Non-linear Interactions in Rotordynamics,*" Ph.D. Dissertation, Michigan State University.

Shaw, S. W., 1988, "Chaotic Dynamics of a Slender Beam Rotating about Its Longitudinal Axis," *Journal of Sound and Vibration,* Vol 124, No. 2, pp. 329-343.

Smith, D. M., 1933, "The Motion of a Rotor Carried by a Flexible Shaft in Flexible Bearings," *Proceedings of The Royal Society,* Vol. 142, Series A, pp 92-118.

Stodola, A. A., 1924, *Dampf und Gasturbinen,* Berlin: Julius Springer.

Taylor, H. D., 1940, "Critical-Speed Behavior of Unsymmetrical Shafts," *Journal of Applied Mechanics,* Trans. ASME, Vol. 62, pp A71-A79.

Tondl, A., 1965, *Some Problems of Rotor Dynamics,* London: Chapman and Hall.

Unger, A. and Brull, M. A.,1981, "Parametric Instability of a Rotating Shaft Due to Pulsating Torque," *Journal of Applied Mechanics,* Vol. 48, pp. 948-958.

Vance, John M., 1987, *Rotordynamics of Turbomachinery,* New York: John Wiley & Sons.

Victor, F. and Ellyin, F., 1981, "Acceleration of Unbalanced Rotor Through the Resonance of Supporting Structure," *Journal of Applied Mechanics,* Vol. 48, pp. 419-424.

Wang, C. Y. 1982, "On the Bifurcation Solutions of an Axially Rotating Rod," *Q. J. Mech. Appl. Math.,* Vol. 35, pp. 391-402.

Wiggins, S., 1988, *Global Bifurcations and Chaos: Analytical Methods,* New York: Springer-Verlag Inc.

Yamamoto, T., 1960, "Response Curves at the Critical Speeds of Sub-Harmonic and Summed and Differential Harmonic Oscillations," *Bulletin of JSME*, Vol. 3, No. 12, pp. 397-403.

Yamamoto, T.,1961, "On Sub-Harmonic and Summed and Differential Harmonic Oscillations of Rotating Shaft," *Bulletin of JSME*, Vol. 4, No. 13, pp. 51-58.

Yamamoto, T. and Hayashi, S., 1963, "On the Response Curves and the Stability of Summed and Differential Harmonic Oscillations," *Bulletin of JSME*, Vol. 6, No. 23, pp. 420-429.